Università degli Studi di Padova

DIPARTIMENTO DI FISICA E ASTRONOMIA GALILEO GALILEI

DOTTORATO IN ASTRONOMIA CICLO XXXV

Probing the nature of GCs multiple populations through chemistry: Li and heavy elements

A THESIS PRESENTED IN FULFILMENT OF THE THESIS REQUIREMENT FOR THE DEGREE OF DOCTOR OF PHILOSOPHY IN ASTRONOMY

AUTHOR

JOSÉ LUIS SCHIAPPACASSE ULLOA

SUPERVISOR: DR. SARA LUCATELLO

MAY 30, 2023

PADOVA, ITALIA

To Vittorio, my brother.

Abstract

Globular clusters have been widely studied in terms of light element variations present in their different stellar populations. However, the nature of the polluter(s) responsible for this phenomenon is still debated. The study of heavy elements and their relation to light ones can provide further constraints. To do so, this thesis studied two samples looking to approach the problem from different aspects.

In the first one 217 stars of the metal-poor globular cluster, NGC 6752 were analysed through spectrum synthesis on GIRAFFE and UVES spectra to get the Li, Na, Mg, Al, Ca, Sc, Cu, Y, and Ba abundances. By doing so, this thesis aims both to gain insight into the nature of the polluter(s) responsible for the abundance variations and the C-N, Na-O, Al-Mg anti-correlations associated with the multiple-population phenomenon and to explore the possible contribution of asymptotic giant branch stars of different stellar masses to the internal pollution in the cluster. In addition to a continuous Li depletion of the average content from unevolved to evolved stars, there was detected a large Li spread at every $\log g$. There were identified second-generation stars with Li content suggesting the need for Li production, known to happen in intermediate-mass ($\sim$4-8 $\mathrm{M}_{\odot}$) asymptotic giant branch stars through the Cameron-Fowler mechanism. Moreover, there were not found clear relations between the light s-process elements (represented by Y II) or heavy ones (represented by Ba II) with light elements (Li, Na, or Al). This indicates that the polluter(s) responsible for the Na (Al) or Li production does not produce large amounts of Y II and Ba II. Furthermore, the comparison with models discards a possibly significant contribution to the cluster pollution from AGB stars with masses lower than 5 $\mathrm{M}_{\odot}$.

In the second one, a large sample of 210 stars of 18 globular clusters with a large range of metallicities was analysed. The abundances of Cu, Y, Ba, La, and Eu were derived through spectral synthesis applied to UVES spectra. Using the mentioned data, the present thesis aims to analyse both the individual chemical enrichment and the overall behaviour of these clusters with respect to the galactic field. With some exceptions these clusters follow closely the patterns found in the field for stars with similar metallicity, however, a significant spread was found in some clusters suggesting enrichment

in s- and/or r-process elements. In addition, it was found evidence of a weak -but significant- correlation between Y/Ba and Na in the mid-metallicity regime, which will be further investigated. Finally, intriguing suggestions of different chemical enrichment in n-capture elements between in-situ and accreted clusters, in which the first display a steeper distribution along with the orbital energy compared to the second ones. This result should be compared with chemical evolution models.

Contents

Chapter 1

Galactic Stellar Clusters: State-of-the-Art and Motivation

When we observe the dark sky, there are a large number of stars lighting up the night. All of them with different colours, ages, metallicity, and masses. The latter determines strongly their lifetime, shorter and more chaotic for more massive ones, longer with a quieter end for less massive ones. Although apparently, they look like isolated points, most of the stars were not born alone. In the most accepted scenario, they come from molecular clouds (Lada and Lada, 2003), which through successive contractions and fragmentation become the molecular clouds onto the hotbeds of thousands of stars. Those stars share some features: because they are born within a short period of time from the same material, and in a relatively small space, they can be considered coeval, homogeneous (in terms of chemical composition), and equidistant to us.

The last paragraph defines a gravitationally bound stellar system with a common origin, which is called a stellar cluster. Although there are also stellar associations, which share some features with stellar clusters, they are not gravitationally bound systems. According to stellar cluster characteristics (stellar populations, morphology, size, and location in the galaxy), they can be subdivided into two groups: open clusters (OCs), and globular clusters (GCs). In our Galaxy, the former is known to be less massive having a younger and a more metal-rich population, and they are located mainly in the Galactic disk. In contrast, GCs used to be located mainly in the Galactic Bulge and

Halo, being more massive,older and having a more metal-poor population. Throughout this thesis, We will be focused on the last group and a deeper discussion about it can be found later.

Over the years, the study of stellar clusters has been fundamental not just to understanding stellar physics, age and evolution of stars, but also to the formation and evolution of stellar populations in general. All this knowledge is relevant to a whole range of astrophysical processes, in particular, to study the composition of stellar populations, investigate the formation of the Milky Way (MW), and test the stellar evolution models.

This thesis is mainly focused on the characterisation of Globular clusters using spectroscopy, which, in combination with photometry, allows us to get fundamental information about these objects, such as distance, reddening, age, chemical composition, radial velocity, and metallicity. For decades these methods have been used to build the foundations of our understanding of both OCs and GCs.

The following sections are a brief description of our background of both GCs and OCs, using these techniques.

1.1 Globular Clusters

The name of this kind of stellar cluster comes from its spherical shape. They are mainly located in the Galactic bulge and halo. In fact, they are thought to have provided a considerable contribution to the build-up of the latter (Martell et al., 2011). GCs are metal-poor objects hosting typically several tens of thousands of stars or more. They are as old as the Milky Way itself, with ages ranging between 10 and 13 Gyr. Currently, these clusters do not have interstellar gas and are not forming new stars. Their spherical shape, high-density environment, and old population can be seen in Fig.1.1, which shows a set of Galactic GCs from the Hubble Space Telescope and MPG/ESO 2.2-metre Telescope.

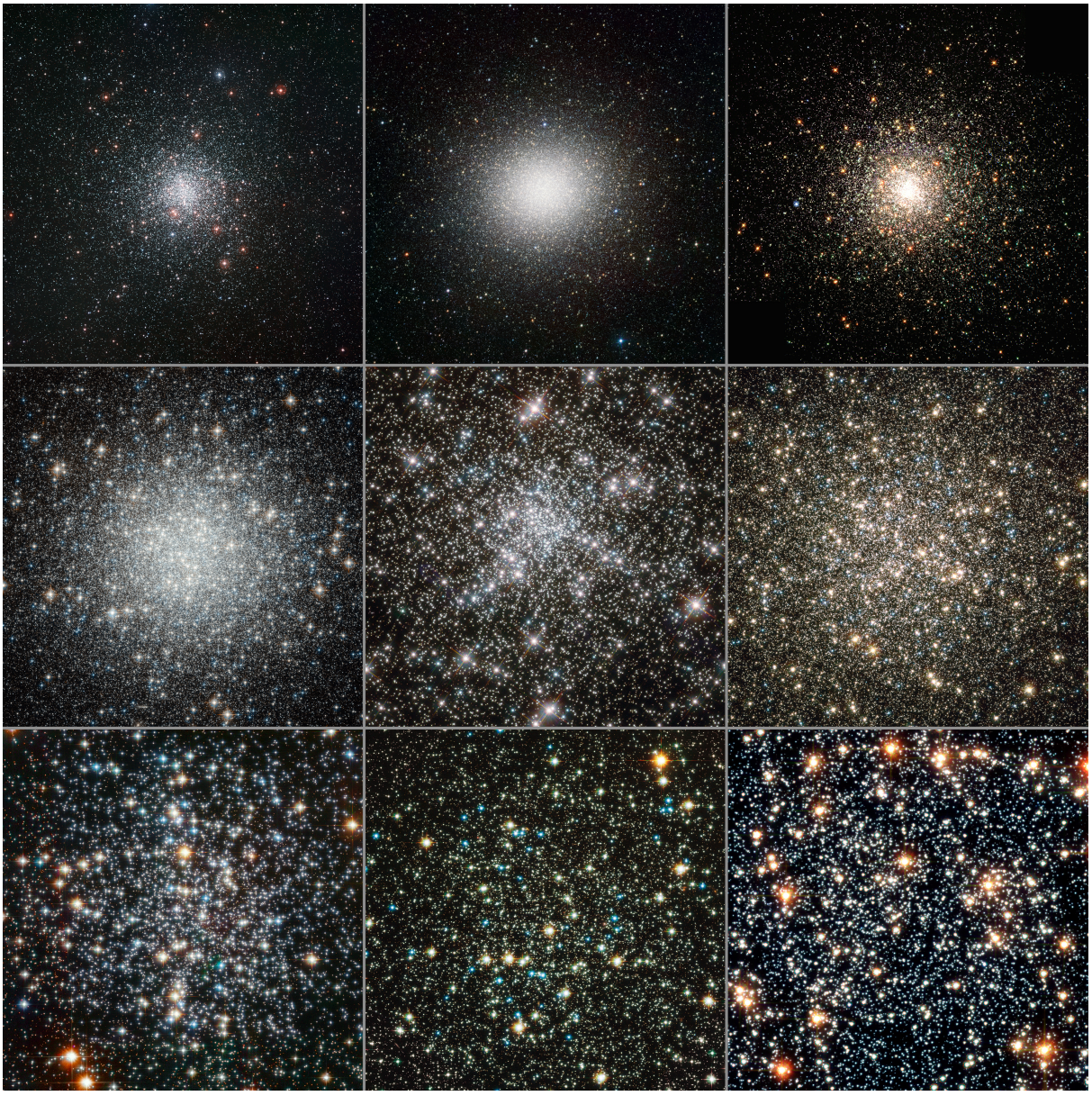

Figure 1.1 Set of globular clusters observed with the Hubble Space Telescope and MPG/ESO 2.2-metre telescope. Source: ESO.

With the exception of some studies exploring the possibility that GCs were more complex objects (e.g., Norris et al., 1981), up to the early 21st century, GCs were considered an excellent example of the simple stellar population (SSP) –a stellar group sharing the same age and initial composition– however early studies would challenge that

idea. The first clues came from different studies (e.g., Osborn 1971, Popper 1947) revealing strong CN variations among giant star members of the same cluster. An example of the findings was shown by Smith and Norris (1982, Fig. 1.2), where there is a clear bi-modality in the strength of the CN bands in three different GCs, however, it was thought to be a purely evolutionary phenomenon. The last indicated that as a star evolves from the main sequence the processed CN is carried from the internal stellar layers to the star surface as a consequence of the continuous mixing (Langer, 1985). Nevertheless, this idea presented shortly some problems, for example, the CN variations were also found in metal-poor GCs where the convective layers are not able to reach deep enough layers to carry the processed material to the stellar surface (Gratton et al., 2004).

The evidence of these features –peculiar to GCS– increased with similar findings which involved altered composition in other elements, such as Na (e.g., Cottrell and Da Costa, 1981, Peterson, 1980), Mg (e.g., Smith and Wirth, 1991), and Al (e.g., Norris et al., 1981). Since the internal mixing was not expected to modify the composition of those species, different ideas were raised, e.g., special mixing associated with dense environments, or a potential relation to non-LTE[1] effects. Furthermore, there were found CN-rich stars to correlate with the Na, and Al content along with depletion of O (e.g., Sneden et al., 1991, 1992). An example is shown in Fig.1.3, where Drake et al. (1992) compared two stars with similar stellar parameters of the GC M4. It shows the CN-strong star is also enhanced in O, Na and Al, in contrast to its CN-weak counterpart.

The presence of those inhomogeneities in GCs left the doubt whether those were caused to internal nucleosynthesis/mixing processes inside the stars or whether the stars were born with altered composition. Additional observations of unevolved stars were needed to shed light on this problem.

Cohen (1999) found for the first time evidence of the CN-CH anti-correlation (see Fig.1.4) in a sample of 79 unevolved stars in the GC M71. This evidence was reinforced by Gratton et al. (2001) by detecting the Na-O anti-correlation among unevolved stars in the GCs NGC 6752 and NGC 6397. In addition, cohen2003 proved that these chemical peculiarities affect the whole star and not only the external layers. The presence of

[1] LTE: local thermodynamic equilibrium

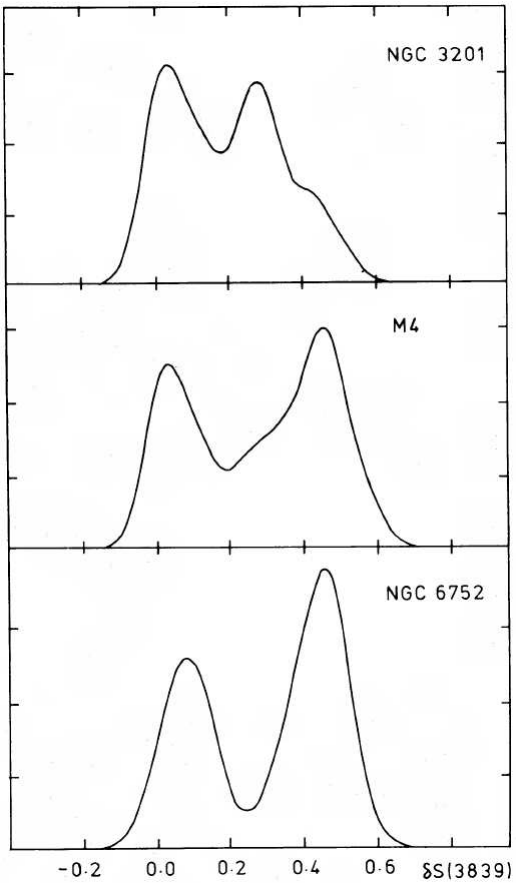

Figure 1.2 Cyanogen (source of CN radicals) distribution in the GCs NGC 3201, M4, and NGC 6752 published by Smith and Norris (1982). It shows a bimodal distribution within giant members of each cluster.

both the particular chemical features among dwarf stars and their effect on the whole structure of the star demonstrates that these chemical peculiarities were part of the stars since their origin.

The list of GCs with these findings increased over the years, however, Carretta et al. (2009) surveyed for the first time a large number of GCs, and through a homogeneous analysis, they confirmed the Na-O anti-correlation in 19 GCs (Fig.1.5). This analysis was later extended, by the same group (Carretta et al., 2009), to Mg and Al (Fig.1.6).

On the other hand, the new photometric instruments have complemented the previous evidence by allowing them to reach dimmer stars and decreasing their photometric errors. In particular, with HST photometry and an appropriate combination of filters,

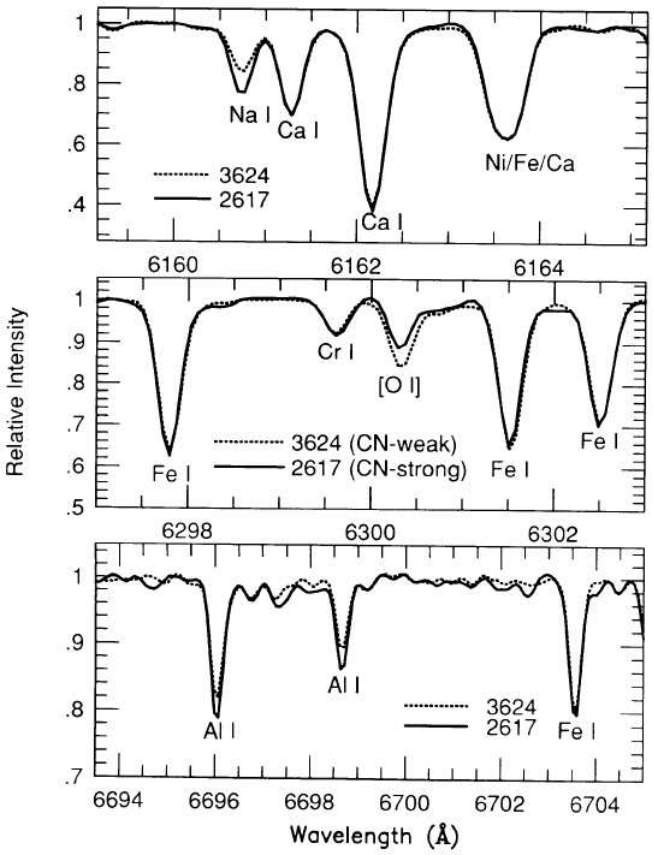

Figure 1.3 Spectra comparison between two M4 members with similar stellar parameters. Drake et al. (1992) showed that the CN-weak star (dotted line) had higher O along with a lower abundance of Na and Al than the CN-strong star (solid line).

we have been able to measure the variation of key molecules, such as NH, CN, CH, and OH even among faint stars. That made possible the study of the phenomenon in a large number of stars along the different evolutionary stages in a considerable number of GCs, which show parallel sequences in every evolutionary stage revealing multiple episodes of star formation. In this regard, important contributions were carried by the confirmation of broad (Milone et al., 2010), or multiple (Piotto et al., 2007) MSs (see. Fig.1.8). The latter, claimed the presence of, at least, three different populations in the GC NGC 2808 each one with a different discrete He content. These multiple sequences have been found also in sub-giant and red giant branch stars being associated with differences in the CNO (Marino et al., 2011) and metallicity (Lee, 2015), respectively.

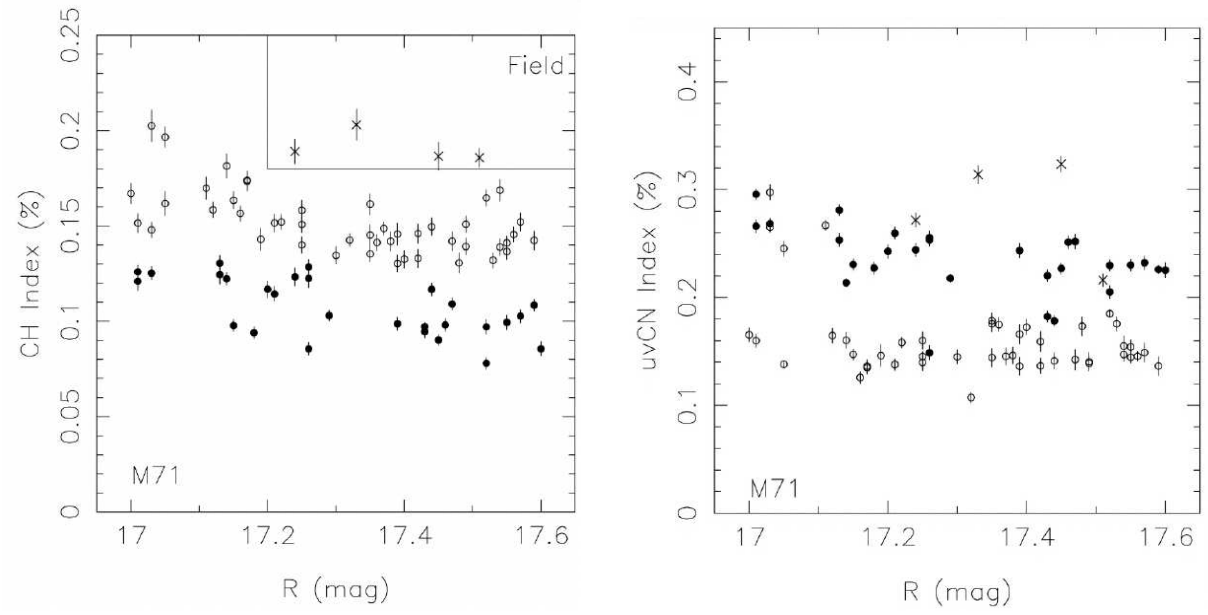

Figure 1.4 CH/CN distribution in a sample of 79 dwarf stars of the GC M 71 reported by Cohen (1999). They constituted the first evidence of CN-CH anti-correlation among unevolved stars within GCs.

Using HST data, Milone et al. (2017) noticed that using a specific combination of pass-bands the stars of a given GCs were grouped in well-defined locus. Fig.1.7 shows an example of the so-called *Chromosome Maps*, which is a pseudo-two-colour diagram which is sensitive to both the He (x-axis) and N (y-axis) content. Most of the GCs display two groups of stars in their diagram: stars with low content of N and He (green symbols) and the ones with high abundances in those species (red symbols). GCs displaying two distinct groups of stars were labelled as Type We clusters. Nevertheless, there are a few GCs that display more than two groups in their diagram reflecting a more complex evolution than Type We clusters. Those GCs were classified as a different type and they were named Type II clusters.

The recently described photometric and spectroscopic findings were part of a long contribution which makes us change our view with respect to GCs. Currently, there is a general consensus that GCs host multiple stellar populations (MSP) which were formed in different star formation episodes. Moreover, these MSPs display chemical inhomogeneities mainly in hot H-burning species. This phenomenon has been observed in all

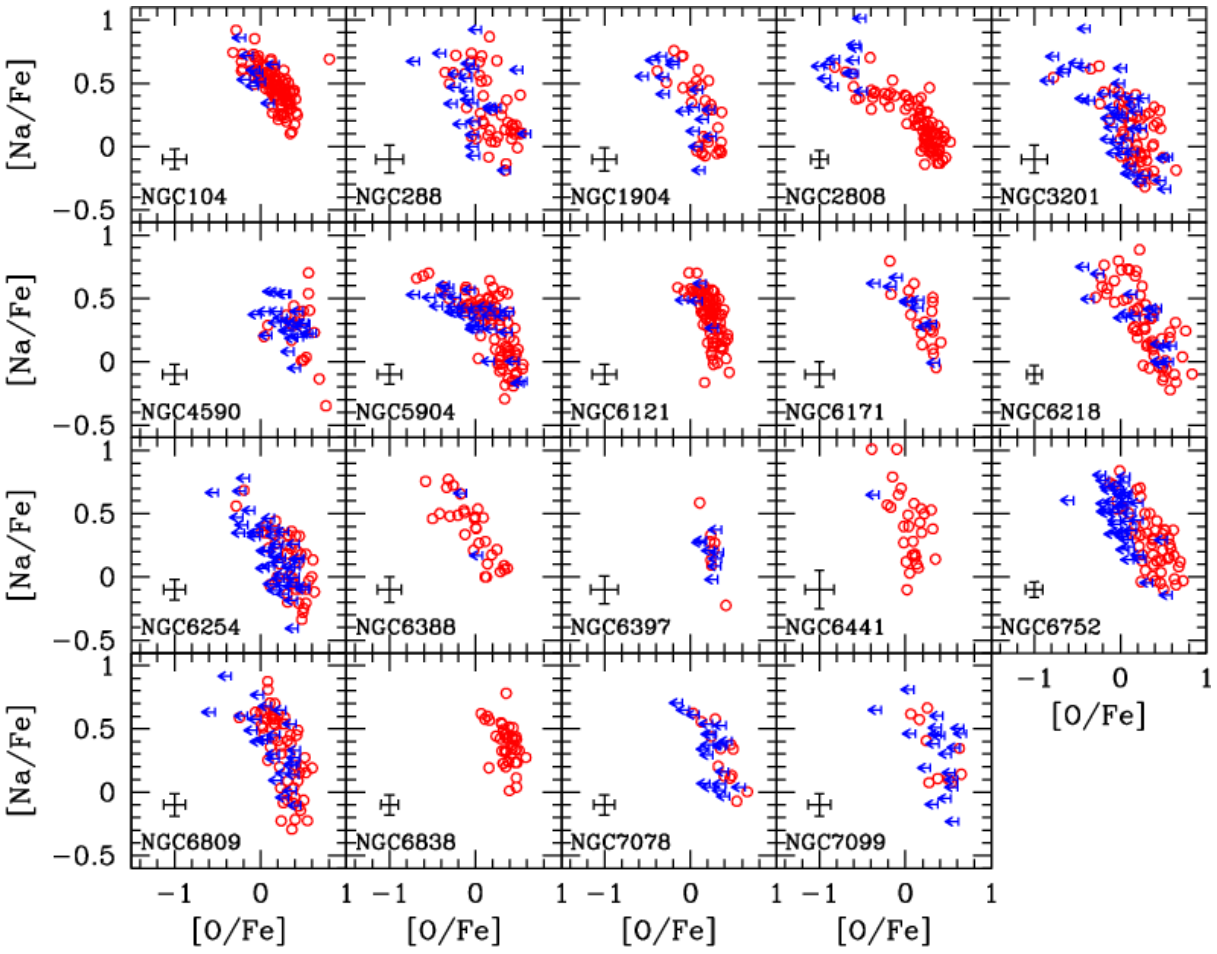

Figure 1.5 Carretta et al. (2009) showed the presence of the Na-O anti-correlation in all the GCs studied, although, the shape and extension vary from cluster to cluster.

the well-studied GCs.

1.1.1 Multiple Stellar Population

The MSP phenomenon is a peculiar feature of GCs, which distinguishes them from stellar association and OCs. While there are many proposed scenarios, the basic assumption (Fig.1.9) is that the first stellar population is formed from the pristine gas of the molecular cloud with a given initial chemical composition. Along their lives, a fraction of these stars evolve modifying their composition. Eventually, all these new set chemical species are released into the intracluster medium, which is mixed with

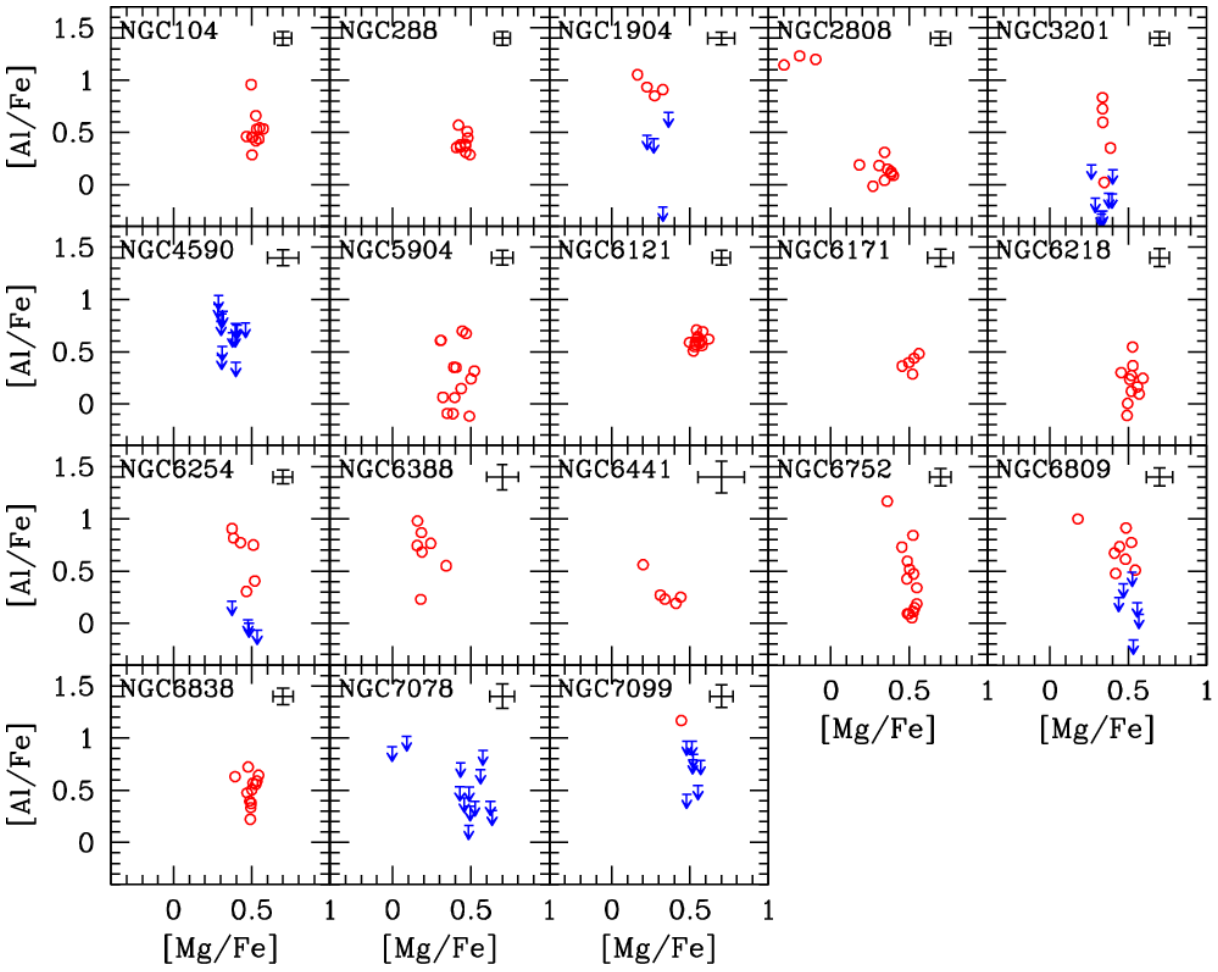

Figure 1.6 Al-Mg anti-correlation found by Carretta et al. (2009). It shows that not all the clusters display this chemical pattern.

the pristine gas. A second generation of stars (and potentially a third one) is created from this material, which keeps the signatures of their progenitors. This phenomenon is present in all the evolutionary phases of the clusters, from unevolved to evolved stars. From the spectroscopic point of view, the relation among the chemical variation of light elements within a given GC follows a clear pattern, which correlates or anti-correlates depending on the pair of elements considered. Always with as starting point the chemical abundances recorded by supernovae, meaning there are no stars with higher O than the SN-II ejecta or with Na lower than the abundance found in the field for the correspondent metallicity (Gratton et al., 2019).

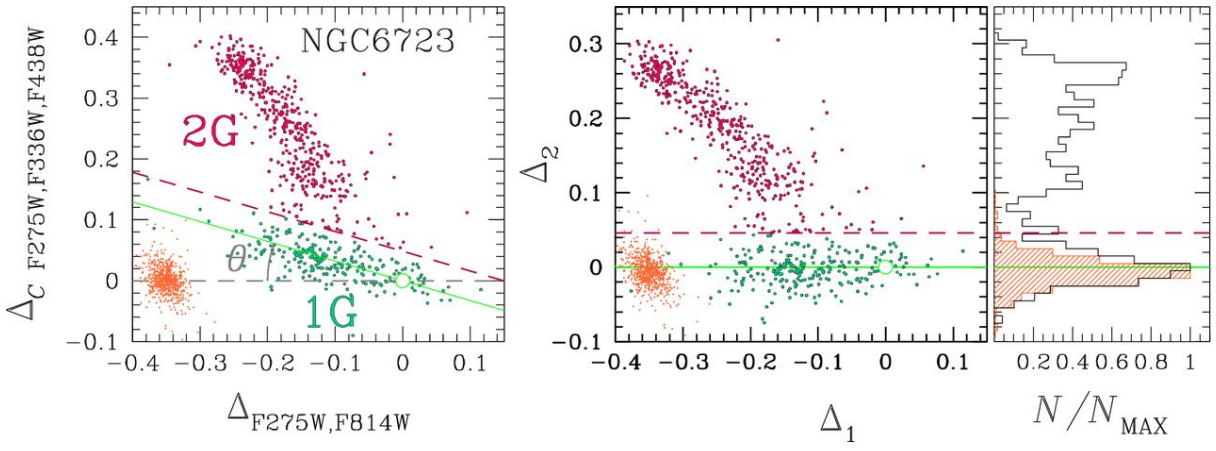

Figure 1.7 Scheme of the multiple stellar population phenomenon.

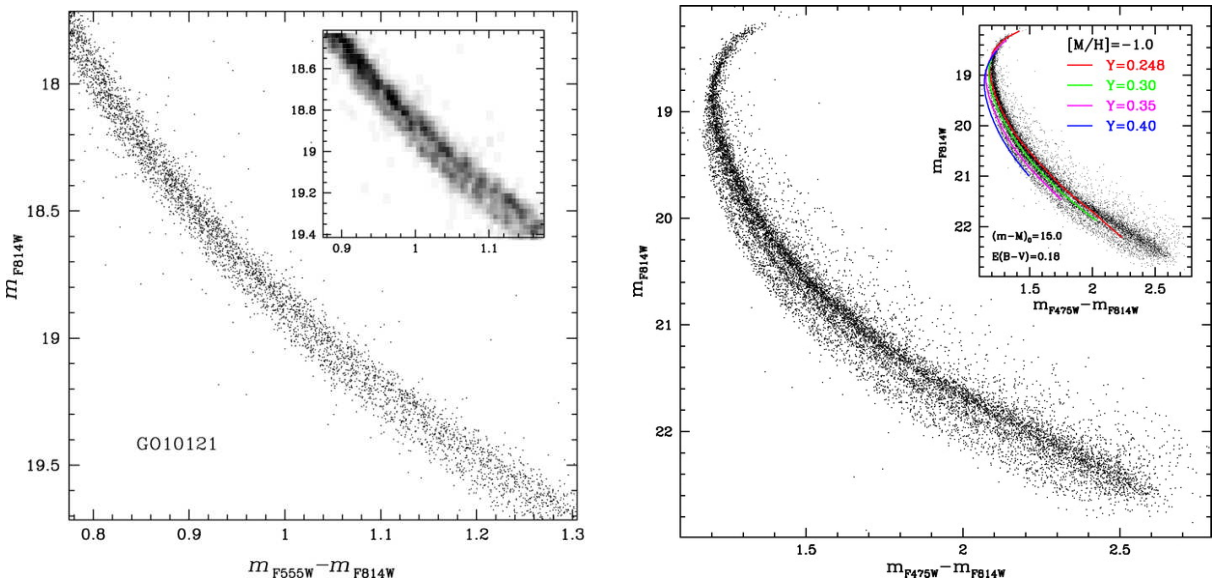

Figure 1.8 Photometric evidence of the broad MS in the GC NGC 6752 (left panel; Milone et al., 2010) and NGC 2808 (right panel; Piotto et al., 2007), which is a clear signature of the presence of MSP.

1.1.2 Peculiar Chemical Patterns

Although not all the anti-correlations are present in the same manner, those peculiar chemical patterns are proper to GCs. The relations between C/N-O, or Na-O, and Mg-Al indicate nucleosynthesis through proton-capture (p-capture) in the H-burning. Those

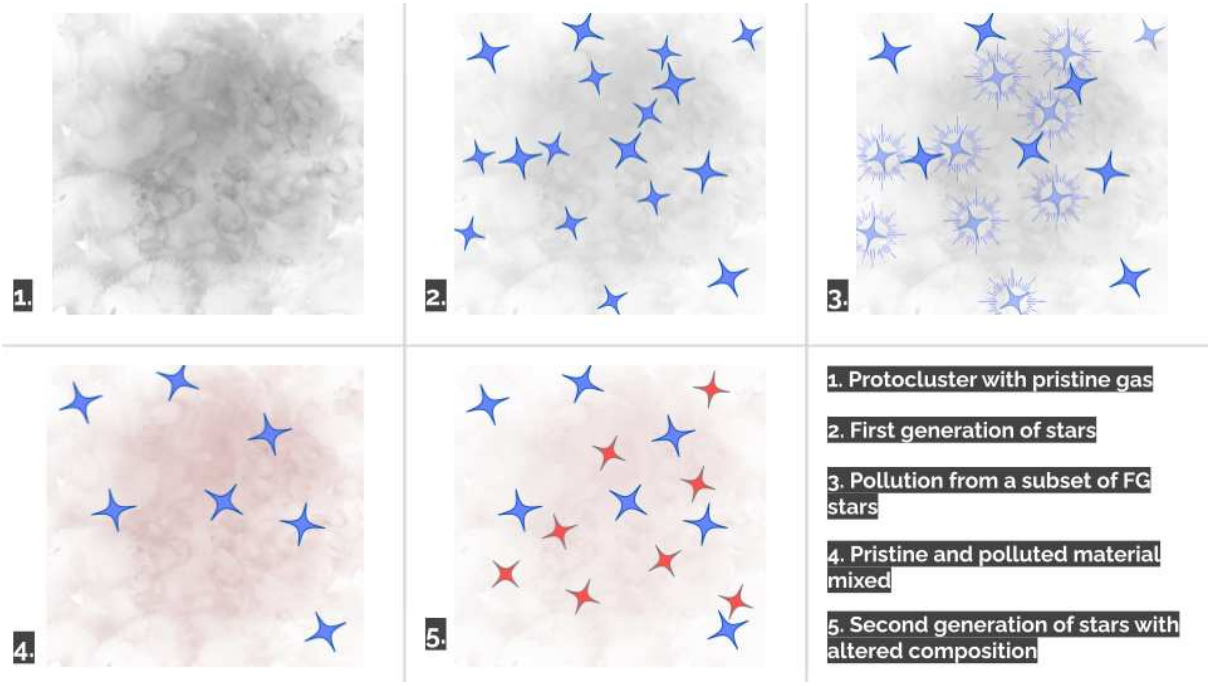

Figure 1.9 Scheme of the multiple stellar population phenomenon.

nucleosynthetic processes occur through the CNO cycle, NeNa cycle, and the MgAl chain.

As it is shown in Fig.1.10, the CN cycle (left branch) is activated at 10 MK and it produces ^{13}C and ^{14}N at expenses of ^{12}C. At temperatures higher than 40 MK, the activation of the NO cycle (right branch) happens and ^{16}O is depleted to produce ^{14}N. Then, the anti-correlation N-O appears as a consequence of this cycle. On the other hand, once the temperature reaches more than 70 MK, the NeNa cycle is activated, producing ^{23}Na. Finally, at temperatures higher than 80 MK, the MgAl chain takes place and the ^{24}Mg gives away to ^{27}Al and ^{28}Si at even higher temperatures, which is reflected in the Al-Mg anti-correlation.

Further, and more recent studies have extended this analysis to other species that could be affected by the MSP phenomenon. For example, (Cohen and Kirby, 2012) showed variations in K, Ca, and Sc in the GC NGC 2419. Elements like K or Ca can be produced from p-capture on Ar nuclei by burning H at even higher temperatures (Ventura et al., 2012) than the one needed in lighter elements. Recently Carretta and

Bragaglia (2021) analysed Ca, and Sc in a large set of GCs finding an enrichment of Ca in NGC 4833, NGC 6715, NGC 6402, NGC 5296, NGC 5824, and ω-Cen with respect to field stars of similar metallicities. In those GCs, they found higher Ca abundances in stars belonging to SG.

Low-mass stars found in Galactic GCs are not capable of reaching the high temperatures as the ones required to ignite those nucleosynthetic processes. Furthermore, the fact that the anti-correlations have been detected all the way down to the main sequence turn-off (e.g., Gratton et al., 2001), and with similar amplitudes to those measured among giants, indicates that the abundance variations are present since birth and involve the entirety of the stars.

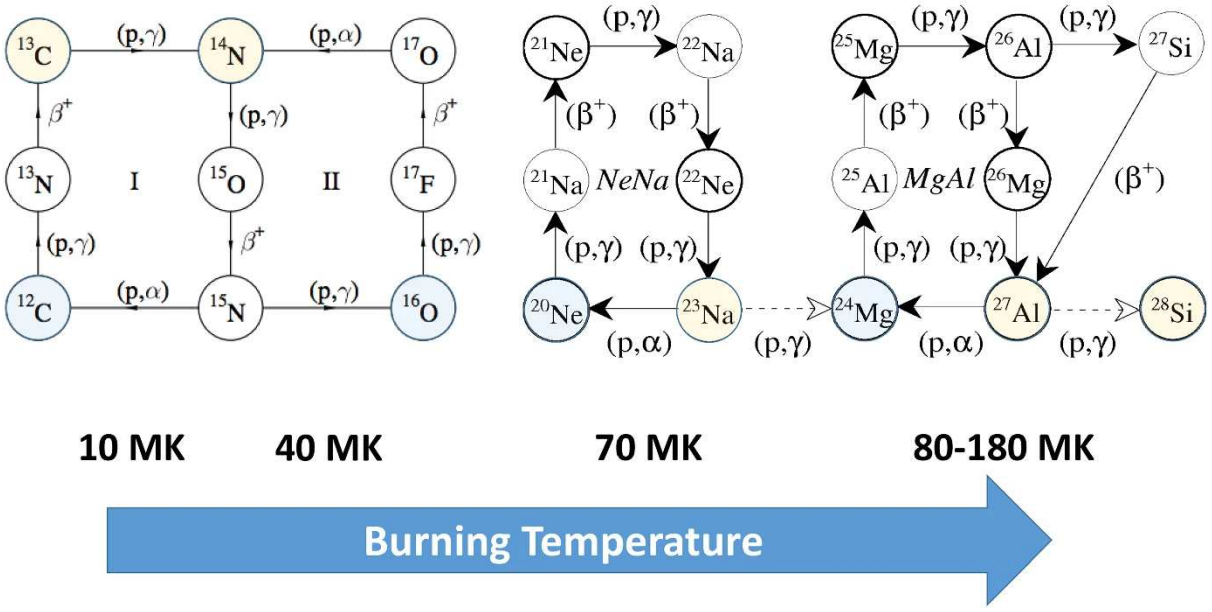

Figure 1.10 CNO, NeNa, and MgAl cycles. It shows activation temperatures, and the main produced (orange) and destroyed (blue) elements. Source: Gratton et al. (2019)

All burning processes mentioned are activated at different temperature scales, then can be related to different stellar masses using stellar evolution models. This information is crucial to understand the nature of the pollution responsible.

1.1.3 Polluters

Because the chemical peculiarities found in SG stars are not produced at their interior, an external source of pollution is needed to reproduce the observational evidence. The source of these anomalies is the so-called *polluters*.

Currently, it is thought that the MSP phenomenon is given by a complex process of pollution from one (or more) source(s). These source(s) must be able to reproduce some key observation in the GCs: the altered light element composition without affecting the iron abundance of the cluster members. Then, the polluters should be able to synthesise hot H-burning species, provide a mechanism to move the altered material to their surfaces, and finally pollute the cluster by releasing the polluted material at low velocities.

Over the years, different studies have speculated on the nature of these polluters. The most discussed candidates are intermediate-mass ($\sim$4-8$M_{\odot}$) asymptotic giant branch (AGB; Ventura et al. 2001) stars, fast-rotating massive stars (FRMS; Meynet et al. 2006), and massive binaries (de Mink et al., 2009). There are, however, a few other proposed such as super-AGB stars and super-massive stars. Nevertheless, none of the candidates accounts for all the observational evidence and in order to match the models with the observations all the polluter candidates require additional conditions, for example, some degree of dilution with the unpolluted gas (or *pristine gas*) from which FG stars were formed (D'Ercole et al., 2011). Then, by studying the chemical footprints present in GCs, the origin of that pollution can be constrained.

In the following, We present the pros and cons of the favourite candidates. For details, We refer to the reader to the cited paper in the previous paragraph.

1.1.3.1 Fast-Rotating Massive Stars

Decressin et al. (2007) proposes fast rotating (V_{ini}=800 km/s), massive ($20_{\odot}$<M<$120M_{\odot}$) stars as the source of the GC abundance variations. Observational evidence indicates these stars are more likely to be present in GCs than in the lesser dense environment (e.g., Dufton et al., 2006). These kinds of stars can produce in their cores the H-burning

elements involved in the MSP phenomenon. Due to their fast rotation are able to efficiently bring the material processed to the surface.

Fig.1.11 shows a representation of the pollution process of a FRMS from (Decressin et al., 2007). Different colours represent the chemical composition, being greenish for the chemical composition at the beginning (FG-like), and blue and red for the one coming from H-burning and He-burning processes. The high rotational velocities reached by those stars produce a large fraction of mass lost through the so-called mechanical wind building up an equatorial disc, which becomes rich in the H-burning products found in SG stars. Later, the material of the disc is released as slow winds which do not leave the cluster. Then the star evolves (lower image of Fig.1.11), and the radiative fast winds take centre stage. This He-burning-rich material is released and it cannot be retained by the cluster. Therefore, the cluster is polluted just with H-burning species through slow winds.

However, the FRMS scenario also fails in the expected nucleosynthesis yields. In particular, as noted by Renzini (2008), because this scenario expects to produce a continuous He spread, it struggles with explaining the discrete He spread observed in GCs, such as ω-Cen and NGC 2808.

1.1.3.2 Interactive Massive Binary Stars

On the report of the observations, most of the massive stars were part of binary systems. In this scenario, two interacting massive stars are the source of intracluster pollution. According the models, a star with 20 $M_{\odot}$ would lose about 10 $M_{\odot}$ through this mechanism (Bastian and Lardo, 2018).

As can be seen from Fig.1.12, one of the binary system members synthesise the elements involved in the MSP phenomenon in its interior. The star increases its size and reaches the critical radius. At this point, the companion strips and accretes the unprocessed material from the external layer and deeper layers which are middle-processed are released out of the binary system at low velocities.

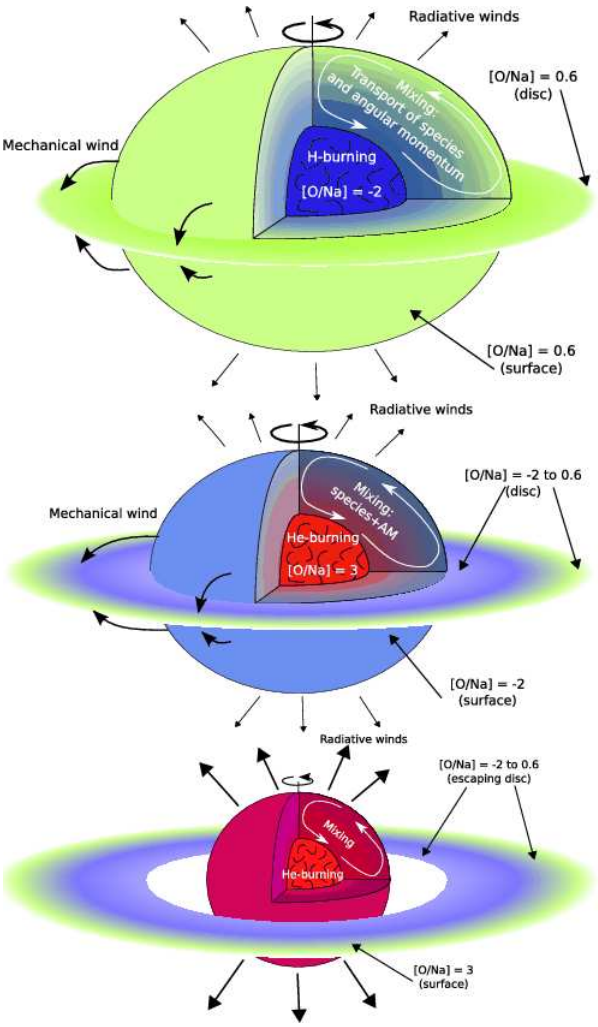

Figure 1.11 Representation of the mechanism through FRMS pollutes the intracluster medium from Decressin et al. (2007). Different colours show different chemical compositions.

Although this mechanism is able to reproduce the chemical variations cluster to cluster (Bastian and Lardo, 2018), the models are highly dependent on different parameters such as the interaction time and the mass ratios between the stars, which require fine-tuning.

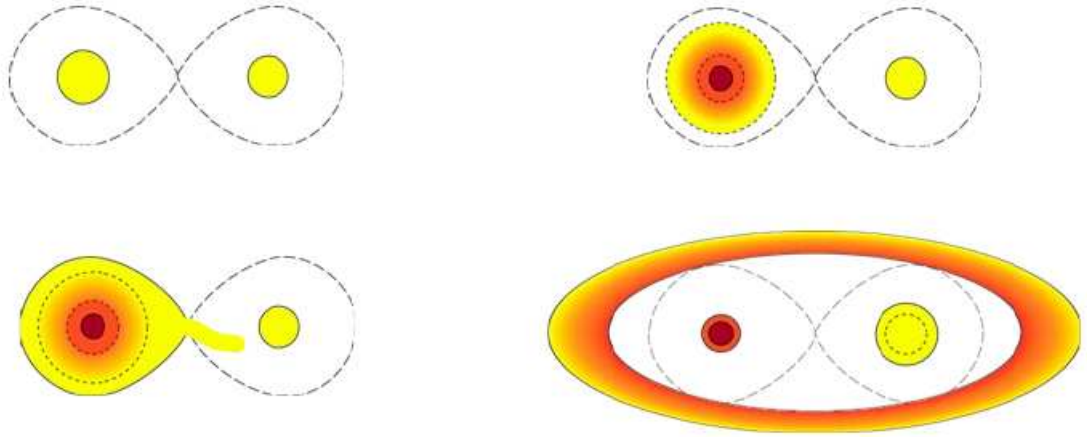

Figure 1.12 Yellow, orange, and red colours represent an unprocessed, middle-processed and strongly-processed material. Source: de Mink slides

1.1.3.3 Intermediate-Mass Asymptotic Giant Branch Stars

Stars with masses between $\sim$1.2$M_\odot$ and 8$M_\odot$ experience the AGB phase, producing a large variety of elements which are released to the intracluster medium through periodic pulsations. Along its evolution, depending on its mass, the star is able to produce H-burning species through the CNO cycle, and MgAl and NeNa chains, which is mainly done during the first and second dredge-up. When the star reaches the AGB phase, the production of neutron capture (n-capture) elements begins in its He-burning shell (See Fig.1.13). The He fusion triggers instability and generates mixing by convection in the shell. The star expands ending up in a dredge-up episode, which brings the processed material to the stellar surface. Finally, the star contracts and the process begins again.

Intermediate-mass AGB stars (4-8$M_\odot$) are able to produce the elements involved in the MSP phenomenon, without altering the Fe content, and to pollute the environment with them through slow winds which are retained by the cluster. However, the AGB model predictions are not in full agreement with the observational evidence (e.g., Doherty et al., 2014, Ventura and D'Antona, 2009).

Some authors have extended the mass range to more massive AGB stars. The so-called super-AGB stars (8-12$M_\odot$) ignite carbon at their nucleus. In this scenario, it

is considered that while the Na-enhance material is mostly produced by lower mass stars, the O-depleted one is provided by more massive stars (Renzini et al., 2015).

There are still many challenges to be addressed such as the efficiency of the third dredge-up, extra-mixing processes, or exploring the effects of magnetic field and rotation (Karakas, 2011). Moreover, there is a lack of AGB yield models for metal-poor for different masses.

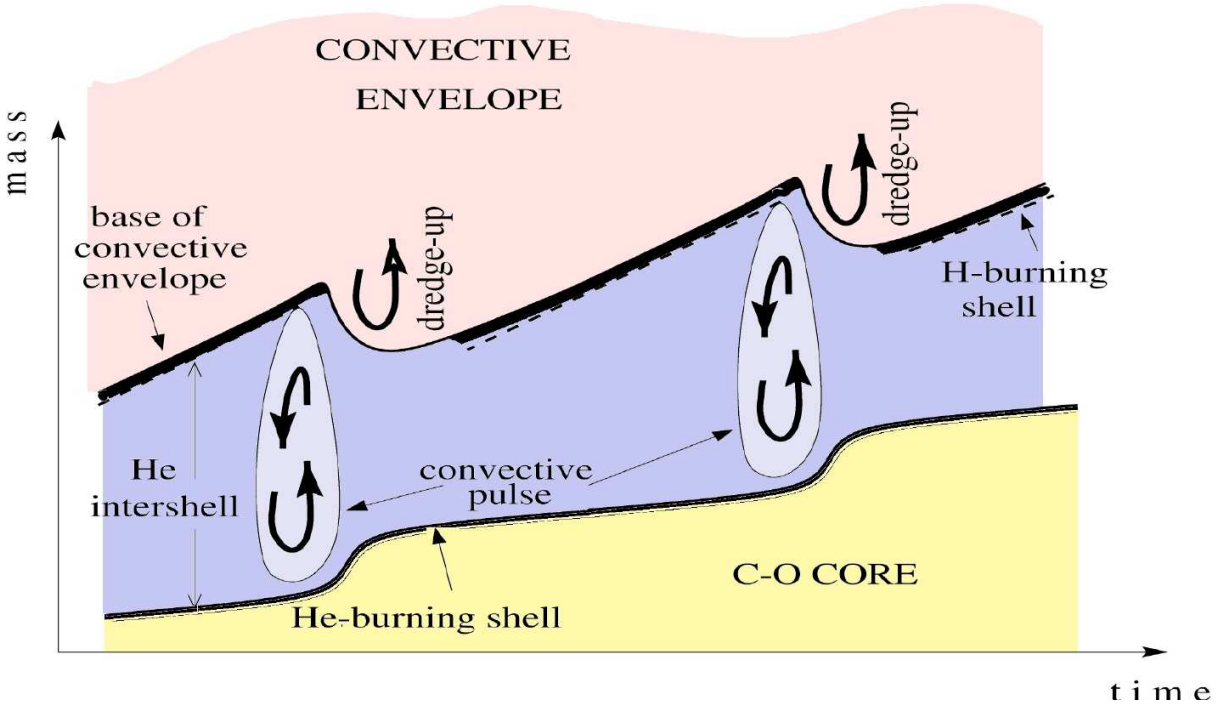

Figure 1.13 Internal structure of an AGB star and its change with time. Source: Modified from Lugaro et al. (2008)

1.1.3.4 Other polluter candidates

A few additional candidates have been proposed, for example, super-massive stars (Denissenkov and Hartwick, 2014). In this scenario, the chemical anomalies are produced by a super-massive star (10^3-$10^4 M_\odot$) formed in the centre of young GCs, where the stars sink and collide (Fig.1.14). The yields of this polluter could match the observed chemical patterns once the dilution with pristine gas is considered. Then, this mixed gas is accreted by the protostars of the cluster.

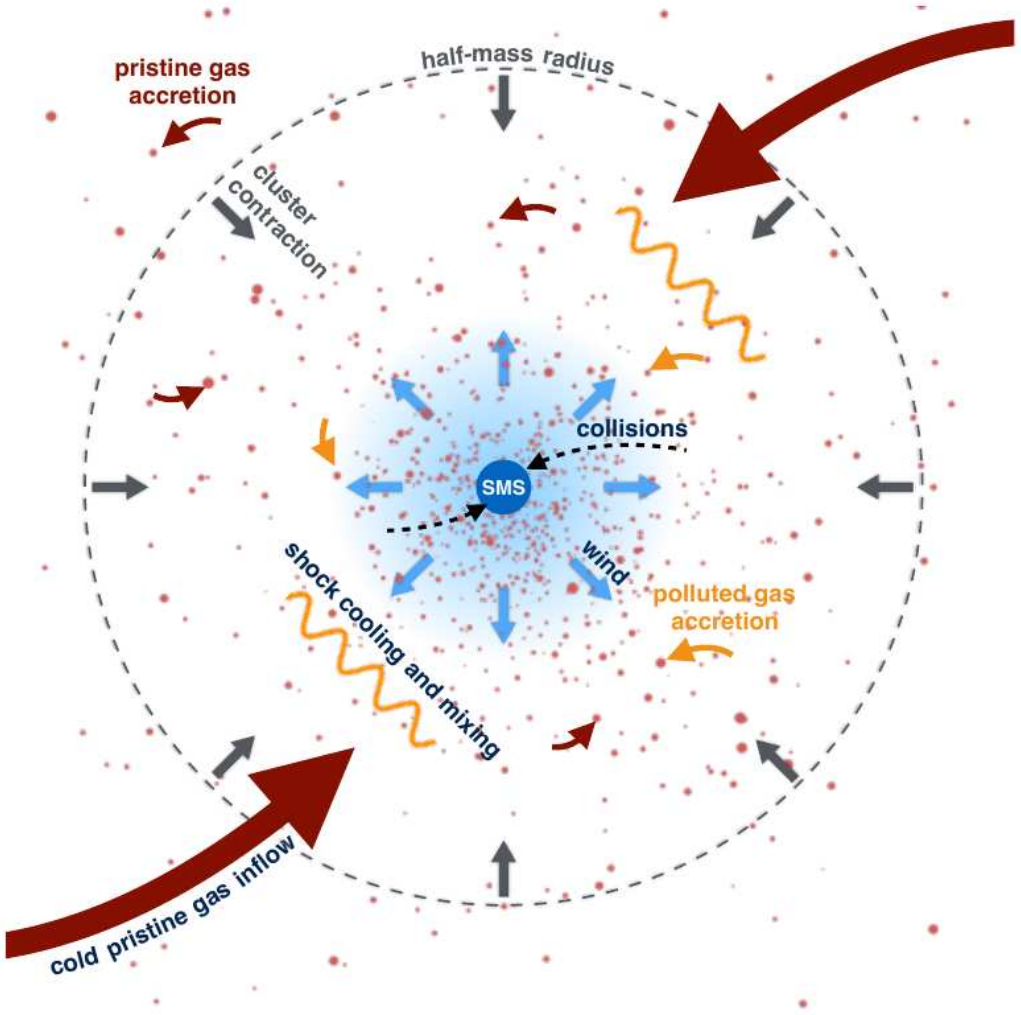

Figure 1.14 Scheme of the super-massive stars as polluter candidate. Source: Modified from Gieles et al. (2018)

1.1.4 Interesting chemical patterns

1.1.4.1 Lithium

Another element which has been the object of interest in this context is Li. A fragile element, it is easily burned into ^{4}He at low temperatures ($\sim 2.5\times10^6$ K). Li is undetectable in stars brighter than the RGB-bump. When the stars leave the main sequence, they go through their sub-giant branch phase and climb up the RGB. Then, the star experiences dredge-up episodes and a mixing process, which brings to the stellar surface

material processed in layers where the temperature is high enough to continuously decrease Li. During the RGB-bump, the bottom envelope of the stars deepens and reaches even higher temperatures probably due to an extra mixing (Lattanzio et al., 2015), which burns the last Li atoms. Gratton et al. (2000) looked at the behaviour of Li in metal-poor field stars as they evolve, finding the expected drop, with negligible dispersion among stars in the same evolutionary stage (Fig.1.15).

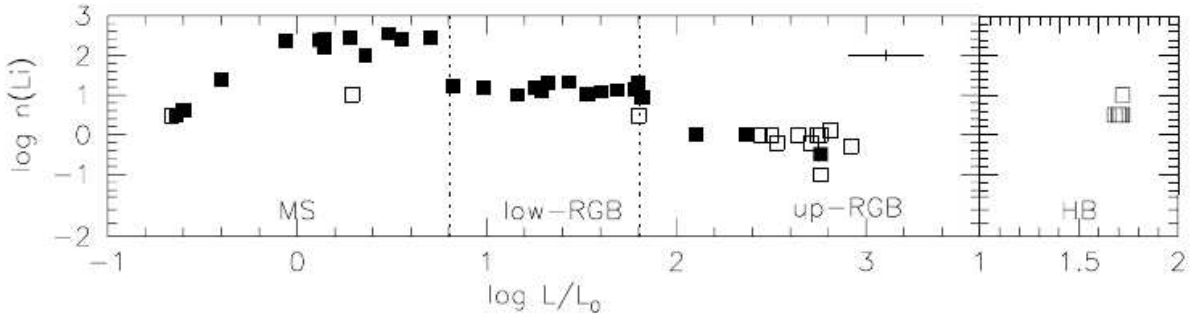

Figure 1.15 log n(Li) as a function of log L/L_0 in metal-poor field stars. Source: Modified from Gratton et al. (2000).

In the hot H-burning processed material – which must have reached considerably higher temperatures to activate the NeNa and MgAl cycles typical of the observed SG abundances – lithium should be obliterated. Therefore, stars belonging to the SG should contain low amounts of Li, anti-correlating with the Na and Al abundances.

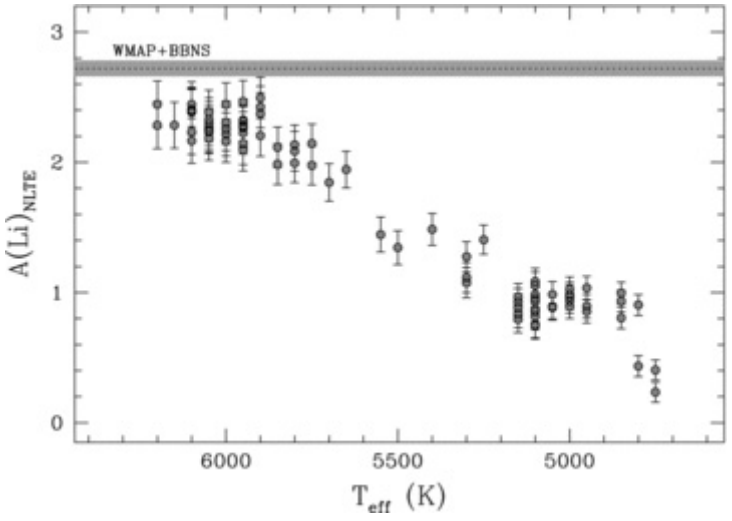

Figure 1.16 $A(Li)_{NLTE}$ as a function of T_{eff} in the GCs M 4. Source: Mucciarelli et al. (2011)

So far, a limited number of studies have looked at Li in GCs in conjunction with other light elements involved in (anti)correlations: as this investigation requires targeting objects below the RGB bump, it is much more observationally expensive. Some studies that have looked at the Li content along with other light elements involved in the MSP phenomenon found surprising results in this regard. For example, NGC 6121 (D'Orazi and Marino, 2010, Mucciarelli et al., 2011), NGC 6218 (D'Orazi et al., 2014), and NGC 1904, NGC 2808, and NGC 362 (D'Orazi et al., 2015) showed considerable Li abundance among SG stars. Shen et al. (2010) analysed a large sample of turn-off (TO) stars in NGC 6752. They found a Li-O correlation with a shallower slope than expected, which they interpret as a need for Li production in the polluters. Later, Gruyters et al. (2014) confirmed the Li-Na anti-correlation in both evolved and unevolved members of the same cluster. They also reported a fraction of intermediate-population (mildly Al-rich) stars with Li abundance similar to the abundance in FG stars. Detecting Li-rich stars among Al-rich (or Na-rich) stars would suggest the need for Li production, and hence the contribution of a mechanism/nucleosynthetic site capable of Li production.

1.1.4.2 Heavy elements

Heavy elements have nuclei where the number of protons is large enough to produce the electrostatic repulsion needed to avoid the fusion with charge particles (α/proton capture). Instead, these elements are produced by capturing neutrons. There are two ways that can make possible these nucleosynthetic processes: rapid neutron capture, and slow neutron capture. These nuclear reactions start with a stable isotope which captures a neutron. Next, the new isotope can either capture another neutron or beta decay to a new stable isotope. The result is going to depend on both the neutron density and the time scale of β^- decay. Then, if the neutron density is high enough for the isotope to capture a new neutron, then the process will continue, if not, the isotope will have time to decay before capturing a new neutron. An example is the following:

$$^{56}Fe + n \rightarrow ^{57} Fe + n \rightarrow ^{58} Fe + n \rightarrow ^{59} Fe \begin{cases} \nearrow + n \rightarrow ^{60} Fe \\ \searrow \ ^{59}Co \end{cases}$$

While the elements made through the rapid process are called r-process elements, the ones made by the slow process are called s-process elements. These two processes are crucial for the understanding of chemical evolution due to they are able to make half of the elements heavier than iron. Figure 1.17 from Kobayashi et al. (2020) shows the linear abundance of the elements with respect to the Sun colour-coded by the source responsible for their nucleosynthesis. Slow and rapid neutron-capture (n-capture) elements are mainly produced by core-collapse Supernovae and AGB stars.

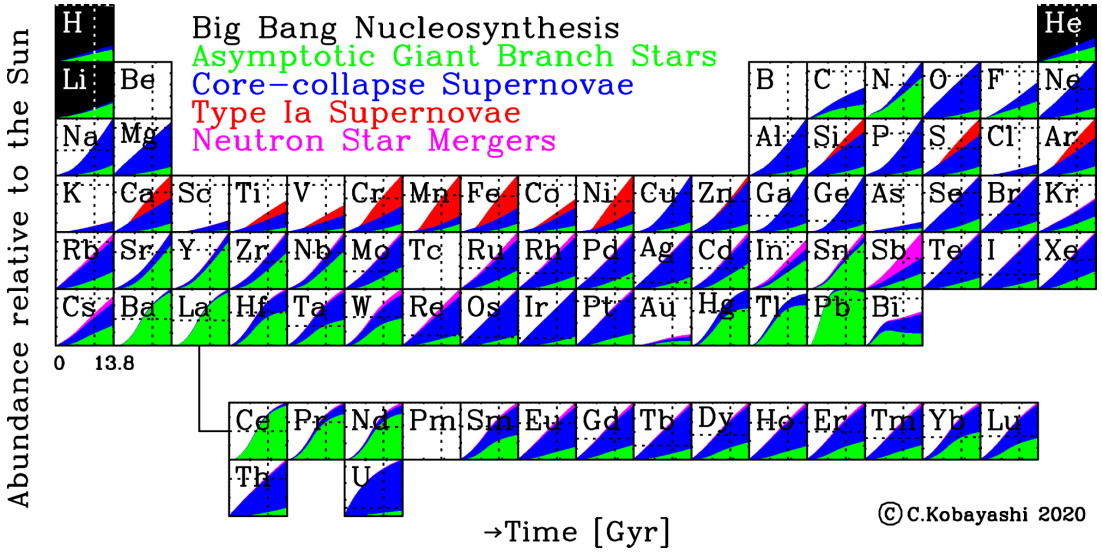

Figure 1.17 Periodic table showing the source of the different elements: Linear abundance with respect to the Sun, as a function of the time (from the Big Bang to the present). Source:Kobayashi et al. (2020)

In the solar system, we see there are clear peaks in specific n-capture elements (see Fig.1.18; Cowan and Thielemann, 2004). This happens in isotopes with a low neutron capture cross-section reducing the probability of capturing a new neutron. The last occurs when either the number of neutrons and/or protons are 2, 8, 20, 50, 82, and 126,

which are known as *magic numbers*. While r-process peaks are produced in unstable isotopes with neutron magic numbers, s-process peaks happen in stable isotopes. As it is shown in the same figure, those peaks are slightly shifted, being r-process peaks located towards lower Z.

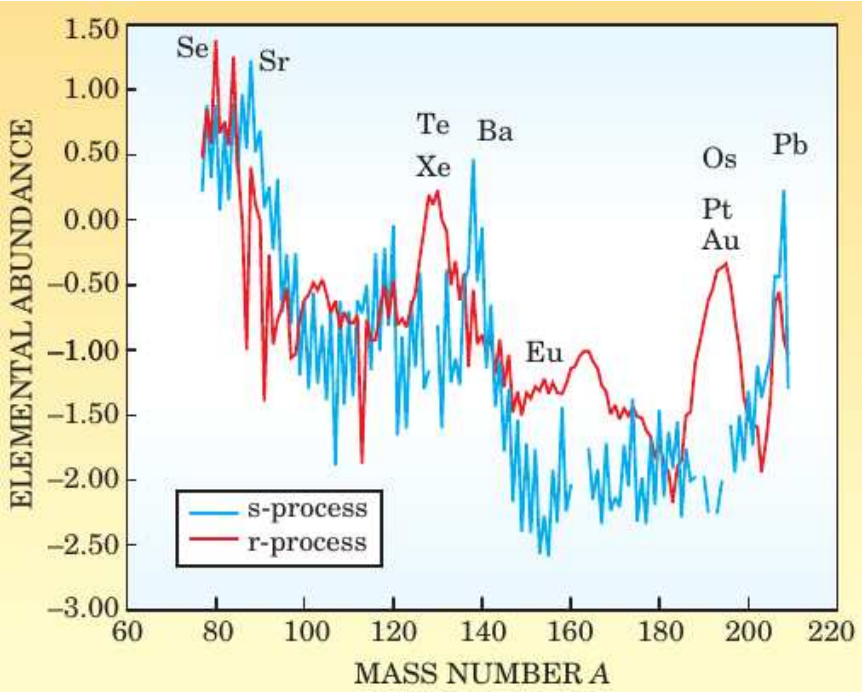

Figure 1.18 Solar abundance distribution of n-capture elements. It shows clearly the s-process and r-process abundance peaks given by the magic numbers. Source: Cowan and Thielemann (2004).

The n-capture species have been the object of limited investigations in GCs so far: studies have shown that they display quite homogeneous abundances in most clusters (e.g., Cohen, 2011, D'Orazi et al., 2010), with a few exceptions (e.g. M22, M15, see below).

1.1.4.3 s-process elements

Slow process elements can be divided into two groups which can be related to different nucleosynthetic sites: i) the weak s-process elements refer to the lighter species (l_s; Z<40, e.g., Y), which are produced in massive stars (M>13$M_\odot$), and ii) the main s-process elements refer to heavier species (h_s; 37<Z<84, e.g., Ba), which are mainly produced in

low-mass AGB stars (1.3$M_{\odot}$<M<4$M_{\odot}$). Other s-process sources have been proposed, for example, it has been shown that fast-rotating massive stars (M≥8-12 $M_{\odot}$) can increase drastically the production of s-process elements, such as Sr, Ba, or La, compared to their non-rotating counterparts (Shingles et al., 2014). Nevertheless, it would produce them at later stages of their evolution, releasing their material during the core-collapse supernova explosion, which cannot be held in most of the cluster (D'Orazi et al., 2013). On the other hand, models have shown that FRMS could also produce the lightest s-process elements. Therefore, the study of the s-process elements can help to shed light on the nature of the polluters.

Nevertheless, the most important contributors are low- and intermediate-mass AGB stars (∼1.2-8.0 $M_{\odot}$) which produce s-process elements during their thermal pulses. During the third dredge-up, the star can make different s-process elements from the lightest to the heavier up to Pb. It is important to note that the AGB star models show that their yields depend strongly on their initial stellar mass (and metallicity), with AGB stars with lower masses more efficiently producing heavier s-process elements (e.g., Ba, and La), and lighter s-process elements (e.g. Sr, and Y) by more massive AGB stars (Karakas and Lattanzio, 2014). Then, by analyzing the behaviour of s-process elements within the cluster populations one can tease out a further piece of the puzzle in the study of the nature of the polluters.

There are only a few GCs that show inhomogeneities in their s-process element distribution. For those clusters, there is also evidence of a considerable iron spread. A classic example is the case of M 22 (Marino et al., 2009), and NGC 7089 (Yong et al., 2014). The first shows a bimodal distribution of s-process elements (Y, Zr, and Ba) without any evidence of correlation with Na, O, and Al. As shown in Fig.1.19, the second displays a potentially bimodal distribution with a large dispersion of heavy elements (Y, Zr, La, Nd, and Pb), however, without strong evidence with Na.

It is worth noticing that even if it is expected some degree of s-process element contribution from AGB, the pollution of intermediate-mass AGB stars of light elements is expected to happen on a timescale of ~ 100 Myr (Schaller et al., 1992), but the contribution of low-mass AGB stars with s-process elements occurs no earlier than ~ 0.5 Gyr (Gratton et al., 2012), which would imply a considerable delay in the cluster pollution

coming from AGB stars. In fact, photometric evidence has shown extended or multiple main sequences in Magellanic Cloud GCs younger than 400 Myr (Milone et al., 2017), which have been associated with the presence of MSP.

1.1.4.4 r-process elements

The production of r-process elements requires very high neutron densities, and it is currently thought to take place in core-collapse Supernovae (Cowan et al., 1991) and neutron stars mergers (Kasen et al., 2017). Such objects would be responsible for the early enrichment of elements like Eu in the MW. Halo field stars, [Eu/Fe] shows a slightly enhanced distribution with respect to the Sun, which decreases toward higher metallicities (Venn et al., 2004), and GCs follow closely the same metallicity.

In most of the clusters, r-process elements display a quite homogeneous distribution with the exception of some metal-poor GCs, e.g., M 15 (Fig. 1.20 Sobeck et al., 2011) which shows a large spread of Eu with a slightly spread in Fe (∼0.1 dex).

1.1.5 Globular Clusters in the Galactic context

As a broader picture, GCs give us clues on the conditions of the early Universe, the formation and evolution of galaxies, and on the stellar dynamic and stellar evolution. In particular, it has been suggested that they play an important role in the Galactic stellar Halo (Carretta et al., 2010), which is thought to be formed by accreting material from smaller systems, and possibly also the Bulge (Lee et al., 2019). Thus, GCs are fundamental for the understanding of the Galactic spheroid formation and evolution.

Currently, there is growing consensus that GCs were more massive than in the present. They could be affected by different effects ranging from mass loss from the more massive stars to two-body encounters that contribute to losing a large fraction of their stellar members. It is estimated that 8 out of 10 GCs were disrupted in the Galactic Halo or the Bulge (Gratton et al., 2019). Observational evidence has been found in tidal disruption of GCs (e.g., Grillmair and Dionatos, 2006), which are later confirmed by the

small metallicity spread (σ[Fe/H]<0.1 dex) found in the potential disrupted members of the cluster. Fig.1.21 shows a case of Pal 5 (Odenkirchen et al., 2003), where a core of the cluster and two tails are clearly identified in the surface density map. Then, as can be supposed, the current GCs would be the remaining much larger clusters. According to the literature, the SG stars in GCs range between 50% and 80% (Carretta et al., 2009). If we consider that the SG stars are formed only from a fraction of FG stars, there would be a considerable amount of FG stars populating the Halo field. Some authors estimate that GCs should have lost around 90% of their FG population (Gratton et al., 2012). However, since they share similar chemical compositions of field stars of the same metallicity, it is difficult to identify them.

Nevertheless, many efforts have been carried out to find field stars with chemical peculiarities found in SG stars, which would be an excellent tracer of their GC origins. With the arrival of high-quality spectroscopic surveys which map a large sample, in the last few years have been reported a considerable amount of field stars enhanced N along with C depletion. Fernández-Trincado et al. (2022) used APOGEE data to report 149 field stars with GC-like composition. The two upper panels of Fig.1.22 show both the N enrichment of these stars (navy circles) and that they display the Al-Mg anti-correlation found in some GCs. On the other hand, the lower panel of the figure shows a group of field N-rich stars (red squares) analysed by Spite et al. (2022) using UVES spectra, which displays a SG-like composition in the Na-O plane.

1.1.6 Open Issues

In the last decades, astronomers have done substantial progress in the understanding of GCs, changing the picture from a SSP to an MSP phenomenon present in all GCs. In this regard, the arrival of new instruments coming with high-quality spectroscopic and photometric data has helped us to better understand their nature and their properties. Nevertheless, there are still a few remaining gaps to fill. In the following, We present some of the most important ones.

1.1.6.1 Polluters and nucleosynthesis

In the previous section, a list of the main candidate polluters was provided, which would be responsible for the chemical contamination of the SG stars. Nevertheless, all the proposed polluters present different problems when contrasted with observation because they cannot account fully for the observables. For example, in the intermediate-mass AGB star scenario, one of the challenges is the timescale for pollution. AGB stars are expected to release the processed material with some lag after the massive stars exploded as supernovae. The ejecta from the latter, however, should be essentially completely expelled, as data indicate that Ca (and Fe) are uniform among GC stars, even in the presence of large variations of elements involved in hot H-burning, which, in this scenario, would imply that the AGB products would be, on the other hand, retained.

On the other hand, even if the last problem is not present in the FRMS scenario, they are expected to produce a large He variation in their SG stars, which is larger than the one observed (ΔY<0.20 dex) in GCs (Martins et al., 2021).

There are a number of model parameters that can be tuned in order to fix it, such as nuclear cross sections, which varies the probability of building species or the efficiency of convection at the interior of the star which strongly modifies their surface abundance (Karakas, 2010). In particular, the AGB models have shown to be highly dependent on the metallicity and the mass of the star (Karakas and Lattanzio, 2014) but also depend on other parameters which are not entirely constrained, such as convection efficiency and mass loss. Moreover, there is a lack of models at low metallicities ([Fe/H]<-2.0 dex) at any stellar mass. On the other hand, while Ventura et al. (2012) have explored models for the low-mass regime (7-8$M_{\odot}$) of super-AGB stars, there are no model yields for such stars for M>8$M_{\odot}$.

Similarly, interactive massive binaries are dependent on both the system mass ratio and the primary star mass, but also on the evolution stage at the moment of the interaction (de Mink et al., 2009). In addition, there is no clarity if the models have represented the whole range of yields. (Bastian et al., 2015) showed that massive interactive

binaries were not able to fit the observed Na-O anti-correlation, mainly because these polluters did not deplete strongly enough the O abundances.

On the other hand, the recently proposed candidate, super-massive stars (Denissenkov and Hartwick, 2014) could reproduce all the chemical features present in GCs, however, there is a lack of the observational counterpart, and simulations describing their contribution to Halo population and hydro simulations showing their effect in the galaxy formation.

Extended spectroscopic studies looking for key elements such as He, Li, F, and s-process elements and their relation with the light element distribution coupled with multi-colour high-precision photometry will help us to constrain better the current models. On the other hand, observation of extragalactic young massive GCs – which have similar conditions to the ones thought for the early stages of Galactic GCs – could also provide key information on the timescale or investigate the presence of super-massive stars at their centre.

1.1.6.2 Dilution

The most accepted scenario to explain the MSP phenomenon suggests that polluting material from FG stars must be diluted with pristine material. In the case of FRMS, the polluting material is expelled through equatorial slow winds in a disk where the SG stars take place. The polluted gas is mixed with the pristine material before its removal due to SN explosions.

For intermediate-mass AGB, the dilution is necessary to explain the observed chemical features in GCs, in particular the Na-O anti-correlation. There is no consensus, however, on the origin of such pristine material. Intrinsic and extrinsic natures have been proposed. According to Gratton et al. (2019), the gas would be present in all Galactic GCs and would vary with the cluster mass or the cluster initial density. Among the main source thought to return material with pristine chemical composition to the intracluster medium are single stars losing mass (Gratton and Carretta, 2010) and intermediate-mass close stars in binaries systems (Vanbeveren et al., 2012). Both sources are able to release pristine gas at low velocity, contemporaneously to the polluters, however, the

amount available would not necessarily match the observations (see also next section). On the contrary, the extrinsic mechanism would occur only in the most massive cluster in a longer timescale than the intrinsic ones. The best candidate responsible to bring the pristine material is the re-accretion (D'Ercole et al., 2016).

Understanding the nature, role and contribution of the different dilution mechanisms would no doubt provide a fundamental piece of information in the study of the formation of GCs and the MSP phenomenon,

1.1.6.3 Mass budget problem

The *mass budget problem* refers to the lack of polluted material from FG stars to form the SG stars that we observe today. Considering standard initial mass function (IMF), the FG stars in GCs would be able to produce only ∼10% of the present SG stars, whereas the observational evidence shows SG stars represent between 30%-90% of the total population in clusters (Milone et al., 2017). In particular, it is estimated that intermediate-mass AGB star polluted represent less than 10% of the initial stellar mass, whereas FRMS would lose less than 5% of their initial stellar mass, which would not be enough to explain the amount of SG stars in a given cluster (de Mink et al., 2009).

Many authors have tried to estimate the contribution of GC to the Halo (e.g., Koch et al., 2019, Martell et al., 2011). One idea to resolve this problem was that most of the FG stars were lost and that today only 5% of them remain in the cluster. Whereas all the polluted gas is concentrated in the cluster centre where the SG stars would be formed. The diverse mechanism could (e.g., SNe and tidal interactions) produce the expulsion of a large percentage of the FG stars, resulting in the scenario that we see today. This large loss of FG stars would also be consistent with the findings that the GCs as one important contributor to the Halo field stars population.

A study of binary systems in GCs can provide helpful hints. As it is known, a large fraction of stars in the solar neighbourhood is in binary systems. While close binary systems can survive in high-density environments, wide binary systems are easily destroyed (Kroupa et al., 1999, Lada and Lada, 2003)Then, the fraction of binaries is an excellent tracer of the density environment where they were born. Lucatello et al.

(2015) estimated a binary fraction in systems with periods shorter than 1000 days. They obtained that the fraction of binary systems in the galactic field is about 20% and in the Galactic GCs, this fraction is drastically affected reaching about 2%. This can be explained due to the high-density environment present in GCs.

The binary fraction in GCs shows quite different results when we take into consideration the population they are associated with. Binary systems represent a ∼15% and ∼1% of the FG and SG stars, respectively. This large different support the idea that SG stars are formed in the central part of the cluster the density is higher than the outskirts (D'Orazi et al., 2010). This supports the idea of looser FG stars being preferentially lost to the field with respect to concentrated SG stars. Moreover, the similar fraction of binary stars among both the field and the FG stars in GCs could closely relate to each other, being the lost FG stars an important contributor to the Halo field stars (Gratton et al., 2012).

The problem of the mass budget is still open. Other proposed solutions include, for instance, a top-heavy mass function for FG stars Marks et al. (2012) or to consider a larger (10-100 times larger) initial cluster mass (Bekki et al., 2007).

1.2 Layout

In the following, We will present the body of the thesis which aims to contribute to the knowledge of the MSP phenomenon in GCs using the chemical patterns of Li and heavy elements. It is worth noticing this thesis is based on a series of three different papers, which can be found below.

Lithium abundances as a tracer of AGB stars pollution in the globular cluster NGC 6752

Authors: J. Schiappacasse-Ulloa, S. Lucatello, M.J. Rain, A. Pietrinferni

Monthly Notices of the Royal Astronomical Society, Volume 511, Issue 1, March 2022, Pages 231–240

https://academic.oup.com/mnras/article/511/1/231/6519781

Neutron-capture elements in NGC 6752 multiple populations

Authors: J. Schiappacasse-Ulloa, S. Lucatello

Monthly Notices of the Royal Astronomical Society, Volume 520, Issue 4, April 2023, Pages 5938-5949

https://academic.oup.com/mnras/article/520/4/5938/7040582

Neutron-capture elements in 18 GCs multiple populations

Authors: J. Schiappacasse-Ulloa, S. Lucatello

Paper submitted to A&A

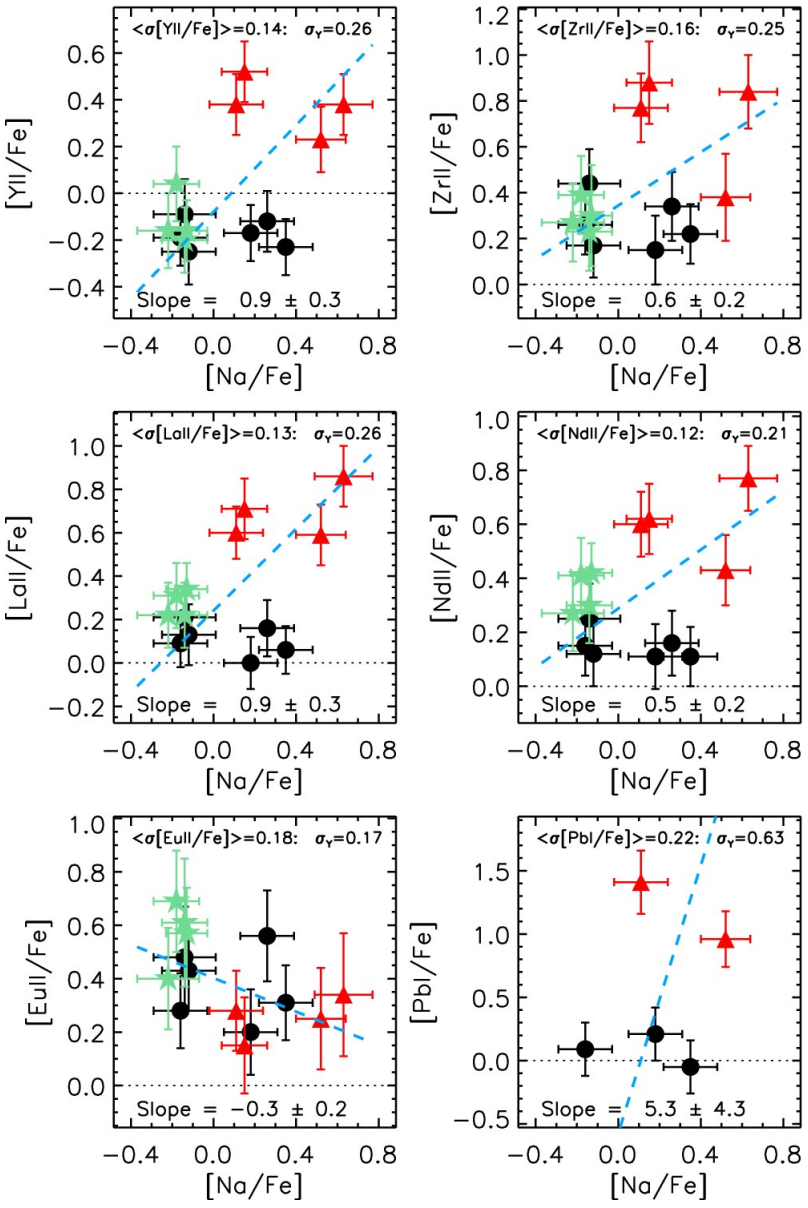

Figure 1.19 Heavy element distribution as a function of [Na/Fe] in NGC 7089 (Yong et al., 2014), which is one of the clusters that show a considerable spread in their abundance. Black symbols represent stars belonging to the canonical RGB. Red and green symbols are stars laying on the non-canonical RGB. In particular, the green ones show an unusually metal-rich content. The blue dashed line is a linear fit to the data.

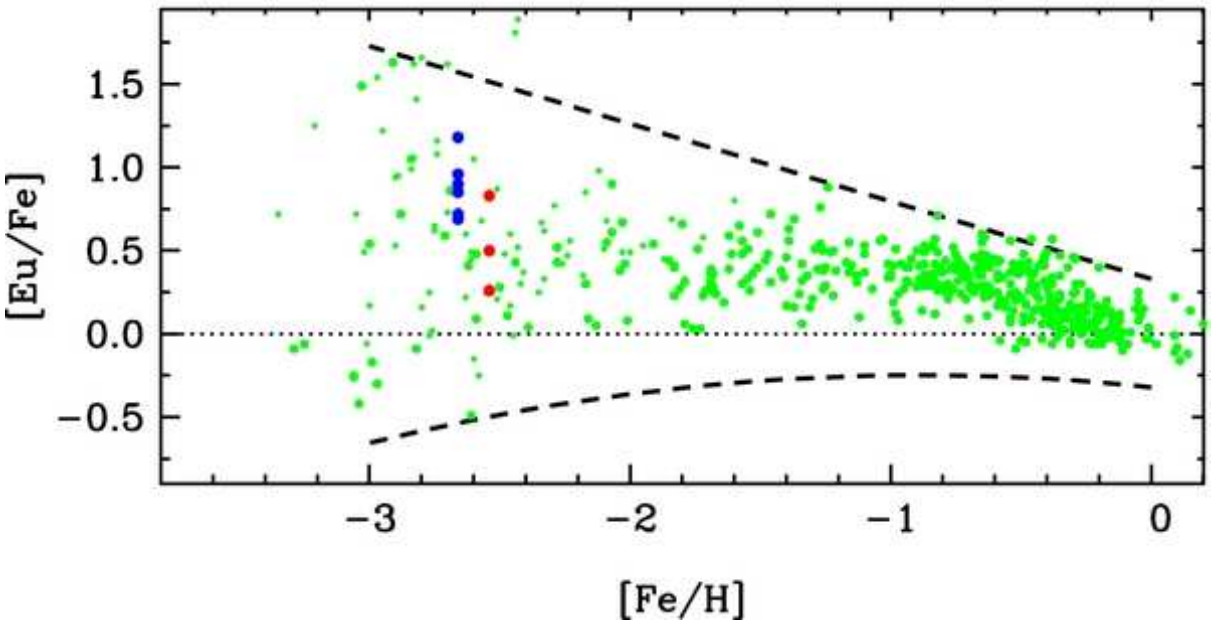

Figure 1.20 Eu distribution as a function of [Fe/H] in the red horizontal branch (blue symbols) and RGB stars (blue symbols) of the GC M 15. Halo field stars are shown in green symbols. Source: (Sobeck et al., 2011).

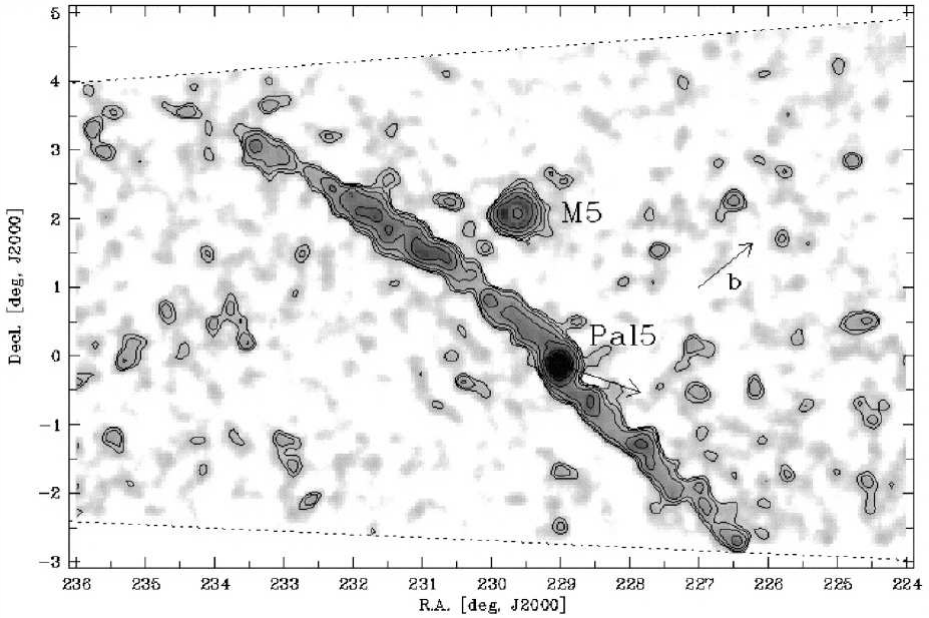

Figure 1.21 Surface density map showing the tidal disruption of the GCs Pal 5. It shows clearly the core of the cluster (labelled with its name) and two long tails left behind.

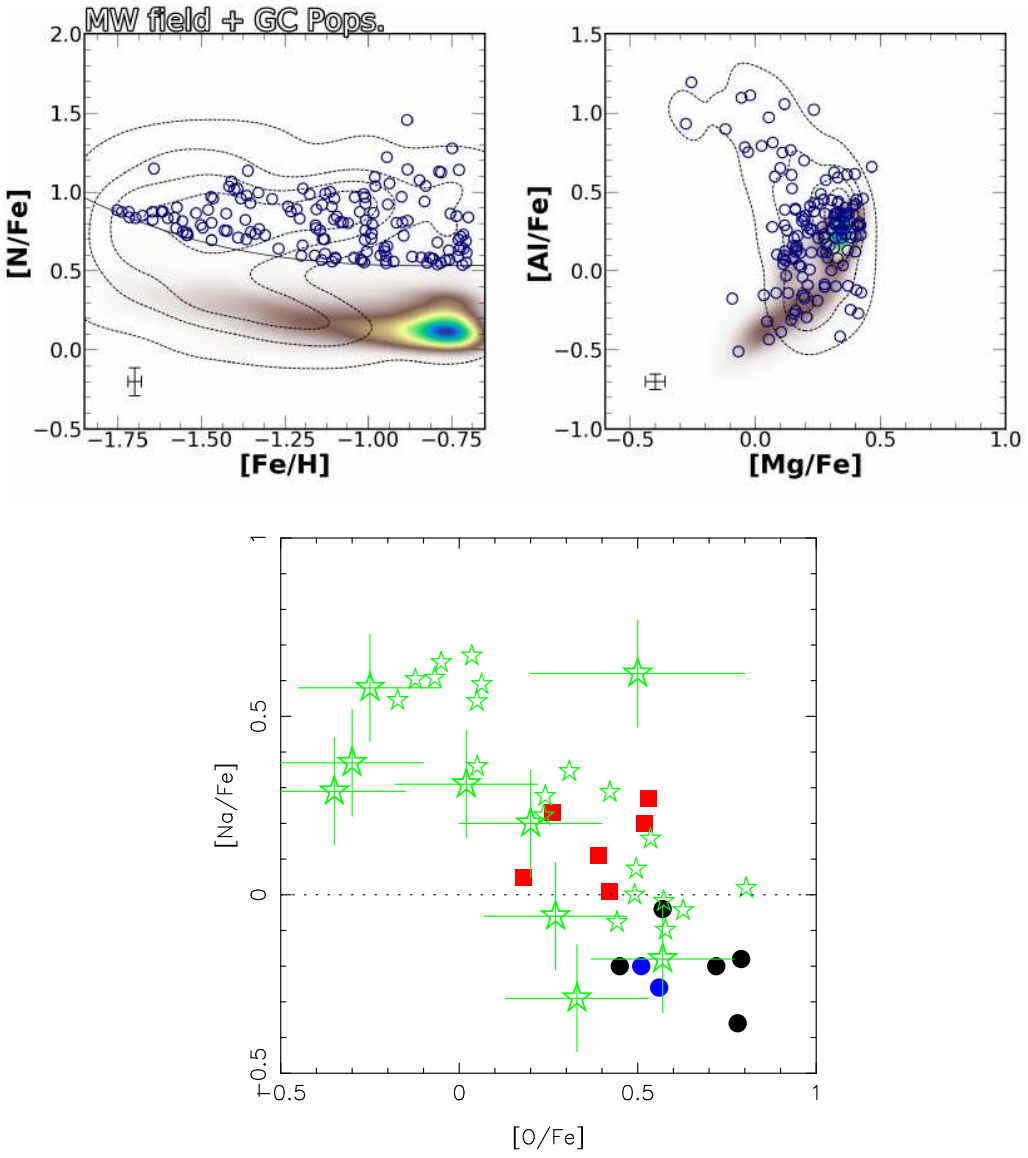

Figure 1.22 The upper panel shows a sample of 149 field stars (navy circles) from Fernández-Trincado et al. (2022) with high N abundance, which also displays the Al-Mg anti-correlation found in GCs. Globular cluster stars distribution is represented with black dashed contours (Mészáros et al., 2020). The MW object density is represented with kernel density estimation models. The lower panel shows a sample of dwarf field N-enhanced stars (red squares) from Spite et al. (2022) with SG chemical patterns in the NaO plane. Dwarf (large green stars) and giant stars (small green stars) represent stars of the GC NGC 6752. Black symbols show stars with normal N abundances. Finally, blue symbols are stars previously reported as N-rich, which ended up being normal N stars.

Chapter 2

Sample and Data Reduction

In the present Chapter, We am going to describe the sample used, their observations, and corresponding data reduction. This PhD thesis is based on two samples which hereafter will be called NGC 6752 sample –from which We analysed both Li and heavy elements–, and the survey sample –from which We extend the previous efforts from Carretta et al. (2009) (hereafter C09)–. In the following, both samples are going to be described in detail.

2.1 Target

NGC 6752 is a metal-poor GC ([Fe/H]∼-1.55 dex) which has been largely studied. Some of them have reported a Li-O correlation with a slope different than 1 and the presence of Li-enriched stars among the SG population (Shen et al., 2010). This evidence suggested that a Li source should be present in the pollution of the cluster. Because intermediate-mass AGB stars are the only candidate polluter able to produce Li, the observational findings argue in their favour. Nevertheless, the presence of Li-poor stars among SG stars suggests that Li production is not always associated with Al and Na production and O depletion, which opens the possibility of the presence of multiple classes of polluters working in the same cluster or Li production in a subset of polluter classes.

NGC 6752 is an excellent candidate for analysing the MSP phenomenon in terms of its Li abundances. Here, it is presented a complete analysis of light and iron-peak elements as a function of Li-rich and Li-poor stars aiming to perform a poorly studied approach to investigate the nature of the phenomenon. The analysis is extended to n-capture elements, as well, as trying to further probe the phenomenon.

2.2 Sample and Observations

The ESO archive was searched for high-resolution, optical spectroscopy of members of the cluster NGC 6752. Spectra for a total of 217 stars are present within 15 arcmin. Of these, a subset is made of the FLAMES/GIRAFFE at ESO VLT spectra for 126 objects, which were previously analysed by Gruyters et al. 2014 (hereafter G14), and the authors kindly provided the reduced and radial-velocity shifted data for this study.

The spectra for the remaining 91 stars were downloaded from the Gaia-ESO collection of the ESO archive, which includes data both from FLAMES/GIRAFFE and FLAMES/UVES. For the archival data, cluster membership was determined by selecting them based on *Gaia* eDR3 (Gaia Collaboration et al., 2021) data. Only stars within 3σ on parallax and proper motion values from the cluster mean value were considered members. Figure 2.2 shows the comparison of the parallaxes and proper motions between our sample and the stars in the cluster field. The typical SNR for our sample range from 80 to 150 around the proximity of 6708Å (Li line) for the fainter and the brighter stars, respectively. The summary of these observations (instrument, setup, wavelength coverage, resolution, and source) is listed in Table 2.1.

2.2.1 GCs survey sample

This sample includes data from Carretta et al. (2009) plus NGC 5634 from Carretta et al. (2017), where p-capture elements abundances for a large number of GCs were presented. The data was collected with ESO VLT FLAMES/UVES spectrograph, with a resolution of ∼40,000 and a wavelength coverage of 4800-6800Å.

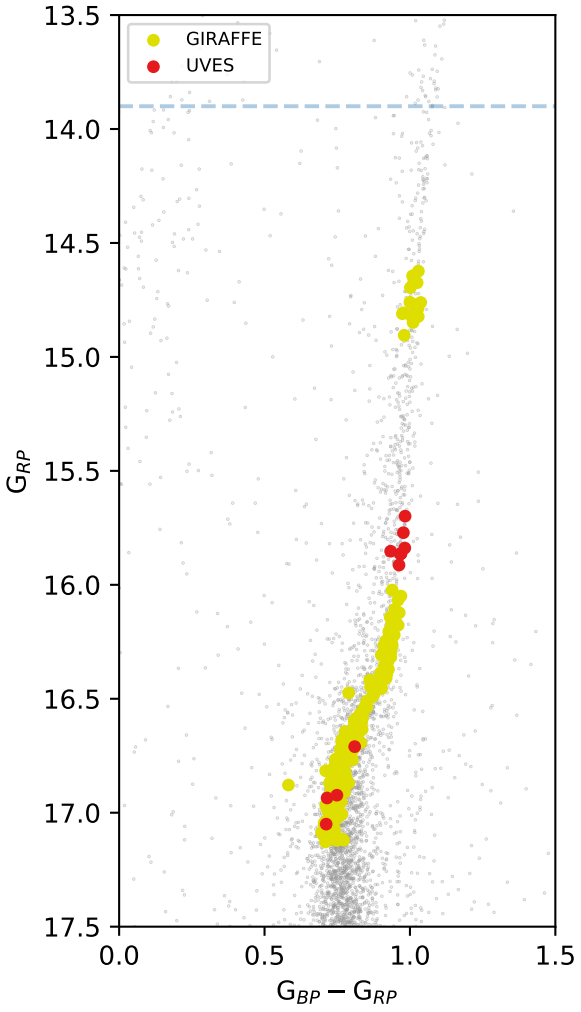

Figure 2.1 CMD of NGC 6752. Red and yellow dots represent UVES and GIRAFFE spectra, respectively. Grey dots are photometric data from Gaia early DR3 in the cluster field. The blue horizontal dashed line shows the RGB-bump.

The sample includes GCs with a wide distribution of stars along their horizontal branch (HB) ranging from stubby red HB to blue ones with long tales. The sample also included the less massive to the more massive GCs and GCs with different ages. On the other hand, the star selection considered members without a close companion brighter (fainter) than -2 (+2) mag. than the target star. Moreover, the authors preferred stars near the RGB ridge over the ones close to the RGB tip to reduce problems with model

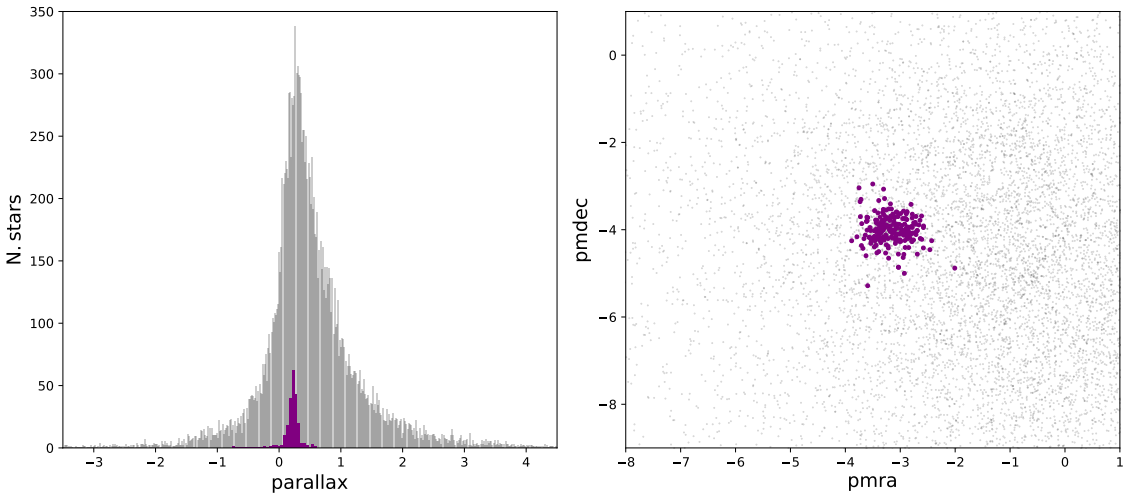

Figure 2.2 Comparison of the parallaxes and proper motions of our sample and stars in the cluster field

Instrument	Setup	Wave. Range Å	Resolution R≡ $\lambda/\Delta\lambda$	Source
FLAMES/UVES	Red Arm	4768-6830	47,000	ESO-archive
FLAMES/GIRAFFE	HR15N	6444-6816	19,200	ESO-archive - G14
FLAMES/GIRAFFE	HR10	5330-5620	21,500	G14
FLAMES/GIRAFFE	HR11	5600-5840	29,500	G14
FLAMES/GIRAFFE	HR13	6120-6405	26,400	G14
FLAMES/GIRAFFE	HR15	6600-6960	21,300	G14

Table 2.1 Summary table of the setup for the NGC 6752 sample, which includes 217 stars.

atmospheres. For a more detailed description of the cluster and star member selection, We refer to the original source. A total of 210 stars in 18 clusters are included in the dataset.

A detailed summary of the cluster used, the star number analysed in each cluster, the mean signal-to-noise ratio (SNR) at 6200Å, and the mean radial velocity (Vr) can be found in Table 2.3. The original table was taken from C09.

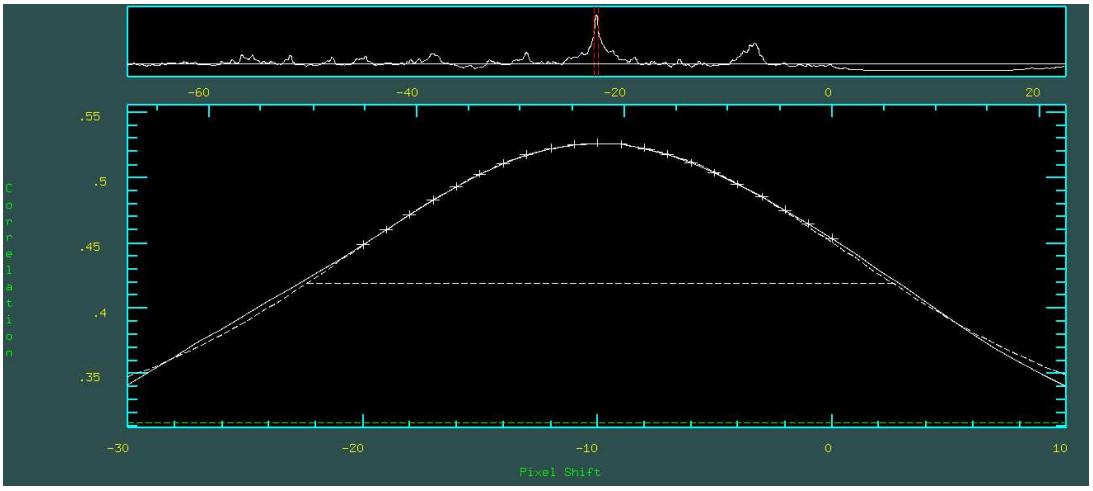

Figure 2.3 Radial velocity fit for one star of the NGC 6752 sample.

ID	V_r	ID	V_r	ID	V_r
19100576-6001009	-18.16±3.38	19103964-6003189	-22.83±4.85	19110616-6002522	-21.43±5.20
19100961-5959534	-21.16±4.27	19103970-6001045	-27.47±0.05	19110785-5954515	-17.93±4.93
19101000-5957525	-25.33±4.71	19104225-6004460	-26.16±0.15	19110798-6003588	-22.23±4.97
19101589-6002252	-23.04±4.06	19104427-6004301	-22.51±4.96	19110863-5957569	-31.12±0.44
19101610-6000035	-32.15±3.92	19104664-5954063	-29.33±4.55	19110907-5955546	-26.83±0.09
19101652-6001094	-24.27±4.52	19104804-6002213	-31.72±0.07	19111018-5954267	-26.92±2.10
19101748-6000324	-16.67±4.91	19104892-5958234	-36.22±3.60	19111078-5956406	-18.34±0.06
19101923-5958596	-23.23±4.08	19104925-5954057	-18.09±6.92	19111338-6002243	-26.23±4.52
19102025-5958306	-30.79±0.62	19104963-5953398	-29.69±4.68	19111612-5954443	-30.32±4.25
19102135-6002166	-22.67±4.42	19105056-6006005	-25.96±4.28	19111644-6002253	-23.18±7.06
19102158-5958179	-16.51±4.42	19105158-5954184	-21.61±4.24	19111828-6000139	-25.99±1.25
19102204-5956597	-23.14±4.70	19105177-6000390	-26.99±0.35	19112070-6001057	-34.82±4.16
19102223-5957192	-21.15±4.79	19105406-5958002	-30.49±4.08	19112071-5956287	-28.48±4.46
19102293-6004232	-21.51±4.65	19105483-6003042	-28.49±3.97	19112091-6002411	-34.34±5.26
19102328-6000498	-22.59±4.69	19105546-5953358	-32.45±5.18	19112132-5956542	-30.02±5.35
19102370-6000209	-23.53±0.10	19105577-5957278	-20.43±0.41	19112258-6002380	-30.38±5.09
19102395-5956202	-27.67±4.56	19105692-6000227	-32.22±0.07	19112339-6001385	-29.38±4.45
19102415-6003445	-35.33±0.18	19105851-5955394	-30.34±0.28	19112451-6000104	-30.84±5.46
19102525-5959409	-27.82±1.41	19105986-6002171	-21.78±0.19	19112587-5958553	-34.92±5.36
19102577-6004439	-22.23±0.11	19105996-5959271	-27.37±0.07	19112720-5955225	-30.54±5.25
19102675-5956553	-30.23±11.7	19110011-6006045	-22.82±4.46	19112749-5958445	-33.61±4.97
19102677-6003089	-28.77±1.88	19110081-6005092	-26.34±9.29	19112818-6000436	-21.11±4.82
19102685-5958251	-24.26±0.18	19110105-6004103	-22.51±4.69	19112987-5956098	-29.26±4.48
19102726-5955194	-24.33±3.52	19110151-6002511	-27.47±4.88	19113071-6003234	-25.51±1.04
19102859-6003539	-21.91±4.55	19110152-6003444	-26.82±4.20	19113087-5958477	-23.38±4.95
19102903-6002535	-26.35±5.95	19110207-5956317	-30.58±0.50	19113088-5957430	-30.61±5.39
19103463-5956357	-20.28±4.80	19110429-6002404	-32.14±4.67	19113168-5957130	-31.82±5.04
19103672-6002011	-14.83±0.67	19110501-5955274	-27.99±1.09	19113298-5958411	-22.44±4.31
19103829-5955070	-24.48±6.16	19110533-5953490	-21.59±4.64	19113393-5958107	-27.61±5.08
19103855-6003361	-28.25±5.41	19110598-5959013	-31.24±0.47	19113403-5957497	-24.07±4.53
				19113655-5959432	-20.68±5.05

Table 2.2 Radial velocities measured on NGC 6752 for the sample of 91 stars. $\langle V_r \rangle$= -26.14±0.50 km s^{-1}

Cluster	a.k.a	n. stars	⟨SNR⟩	⟨V_r⟩
NGC 104	47 Tuc	11	95	-19.86
NGC 288	—	10	101	-46.15
NGC 1904	M 79	10	69	204.82
NGC 2808	—	12	97	104.09
NGC 3201	—	13	83	494.57
NGC 4590	M 68	13	86	-94.35
NGC 5634	—	7		18.54
NGC 5904	M 5	14	70	53.78
NGC 6121	M 4	14	91	71.95
NGC 6171	M 107	5	40	-38.82
NGC 6218	M 12	11	80	-41.25
NGC 6254	M 10	14	88	74.57
NGC 6397	—	13	79	22.75
NGC 6752	—	14	100	-26.96
NGC 6809	M 55	14	77	174.83
NGC 6838	M 71	12	92	-23.97
NGC 7078	M 15	13	84	-107.34
NGC 7099	M 30	10	84	-188.05

Table 2.3 Summary table of the cluster used, the star number analysed in each cluster, the mean SNR, and the mean Vr. Original table from C09. In addition, NGC 5634 was also analysed (Carretta et al., 2017).

2.3 Data Reduction

2.3.1 NGC 6752 sample

The G14 spectra were provided at rest-frame and continuum normalised. For the ESO archival spectra, they were downloaded extracted and wavelength calibrated from the archive, as processed by pipeline version 5.5.2. We used `IRAF`[1] tasks `CONTINUUM`, `FXCOR`, and `DOPCOR` to perform the continuum normalization, the radial velocity (V_r) measurement, and the shift to rest-frame, respectively. We found a ⟨V_r⟩= -26.14±0.50 km s^{-1}, based on 91 individual stars. The V_r for each individual star is listed in Table 2.2. The

[1] `IRAF` is the Image Reduction and Analysis Facility, a general-purpose software system for the reduction and analysis of astronomical data. `IRAF` is written and supported by National Optical Astronomy Observatories (NOAO) in Tucson, Arizona.

radial velocity is in excellent agreement with the one reported in the Harris Catalog[2] Harris (1996), which is V_r = -26.70±0.75 km s^{-1}. Fig.2.3 shows an example of the radial velocity fitting for a sample star.

2.3.2 GCs survey sample

The reduced spectra were kindly provided shifted at rest-frame by Carretta et al. (2009) and Carretta et al. (2017). As they described in their article, they reduced spectra using the ESO UVES-FLAMES pipeline (uves/2.1.1 version). The V_r were measured for each spectrum using `IRAF` task called `rvidlines`. As for the other sample, We performed the continuum normalization using the `continuum` task from `IRAF`.

[2] `https://www.physics.mcmaster.ca/~harris/mwgc.dat`

Chapter 3

Data Analysis

In the present Chapter, We will discuss the stellar parameters derivation, the abundance ratios determinations and their associated errors.

3.1 Stellar Parameters Determination

3.1.1 NGC 6752 sample

Because this sample is composed of both UVES and GIRAFFE spectra, We determined the stellar parameters using two different methods: photometric, and spectroscopic derivation. It is worth noticing because of the short wavelength range in GIRAFFE spectra, their stellar parameters were derived only using the first technique. Whereas for UVES spectra both methods were used. Nevertheless, for homogeneity reasons, the abundance derivation was performed using the photometric stellar parameters for the whole sample. In the following, We describe them in detail.

3.1.1.1 NGC 6752 sample: Photometric Stellar Parameters

The GIRAFFE spectra for our sample have somewhat limited coverage in wavelength[1], and hence a limited number of Fe lines, leading to considerable uncertainties in the determination of atmospheric parameters from spectroscopy. On the other hand, the high-quality Strömgren photometry from Grundahl et al. (1999) provides precise colours and magnitudes, thus minimising random errors. Hence our approach is to adopt the photometric $T_{\rm eff}$, $\log g$, and v_m.

The NGC 6752 sample includes objects covering an extensive range of evolutionary stages (see Fig. 2.1), and the derivation of the homogeneous atmospheric parameters is crucial in the analysis. We derived the stellar parameters from photometry as follows. Colour-temperature relations are generally provided separately for unevolved and evolved stars. This is the case of two commonly used temperature scales, reported by Alonso et al. (1996) and Alonso et al. (1999). In order to make sure that photometric effective temperatures ($T_{\rm eff}$) are on a homogeneous scale for both TO/SGB and RGB stars, We adopted the corrections described in Korn et al. (2007), based on the $(v-y)$ colour from Strömgren photometry Grundahl et al. (1999) adopting E(B-V) = 0.04 mag (Harris, 1996). The reddening has been transformed in the appropriate bands following Crawford (1975). To find the $\log g$ — corresponding to the photometric temperatures of our targets — We used the isochrone from Bressan et al. (2012), adopting an age of 13.5 Gyr (Gruyters et al., 2013), and [Fe/H]=-1.56 dex (Carretta et al., 2009). It is worth noticing that the adoption of age from a different source (e.g., 12.5 Gyr VandenBerg et al., 2013) produces a negligible difference ($\Delta\log g\sim$0.02) in the determination of the stellar parameters. Finally, We used the formula[2] described in Gratton et al. (1999) to estimate the microturbulence velocity (v_m) of the stars. The latter formula was calibrated in metal-poor F-K stars of different gravities. For details about its determination, we refer to the reader to the cited article.

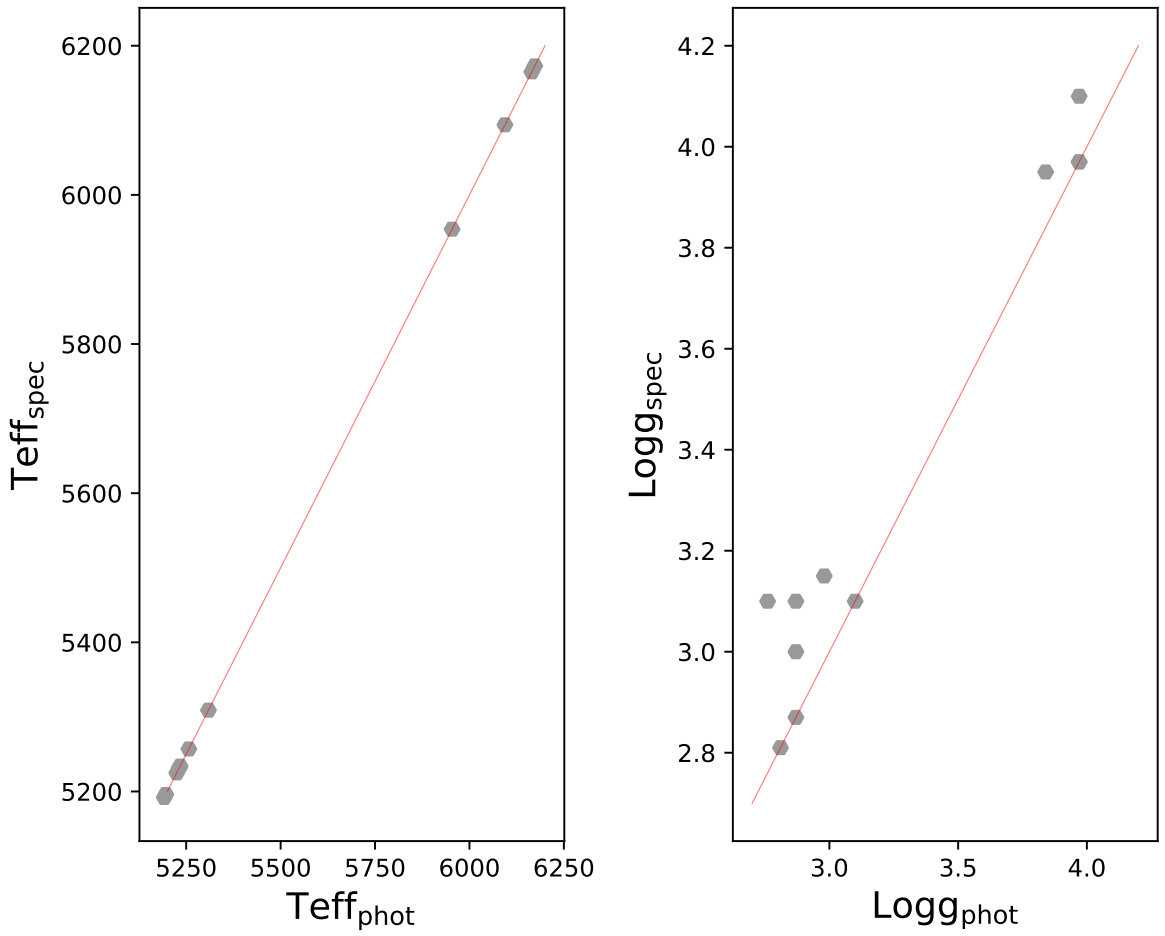

Figure 3.1 Comparison between the stellar parameters obtained from photometry and spectroscopy.

3.1.1.2 NGC 6752 sample: Spectroscopic Stellar Parameters

For UVES spectra, which have a much broader wavelength coverage, stellar parameters can, on the other hand, be reliably derived spectroscopically, using the photometric ones as an initial guess. We performed a traditional spectroscopic analysis to derive the atmospheric parameters. Equivalent widths for iron lines were measured using

[1]A fraction of the stars have two orders available in the archive and an even smaller fraction has more.

[2]$V_m = 2.22 - 0.322 \log g$

ARES (Sousa et al., 2007), which were analysed later using `abfind` driver from `MOOG`[3] (Sneden, 1973), a 1-D LTE line analysis code, to get the final set of stellar parameters, and the Kurucz (1992) grids of model atmosphere. An example of the spectroscopic determination of the stellar parameter can be seen in Fig. 3.2, which shows no trend between the abundance obtained from Fe I and Fe II lines with E.P and $\log(\mathrm{EW}/\lambda)$. The comparison between photometric and spectroscopic stellar parameters is shown in Figure 3.1. As can be seen, $T_{\rm eff}$ obtained using both methods are in overall excellent agreement. Spectroscopic gravities are on average 0.10±0.01 dex larger than their photometric counterparts. Nevertheless, We adopted the photometric set of stellar parameters even for UVES stars to have complete consistency across the whole sample and minimise internal errors.

Figure 3.3 shows the adopted stellar parameters for the whole sample in the $T_{\rm eff}$ – $\log g$ plane. The black-filled hexagons represent our targets and the red line is the theoretical $T_{\rm eff}$, and $\log g$ from isochrones.

3.1.1.3 $T_{\rm eff}$ – $\log g$ Comparison with G14

As discussed above, 126 of the stars in our sample are in common with G14 (they present the analysis for 193 NGC 6752 stars, but only 126 have the spectral coverage suitable for our purposes). In Figure 3.4, We compare our stellar parameters with those reported by them. They used the Korn et al. (2007) modified color–$T_{\rm eff}$ relations of Alonso et al. (1996) and Alonso et al. (1999) for both TO and RGB stars. The temperatures were linearly interpolated for SGB.

While there is a good agreement in $T_{\rm eff}$ for evolved stars, the presently derived temperatures are systematically lower $T_{\rm eff}$ ($\sim$ 80 K) that G14 for unevolved ones. The reason is likely due to their adopting the flux method calibration to the derived $T_{\rm eff}$ and slightly lower adopted ([Fe/H]=-1.60 dex) metallicity. I also have different approaches in the $\log g$ determination. While We obtained it directly from isochrones, they use canonical formula (e.g., equation 1 in Rain et al. 2019). As can be seen from the Figure, there is

[3] I used `pyMOOGi` version November 2019. It can be downloaded from: `https://github.com/madamow/pymoogi`

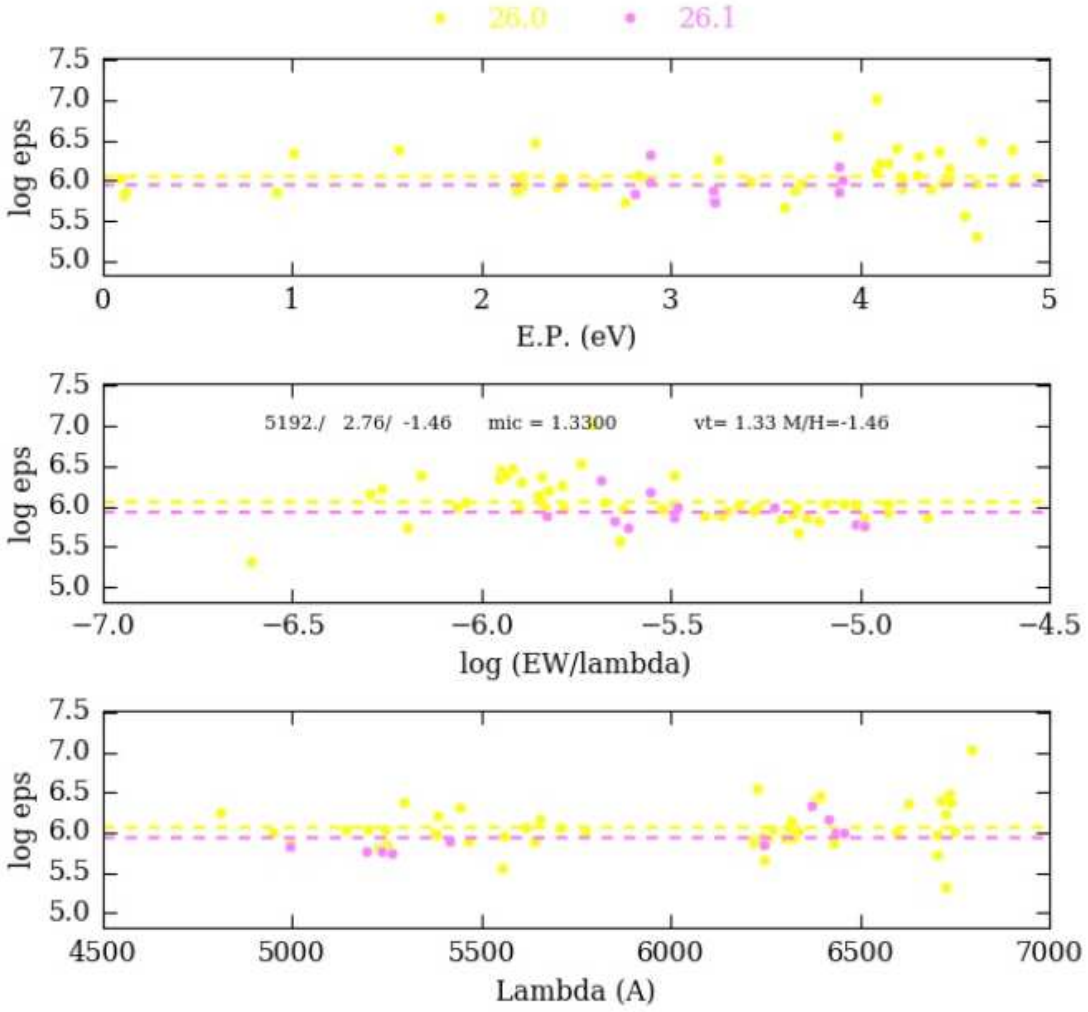

Figure 3.2 Example of the spectroscopic determination of the stellar parameters for one star of our UVES sample (ID: 19104804-6002213). From the top to the bottom the shows the relation between the Fe I (yellow symbols) and Fe II (pink symbols) lines as a function of E.P, $\log(\mathrm{EW}/\lambda)$, and wavelength, respectively.

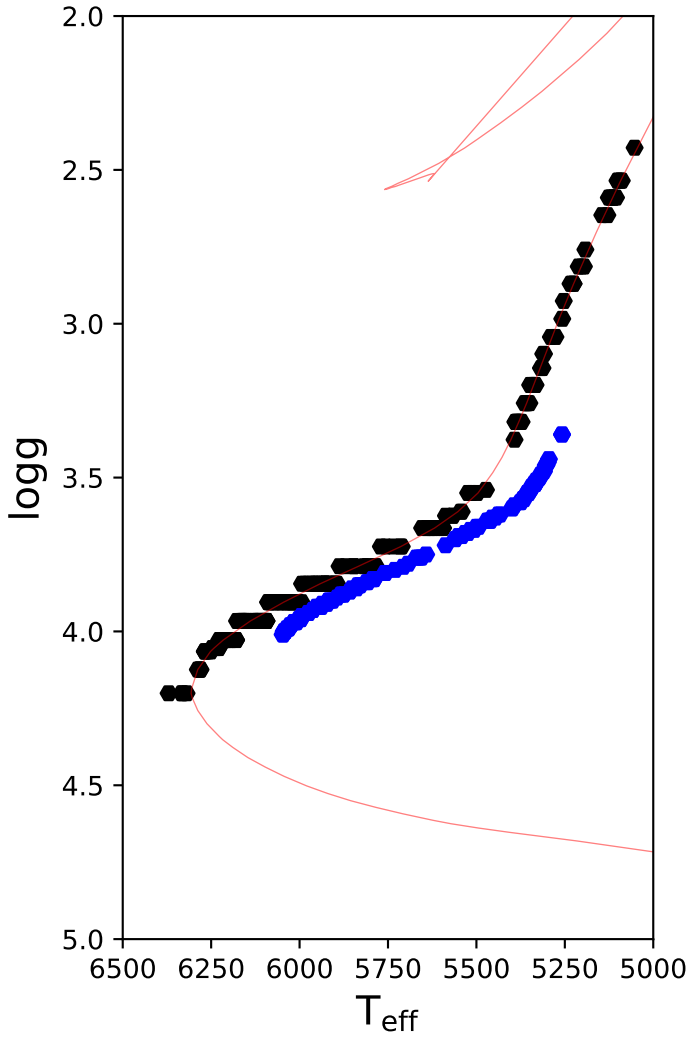

Figure 3.3 Distribution of our sample in the T_{eff} – $\log g$ plane. Black filled hexagons represent our T_{eff} and logg. The red line shows their theoretical values from isochrones.

good agreement among unevolved stars, but a considerable difference between our $\log g$ and G14's among the evolved ones (mean difference of 0.3 dex). We note, however, that the species of present interest are not strongly dependent on this parameter (see table 3.7). It is important to note, however, that for the purpose of this paper, the priority is to be fully homogeneous and internally consistent, and that consistency with the literature is of lesser importance.

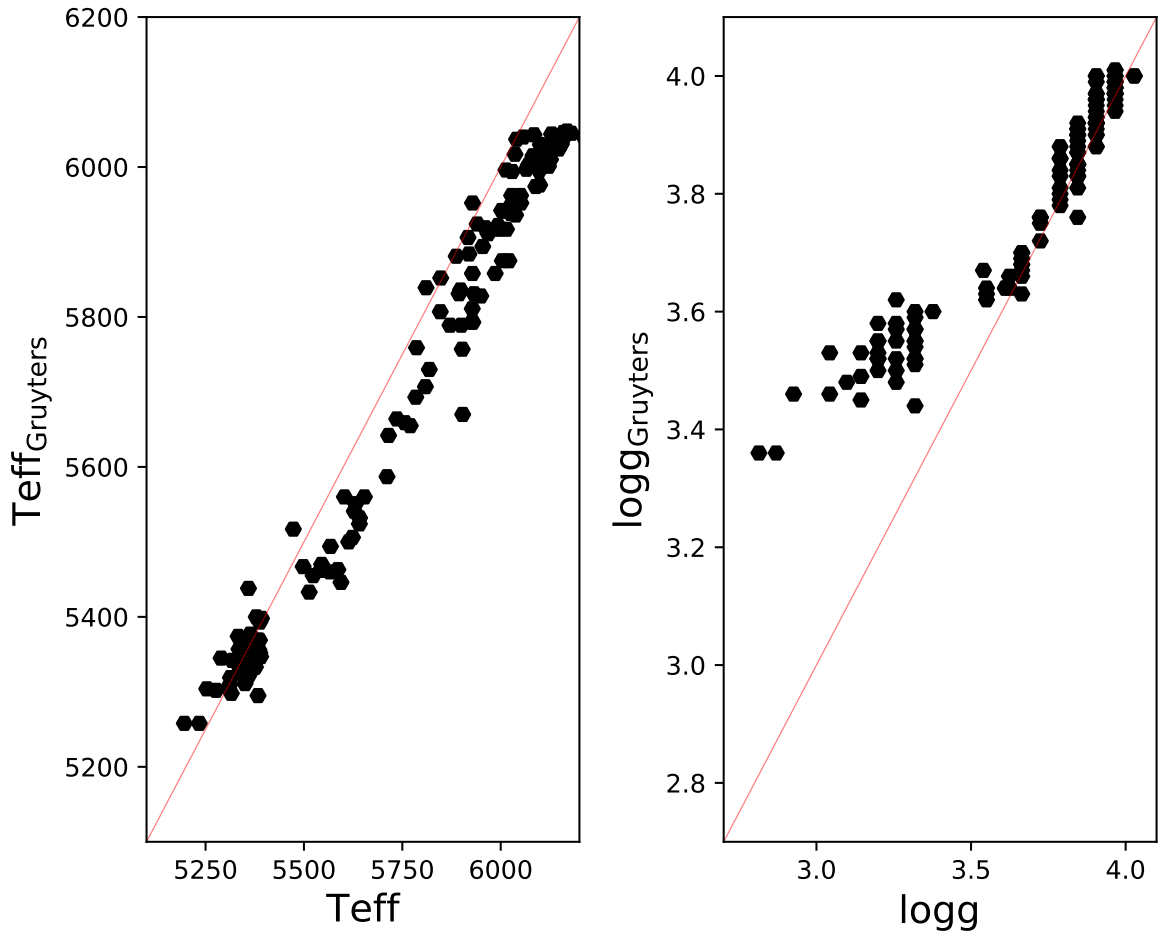

Figure 3.4 Comparison between our T_{eff} and logg and the ones reported by G14. The red line indicates a one-to-one relation.

3.1.2 GCs survey sample

For homogeneity with the abundances reported by C09, We decided to use the same stellar parameters derived by them. The procedure adopted by the author for the atmospheric parameters determination in the survey sample is clearly described in the cited paper. Here, We summarise their method.

They used 2MASS (Skrutskie et al., 2006) photometry (J and K filters), which were transformed into the TCS system as was indicated in Alonso et al. (1999). Using the relations for V-K colours given in the mentioned article, the authors computed the T_{eff} and the

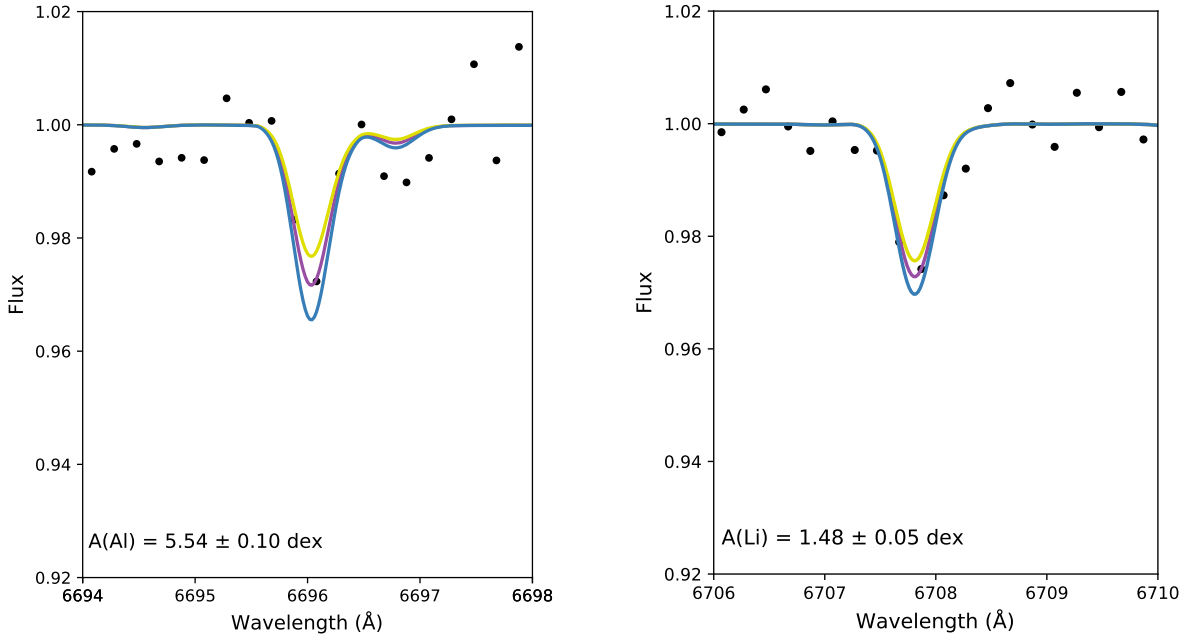

Figure 3.5 In the left (right): Instance of aluminium (lithium) line synthesis for a star member of NGC 6752. Black dots show the observed spectrum, and yellow, purple, and blue lines are the synthetic spectra: for aluminium 5.44 dex, 5.54 dex, 5.64 dex, and for lithium 1.38 dex, 1.48 dex, and 1.58 dex, respectively. The best fit (purple line) corresponds to A(Al) = 5.54 dex and A(Li) = 1.48 dex.

bolometric corrections (B.C.). The final $T_{\rm eff}$ were computed with a relation between the former $T_{\rm eff}$ and the V mag., which was built based on a sub-sample of *well-behaved* stars. It is worth noticing that these stars were defined as well-behaved if they have magnitudes in the J, K, B, and V filters and they lay on the RGB. Secondly, the $\log g$ was obtained using the $T_{\rm eff}$ and B.C. for a stellar mass of $0.85 M_{\odot}$ and a $M_{bol,\odot}$=4.75. On the other hand, the authors determined the V_m by removing the dependency of the Fe I abundances with the strength of the lines measured. They preferred this method instead of the classic functions of $V_m(T_{\rm eff}, \log g)$ to reduce the scatter on the obtained abundances. Finally, the metallicities were derived after interpolation of Kurucz (1993) model atmospheres grid with overshooting. The selected model was the one with the proper stellar parameters whose abundance was the same as the ones derived from the Fe I lines.

3.2 Abundance Determinations

3.2.1 NGC 6752: Measurement of Li Na, Mg, Al, Ca, Sc, Cu, Y, and Ba

Cayrel (1988) (his equation 7) describes how to derive the uncertainty associated with EW measurements based on spectral resolution and signal-to-noise ratio. Following Mucciarelli (2011), We assumed three times this uncertainty as the minimum reliably measurable EW. In the neighbourhood of the wavelength corresponding to the relevant transitions (Li and Al), this value ranges from 8 mÅ to 30 mÅ, and from 3 mÅ to 5 mÅ, for GIRAFFE and UVES spectra, respectively. We established that Li and Al are measurable in 153 and 34 stars, respectively, based on these cutoffs. In contrast, no meaningful measurement can be derived for the remaining stars, but only upper limits.

Li and Al abundances were measured via spectral synthesis using the `synth` driver from `MOOG`. The line list adopted is the one used by D'Orazi et al. (2015). I corrected our Li measurements for NLTE effects using corrections obtained from the `INSPECT` database version 1.0[4], which are based on the ones provided by Lind et al. (2009). These corrections range from ~ -0.02 dex to ~ -0.06 dex for unevolved and evolved stars, respectively. Just as a comparison, we computed the NLTE from 3D-NLTE for Li in the same stars, and according to the reported by Wang et al. (2021) the corrections range from $\sim +0.02$ dex to ~ -0.09 dex, respectively. The Al lines used are also affected by NLTE effects; hence We applied the corrections given by Nordlander and Lind (2017). While the Al corrections are quite small for evolved stars (mean correction of 0.02 dex), the unevolved stars are more affected by this phenomenon (mean correction of 0.09 dex).

The wavelength range covered by the presently analysed GIRAFFE and UVES spectra allows measuring both Li doublet at 6708Å, Al lines at 6696Å and 6698Å. In particular, we decided to analyse the Al line with spectral synthesis due to it weakness. Figure 3.5 shows examples of spectral synthesis fitting to the Al (6696 Å) and Li doublet at (6708 Å). The purple lines indicate the best fit, which corresponds to an A(Al) = 5.54 dex[5] and

[4] `http://inspect-stars.com/`

[5] $A(X) = \log(N_X / N_H)+12$, where N_X is the number density of the relevant species.

A(Li) = 1.48 dex. Two more synthetic models are shown in yellow and blue, with an aluminium and lithium abundance difference with respect to the best one of 0.10 dex and 0.05 dex, respectively. The Al line at 6698 Å is expected to be ∼2 times weaker than the one at 6696 Å, which is already weak in our spectra; hence our results are based on the measurements done in the latter. Given the weakness of the Al line, the fitting of those lines has large uncertainties in many of the objects in our sample. However, the strictly uniform procedure followed for all the analysed spectra minimises the random errors due to fitting and atmospheric parameters uncertainties.

In addition, We derived the Na, Mg, Ca, Sc, Cu, Y, and Ba abundances. We also investigated O and Eu abundances but could only derive upper limits. While for UVES spectra all these species were analysed, in GIRAFFE spectra they were examined whenever the order was available: HR10 (Mg: 5528Å, and Y: 5509Å), HR11 (Na: 5682Å -5688Å, Mg: 5711Å, and Cu: 5105 Å), HR13 (O: 6300 Å, and Ba: 6141Å), HR15 (Ba: 6496Å, and Eu: 6645Å). Table3.1 summarises the average number of lines used for the abundance determinations for each element. The line list with EP's and $\log gf$ used for the abundance determination can be found in Table D.1. The adopted solar abundances were taken from Asplund et al. (2009a), noting that our solar analysis yields very similar results. The individual abundance determination was done as follows.

I used the model atmospheres grids from Kurucz (1992) for our abundance determination. In particular, Mg, Ca, and Sc were measured automatically via equivalent widths (EW) using **ARES** (Sousa et al., 2007). The line list is the one reported in D'Orazi et al. (2015). On average, **ARES** could detect 17, 7 and 2 Ca I, Sc II and Mg I lines respectively. It is worth noticing that one of the Mg lines (5528Å) becomes saturated, showing damped wings in giant stars, which could make them less sensitive to the change of abundance. Lines with large fitting errors or that resulted in strongly discrepant abundances were checked manually using **iraf**. Abundances were derived from these EWs using **abfind** driver form **MOOG**

The abundance derivation for O, Na, Cu, Y, Ba, and Eu was done through spectral synthesis using **MOOG** with its driver **synth**, which is a 1D LTE line analysis code. The line lists for this method were generated with **linemake** code[6] (Placco et al., 2021), which

[6]Github site: **https://github.com/vmplacco/linemake**

Element	n	λ (Å)
Li	1	6708
Na	2	5682; 5688
Mg	2	5528; 5711
Al	1	6696
Ca	21	5260; 5261; 5349; 5588 5590; 5594; 5857; 5867 6161; 6163; 6166; 6169 6439; 6449; 6455; 6462 6471; 6493; 6499; 6572 6717
Sc	10	5318; 5526; 5640; 5657 5667; 5669; 5684; 6245 6279; 6604
Cu	1	5105
Y	3	5087; 5200; 5509
Ba	3	5853; 6141; 6496

Table 3.1 Average number of lines used for the abundance determination in the NGC 6752 sample for each element. Lines used for the abundance determination.

considers hyperfine splitting for Ba II (Gallagher, 1967), Cu I[7] (Kurucz and Bell, 1995), and Eu II (Lawler et al., 2001). I assumed solar isotopic ratios from Asplund et al. (2009b) for Cu, Y, Ba and Eu. Although the solar isotopic ratios for these elements are not necessarily appropriate for Population II stars, We note that this has negligible impact on the results at the spectral resolution under discussion.

I analysed the O atomic line at 6300Å and the Na doublet at 5682-5688Å. Both O and Na abundances were derived via spectral syntheses: because of the line weakness **ARES** was either unable to measure the EWs or returned very large associated errors. In fact, for O, no detection was possible even via synthesis, hence only upper limits were derived. We applied non-LTE corrections to the Na abundances using the corrections reported on INSPECT database, which is based on those provided by Lind et al. (2011).

Ba II lines (5853Å, 6141Å, and 6496Å), Y II (5087Å, 5200Å, and 5509Å), Cu I (5105Å) and Eu II (6645Å) are lines affected by isotopic and hyperfine splitting, and the determination of the abundances was done by matching the synthetic spectra with the observed ones.

[7] `http://kurucz.harvard.edu/atoms.html`

Specie	UVES	GIRAFFE
Li	10 (1)	63 (143)
Al	2 (9)	32 (174)
O	— (10)	— (—)
Na	10 (1)	70 (33)
Mg	11 (—)	76 (15)
Ca	11 (—)	— (—)
Sc	10 (—)	— (—)
Cu	7 (4)	— (—)
Y	9 (2)	20 (64)
Ba	11 (—)	117 (1)
Eu	— (11)	— (81)

Table 3.2 The number of stars for which We reported actual measurement (upper limits) for each element analysed in the NGC 6752 sample.

3.2.1.1 Y and Ba trends along with microturbulence

Ba abundances, which are based on three rather strong lines, show considerable sensitivity to the adopted v_m. This is a common finding in cool giants, as discussed, e.g., by Worley et al. (2013). This effect can be clearly seen in the high sensitivity of Ba abundances to the variations of this parameter reported in Table 3.8. It is worth noticing that the sensitivity of these species to v_m does not seem to depend on the method used for the v_m derivation. For example, by using the relation given by Mucciarelli and Bonifacio (2020), the v_m were systematically lower (by, on average 0.3 km/s), but the trends with Ba were still present. Figure 3.6 shows the distribution of the abundance obtained for each line as a function of v_m. We explored averaging Ba abundances weighted by their respective errors using the different combinations of lines to minimise this effect and concluded that the best combination is indeed the use of all three. We opted to use from hereinafter all the tree lines for our final abundance, due to the reduction of both the spread and the lessening of the v_m dependence. Similar considerations apply to the Y II lines used to derive [Y/Fe]II abundances. These dependencies are further discussed later in this paper. Cu abundances do not show any significant trend with v_m, which is expected for weak lines.

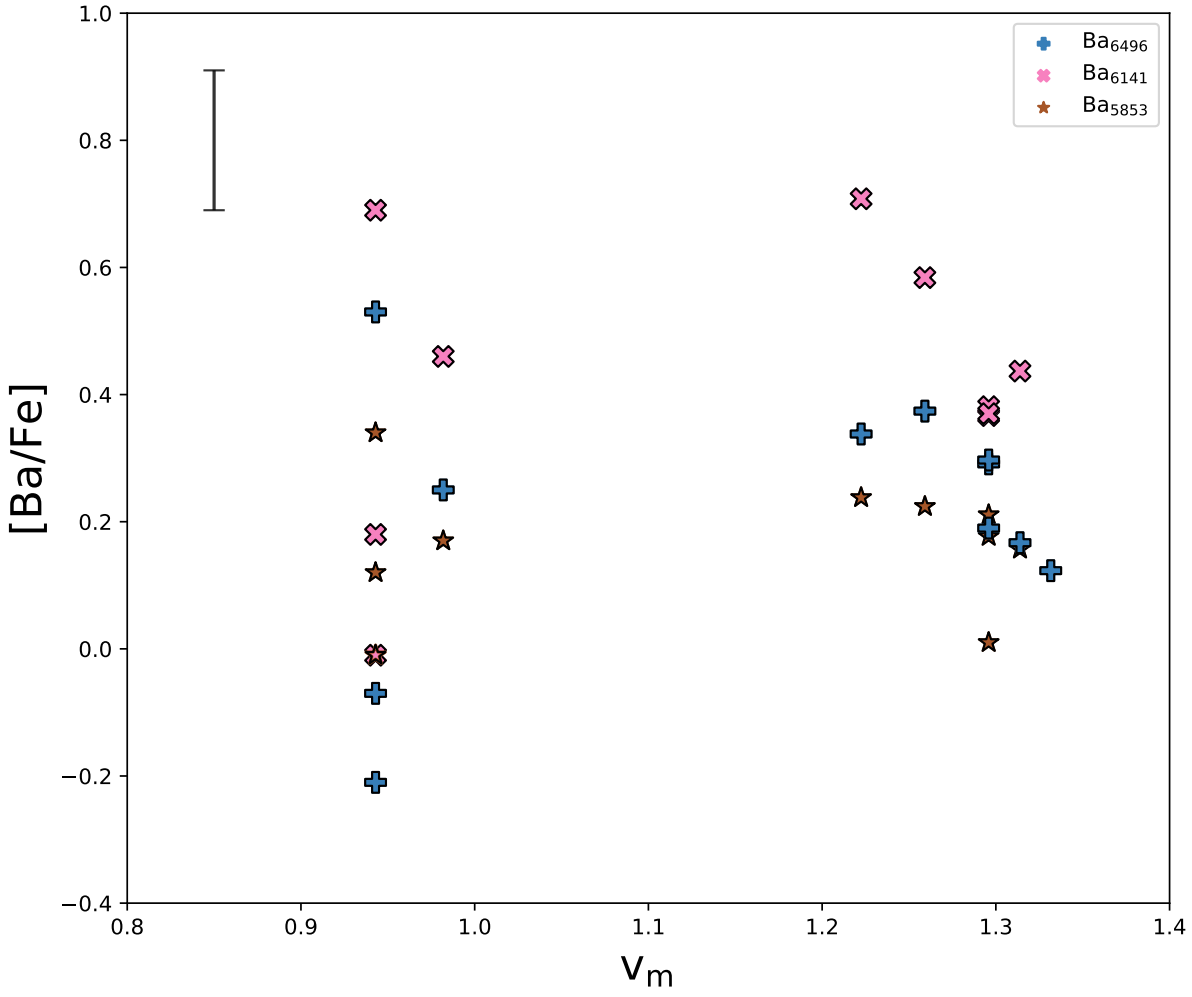

Figure 3.6 Ba abundances as a function of v_m for our UVES sample. Three different symbols represent the Ba lines at 5853Å, 6141Å, and 6496Å.

Table 3.2 shows a summary with the number of analysed targets for which We reported actual measurements/upper limits in the present sample.

3.2.2 GCs survey sample

In the present thesis, were used the abundances reported by Carretta et al. (2009) for O, Na, Mg, Al, and Si and their respective errors. These abundances were determined by measuring the EWs of the mentioned species. A detailed description of the whole

Element	n	λ (Å)
O I	2	6300; 6363
Na I	4	5682; 5688; 6154; 6160
Mg I	3	5711; 6318; 6319
Al I	2	6696; 6698
Si I	14	5645; 5665; 5684; 5690
		5701; 5708; 5772; 5780
		5793; 5797; 5948; 6125
		6142; 6145

Table 3.3 Lines used for the abundance determination. Source: Carretta et al. (2009).

procedure can be found in Bragaglia et al. (2001). In the following, We am going to summarise some considerations for each element described by Carretta et al. (2009).

Since one of the two O lines could be affected by telluric lines, they used a synthetic spectrum to remove those features. The Na abundances were NLTE corrected according to the result given by Gratton et al. (1999). The Si measurements were derived using EW from a large number of lines laying between 5645Å and 6145Å. While Table 3.3 displays the detailed list of lines used by the authors, Table 3.4 shows the number of stars used for the abundance determination in each cluster. Finally, Table 3.5 shows the abundances reported in Carretta et al. (2009) for each cluster.

These spectra allow me to extend the analysis done by Carretta et al. (2009) to heavier elements. In particular, were analysed Cu, Y, Ba, La, and Eu. Although the number of lines used by the abundance determination can vary due to specific features of the spectra (e.g., SNR), in general, the lines considered for abundance determination can be found in Table 3.6. It is worth noticing that the abundances for Cu, Y, Ba, and Eu were derived with spectral synthesis considering the same model atmosphere generator code, line list, hyperfine splitting, and isotopic ratios described in Subsection 3.2.1. The spectrum synthesis for La was done using the 1D-LTE code `PySME`[8] (Wehrhahn, 2021) abundance Moreover, as was done for the NGC 6752 sample, the upper limits for all the elements were estimated using `pyMOOGi` and they are based on the Mucciarelli (2011) criteria described previously.

[8]webpage: `https://pysme-astro.readthedocs.io/en/latest/index.html`

Cluster	n_O	n_Na	n_Mg	n_Al	n_Si
NGC 104	11	11	11	11	11
NGC 288	10	10	10	10	10
NGC 1904	9	10	10	8	10
NGC 2808	12	12	12	12	12
NGC 3201	13	13	13	13	13
NGC 4590	13	12	13	13	13
NGC 5634	2	2	2	1	4
NGC 5904	14	14	14	14	14
NGC 6121	14	14	14	14	14
NGC 6171	5	5	5	5	5
NGC 6218	11	11	11	11	11
NGC 6254	14	14	14	10	14
NGC 6397	13	13	13	—	13
NGC 6752	14	14	14	14	14
NGC 6809	14	14	14	14	14
NGC 6838	12	12	12	12	12
NGC 7078	13	13	13	13	10
NGC 7099	10	10	10	10	9

Table 3.4 Number of stars used to the abundance derivation for each element. Source: NGC 5634 obtained from Carretta et al. (2017) the rest of the sample was taken from Carretta et al. (2009).

3.2.3 Y and Ba trends along with microturbulence

As was explained in the Subsection 3.2.1.1, both Y and Ba display strong trends with V_m. Like was done for the NGC 6752 sample,We computed ΔY and ΔBa to avoid any trend given by V_m in the whole sample. An illustrative example for the present sample is shown in the Fig. 3.7 and Fig. 3.8 for the GC NGC 1904. In the left panel of both figures, it is clearly shown a strong negative Spearman correlation (about 0.85). The right panels show how the trend is avoided by using the Δ_s. The whole set of plots (Fig. C.1 to Fig. C.6)is attached in the Appendix C.

Star	[O/Fe] (dex)	rms	[Na/Fe] (dex)	rms	[Mg/Fe] (dex)	rms	[Al/Fe] (dex)	rms	[Si/Fe] (dex)	rms
NGC 104	0.25	0.15	0.53	0.15	0.52	0.03	0.52	0.17	0.40	0.02
NGC 288	0.34	0.14	0.29	0.28	0.45	0.03	0.40	0.09	0.37	0.03
NGC 1904	0.05	0.29	0.42	0.29	0.28	0.06	0.64	0.41	0.29	0.03
NGC 2808	0.07	0.36	0.20	0.24	0.20	0.25	0.40	0.49	0.28	0.05
NGC 3201	0.03	0.28	0.16	0.31	0.34	0.04	0.14	0.38	0.30	0.05
NGC 4590	0.41	0.11	0.33	0.19	0.35	0.06	0.74	0.18	0.40	0.05
NGC 5634	0.29	0.13	0.17	0.27	0.52	0.04	0.50	0.29	0.30	0.03
NGC 5904	0.08	0.23	0.25	0.24	0.41	0.07	0.27	0.29	0.30	0.05
NGC 6121	0.26	0.10	0.40	0.15	0.55	0.03	0.60	0.05	0.52	0.06
NGC 6171	0.12	0.13	0.49	0.15	0.51	0.04	0.39	0.07	0.53	0.08
NGC 6218	0.34	0.14	0.30	0.27	0.52	0.04	0.20	0.18	0.35	0.06
NGC 6254	0.41	0.15	0.17	0.19	0.49	0.04	0.41	0.37	0.28	0.05
NGC 6397	0.29	0.09	0.18	0.19	0.46	0.04	—	—	0.34	0.05
NGC 6752	0.16	0.28	0.33	0.27	0.50	0.05	0.41	0.33	0.38	0.05
NGC 6809	0.16	0.11	0.38	0.23	0.47	0.1	0.49	0.32	0.38	0.06
NGC 6838	0.31	0.13	0.45	0.16	0.49	0.04	0.50	0.15	0.38	0.06
NGC 7078	0.34	0.19	0.20	0.25	0.45	0.19	0.57	0.26	0.43	0.10
NGC 7099	0.46	0.20	0.35	0.25	0.51	0.04	0.77	0.32	0.34	0.07

Table 3.5 Average abundance for all the elements measured by the authors. Source: Carretta et al. (2009)

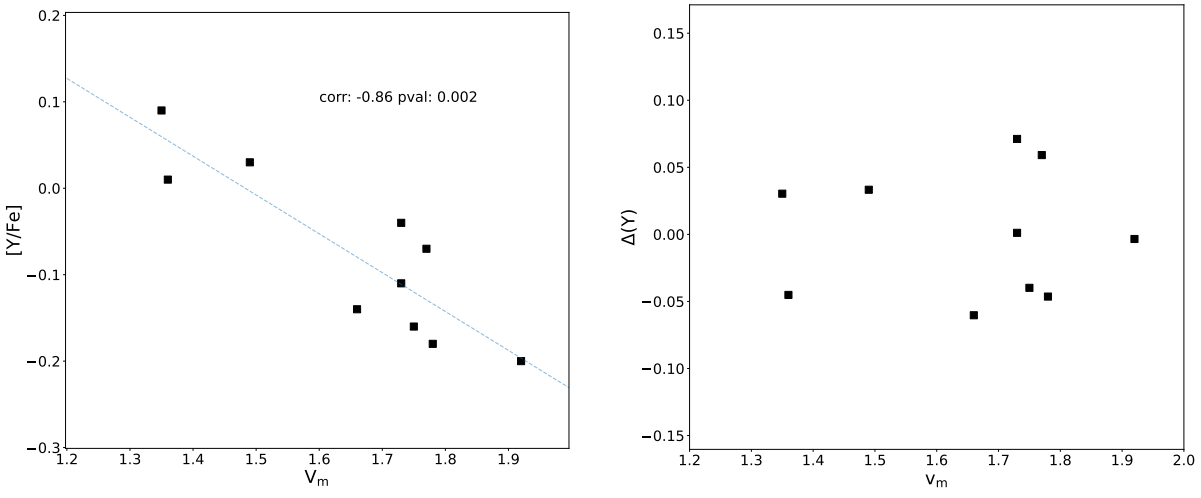

Figure 3.7 [Y/Fe] (left panel) and Δ(Y) (right panel) as a function of V_m for the GC NGC 1904. The blue dotted line shows the linear fit.

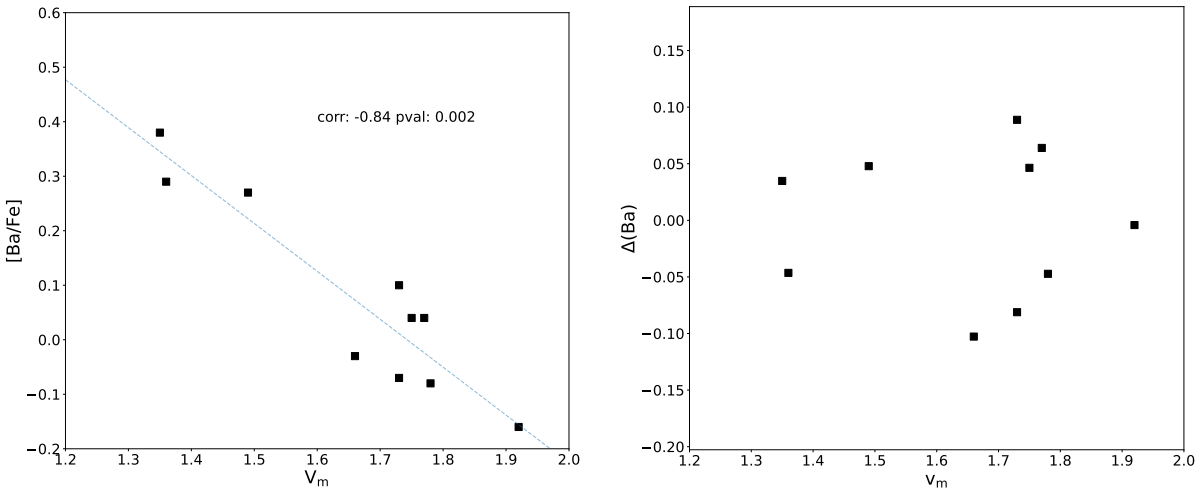

Figure 3.8 [Ba/Fe] (left panel) and Δ(Ba) (right panel) as a function of V_m for the GC NGC 1904. The Blue dotted line shows the linear fit.

Element	n	λ (Å)
Cu I	1	5105
Y II	4	4883; 5087; 5200; 5509
Ba II	3	5853; 6141; 6496
Eu II	1	6645

Table 3.6 Lines used for the abundance determination of heavier element in the present extended survey

3.3 Observational uncertainties

3.3.1 NGC 6752 sample

The uncertainty associated with the measurements combines the uncertainties of the best-fit determination and those associated with the uncertainties in the adopted atmospheric parameters. To determine them,We followed the approach described by D'Orazi et al. (2014). The first is either by the error on the best-fit determination (for abundances derived via synthesis) or line-by-line abundance scatter (for abundances

ID	Element	T_{eff} (+100)	$\log g$ (+0.2)	v_m (+0.1)	[Fe/H] (+0.1)
#3081	A(Li)	0.08	0.01	0.01	0.01
	A(Al)	0.02	0.01	0.01	0.00
#2245	A(Li)	0.10	0.00	0.01	0.01
	A(Al)	0.05	0.01	0.01	0.01

Table 3.7 Elements sensitivity to the change in stellar parameters on representatives of TO/SGB star (#3081) and RGB star (#2245).

determined with EWs analysis). The second is derived by evaluating the variation of the abundances to the change in each of the parameters (T_{eff}, $\log g$, v_m, and [Fe/H]), keeping fixed the remaining ones.

I selected two stars to represent the sample: #3081 for TO/SGB and #2245 for RGB ones to estimate the sensitivity of the Li and Al abundances measured to the change of stellar parameters. The variations assumed in stellar parameters are: $\Delta T_{eff} = 100$ K, $\Delta \log g = 0.2$ dex, $\Delta v_m = 0.1$ km s^{-1}, and Δ[Fe/H]$= 0.1$ dex. This sensitivity matrix can be found in the table 3.7.

To derive the sensitivity of the derived abundances to atmospheric parameters for the heavier elements, We selected two stars with a suitable spectral range to measure those elements. The representative stars of the whole sample were an unevolved (#19102677-6003089) and an evolved (#19102025-5958306) star. As was done for Li and Al, the perturbations in stellar parameters to estimate the sensitivity of the element are $\Delta T_{eff} = 100$ K, $\Delta \log g = 0.2$ dex, $\Delta v_m = 0.1$ km s^{-1}, and Δ[Fe/H]$= 0.1$ dex. The abundance errors are based on the sensitivity matrix shown in Table 3.8.

The full tables with stellar parameters and their uncertainties (Table A.1), as well as, the abundances measured and their respective errors (Table A.2) for the whole NGC 6752 sample are attached in the Appendix A.

3.3.2 Fe spread

Milone et al. (2017) developed a two-colour diagram so-called chromosome map to disentangle the different populations in GCs. They have found that FG stars display

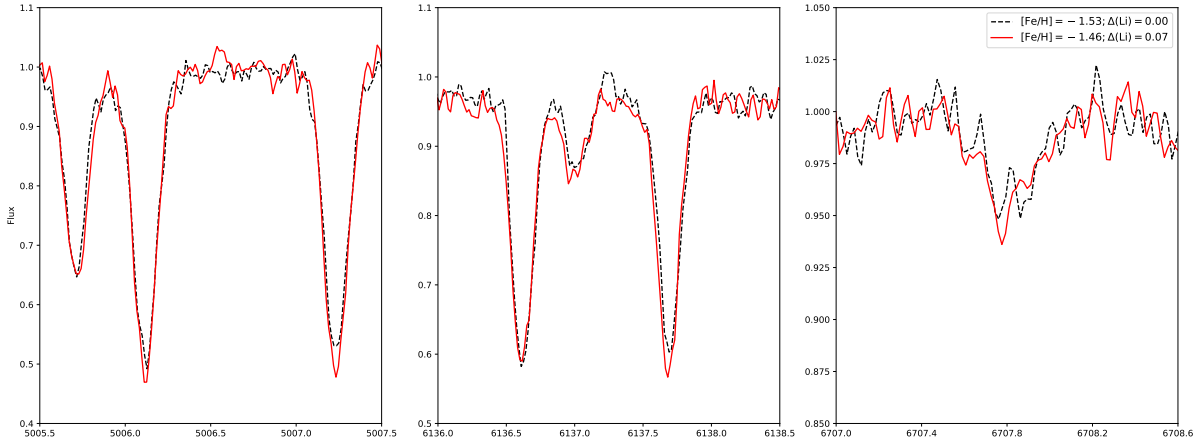

Figure 3.9 Comparison of Fe lines for two stars with similar stellar parameters. The red solid and the black dashed line represent two evolved stars with a $T_{\rm eff}$ of 5257 K and 5232 K, respectively.

an extended sequence in the diagram. Marino et al. (2019) claimed it could be either given by a He- or Fe-spread among FG stars, meaning those stars were not as homogeneous as was thought. Legnardi et al. (2022) analysed a large sample of GCs and they determined the extended FG sequence was produced due to an iron dispersion among their members. In particular, they estimated the Fe-dispersion in NGC 6752 to be 0.106±0.017.

We performed Fe abundance determination for our UVES sample, which has a broader wavelength range than the GIRAFFE ones to analyse the Fe-dispersion among FG stars. For those stars, we found an intrinsic internal iron variation of 0.12±0.05 dex, which is in principle good agreement with the spread reported by Legnardi et al. (2022), but at the same time is also consistent with no Fe spread. To investigate this further, we compared the spectra of FG stars with similar stellar parameters with resulting different Fe. In our UVES sample, we have four FG stars with a difference in $T_{\rm eff}$ of about 25 K. Fig.3.9 shows a limited wavelength range with Fe lines for a graphical comparison of the two stars with the most different iron abundance. The [Fe/H] in our four stars range from -1.53±0.05 dex to -1.46±0.05 dex, meaning that considering the associated errors, we did not find a significant difference in their iron abundances. Nevertheless, due to our small sample, it must be taken with caution.

	19102677-6003089					19102025-5958306				
	Best$_{fit}$	ΔT$_{\rm eff}$ (100 K)	$\Delta\log g$ (0.2 dex)	Δ[Fe/H] (0.1 dex)	Δv_m (0.1 km s^{-1})	Best$_{fit}$	ΔT$_{\rm eff}$ (100 K)	$\Delta\log g$ (0.2 dex)	Δ[Fe/H] (0.1 dex)	Δv_m (0.1 km s^{-1})
Na	0.10	0.07	0.06	0.06	0.01	0.05	0.04	0.00	0.00	0.00
Mg	0.15	0.05	0.03	0.00	0.01	0.05	0.08	0.04	0.00	0.01
Ca	0.10	0.05	0.01	0.00	0.01	0.05	0.05	0.03	0.01	0.02
Sc	0.10	0.03	0.07	0.00	0.01	0.10	0.03	0.07	0.01	0.01
Cu	0.10	0.10	0.01	0.01	0.00	0.05	0.11	0.01	0.02	0.01
Y	0.10	0.05	0.06	0.02	0.01	0.10	0.06	0.07	0.01	0.02
Ba	0.10	0.07	0.04	0.01	0.05	0.10	0.07	0.05	0.01	0.07

Table 3.8 Sensitivity matrix for Na, Mg, Ca, Sc, Cu, Y, and Ba on representatives of TO/SGB star (#19102677-6003089) and RGB star (#19102025-5958306).

3.3.3 GCs survey sample

Because this sample will be compared to different GCs, the observational uncertainties should consider both the individual star error and the cluster systematic error. While the first is an error that arises in the internal comparison of stars in a given cluster, the second one takes into account the comparison with other GCs. It is worth noticing that, for the extended analysis of the present sample, one representative star of each cluster is used to evaluate the sensitivity of the elements to the stellar parameter variations. The sensitivity matrix can be found in Appendix E (Table E.1).

Table 3.9 summarises the errors described above for each cluster reported by Carretta et al. (2009). In the following, We describe their determination.

3.3.3.1 Individual star error

It is worth noticing that, for the species analysed in Carretta et al. (2009) and Carretta et al. (2017), the error associated with $\log g$ and [Fe/H] have a lower influence on the budget of the total error. This is not the case for the extended analysis of heavier elements of the present thesis, which are more sensitive to $\log g$ variations.

The error coupled to $T_{\rm eff}$ was estimated from the slope in the empirical function $T_{\rm eff}$(V-K) described by (Alonso et al., 1999). To compute the error coming from the EW determinations, the authors took the mean rms scatter of the Fe abundance in a sub-sample of stars per cluster and divided it by the square root of the number of measured lines. It is worth noticing that for the extended analysis in the present thesis, it was performed a spectral synthesis analysis, and then this error source will be replaced by the fitting uncertainty. Finally, the internal V_m error was derived by varying 1σ the slope between the strength of the Fe I line and the abundance.

3.3.3.2 Cluster systematic error

The error coupled to $T_{\rm eff}$ comes from the empirical relation between $T_{\rm eff}$ and the (V-K) color given by (Alonso et al., 1999). Since the V-K are dereddened, they estimated the

	Star-to-star errors					Cluster errors			
Cluster	T_{eff} (K)	$\log g$ dex	[A/H] (dex)	V_m (km/s)	*EW* (dex)	T_{eff} (K)	$\log g$ dex	[A/H] (dex)	V_m (km/s)
NGC 104	6	0.02	0.05	0.06	0.01	40	0.06	0.03	0.02
NGC 288	6	0.04	0.05	0.08	0.01	63	0.06	0.07	0.02
NGC 1904	5	0.04	0.03	0.06	0.01	57	0.06	0.07	0.02
NGC 2808	44	0.02	0.07	0.06	0.01	42	0.06	0.05	0.02
NGC 3201	4	0.04	0.06	0.05	0.01	62	0.06	0.07	0.01
NGC 4590	4	0.04	0.05	0.38	0.02	69	0.06	0.07	0.10
NGC 5904	12	0.04	0.05	0.05	0.01	54	0.06	0.06	0.01
NGC 6121	4	0.04	0.05	0.04	0.01	54	0.06	0.05	0.01
NGC 6171	2	0.04	0.06	0.07	0.01	26	0.06	0.04	0.03
NGC 6218	6	0.02	0.04	0.04	0.01	48	0.06	0.07	0.01
NGC 6254	4	0.04	0.06	0.09	0.01	67	0.06	0.08	0.02
NGC 6397	4	0.04	0.04	0.08	0.02	64	0.06	0.06	0.02
NGC 6752	5	0.04	0.05	0.03	0.01	58	0.06	0.07	0.01
NGC 6809	5	0.04	0.06	0.13	0.01	58	0.06	0.07	0.03
NGC 6838	5	0.04	0.06	0.06	0.01	45	0.06	0.05	0.02
NGC 7078	5	0.04	0.06	0.26	0.02	67	0.06	0.07	0.07
NGC 7099	5	0.04	0.05	0.12	0.02	71	0.06	0.07	0.04

Table 3.9 Individual stars errors and cluster systematic errors. Source: Carretta et al. (2009)

error coming from the reddening adopted, which affects their T_{eff}. To get the internal error of the $\log g$, they propagate the uncertainties in distance modulus, in the mass of the star, and the error associated to T_{eff}. The one associated with V_m is given by its internal error divided by the square root of the star number. Finally, the error coupled to the metallicity was given by the quadratic sum of the systematic error contribution of the systematic contribution T_{eff}, $\log g$, and V_m multiplied with their correspondent abundance sensitivity. The last term was given by the rms scatter in a given element divided by the square root of the star number of a given cluster.

Chapter 4

Discussion on the NGC 6752 sample

In the present chapter, We summarise the results obtained and discuss their implication. The chapter starts with a full analysis of the Li evolution and its comparison with models, the distribution of Al, and the abundance patterns in both light and heavy elements in the NGC 6752 sample.

4.1 NGC 6752 sample

4.1.1 Li evolution and model predictions

Figure 4.1 shows the distribution of A(Li)$_{NLTE}$ as a function of the $\log g$. The overall Li abundance shows a continuous decrease from a plateau at A(Li)$_{NLTE}$=2.33±0.06 dex, where TO stars show the highest Li abundance. We estimated this value by averaging the measurements for the stars in the upper quartile of the distribution of Li measurements, with $\log g$ > 3.87. This choice was determined by the need to avoid the influence of Li-depleted stars. This plateau is in agreement with previous studies (Mucciarelli 2011, G14), showing a significant difference from the lithium abundance expected from the Big Bang nucleosynthesis. This discrepancy goes beyond the scope of the present paper, but We refer the interested readers to the relevant literature on the topic, e.g., Fu et al. (2015), Matteucci et al. (2021).

The observed drop of the lithium abundance with decreasing $\log g$ is expected based on stellar evolution. After stars leave the main sequence, stars go through their sub-giant branch phase and climb up the RGB. Then they experience dredge-up episodes and mixing process, which bring to the stellar surface material processed in layers where the temperature is high enough to burn Li, decreasing the Li content, until it is essentially completely destroyed after RGB-bump. Gratton et al. (2000) showed the depletion of Li observed in metal-poor field stars as they evolve, finding however negligible dispersion among stars in the same evolutionary stage.

We used six different evolutionary tracks from Pietrinferni et al. (2021) to derive the theoretical predictions for Li abundances and evolutionary depletion. The tracks consider convective core over-shooting, atomic diffusion, and mass loss. To our aim, we use tracks with stellar masses of 0.70$M_{\odot}$, 0.75$M_{\odot}$, 0.80$M_{\odot}$, 0.85$M_{\odot}$, 0.90$M_{\odot}$, and 1.0$M_{\odot}$, which correspond to stars between the TO and the bottom RGB for a cluster of 12 Gyr and a [Fe/H]=-1.55 dex. The expected Li abundance for a GC of this age, for each track at a given $\log g$ is shown with pink stars in Fig.4.1. The dashed line interpolates these points by fitting a first- and sixth-order function for unevolved and evolved Li prediction. Note that the fitting of the evolutionary Li is not intended to be rigorous, but to follow the Li variations at different evolutionary stages. Although the overall Li predicted is overestimated, the upper envelope of the Li observed of FG stars tends to follow the prediction closely, indicating a good agreement with the models. It is worth noticing that the Li predictions are pretty sensitive to the models' mixing processes. The good match between predictions and observations supports the treatment of mixing processes in the models. In addition, according to the figure, models predict a Li abundance peak close to the TO stars. However, this is not clear from the observations. In fact, fainter stars than the TO with abundances belonging to the upper quartile of the Li distribution display a flat trend. As shown in Fig. 4.1, in addition to the evolutionary Li decrease, at each $\log g$. Gruyters et al. (2014) showed evidence of a small effect of atomic diffusion in the Li abundance of stars along every evolutionary stage. Nevertheless, the considerable range of Li suggests that there is an additional factor involved. This is peculiar to GCs, and it is a behaviour thought to be related to the MSP phenomenon present in GCs.

In order to better probe the variations of Li not due to evolution, We have to account for the latter. We have thus defined the quantity ΔA(Li), the difference between the Li measured and its corresponding Li from the fitting line (see Fig. 4.1) at every $\log g$.

Figure 4.2 shows the ΔA(Li)–$\log g$ plane. If the only factor determining Li depletion were evolution, then the expectation is that stars would follow the red dashed line of Fig.4.2. In fact, it is not worth it that there is a lack of stars on and above the curve. As mentioned earlier, Gratton et al. (2000) showed that metal-poor field stars exhibit decreasing Li abundance as they evolve. In this regard, assuming that FG stars will follow the evolutionary Li behaviour, we can expect that a few of them –for statistical reasons– would have their measurement above the curve. A lack of them could indicate a potential systematic underestimation of our values, which, however, would not affect our conclusions. On the other hand, a large fraction of stars in the sample is considerably depleted in Li for their evolutionary status, a characteristic that is peculiar to GCs.

It is interesting to look at the fraction of Li-poor stars: Gratton et al. (2019) found a strong correlation between the fraction of Li-poor population of a GC with its extreme fraction of stars as determined by Carretta et al. (2009), which is 0.4 for this cluster. We adopt as a working definition of Li-poor stars that of being 6σ below the theoretical prediction. In Fig.4.1 the blue shading shows the area corresponding to the >6σ from the fit. Note that it is split in unevolved and evolved stars, adopting $\log g$=3.87 (grey line) as separation, as it is the point where the overall Li abundance starts being affected by evolutionary depletion (see Fig. 4.1) and it is approximately the point where the stars leave the TOP. Based on this definition, the fraction of Li-poor stars is 0.43±0.05. This result is in good agreement with the expected fraction of Li-poor stars shown in Fig. 18 of Gratton et al. (2019), and in better agreement than that reported by Shen et al. (2010), 0.30±0.05. However, they analysed only unevolved stars, in which, due to their temperatures, Li is measurable only when relatively high, leading to a selection effect. Finally, one could try to explain the presence of Li-poor stars (upper limits) with stars belonging to binary systems. Binary stars can transfer mass, which could lead to enhanced mixing leading to a lower Li content. However, this effect would only be applicable to a small fraction of stars, as binary systems in GCs are generally not

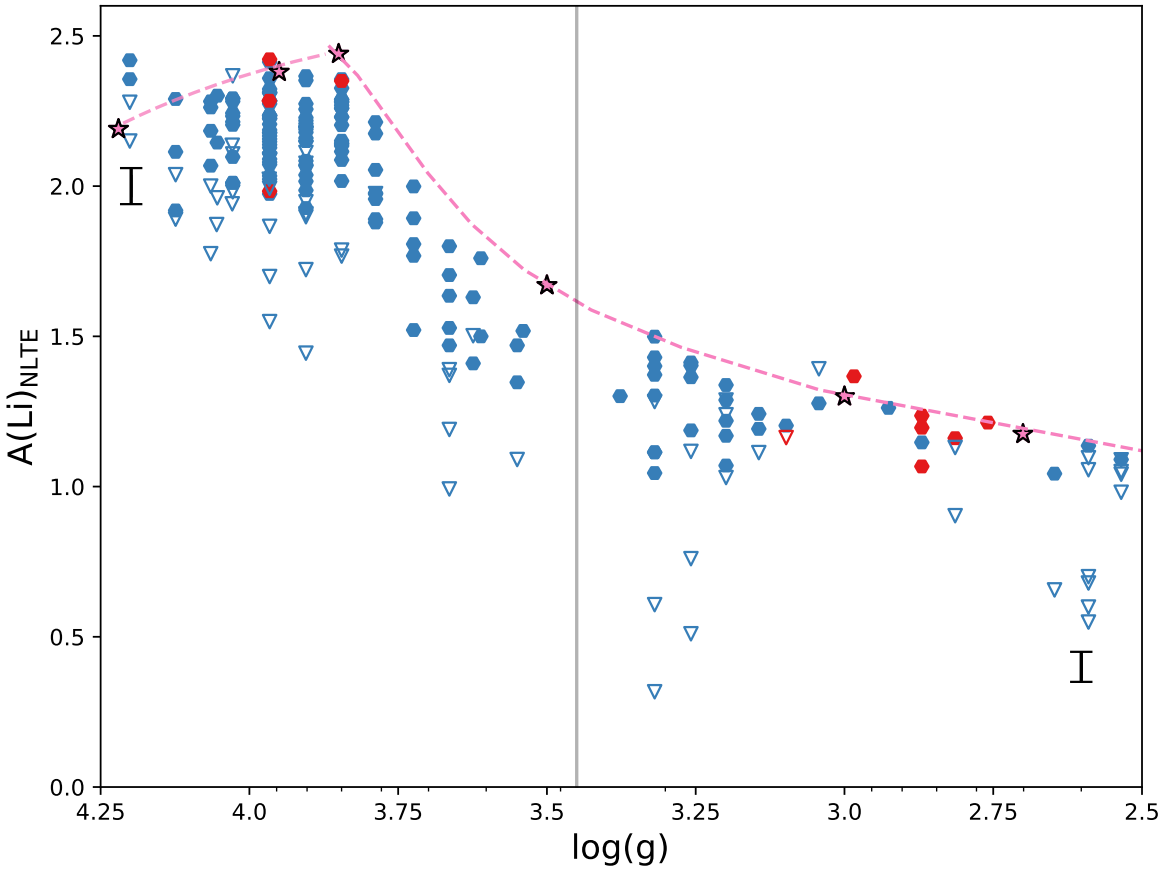

Figure 4.1 Li_{NLTE} abundance as a function of the $\log g$. Red and blue symbols show UVES and GIRAFFE spectra, respectively. Closed hexagons are measurements, while open triangles represent upper limits in Li. The pink stars and the dashed line indicate the expected evolution of Li. The vertical solid line shows the $\log g$ at the bottom of the RGB.

common (see e.g. Lucatello et al., 2015) and could not explain the number of stars with upper limits in Li in our sample (∼25%).

It is clear here that there is an intrinsic spread at every evolutionary stage, which We expect to be related to the MSP phenomenon. Moreover, the spread seems roughly the same even beyond the TO, suggesting that the stars had different Li content from their birth, and the spread is maintained through the depletion due to stellar evolution.

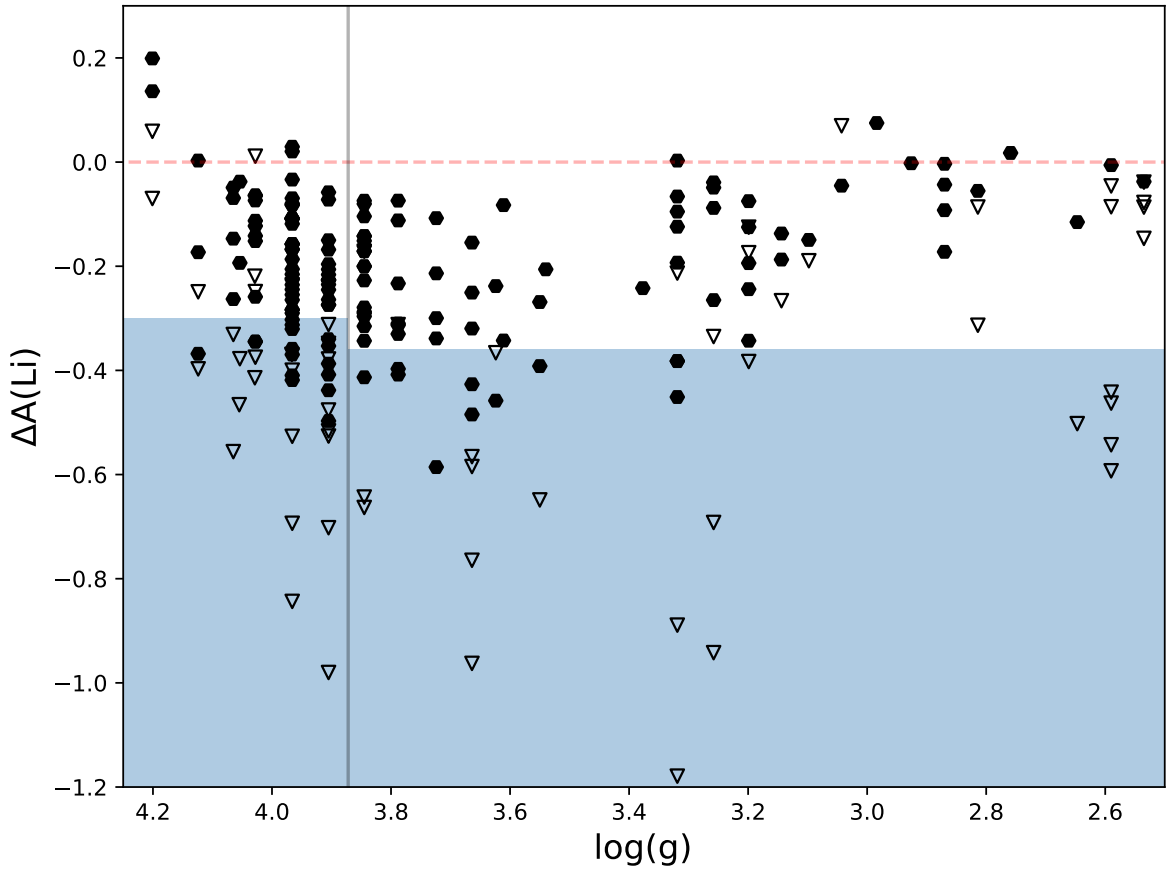

Figure 4.2 Δ(Li)–$\log g$ plane. The blue area shows the values larger than >6σ from the fit. Symbols follow the same description as Fig. 4.1 for Li.

4.1.2 Li and Fe

The Li content in FG stars is only expected to be affected by the evolutionary effects. Li abundance determinations should not be affected by small Fe variations, hence its measurement should be quite robust with respect to a potential Fe spread. The 4 stars mentioned in Sec.3.3.2 are evolved stars, so we compared their ΔLi abundances, which range from -0.17±0.05 to 0.07±0.05. This Li spread should be further investigated in a larger sample, but it could suggest a spread in elements other than Fe in FG stars, which could also be a potential explanation for part of the spread in the SG ones. Similar Li spread in FG stars have been found previously in other GCs: D'Orazi et al.

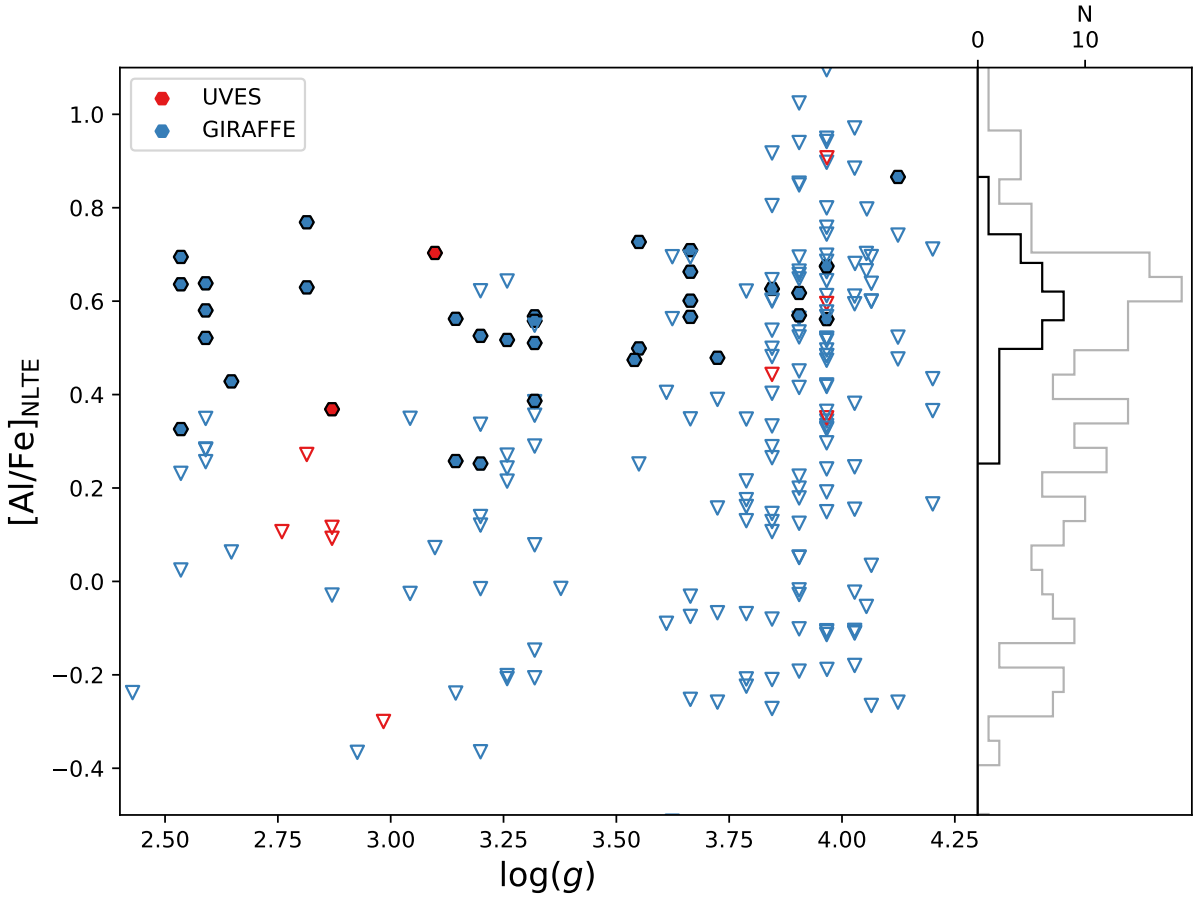

Figure 4.3 [Al/Fe] as a function of $\log g$. Blue and red symbols represent GIRAFFE and UVES spectra. Empty down-pointing triangles represent upper limits in Al. The black and grey histograms on the right show the counts of actual measurement (only filled hexagons) and the whole sample, respectively.

(2014) reported a Li difference of ∼0.25 dex among their FG sample in NGC 6218 and NGC 5904, and later in the GCs NGC 2808 and NGC 362 (D'Orazi et al., 2015).

4.1.3 Al distribution

Figure 4.3 shows the distribution of Al measurements and upper limits as a function of $\log g$. Detection was possible only in Al-rich stars, while most stars have an Al content too low to produce a detectable line at the temperature and signal-to-noise ratio of the star. The results show a dispersion of Al content in the sample, consistently with

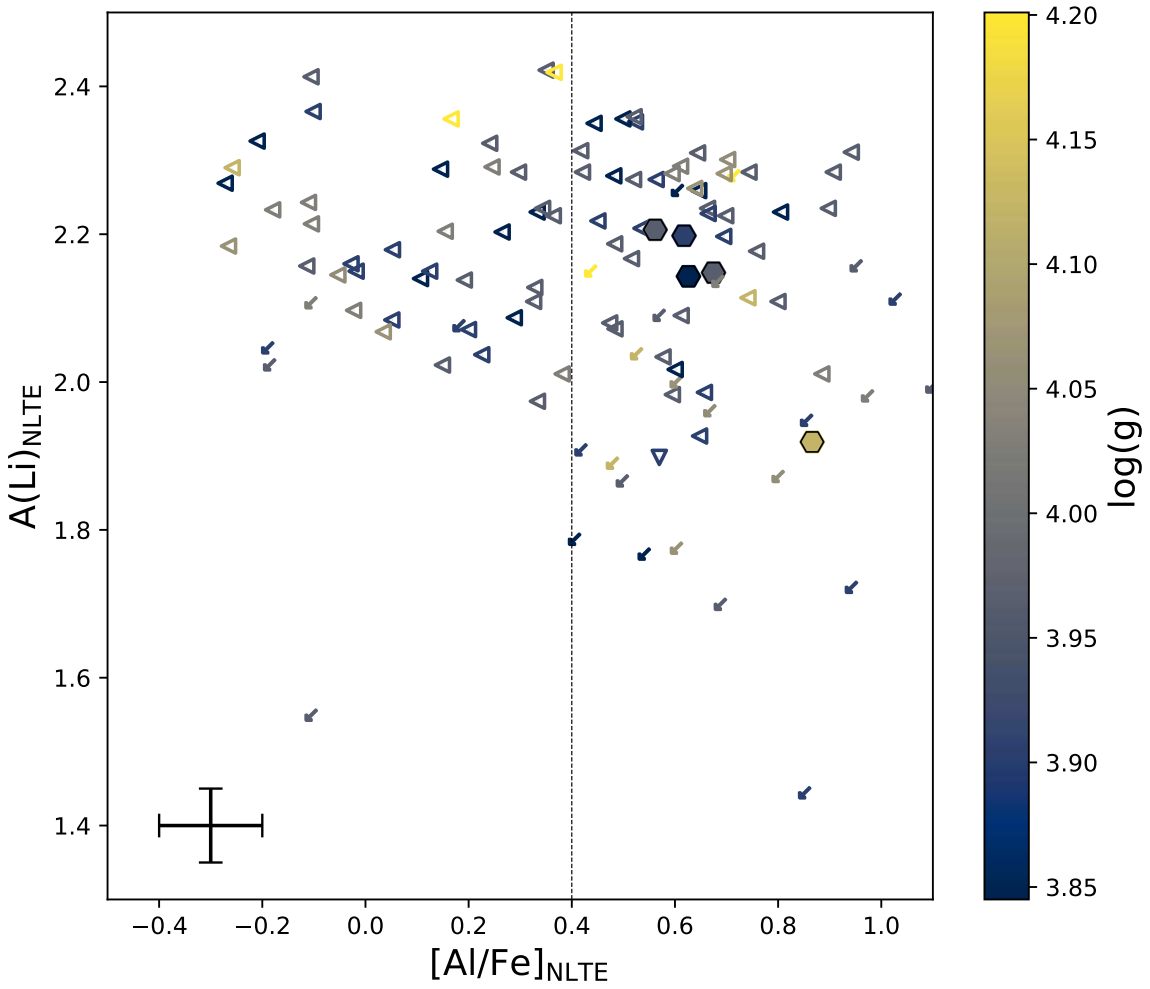

Figure 4.4 Relation between aluminium and lithium abundances. It shows the results for stars with higher $\log g$ than 3.85. Symbols are coloured based on the $\log g$ scale. The vertical dashed line at [Al/Fe]=0.4 dex is the threshold value used by (Carretta et al., 2012) to separate the first and second generation in NGC 6752. Left-pointing triangles show upper limits in Al. Diagonal arrows represent the upper limits in both Li and Al. Finally, down-pointing triangles represent upper limits in Li.

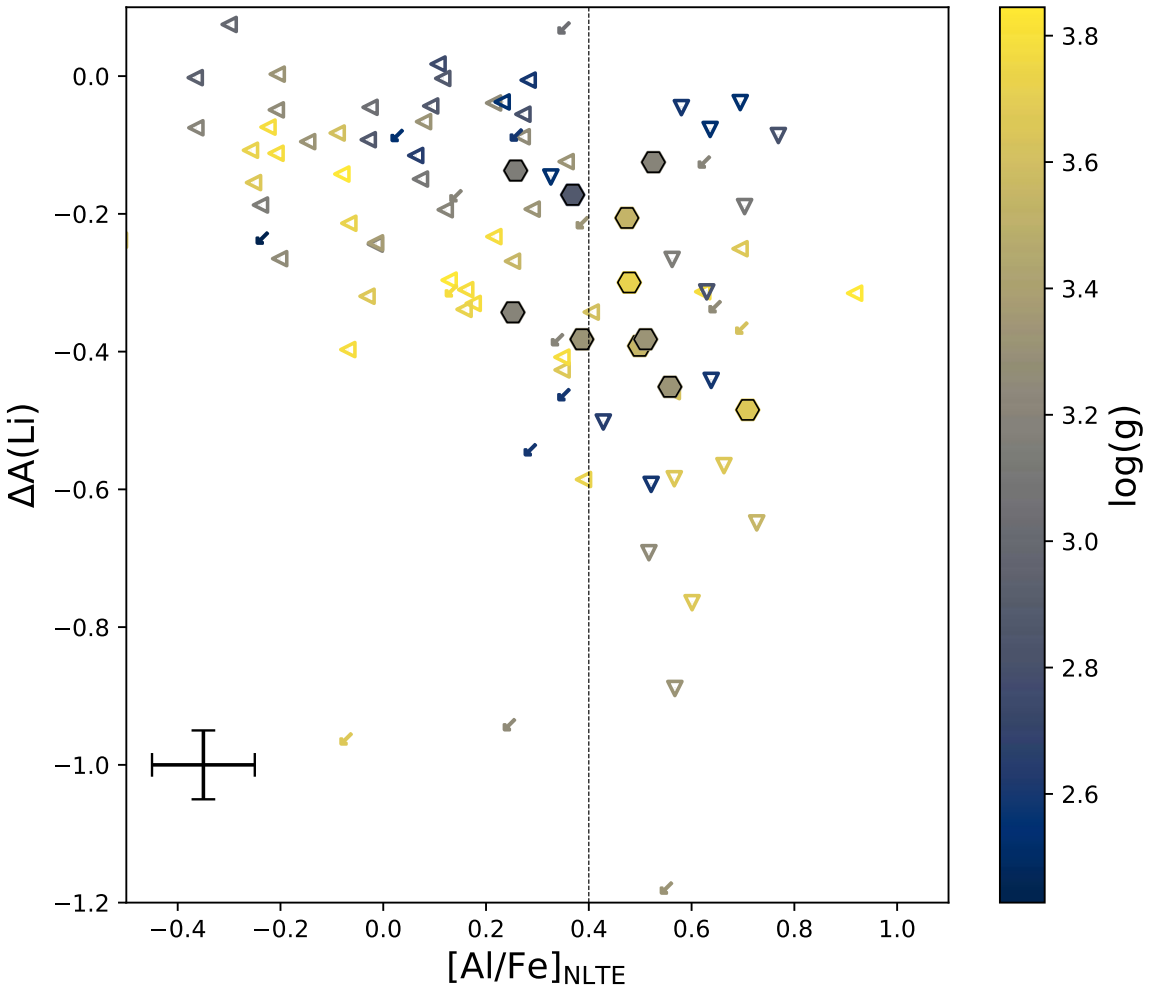

Figure 4.5 Relation between aluminium and lithium abundances. It shows the results for stars with lower $\log g$ than 3.85. Symbols and colours follow the same description as Fig.4.4.

previously published studies (Carretta et al., 2009, 2012, Mészáros et al., 2020). The spread is found at all evolutionary stages.

Considering upper limits and detections, We can estimate that the Al spread is at least 1.2 dex. It is worth noticing that there is no evidence of an offset in the Al content between TO/SGB and RGB stars, which argues in favour of the approach in the derivation of a uniform temperature scale for the whole sample. The Al spread is lower than the spread reported by Carretta et al. 2012 (∼1.75 dex), but it is in good agreement with

Carretta et al. 2009, who reported an Al spread of ∼1.11 dex. This could be due to the fact that the former is based on a different set of lines (Al doublet at 8772–8773Å), while the second uses the same set of Al lines as us.

The distribution of the Al abundance is of interest in the context of the multiple-generation scenario for the MSP (e.g. Carretta et al., 2013): a clumpy distribution would argue in favour of different episodes of star formation, while a smooth one would be consistent with continuous star formation. In the sample, We do not find any evidence for clumpy distribution, as can be seen from Fig 4.3. Note that this is not inconsistent with previous findings of a clumpy distribution (see e.g., Carretta et al. 2012) as there are only a small number of actual Al detections (as opposed to upper limits) in this sample.

4.1.4 Li and Al

It is interesting now to examine the relation between Li and Al in the cluster's stars. Figures 4.4 and 4.5 show the Li abundance as a function of [Al/Fe]. The former shows the results for stars where the evolutionary effect on Li has not taken place yet, while the last is for evolved stars.

Carretta et al. (2012) considered [Al/Fe] = 0.40 dex as the threshold between two populations, with the first- and second-generation stars being the ones with smaller and larger aluminium abundance than the threshold value, respectively. However, the threshold is based on a distribution derived with a different set of aluminium lines (the Al doublet 8772–8773 Å), and thus in principle, not fully consistent with the Al abundances, which are based on the 6696 and 6698 Ålines. In fact, Carretta et al. (2012) obtained a larger Al abundance spread (∼1.5 dex) than the present ones or that of Carretta et al. (2009) (also based on the 6696 and 6698 Ålines). In order to investigate potential offsets in the Al distributions derived using the two sets of lines mentioned above, We examined the Al abundances in 3 stars in common between Carretta et al. (2009) and Carretta et al. (2012). Note that We have no star in common with either of these studies, so a direct comparison was not possible. We find that [Al/Fe]=0.4 dex as derived from the 8772Å and 8773 Å lines correspond to 0.34±0.07 dex derived from

the lines used in this work. Given that, only three stars were available for this exercise and that the rescaled Al threshold value is consistent with the original one within the error, We adopt the 0.4 Carretta et al. (2012) value as the threshold between the first and second-generation stars in the rest of the discussion.

In Fig. 4.4, the measurements of Al and the upper limits on the left-hand side show that there is a considerable Al spread even among stars with high Li (A(Li)$\sim$ 2.25). In other words, We found Li-rich stars both among first- (Al-poor) and second- (Al-rich) generation stars. This is not an evolutionary effect, nor is it expected from the pure pollution scenario from hot H-burning processed (Na, Al, N rich and C, Mg and Li poor) material.

In Fig. 4.5, We probe the same relation for evolved stars. As this sample includes stars that have experienced various amounts of evolutionary Li depletion, to single out the effect of MSP, We considered the previously defined term, ΔA(Li) instead of the A(Li). After the evolutionary effect has been removed, besides Li-rich, Al-poor stars, and Li-poor, Al-rich stars, there is also a number of Al-rich, SG stars, with the same Li content as their FG, Al-poor counterparts.

In Fig. 4.6, We show a comparison between stars with similar stellar parameters and the same Li abundance (within the errors). Their quite different Al abundances show that they belong to different populations.

As was discussed in the introduction, the simplistic expectation is that the content of Li and p-capture elements should be anti-correlated. The stars could be divided into i) a Li-rich and Al-poor population (so-called first-generation stars) and ii) a Li-poor and Al-rich population (so-called second-generation stars). These stars are, in fact, found in both unevolved and evolved stars. However, in addition, We find a third group, an unexpected portion of stars that have both high aluminium and lithium.

As it is predicted for the models, in a GC of this metallicity, the initial Li abundance decreases by a factor of $\sim$20 after the first dredge-up (e.g.,Mucciarelli et al. 2012). This drop is consistent with the drop that We found in the evolved FG stars with respect to unevolved FG stars. On the other hand, although Li upper limits dominate the second group, the results are consistent with stars created from a material with low lithium

content or even from Li-free material. The chemistry of this group is consistent with having formed from material enriched by p-capture-rich, Li-poor material. Finally, the stars in the third group suggest the presence of some source of Li production, which enriches a fraction of the SG stars. It is interesting to note that the Li abundance never exceeds that of the plateau. The Li production seems to at most compensate the Li destruction, and it does not reach a Li content above such abundance value. It is worth noticing that all these three groups are visible in both panels.

Among the candidate polluters for GCs, the only nucleosynthetic site known to produce Li are intermediate-mass AGB stars (see, e.g., Gratton et al., 2019, for further details) and the findings suggest that these stars must have contributed to the pollution of the observed stars in the cluster under discussion. The same conclusion was reached for other clusters (see e.g., D'Orazi et al. 2014 for NGC 6218 and D'Orazi et al. 2015 for NGC 362). Moreover, the fact that We am finding different Li abundances among stars with similar Al abundance in the same evolutionary stage hints at the possibility of Li production in just a subset of the polluters. Probing the content of other chemical species could provide further insight into this issue. This is discussed further down.

According to models, AGB stars can produce the p-capture elements involved in the anti-correlations and Li (Ventura and D'Antona, 2008, 2009), which is produced through the Cameron-Fowler mechanism (Cameron and Fowler, 1971), in non-negligible amounts. Therefore, in principle, these polluters can explain the observed patterns not only for what concerns C, N, O, Na, Mg, and Al but also for Li elements.

However, it must be kept in mind that the details of the Li production are quite uncertain, so the quantitative predictions should be taken with some caution. The production of Li varies strongly with the mass of the AGB star, as shown in D'Antona et al. (2019a) who modelled the Li yields in different AGB masses. They used NGC 2808 as a GC prototype to explain the MSP phenomenon in GCs. They claimed that the chemical abundances of non-extreme SG stars could be explained by the diluted pollution of AGB stars, of different masses, with pristine gas.

We note that Li-rich giants (with A(Li) larger than expected for their evolutionary stage by ∼0.5-3.0 dex) are a known and rare phenomenon found both in the field and stellar clusters (e.g., Mucciarelli et al. 2021, Sanna et al. 2020). The nature of these rare objects

is still under debate. They are not expected to be related to the MSP phenomenon, but to an evolutionary effect. We refer the reader to the mentioned papers for a detailed discussion. Given the rarity of the phenomenon, it is unlikely that classical Li-rich giants account for a non-negligible fraction of the high Li, SG evolved stars We am observing. In fact, there is no evidence of an excess of Li-rich stars among evolved stars with respect to unevolved stars. However, it is important to keep in mind that the minimum measurable Li (or the minimum value of upper limits) in dwarves is higher than in evolved stars.

It has also been reported (e.g., Magrini et al. 2021, Mori et al. 2021) that red clump stars undergo a Li-enhanced phase just after the upper RGB, and in principle, they could also contribute to the Li production in the cluster. However, these Li enhancements are not expected at the metallicity of GC and at the evolutionary stages of the sample. Besides, even at higher metallicities, they are quite modest (∼0.6 dex; Zhang et al. 2021), not enough to explain the Li abundances found in the sample.

Finally, some studies have argued that the observational evidence in several clusters can not be reconciled with a single class of polluter (e.g., Carretta et al. 2018). The present data do not allow speculating further on this issue. However, they provide a strong indication that AGB stars must have contributed to the pollution of the SG stars also in NGC 6752.

4.1.5 Oxygen, Sodium, Magnesium

O, Na, Mg, and Al have been used as tracers of the MSP phenomenon. GCs display the well-known anti-correlations among pairs of these elements, which are thought to reflect different nucleosynthetic processes inside of the cluster polluters. Hot H-burning results in the production of Na by proton-capture processes through the NeNa chain and of Al, through the AlMg chain, while O and Mg get depleted. However, Mg gets a more modest depletion than Al because the Mg number density is much higher than the one for Al.

The spectroscopic indicators associated with the MSP phenomenon present in GCs were analysed. We note the Na-O anti-correlation is not significant in our sample, as

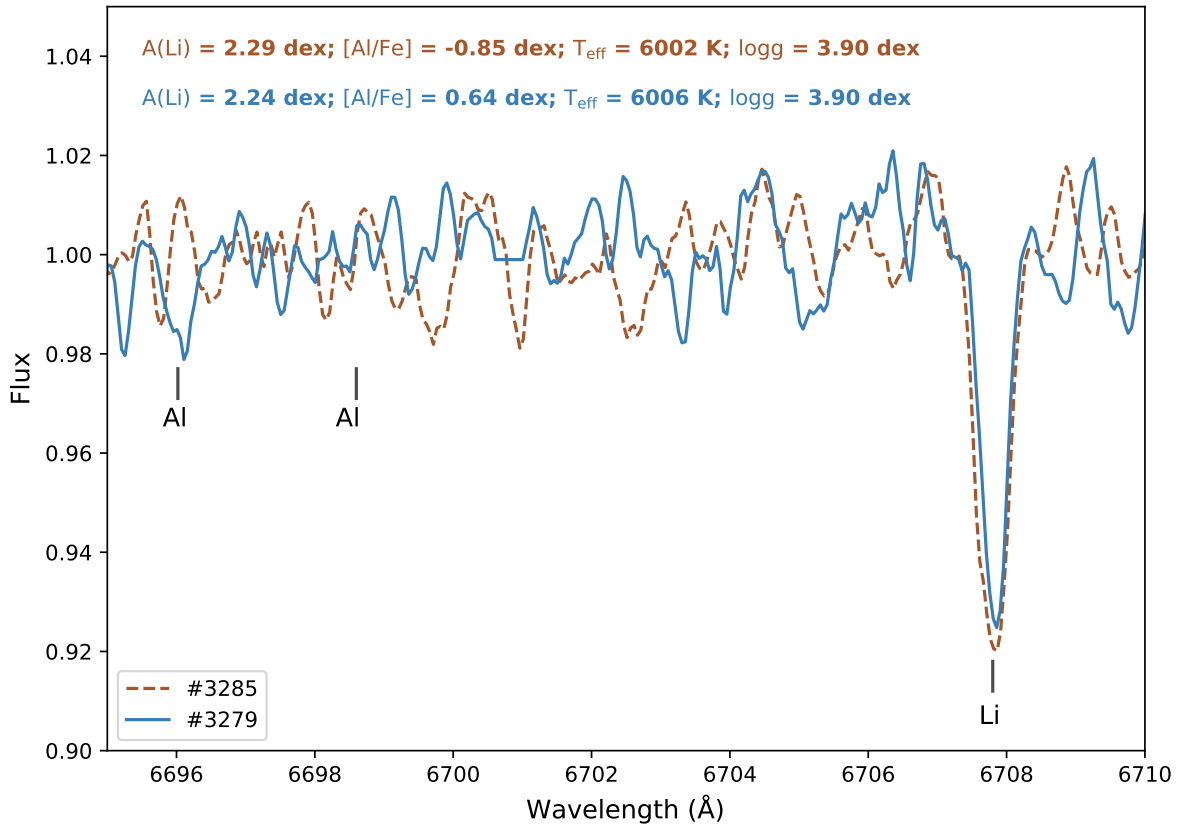

Figure 4.6 Comparison between star #3285 (dashed brown line) and star #3279 (solid blue line). Both have similar stellar parameters with similar Li abundance. While could only place an Al upper limit for the star #3285, the star #3279 shows a higher Al abundance of [Al/Fe]=0.64 dex. We recall to the reader that the results are based just on the Al line at 6696Å.

our oxygen measurements are scarcely significant upper limits. Fig.4.7, shows Na along with the Mg abundances. If both NeNa and AlMg chains were activated, SG stars are expected to be Na enhanced and Mg depleted with respect to their FG counterparts. In the figure, these two species are consistent with a statistically significant moderate negative correlation (Spearman corr. = -0.41 and p-value∼0.0) and display a spread larger than the associated error. In particular, we found a [Na/Fe] range of at least 1.1 dex, which is in excellent agreement with the [Na/Fe] range (∼1.1 dex) reported by Carretta et al. (2007) for this cluster. On the other hand, the Mg spread is more modest (∼0.50 dex), and it agrees with the Mg spread (∼0.55 dex) reported by Carretta et al.

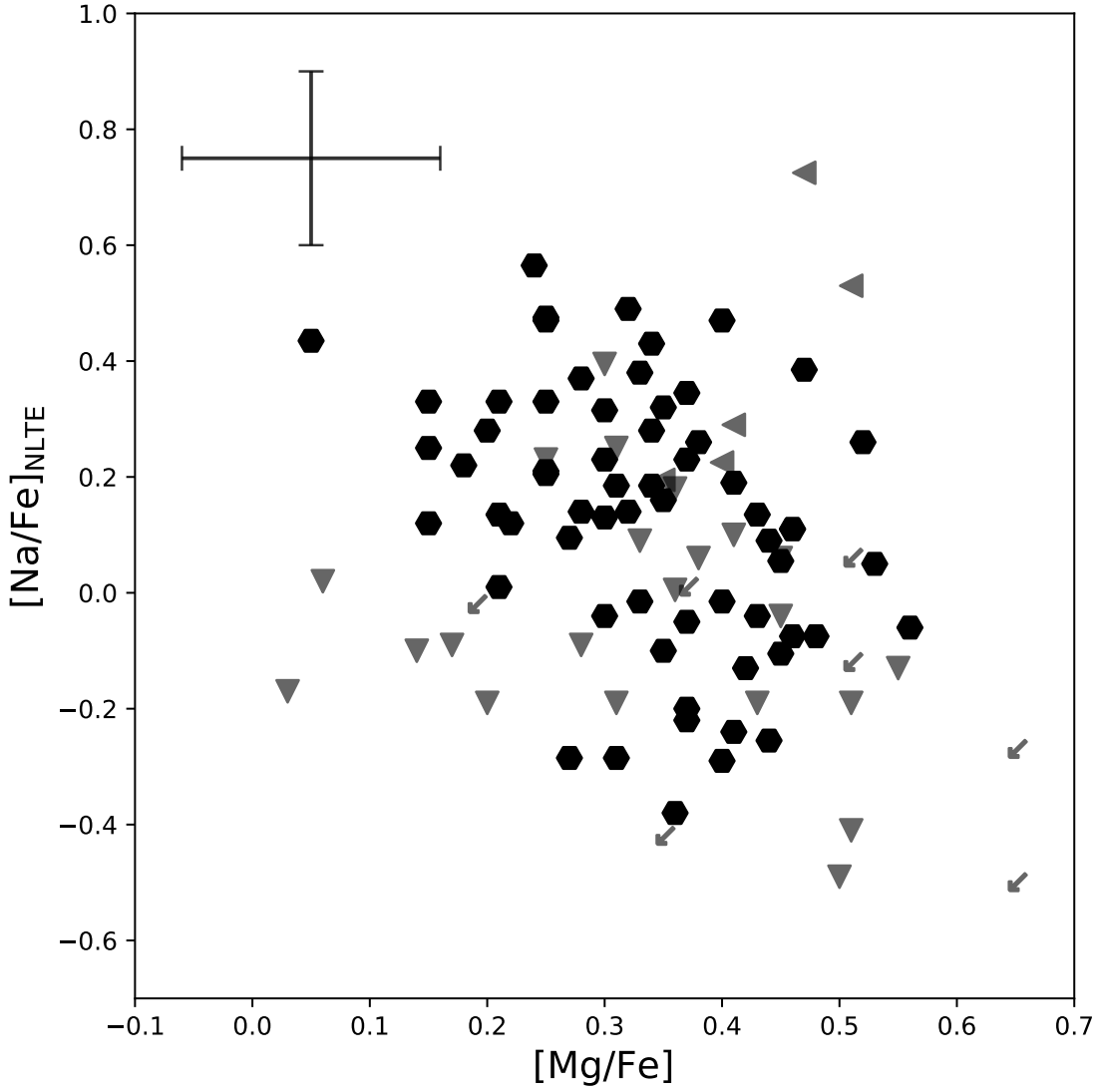

Figure 4.7 Mg-Na distribution in the sample. Symbols represent actual measurements (circles), Mg upper limits (left-pointing triangles), Na upper limits (down-pointing triangles), and the upper limits in both elements are represented by arrows.

(2012).

In addition, we examined the behaviour of Al along with Mg. Our results are shown in Fig. 4.8. Although the results are highly dominated by upper limits, the actual measurement in both elements draws a statistically significant moderate negative correlation

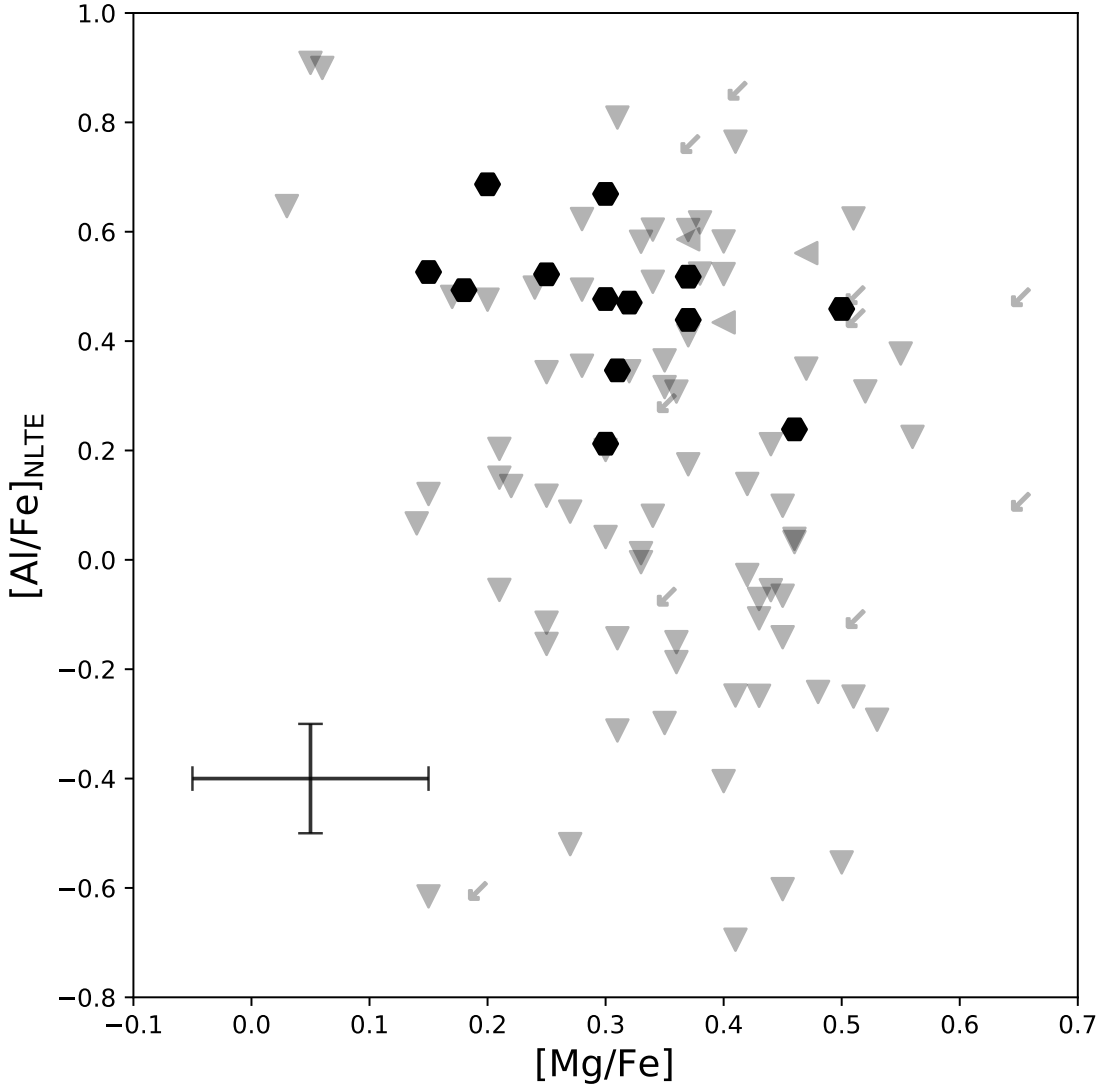

Figure 4.8 Mg-Al anti-correlation in the sample. Symbols follow the same description as Figure 4.7

(Spearman corr.=0.59 and p-value=0.03), which is consistent with the anti-correlation reported in the literature.

Figure 4.9 shows the Li abundance as a function of Na for unevolved (upper panel), and evolved stars (lower panel), being defined as unevolved stars the ones with $\log g$>3.87. The dashed line indicates the threshold [Na/Fe] value reported by Carretta et al. (2010) to split the two generations for NGC 6752. Symbols were colour-coded according to

the stars' $T_{\rm eff}$. In both panels is clear the presence of an anti-correlation, where the stars get depleted along with the Na enrichment. As was found by the Li-Al abundance distribution, there is a group of stars that belong to the SG that show a high Li abundance, which in some cases reaches comparable Li content as FG stars. The last indicates the contribution of Li pollution from AGB stars. As was mentioned by D'Antona et al. (2019b), the chemical pattern of SG star with 0.2 dex$\lesssim$[Na/Fe]$\lesssim$0.4 dex, could be explained by AGB stars of different masses.

Different studies have found Li-rich SG stars with the very same Li content as the one detected in FG stars (e.g., NGC 6218 D'Orazi et al. 2014 or NGC 362 D'Orazi et al. 2015). Other GCs such as NGC 1904 and NGC 2808 showed a comparable Li content in the FG and SG Li-rich stars (D'Orazi et al., 2015). Evidence of similar behaviour has been found also in the extragalactic GCs M 54 where the Li content is constant in both stellar populations (Mucciarelli et al., 2014). Unlike the mentioned studies, we detected in both panels that SG stars have on average a lower Li abundance than the FG ones. We did not detect any obvious dependence of this effect with stars' $T_{\rm eff}$. Finally, we note that there seems to be a larger dip in Li between FG and SG stars among evolved stars with respect to unevolved ones, which could be due to an under-correction of the evolutionary depletion.

4.1.6 Calcium and Scandium

Ca is an α-element produced in SN-II (Woosley and Weaver, 1995), while Sc is often categorised as an iron-peak element, it is produced mostly in SN-II (Battistini and Bensby, 2015). These elements have only recently started to be considered in the framework of MSP. Carretta and Bragaglia (2021) analysed the Mg, Ca, and Sc in a large sample of GCs finding Ca excess with respect to the field stars in a handful of them (NGC 4833, NGC 6715, NGC 6402, NGC 5296, NGC 5824, and ω-cen). They quantified that Ca excess, through a Kolmogorov–Smirnov test, getting statistically robust results. They claimed that such Ca excess could be produced either by a common kind of star in all the GCs being activated under specific conditions or by the presence (or absence) of an on-off mechanism in a peculiar kind of star.

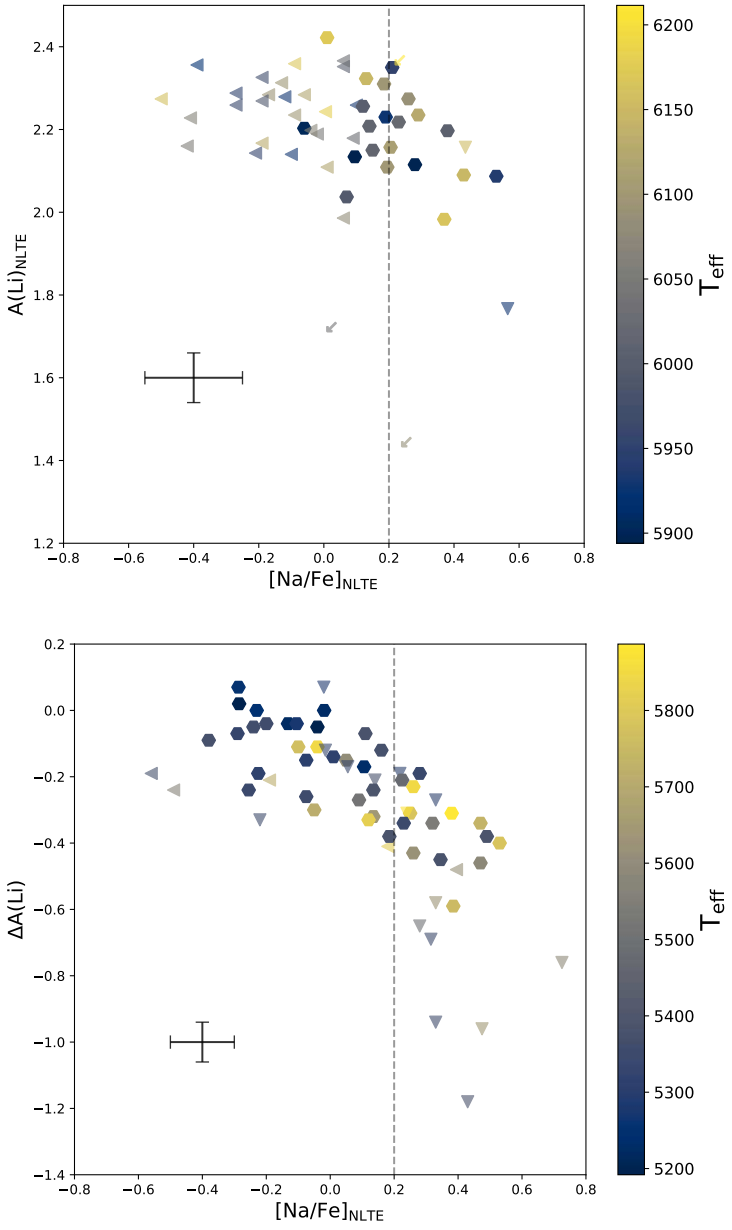

Figure 4.9 Li/ΔA(Li) as a function of the Na abundance for unevolved (upper panel), and evolved stars (lower panel). The dashed line indicates the threshold [Na/Fe] value which splits the two generations in NGC 6752. Symbols follow the same description as the Figure 4.7, which are colour-coded depending on their T_{eff}

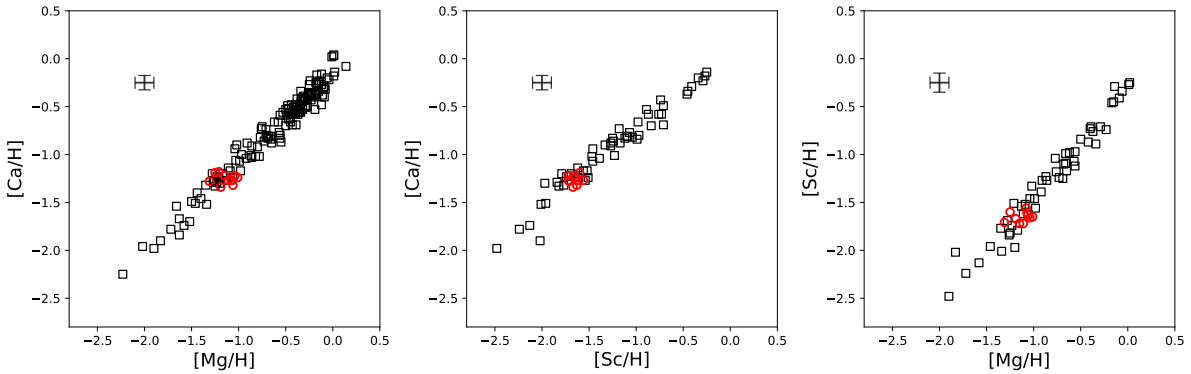

Figure 4.10 Mg, Ca, and Sc distribution. Black squares and red circles represent field stars from Gratton et al. (2003) and the UVES sample.

We check the same elements as Carretta and Bragaglia (2021) using our UVES sample. The Fig. 4.10 shows the [Mg/H], [Ca/H], and [Sc/H] measured in our sample along with fields stars from Gratton et al. (2003). Mg, Ca, and Sc follow quite clearly the field stars' distribution of similar metallicity, which is consistent with the result found by Carretta and Bragaglia (2021) for NGC 6752. We find no evidence of a significant spread in Ca and Sc in this cluster, meaning our results do not support the contribution of explosive polluters to cluster pollution.

4.1.7 Copper

According to the literature (e.g., Ernandes et al., 2020, and references within), Cu is an iron-peak element mainly produced from a secondary weak s-process in massive stars (Romano and Matteucci, 2007) with a small contribution from other sources such as intermediate-mass AGB stars (Raiteri et al., 1992) and SNIa (Kobayashi et al., 1998).

We studied the Cu line at 5105Å. While we could only set upper limits in unevolved stars, we derived actual measurements in evolved ones. Among the latter, data show some spread among stars in the same evolutionary stage, which is slightly larger than the error, but there is no trend. According to the literature, copper is under-abundant for stars with metallicity lower than -0.90 dex. Our results show good agreement with field stars at this metallicity.

Figure 4.11 shows the [Cu/Fe] relation with both $[Na/Fe]_{NLTE}$ (upper panel), and [Mg/Fe] (lower panel). Although the Cu spread is small and within the errors, copper seems to slightly correlate with Na (corr:0.56, p-val:0.19), however, according to a Spearman correlation analysis, the correlation is not significant. Similarly, [Mg/Fe] does not display a significant correlation with Cu (corr:0.67, p-val:0.10). Unfortunately, our upper limits are not significant and they do not provide further information.

4.1.8 Yttrium

Y together with Sr and Zr are known as light-s process elements. They constitute a group of species around the neutron magic number N=50 where arise the first peak of heavy elements (Busso et al., 2022). Unlike Ba, Y production in AGB stars does not strongly depend on masses at this metallicity (2 - 6$M_{\odot}$ range; Straniero et al., 2014). The yttrium abundance in field halo stars is found to be slightly sub-solar although with a large scatter (Venn et al., 2004, Yong et al., 2005).

Figure 4.12 shows the distribution of the [Y/Fe]II along with $[Na/Fe]_{NLTE}$ among both unevolved (upper panel), and evolved stars (lower panel). The symbols are colour-coded by their Li/ΔA(Li) abundances. Our results among unevolved stars are dominated by Y II upper limits, making it impossible to probe any trends. The lower panel suggests a positive correlation, with evolved stars belonging to the SG appearing more Y II-rich than their FG counterparts. The Spearman correlation ($\sim$0.65), however, is of poor statistical significance. On the other hand, as colours reflect the Li abundance, a prevalence of blueish (yellowish) colours among Na-rich (Na-poor) stars reflects the finding discussed in Sect 4.1.5, that Na-rich stars are on average more Li-poor.

Similar behaviour can be found between Li and Y II among evolved stars. To investigate the reliability of this trend, we selected the five most Li-poor and the five most Li-rich stars among the SG population, to study if they have different production of Y II. We found a constant Y II abundance within the errors among these two groups of stars.

To further analyse the Y II-Na trends among evolved stars, we divided our measurements into four bins. Those bins are given by their Na content, being $[Na/Fe]_{NLTE}$<-0.1

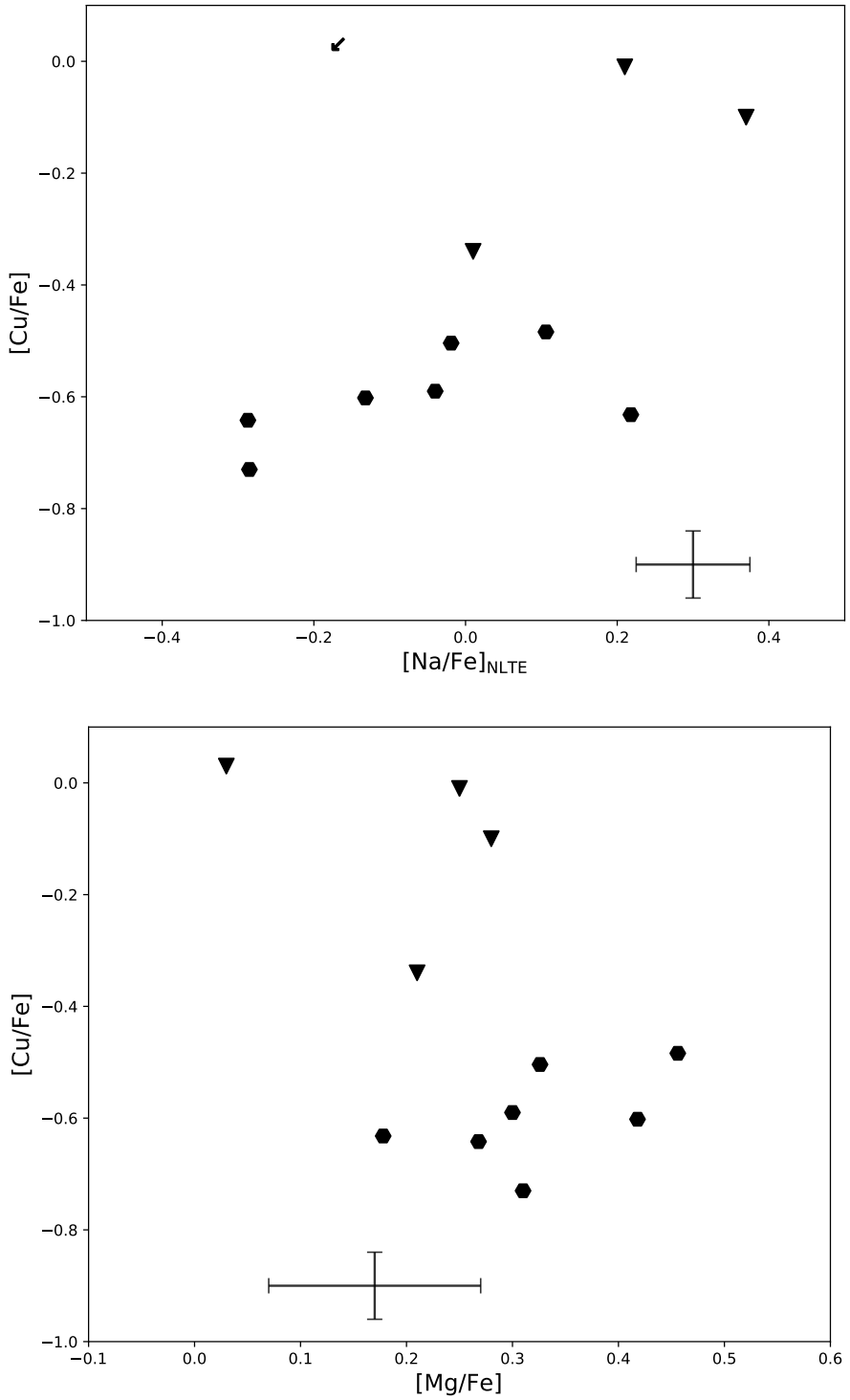

Figure 4.11 Relation between [Cu/Fe] and $[Na/Fe]_{NLTE}$ (upper panel), and [Cu/Fe] and [Mg/Fe] (lower panel). Symbols follow the same description as Figure4.7

	Dwarves				Giants			
Element	FG	n	SG	n	FG	n	SG	n
Y	+0.11	(1)	+0.18±0.09	(2)	+0.01±0.15	(13)	+0.25±0.12	(8)
Ba	+0.38±0.20	(12)	+0.30±0.24	(6)	+0.24±0.13	(18)	+0.33±0.19	(12)

Table 4.1 Yttrium average abundances among FG and SG populations in dwarves and giants. The number of stars considered to compute the averages is indicated in parentheses.

dex, -0.1 dex <[Na/Fe]$_{NLTE}$<0.2 dex, 0.2<[Na/Fe]$_{NLTE}$<0.5 dex, [Na/Fe]$_{NLTE}$>0.5 dex. The corresponding average [Y/Fe]II abundances are 0.00±0.15 dex, 0.04±0.15 dex, 0.24±0.11 dex, and 0.15 dex. They do not show a difference within the errors, therefore it does not support a conclusion of correlation.

For sanity check, and to rule out any dependency of Y II and Na on v$_m$ (which as discussed in Subsection 3.2.1.1 might be an issue, at least for Y), we defined ΔY II (ΔNa) as the difference of the reported [Y/Fe] II ([Na/Fe]) abundance and a linear fit between the [Y/Fe] II ([Na/Fe]) and v$_m$. Fig. 4.13 shows the distribution of these two variables in our sample. A Spearman correlation indicates a weak correlation with low significance. The lack of correlation between Na and Y II suggests that the source responsible for the Na enrichment has quite limited Y II production if any.

Fig.4.14 shows the distribution of [Y/Fe]II along with the Mg abundance. These two species do not display any correlation which agrees with the previous figure. A similar test can be done taking into account the Al abundance (see Fig. 4.15). Although the figure is dominated by upper limits in both elements, there is once again no clear evidence [Y/Fe]II enrichment in SG with respect to the FG population.

4.1.9 Barium

Ba is mainly produced by the main s-process, which happens typically in low-mass ($\sim$1.2 - 4.0$M_\odot$ exact range depending on metallicity) AGB stars during their thermal pulses (Cristallo et al., 2015).

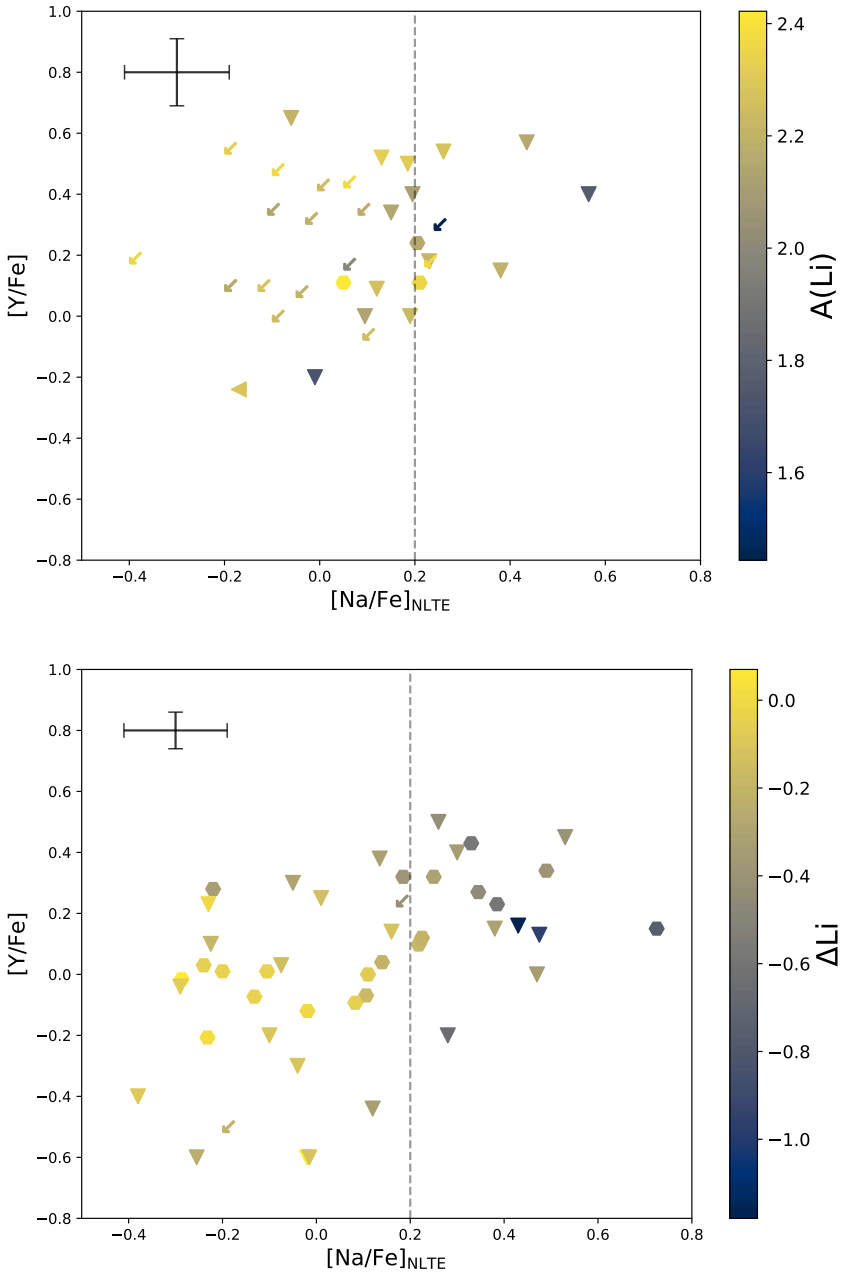

Figure 4.12 Weighted Y II abundance using the lines at 5087Å, 5200Å, and 5509Å as a function of $[Na/Fe]_{NLTE}$. Results for unevolved, and evolved stars are shown in the upper and lower panels, respectively. Symbols are colour-coded by the star's lithium abundance. Circles and triangles indicate actual measurement and upper limits, respectively. Diagonal arrows indicated the upper limit in both elements.

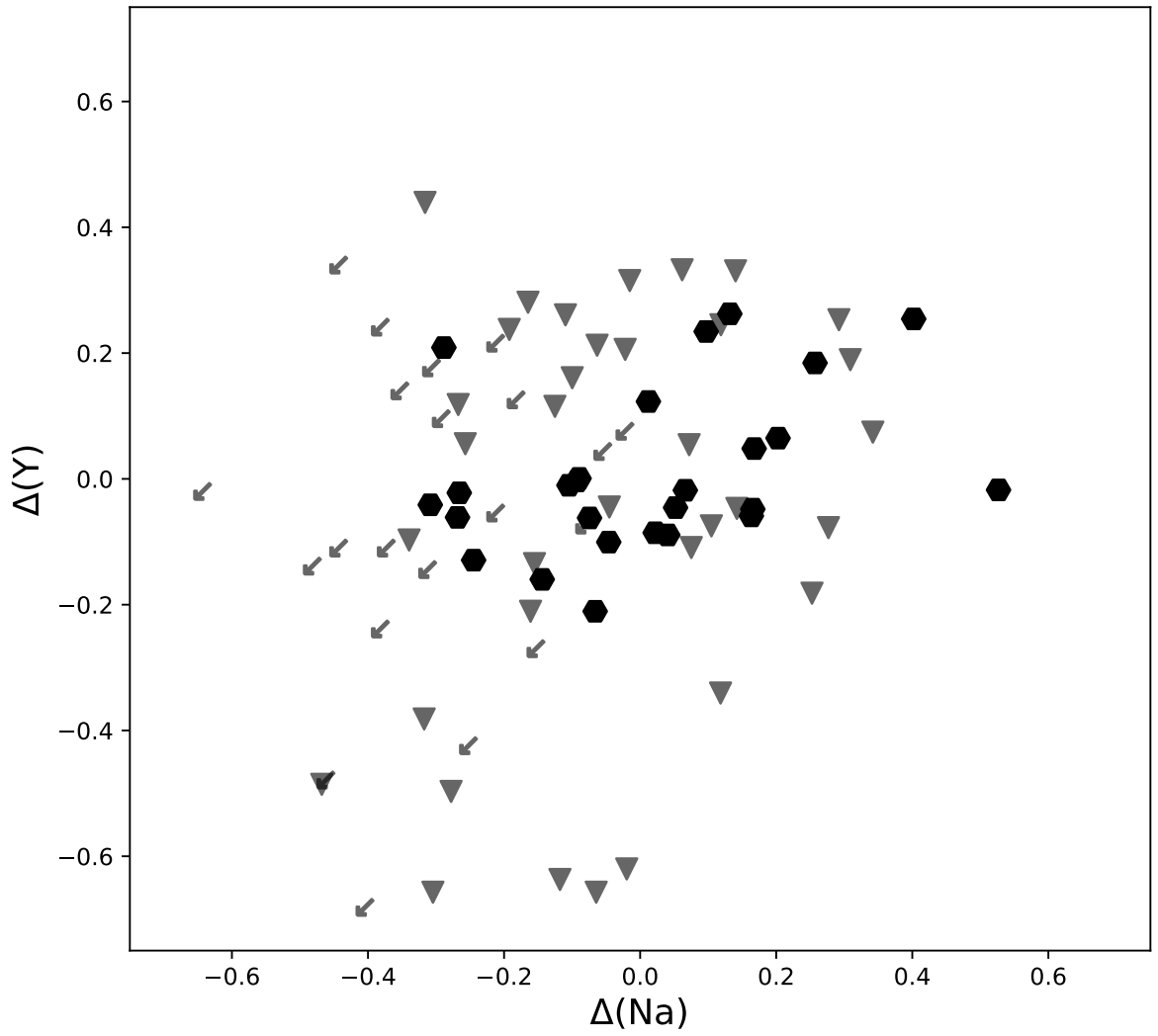

Figure 4.13 Distribution of Δ[Y/Fe] II and Δ[Na/Fe] in the sample. Symbols follow the description as Fig.4.7

Figure 4.16 displays the Ba abundance as a function of Na. The figure's colour and symbols follow the same description as Fig.4.12. The upper panels show the results for unevolved stars. In both figures, the Ba spread and the Na abundances do not display any obvious correlation. In other words, there is no evidence of a difference in Ba abundance between Na-rich and Na-poor stars. We note, however, that the FG stars are dominated by Na upper limits. Furthermore, the colours do not reveal any obvious correlation between the [Ba/Fe] II and Li abundances. In the lower panels, we

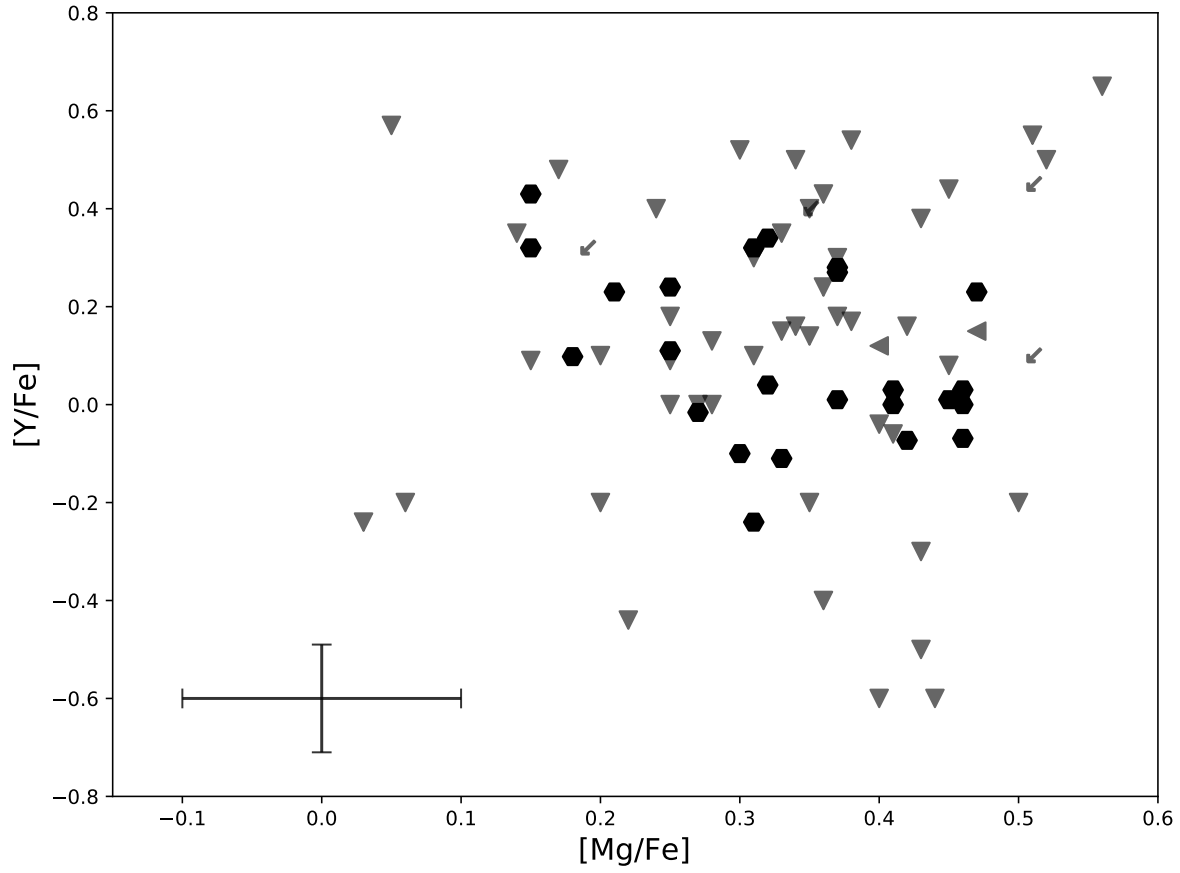

Figure 4.14 Y and Mg abundance in the sample. Symbols follow the description as Fig.4.7

present the results for evolved stars, which seems to indicate a possible correlation. However, the Ba II content in the five more Li-poor SG and the five more Li-rich SG stars, does not reflect any correlation considering the associated errors, meaning that the polluters responsible for the Li pollution does not have relevant production of Ba II.

Furthermore, as was done previously with Y II, we compared the mean Ba abundance among both unevolved and evolved FG and SG stars. No systematic trends in Ba with any of these groups are seen. Also, we defined Δ[Ba/Fe] II as was done Δ[Na/Fe], and we compared them in Fig. 4.17. The results confirm that there is no trend with Na, suggesting that the possible trend observed in Fig. 4.16 might arise from dependencies

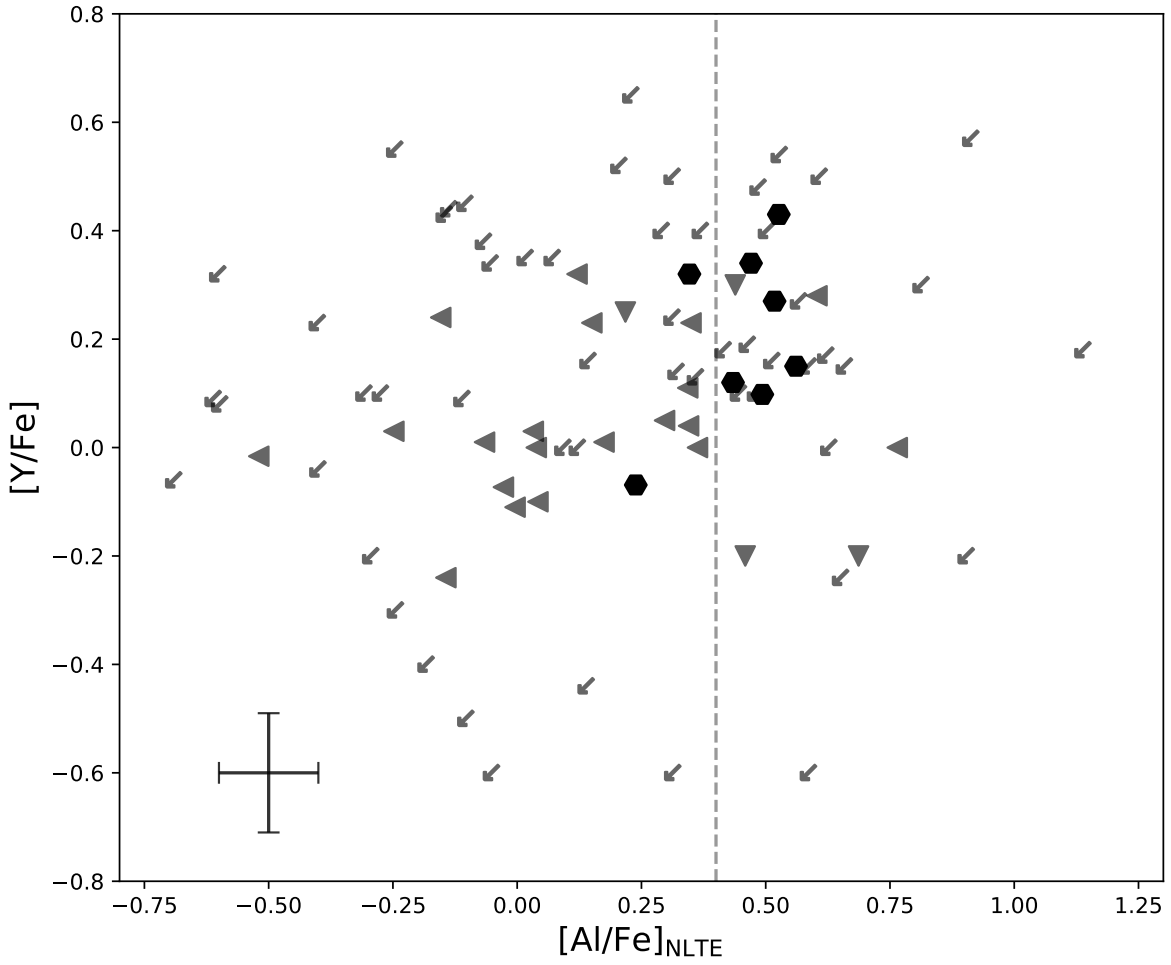

Figure 4.15 Y abundances as a function of Al. Symbols follow the description as Fig.4.7

from microturbulence and that the first and second generation of stars displays a similar Ba abundance and the Na producer is not related to the production of Ba.

Figure 4.18 displays the Ba abundance of our sample as a function of the Mg content. It is clear there is no correlation between these two elements, then there is no evidence indicating that Ba is produced in the same site where Mg is destroyed. Fig. 4.19 shows the distribution of Ba along with the Al abundance. The figure is dominated by Al upper limits, however, the reported measurements do not reveal any correlation, then one generation does not seem to be Ba enriched with respect to the other.

On the other hand, we found evidence of a Ba spread in both unevolved and evolved

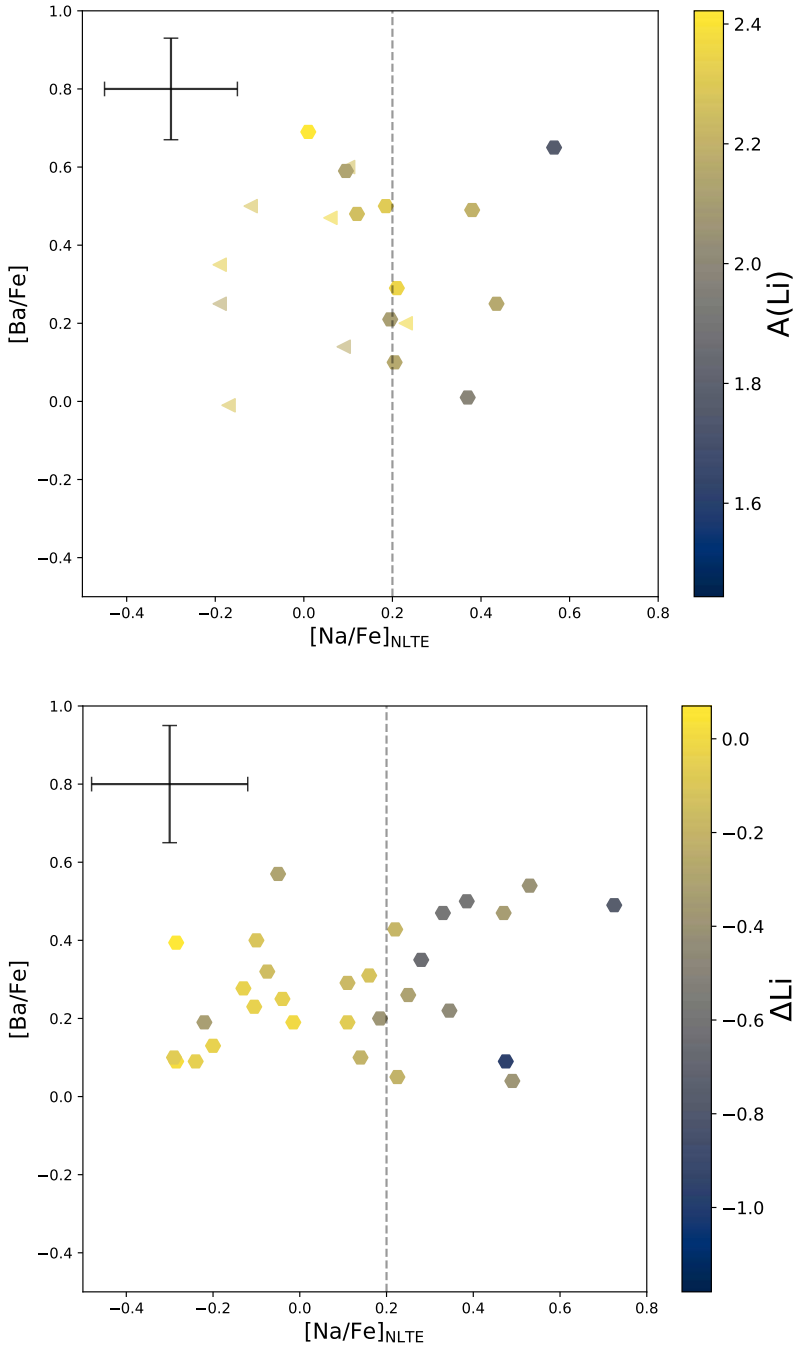

Figure 4.16 Weighted Ba abundance using the lines at 5853Å, 6141Å, and 6496Å as a function of $[Na/Fe]_{NLTE}$. The panels, symbols and colours follow the same description given in Fig.4.12.

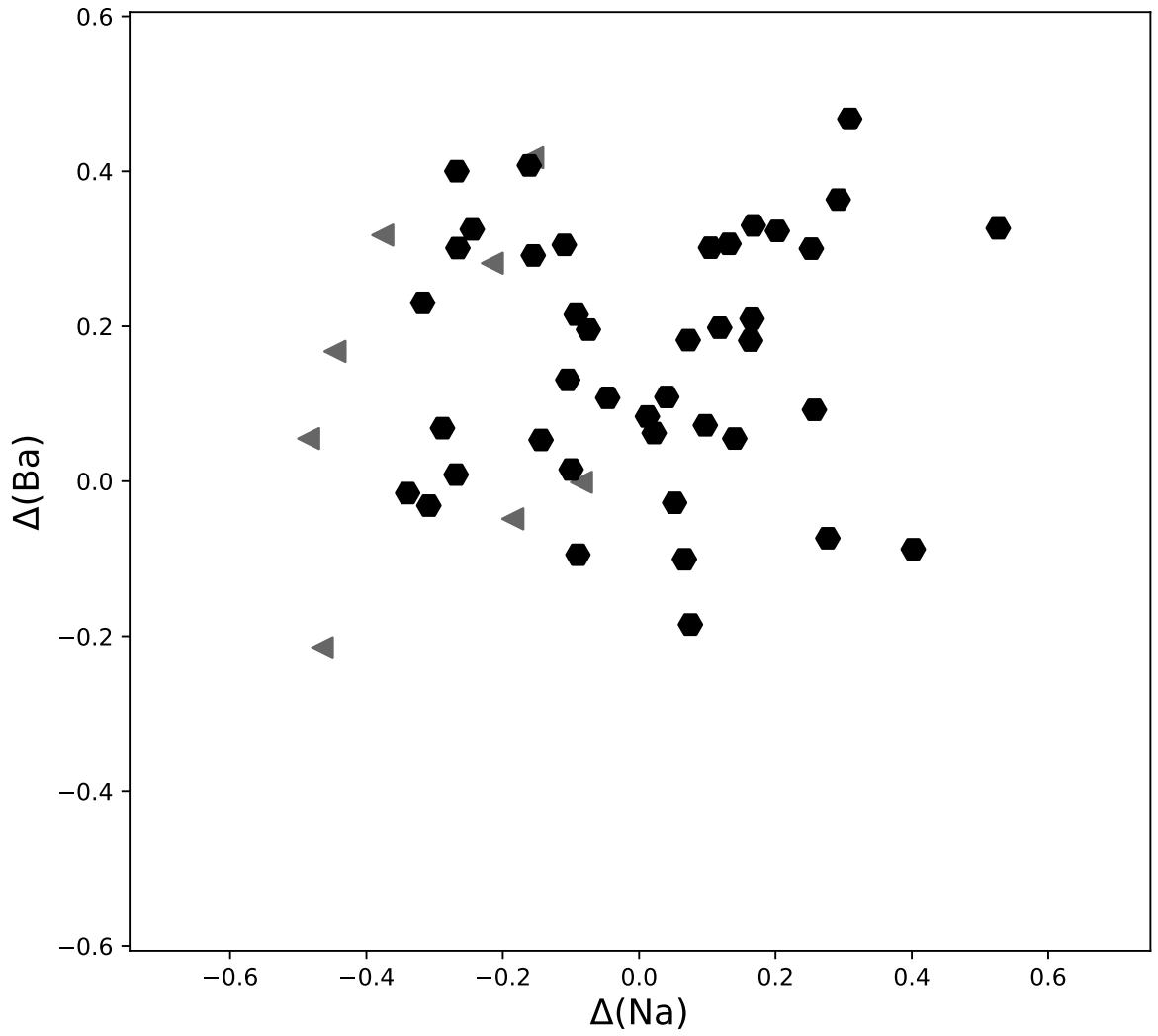

Figure 4.17 Distribution of ΔBa and ΔNa in the sample. Symbols follow the description as Fig.4.7

stars, which given the reported error is mildly significant. The spread seems to be constant in the different stellar populations. The spread in heavy elements has been reported in a few GCs before, e.g., NGC 7089, and M 22.

We noted a star with particularly high Ba, and we performed a direct comparison to another star with similar stellar parameters, but different Ba content. Figure 4.20 shows a line-to-line comparison between these two stars for Y and Ba at 5087Å and 6496Å respectively. As can be seen from the figure, the Ba lines are quite different, consistently

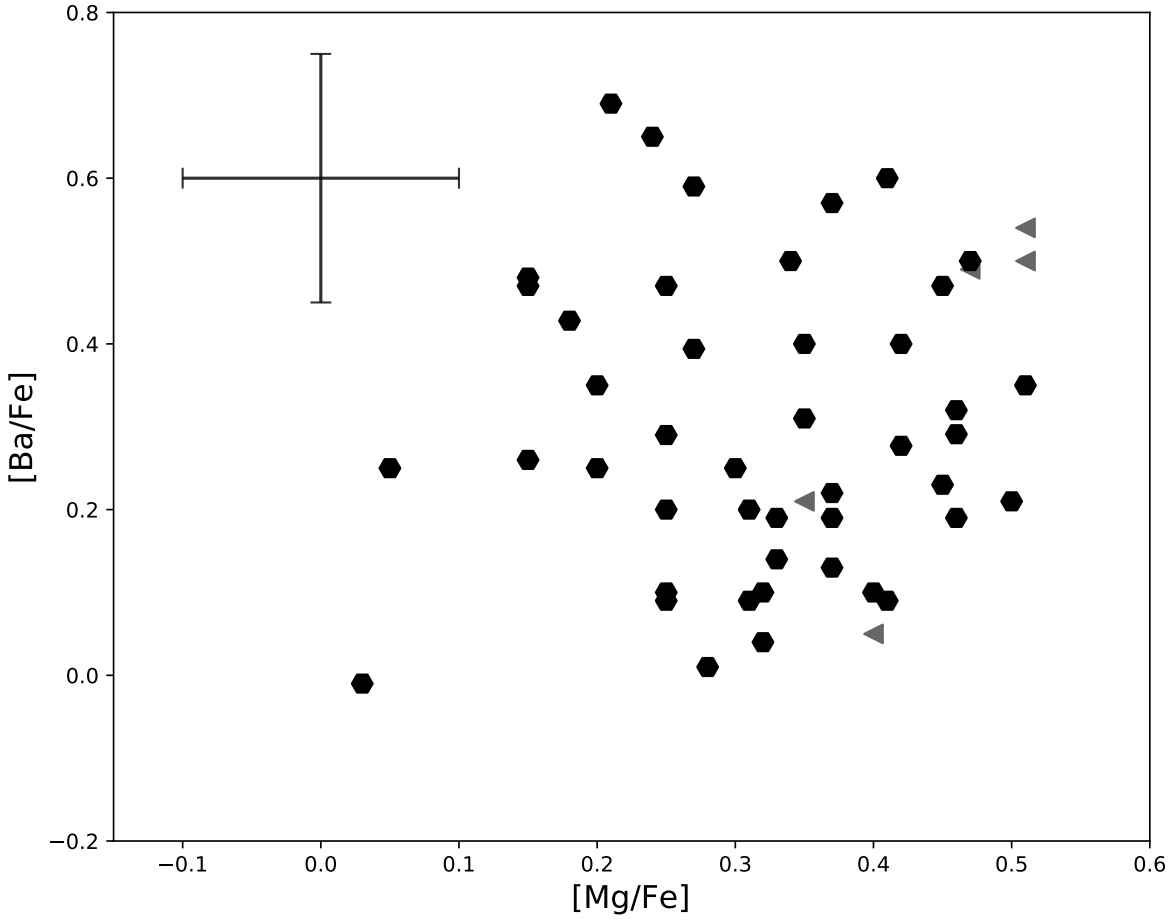

Figure 4.18 Ba abundances along with the Mg content in the sample. Symbols follow the description as Fig.4.7

with the A(Ba) abundances that have been measured in the two stars, arguing in favour of a real difference in Ba rather than uncertainties in the parameters. The abundance of Y II seems to follow the same pattern as Ba II, although with a smaller effect. As we could only place upper limits for Cu and Eu, no meaningful comparison can be performed for these species.

The measured abundances of s-process elements and the low Eu upper limit, suggest an enrichment by the s-process. This anomalous n-capture abundance could be explained by it being a CH-stars. Those stars, and their metal-rich counterparts Ba-stars, have been the object of a number of literature studies. In GCs, Ba-rich stars are mostly

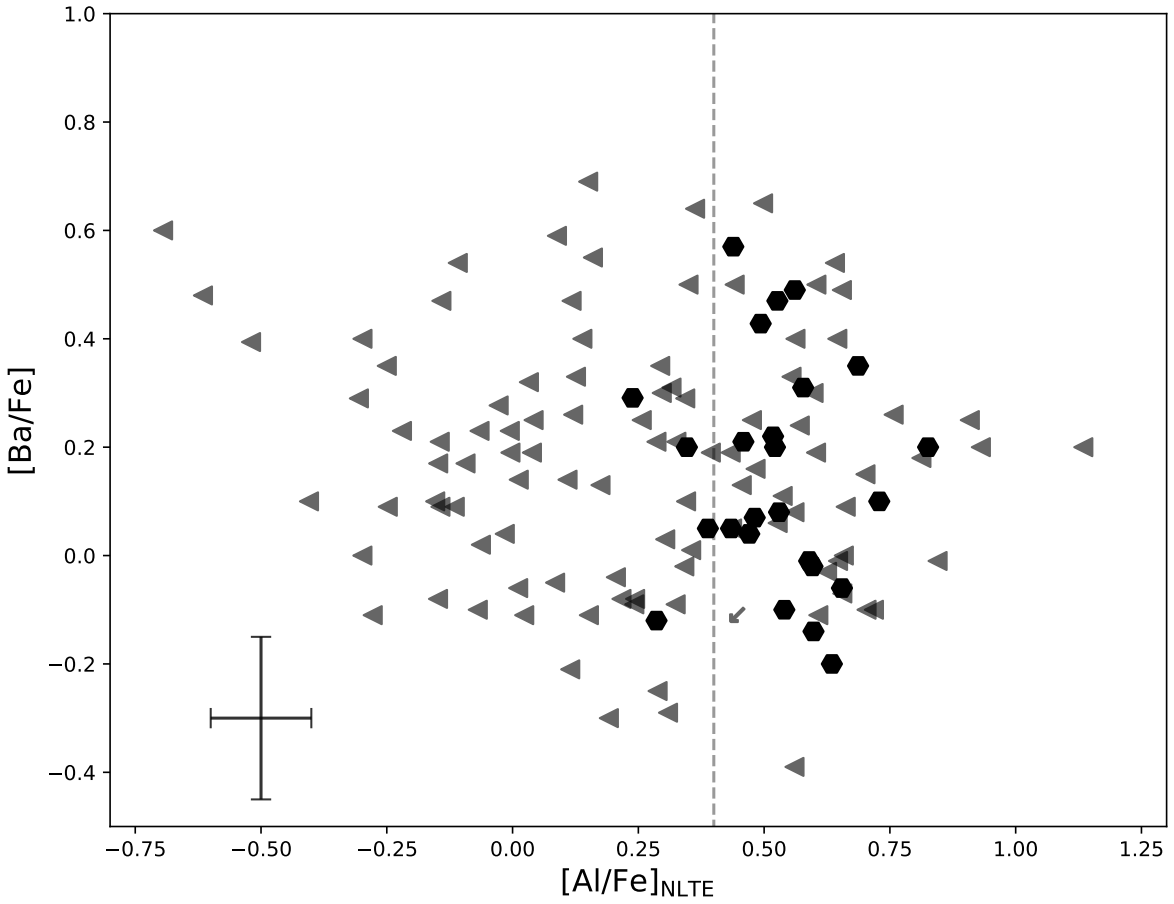

Figure 4.19 Ba abundances as a function of Al in NGC 6752. Symbols follow the description as Fig.4.7

FG (e.g., D'Orazi et al., 2010) and they are thought to be part of binary systems, which is consistent with the fact that binary fraction is higher in FG than in SG stars (e.g., Lucatello et al., 2015). In these binary systems, the primary was a star with 1.5-4.0$M_{\odot}$ which evolved long ago and is now a faint white dwarf. Such a star, after its AGB phase, transferred mass to the secondary – the star we are now observing –, enriching the atmosphere of the latter with products of the AGB shell nucleosynthesis. The result is that the surface composition is enriched in s-process elements, but also C.

Our Ba-enhanced star has a high A(Ba)=0.92 dex ([Ba/Fe]=0.52 dex), and the expectation is that it would also be C-rich. Given the temperature/metallicity of the object, the CH G-band at 4300 Å is the best feature to check for C enhancement. Our spectral

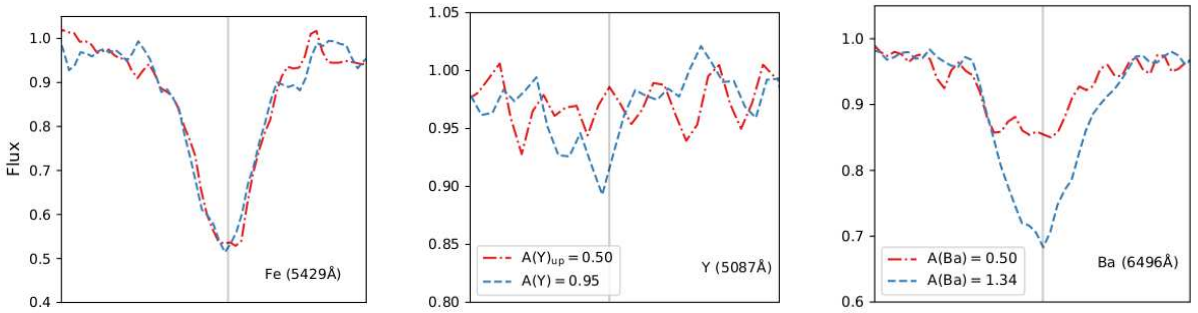

Figure 4.20 Line-by-line comparison between two members with similar stellar parameters (ΔT_{eff} ∼80 K). The referred lines are indicated in the right upper corner of each panel. The gray solid line indicates the position of the line centre.

coverage, however, does not allow that. The C_2 Swan band at ∼5250 Å requires a quite high C enhancement to be detectable, and a visual inspection does not reveal a clear presence of this band in the spectrum of the star. Given the atmospheric parameters of the stars and the spectral SNR in the region, we estimated in [C/Fe]=1.7 dex the minimum C-abundance to lead to a detectable C_2 Swan band. Then, we compared these abundances with the expected AGB yields for a star with $1.50 M_{\odot}$ from F.R.U.I.T.Y models. The predicted [Ba/Fe] and [C/Fe] abundances should be about 1.45 dex, and 2.30 dex, respectively. That means the [Ba/Fe] coming from the material of the companion of our CH-star should have been diluted by about 0.9 dex to get to the observed [Ba/Fe] abundance of 0.52 dex. If we consider the same dilution for C, the [C/Fe] expected in our star should be around 1.4 dex, which would result in an undetectable Swan band in our spectra. Therefore, the lack of Swan band is not an argument against the target being a CH-star, which remains the most likely cause of the observed s-process enhancement.

We attempted to measure Eu abundance from the 6645 Åline, however, the feature was too weak at the atmospheric parameter of the sample and SNR of the observed spectra. We hence only derived upper limits of scarce significance.

4.1.10 n-capture elements distribution

Figure 4.22 shows the [Y/Fe]II abundance versus Ba. The distribution presents the dispersion discussed previously, but there is no evidence of any correlation. It is worth noting that, although AGB stars are the main ones responsible for the s-process nucleosynthesis, Y and Ba can be produced by stars of different stellar masses, then a correlation between these two species is not granted when a range of AGB masses is involved in the pollution.

4.1.11 n-capture elements and AGB predictions

In the scenario where AGB stars are the polluters responsible for the abundance variations, we can take advantage of the measured Y and Ba abundances to explore the mass of the AGB involved in the process. Under the simplistic approximation that polluters are all identical, that the composition of the diluting gas is the same as the FG stars and that the Na and Y content in FG stars is negligible with respect to the Na and Y content coming from the AGB ejecta, we expect that Na and Y would vary proportionally to the yields of the polluter. We robustly estimate the overall increase in Na, and we calculated the difference between averaging the five Na-richest and five poorest measured abundances. An analogous procedure was applied to Y, deriving 1.05±0.13 dex, and 0.88±0.13 dex for [Na/Fe] and [Y/Fe] II, respectively.

These quantities were compared to results from nucleosynthetic models from the FUll-Network Repository of Updated Isotopic Tables & Yields[1] (F.R.U.I.T.Y; Cristallo et al., 2011), providing theoretical predictions for the yields of a range of AGB masses, from 1.5 to $6M_{\odot}$. Table 4.2 displays the final composition of diverse elements for a given AGB mass. The model is for Z=0.0003, [α/Fe]=0.5 dex, and a standard C-pocket. The $4M_{\odot}$ model actually predicts that the Y production is actually slightly higher than that of Na, something that is not consistent with our data, where the estimated Na increase is equivalent to Y, considering the errors. The 5 and $6M_{\odot}$ model predictions are on the other hand fully consistent within the errors in our findings.

[1] `http://193.204.1.214/modelli.pl`

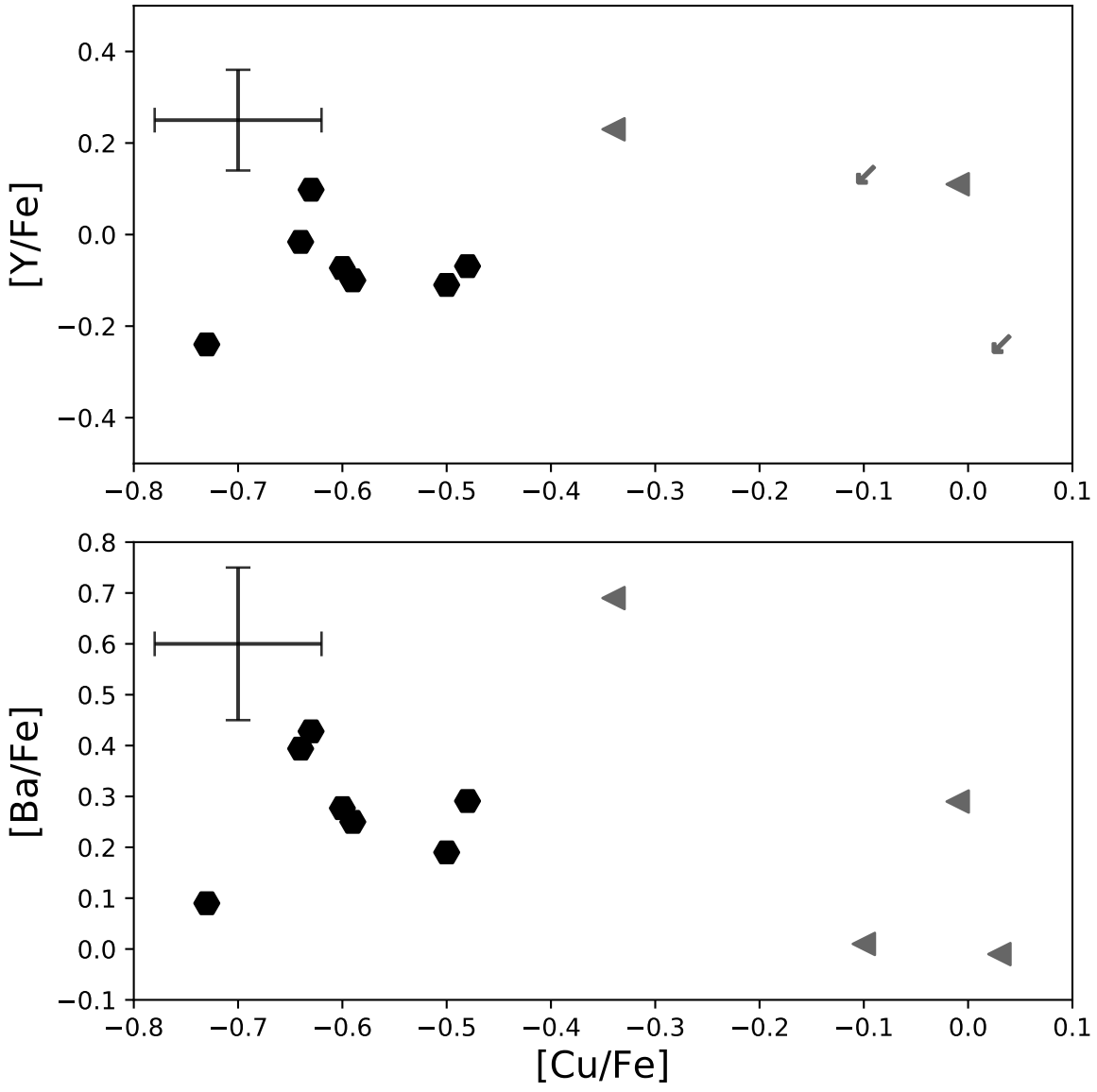

Figure 4.21 The panel shows the abundance of Y and Eu as a function of Cu, which are available only in UVES spectra.

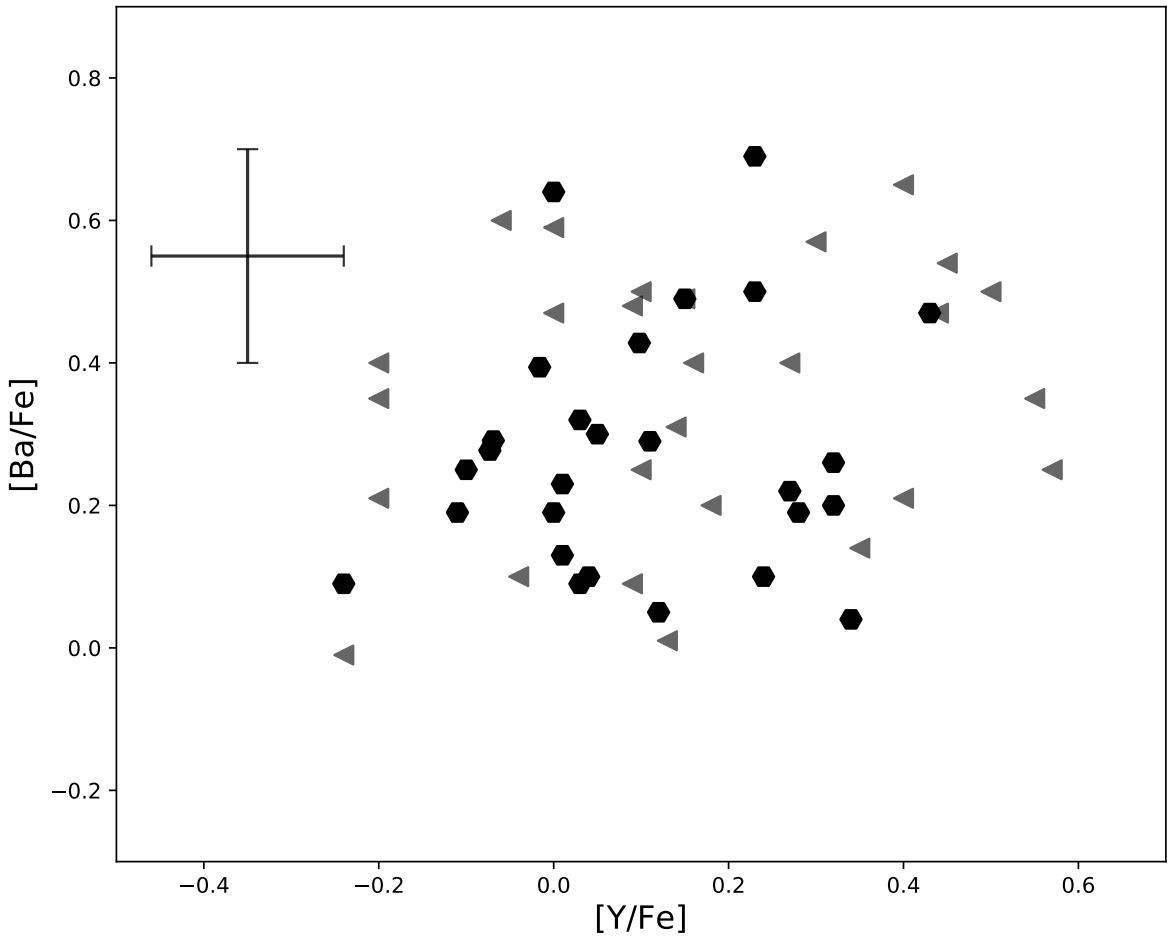

Figure 4.22 Barium abundances as a function of [Y/Fe] II. Symbols follow the same description as the previous figures.

We cannot extend the exercise to higher masses for the lack of available models at the appropriate mass-metallicity combination. Some qualitative insight could potentially be gained by comparing the FRUITY models with others for larger masses, like e.g. Karakas et al. (2018) which extends to $7\mathrm{M}_{\odot}$ but only at higher metallicity. However, their predictions for Na, Y and Ba abundances at a similar metallicity ([Fe/H]$= -0.7$) and in the range of overlapping masses (5 and $6\mathrm{M}_{\odot}$) are only in moderately good agreement, suggesting extreme caution in even qualitative speculations on the behaviour of the predictions for Na, Y and Ba at higher masses.

Similar reasoning can be applied to Na and Ba with the estimated overall [Ba/Fe] II

Mass	[Na/Fe]	[Y/Fe]	[Ba/Fe]
$4M_{\odot}$	0.81	0.89	0.99
$5M_{\odot}$	0.93	0.94	0.77
$6M_{\odot}$	0.98	0.73	0.50

Table 4.2 The final composition of the AGB star for each species from F.R.U.I.T.Y models for different stellar masses.

increase of 1.01±0.18 dex. We found a similar Ba and Na production in our sample, however, none of these models predicts such a pattern. Models of $5\mathrm{M}_{\odot}$ and $6\mathrm{M}_{\odot}$ show a comparable Na increase to our result, but a much lower Ba increase. Within the mentioned assumptions, the findings can not be attributed to an enrichment coming from an AGB of a single mass.

Chapter 5

Discussion on the survey sample

In the present chapter, the results obtained and their implication is summarised. The chapter starts with a full analysis of Cu, Y, Ba, La, and Eu for 18 GCs and their comparison with field stars. There were analysed chemical ratios, such as [Ba/Y] and [Ba/Eu]. The behaviour in terms of heavy element content of GCs formed in the Galaxy (in-situ) versus those accreted (ex-situ) is also examined.

5.1 Chemical Abundances Distribution: Cu

5.1.1 Internal spread

Copper in GCs has been the object of just a few studies (e.g., Cunha et al., 2002, Simmerer et al., 2003), which found no evidence of internal variation in its abundance for these objects. As Cu abundances are derived from relatively strong lines, we tested whether there is any dependency of the derived values on V_m. We note that in the more metal-poor cluster, the Cu abundances are dominated by upper limits. Due to the large Cu range covered by the whole sample, Figure 5.1 shows the Cu abundance obtained re-scaled to the mean Cu found in each cluster. In general, the results do not show a clear trend with microturbulence, with the exception of NGC 6121.

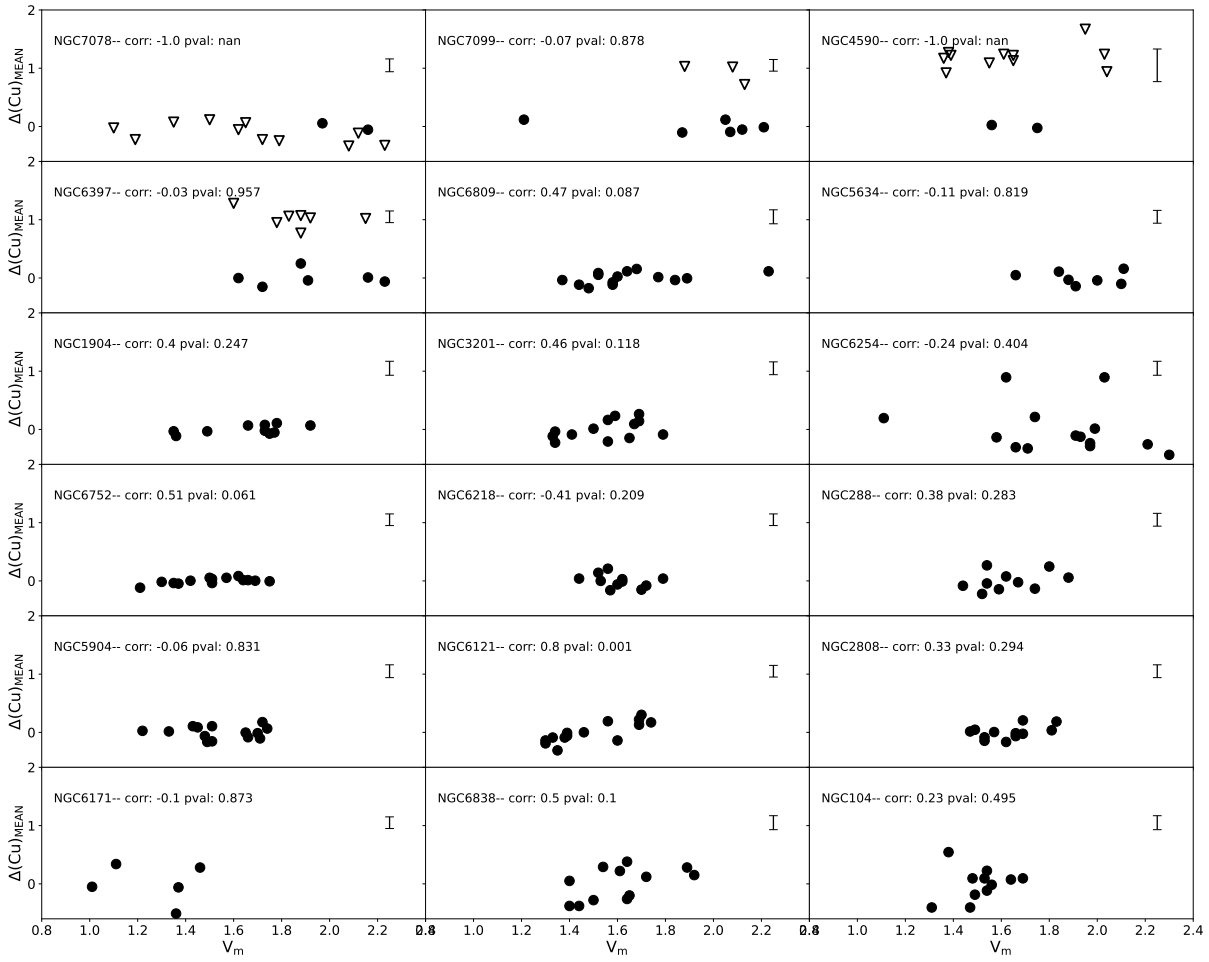

Figure 5.1 $\Delta(\mathrm{Cu})_{MEAN}$ along with V_m for each GC of the sample. The respective Spearman corr. and p-values are indicated on each panel. Filled circles and empty triangles represent actual Cu measurements and upper limits, respectively.

In most of the cases, the results for Cu seem to be, within the errors, quite flat and without spread. However, the most metal-rich GCs (NGC 6171, NGC 6838, and NGC 104) display a spread larger than the associated error. On the other hand, the GC NGC 6254 has two stars with slightly higher Cu abundances considering the associated errors.

To further analysed if this discrepancy is real, Fig. 5.2 shows the comparison of two stars of the cluster with similar stellar parameters. The difference in A(Cu) is about 1.0 dex which goes beyond the associated errors and cannot be explained by the slight difference in V_m. It is worth noticing that the Cu enrichment goes in the opposite

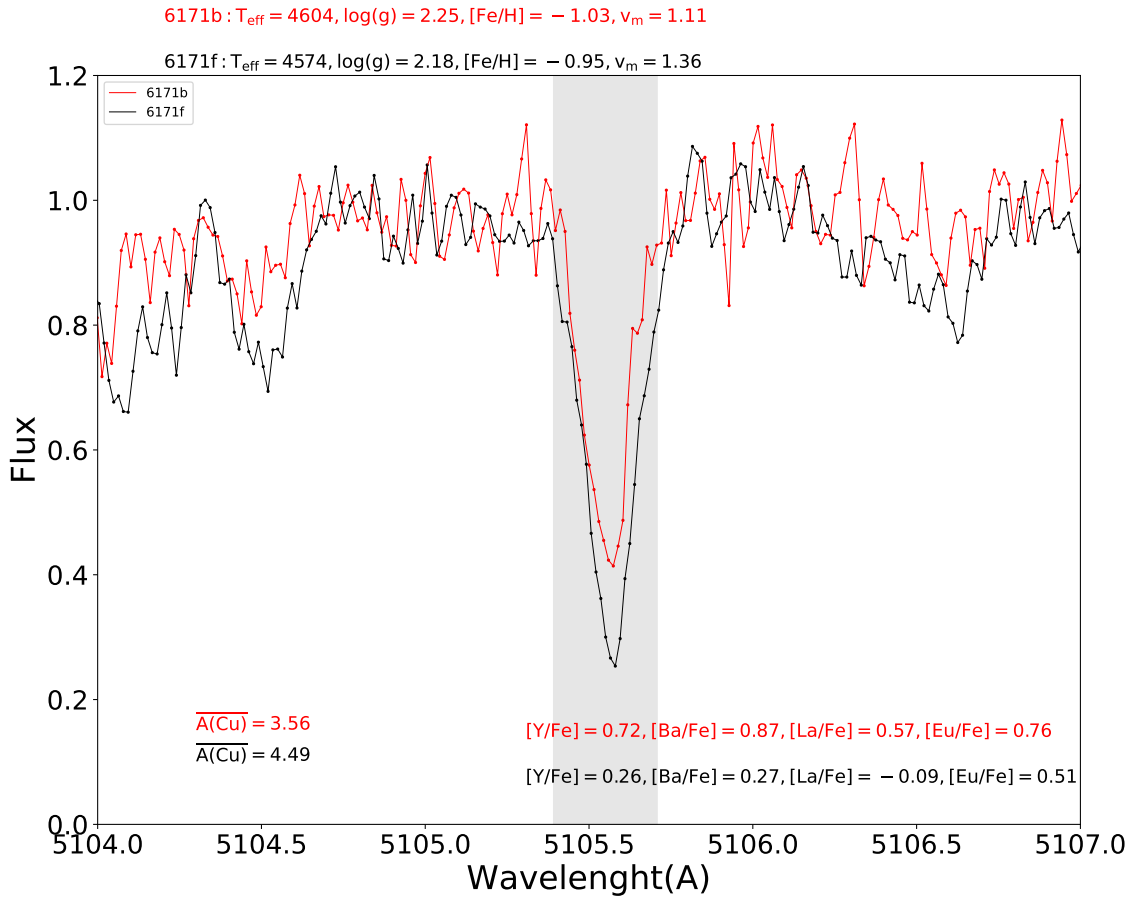

Figure 5.2 Pair of stars of the GC NGC 6171 with similar stellar parameters as reported by Carretta et al. (2009), a different Cu abundance. Black and red lines represent the spectra of ID= b and ID=f, respectively.

direction of the n-capture enrichment for the pair. This suggests that the nucleosynthesis process(s) responsible for the n-capture production is(are) not linked to the one responsible for the Cu production.

Fig. 5.3 shows the distribution of Cu abundances as a function of the Na content in each cluster. The distribution seems to be quite flat along with Na, meaning that there is no obvious link in the production between these two species.

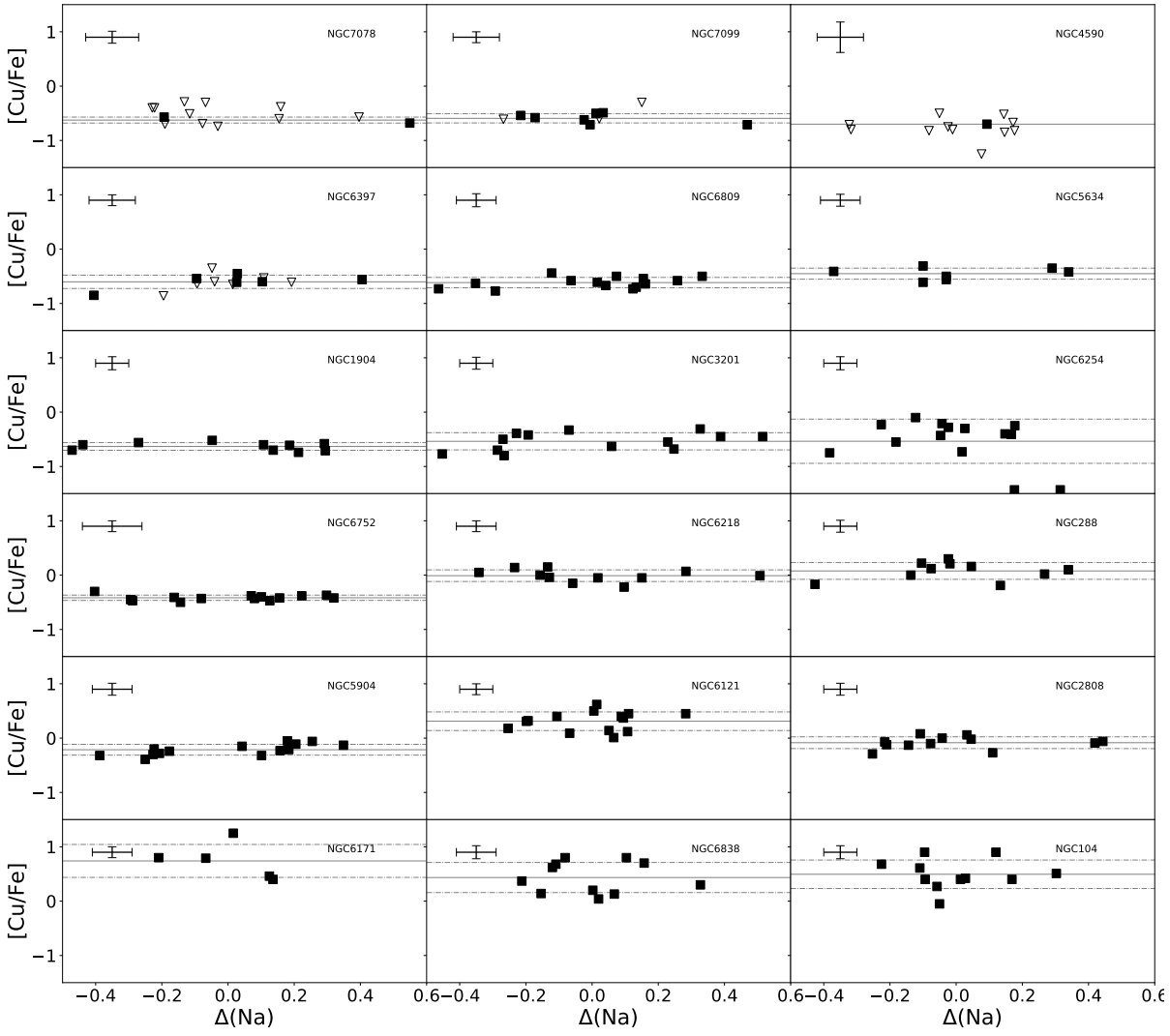

Figure 5.3 [Cu/Fe] distribution along with Δ(Na) for each GC analysed. The respective average and standard deviation Cu abundance are indicated in solid and dashed lines, respectively. Symbols follow the same description as in Fig. 5.1.

5.1.2 Cu overall distribution

Fig. 5.4 shows the Cu distribution along the [Fe/H] in the Galactic field and in GCs. In the present figure, grey crosses represent the Cu field star abundances reported by Ishigaki et al. (2013). The colours were assigned to each solid symbol to represent the different GCs present in this sample. They display a steep increase for metallicities higher than -2.0 dex. Also, there seems to be a small offset between the field stars and GC results probably due to different assumptions (they used a $\log gf$=-1.10, whereas we a $\log gf$=-1.52) with the cited paper. Ishigaki et al. (2013) does not report Cu abundance in a reference stars (e.g. sun or Arcturus), but We note that the Cu abundance reported for Arcturus by (A(Cu)=4.09 dex Ernandes et al., 2020) is in good agreement with our result (A(Cu)=4.12 dex).

In Fig. 5.4 most of the GCs closely follow the upper envelope of the field star distribution, meaning that they do not experience a particular Cu enrichment. Nevertheless, the more metal-rich ([Fe/H]$\gtrsim$-1.3 dex) GCs display a relatively high Cu abundance compared with field stars of the same metallicity. A possible explanation for this discrepancy could be due to both the sensitivity of the line at 5105Å to the changes in V_m (as mentioned for NGC 6121) and the presence of many MgH lines. Both effects affect especially at higher metallicities, as reflected in the results, then must be taken with caution. In addition, this line seems to be less sensitive to the change of abundances for GCs with [Fe/H]$\gtrsim$-1.0 dex. In this regard, a better Cu indicator could be the line Cu line at 5787Å, which is neither saturated nor crowded by other species. Unfortunately, the mentioned line is located just in the gap of the spectra analysed here.

Simmerer et al. (2003) analysed Cu abundance in a large sample of GC using the Cu lines at 5105Å and 5787Å. As expected from the exposed reasons in the last paragraph, among in-common GCs with higher metallicities (NGC 6838, NGC 6121, NGC 5904, and NGC288), the cited article reported considerably lower Cu abundances –with differences ranging from 0.30 to 0.60 dex– than the ones reported in the present thesis. In contrast, there is good agreement among in-common GCs with lower metallicity (NGC 6254 and NGC 7078). In particular, the large spread found in the present thesis for NGC 6254 was also reported by Simmerer et al. (2003). In addition, they also reported a

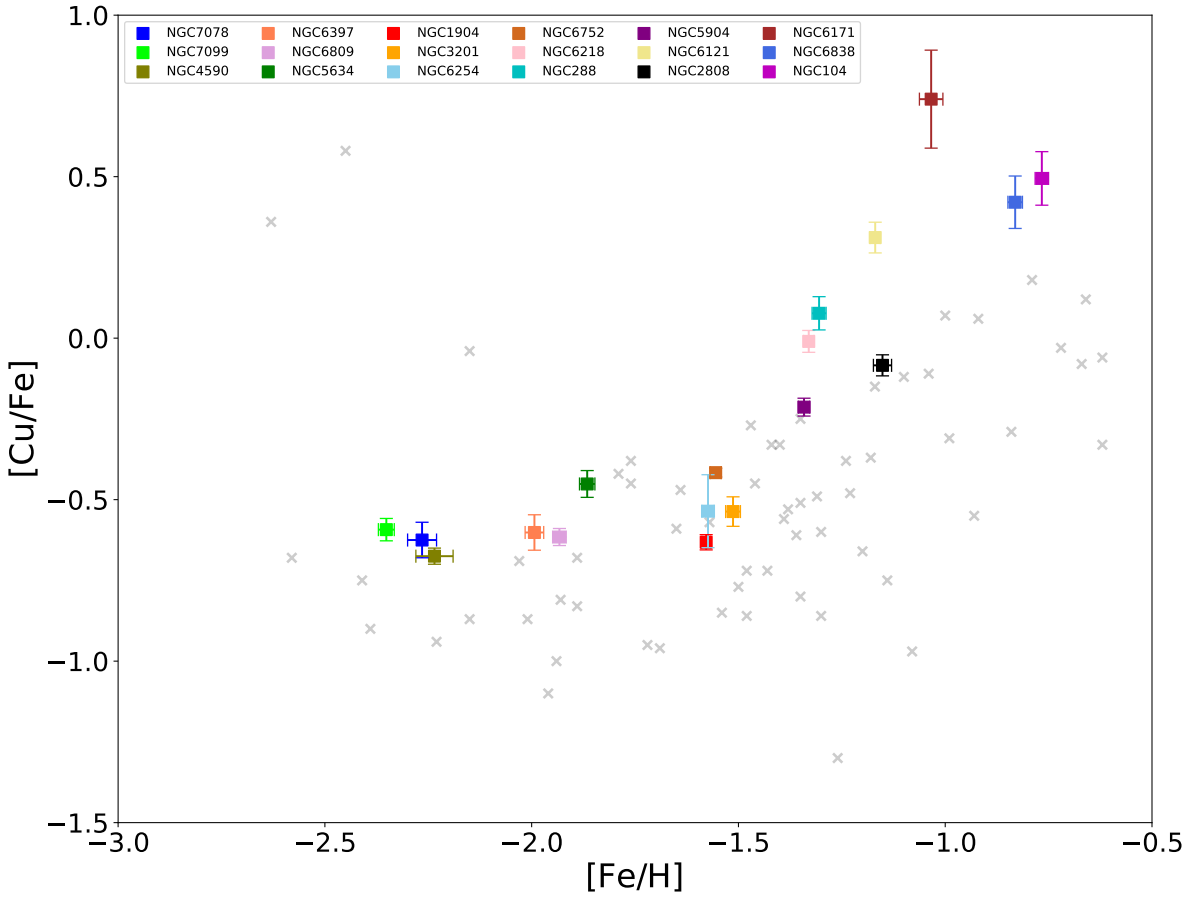

Figure 5.4 [Cu/Fe] distribution along the [Fe/H] for the whole sample. The analysed GCs are shown with coloured squares. Grey crosses show the field star abundances from Ishigaki et al. (2013).

particularly high Cu content in NGC 6121 compared with other GCs with similar metallicities. In this regard, it is worth noticing that the GC NGC 2808 has similar metallicity as NGC 6121, but they display quite different Cu. To clarify this a line-to-line Fig. 5.5 shows a comparison between one star of each cluster with similar stellar parameters was compared. The figure reinforces that the difference is real and is not due to any dependency on stellar parameters. In the case of NGC 6171 the trend with V_m does not seem to be present, but as was shown previously this cluster displays a particular Cu enrichment.

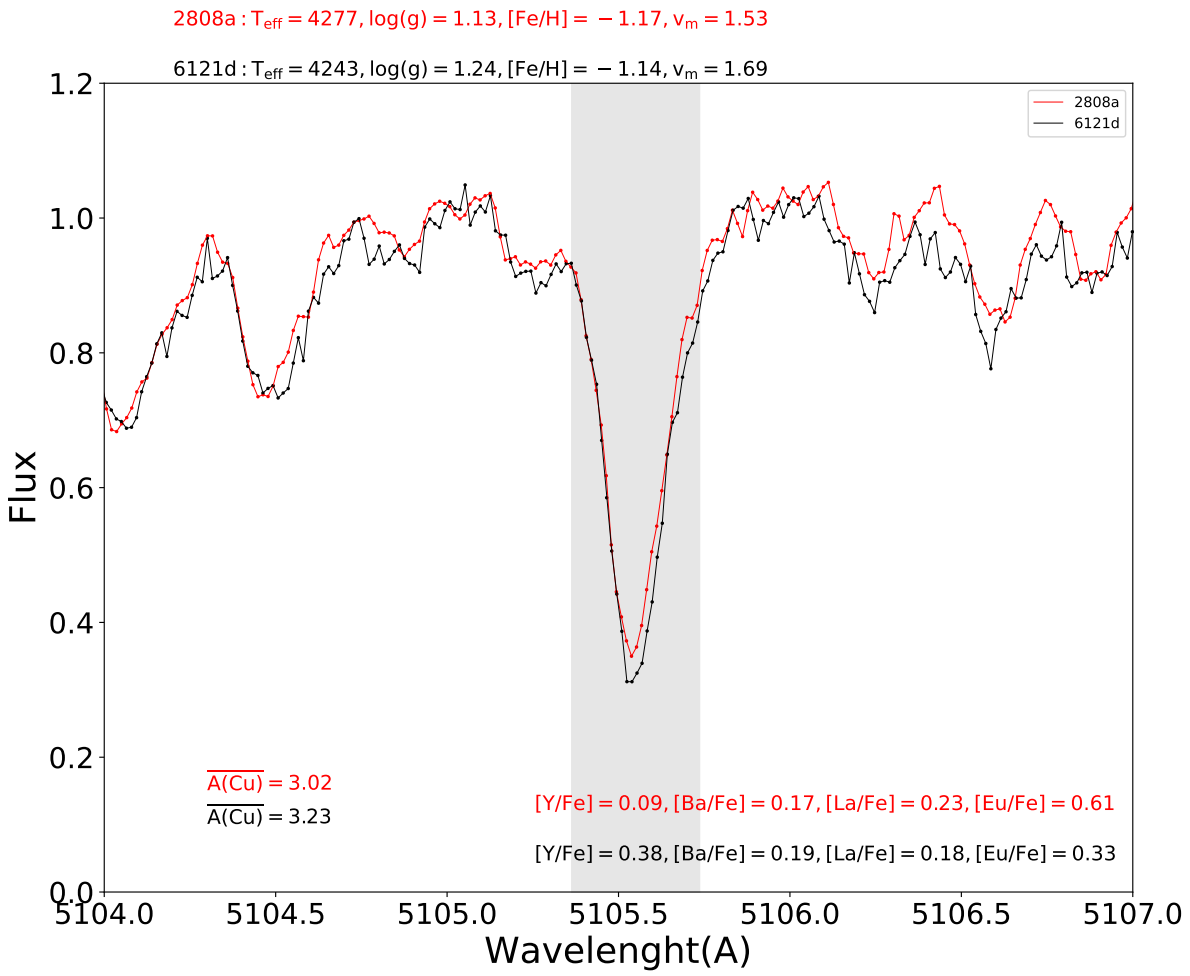

Figure 5.5 Pair of stars of the GCs NGC 2808 (ID=a; red line) and NGC 6121 (ID=d; black line) with similar stellar parameters and different Cu abundance.

5.2 Chemical Abundances Distribution: Y, Ba, La, and Eu

5.2.1 Internal n-capture spread

The sample spectra cover transitions for Y and Ba which are pretty strong, forming in the upper layers of the atmosphere, where models (and in particular 1D models, such as those used in the present analysis) and LTE approximation might be plagued

by considerable uncertainties. These saturated lines are highly sensitive to microturbulence (and its associated uncertainties). To show their dependency were defined Δ(Ba,Y)$_{MEAN}$. The latter is shown in Fig. 5.6 and how it affects every single GCs. This effect makes it challenging to assess the existence of internal variation in Ba and Y, while for Eu and La the estimates are more robust. Because of this effect, in general, the larger the range covered by V$_m$ the larger the dispersion driven by this parameter. Table 5.2 display both the rms error for Δ (Y,Ba)$_{MEAN}$ and the observational one for each cluster. It is worth noticing the observational error reported here is not taking into account the uncertainty coming from V$_m$.

As can be seen from the figure and the table, the GCs NGC 6171 and NGC 7078 display an rms error comparable to the observational error in their Ba abundances revealing a mildly significant dispersion. The Ba dispersion plus the constant Y found in NGC 7078 is in good agreement with previous results in the literature, where NGC 7078 has been reported as an r-process enriched cluster (Kirby et al., 2020). At the cluster metallicity, there is a strong contribution of Ba coming from r-process synthesis. On the other hand, NGC 6171 shows a larger rms error than the observational error in both Δ (Y)$_{MEAN}$ and Δ (Ba)$_{MEAN}$ which has not been reported previously in the literature. This mildly significant spread agrees with O'Connell et al. (2011) who speculated about a potential early r-process enrichment in the cluster due to the evidence of La and Eu spread in the cluster. In contrast, Fig. 5.7 shows the analogous plot for La which is measured from weaker lines –as it is also the case of Eu–. It is clear that the abundance shows a flat distribution along the different V$_m$ independent of the range covered by the cluster members.

5.2.2 n-process elements and their relation with Na

As mentioned in the Introduction, with a few exceptions, GCs have not shown heavy element variations among their different populations and they have not been found to be involved in the MSP phenomenon. Similarly to the analysed done for NGC 6752 (Chapter 4), and in order to disentangle the internal variation from that due to the effect of microturbulence, the variation of Y and Ba with respect to Na was explored.

Clusters	[Ba/Fe]	σ	rms	Ba_n	[Y/Fe]	σ	rms	Y_n	[La/Fe]	σ	rms	La_n	[Eu/Fe]	σ	rms	Eu_n
NGC 104	0.06	0.12	0.06	11	-0.17	0.11	0.03	11	-0.06	0.12	0.02	11	0.37	0.10	0.02	11
NGC 1904	0.08	0.11	0.06	10	-0.08	0.10	0.03	10	0.3	0.11	0.11	2	0.49	0.10	0.04	7
NGC 2808	0.13	0.12	0.04	12	0.07	0.11	0.03	12	0.23	0.10	0.04	12	0.63	0.10	0.03	12
NGC 288	0.33	0.13	0.05	10	0.32	0.12	0.03	10	0.36	0.11	0.03	10	0.58	0.10	0.02	10
NGC 3201	0.10	0.11	0.05	13	-0.03	0.11	0.04	13	0.04	0.12	0.03	13	0.38	0.10	0.04	10
NGC 4590	-0.10	0.22	0.05	13	-0.27	0.13	0.04	13	—	—	—	—	—	—	—	—
NGC 5634	0.08	0.11	0.06	7	0.10	0.10	0.09	7	0.42	0.12	0.04	6	0.56	0.10	0.03	7
NGC 5904	0.25	0.12	0.05	14	0.17	0.10	0.03	14	0.17	0.10	0.03	13	0.64	0.10	0.03	8
NGC 6121	0.62	0.11	0.06	14	0.46	0.10	0.04	14	0.37	0.10	0.02	14	0.49	0.10	0.04	14
NGC 6171	0.71	0.12	0.17	5	0.52	0.11	0.17	5	0.44	0.13	0.10	3	0.64	0.10	0.11	5
NGC 6218	0.19	0.11	0.04	11	0.20	0.10	0.04	11	0.15	0.10	0.02	11	0.42	0.10	0.02	10
NGC 6254	0.16	0.12	0.07	14	0.08	0.11	0.03	14	0.33	0.11	0.03	11	0.52	0.10	0.03	11
NGC 6397	-0.03	0.11	0.03	13	-0.08	0.10	0.01	13	—	—	—	—	0.63	0.10	0.05	5
NGC 6752	0.33	0.11	0.06	14	0.11	0.11	0.03	14	0.14	0.10	0.02	14	0.43	0.12	0.02	14
NGC 6809	0.32	0.16	0.06	14	0.07	0.11	0.03	14	0.42	0.10	0.04	7	0.74	0.12	0.03	13
NGC 6838	0.08	0.15	0.07	12	-0.06	0.11	0.04	12	0.21	0.10	0.02	12	0.50	0.12	0.03	12
NGC 7078	0.24	0.19	0.11	13	0.06	0.10	0.03	13	0.32	—	—	1	0.90	0.12	0.09	6
NGC 7099	-0.16	0.11	0.06	10	-0.07	0.10	0.03	10	—	—	—	—	—	—	—	—

Table 5.1 Summary table with mean n-capture abundances for each cluster. The number of stars used for the mean abundance determination for each element is also indicated (X_n), as well as the observational and rms errors.

Fig. 5.8 shows the results for the Y and Ba abundances as a function of the Na ones for each cluster of the sample. To avoid the recently shown trends with V_m, Δ(Y) and Δ(Ba) –as was defined in Chapter 4– are used. The results for Y seem to display quite constant abundances within the associated errors along the different Na, meaning in every individual cluster there is no evidence of the production of Na and Ba and Y from the same sources.

Fig. 5.9 shows the analogous results for Eu and La. As the measured abundances of these two elements are based on weak lines, they are scarcely affected by V_m. Hence the plot displays directly [La/Fe] and [Eu/Fe] along with Δ(Na). Although La abundances are dominated by upper limits in the more metal-poor clusters, the distribution of La seems constant along with the Na abundances without considerable spread. As for La, Eu is dominated by upper limits in the low metallicity regime. Their results display a constant abundance along Na showing the lack of correlation between these species. The only exceptions are the GCs NGC 7078 and NGC 6171 which display a larger spread Eu confirming the r-process enrichment mentioned previously.

The previous analysis was extended to the whole sample. To do so, Fig. 5.10 shows the Δ(Y) (upper row) and Δ(Ba) (lower row) as a function of Δ(Na) for each GC. It is

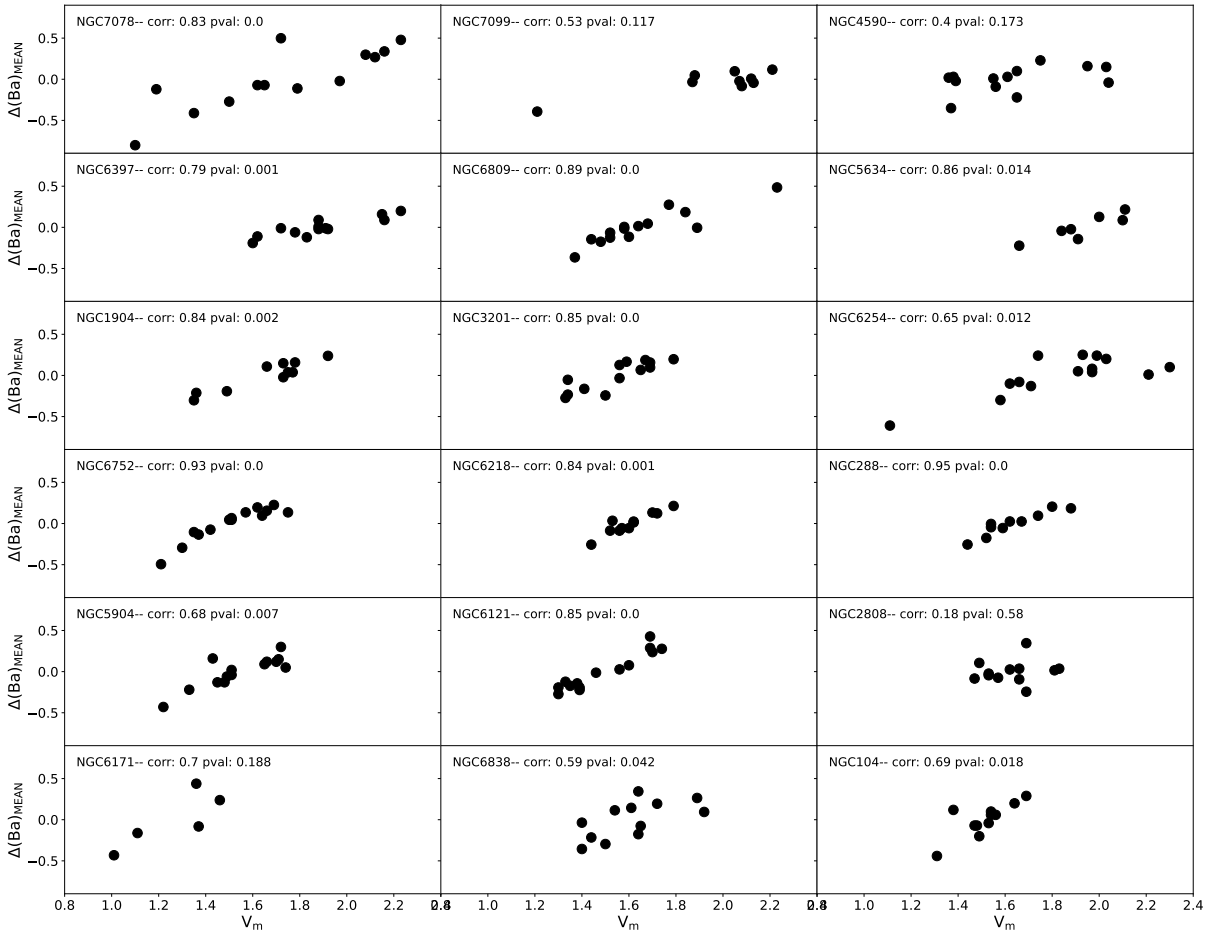

Figure 5.6 $\Delta(\mathrm{Ba})_{MEAN}$ along with V_m for each GCs of the sample. The respective Spearman coefficient and p-value are reported.

important to note that this exercise aims to analyse the variation of s-process elements along with the Na abundance. Then, the GC NGC 7078 was excluded due to its particular r-process enrichment (affecting the Ba content) found in the literature and in the present thesis. The figures display the distribution for three metallicity slots: [Fe/H]>-1.10 dex (metal-rich; left panels), -1.80 dex <[Fe/H]<-1.10 dex (metal-mid; mid panels), and [Fe/H]<-1.80 dex (metal-poor; right panels). Each figure indicates both the correspondent Spearman coefficient and p-value for each metallicities slot. All the panels show quite flat distributions and weak correlations, which is valid for both the whole sample and each individual metallicity slot. This lack of correlation confirms the finding reported in Chapter 4 for the GC NGC 6752.

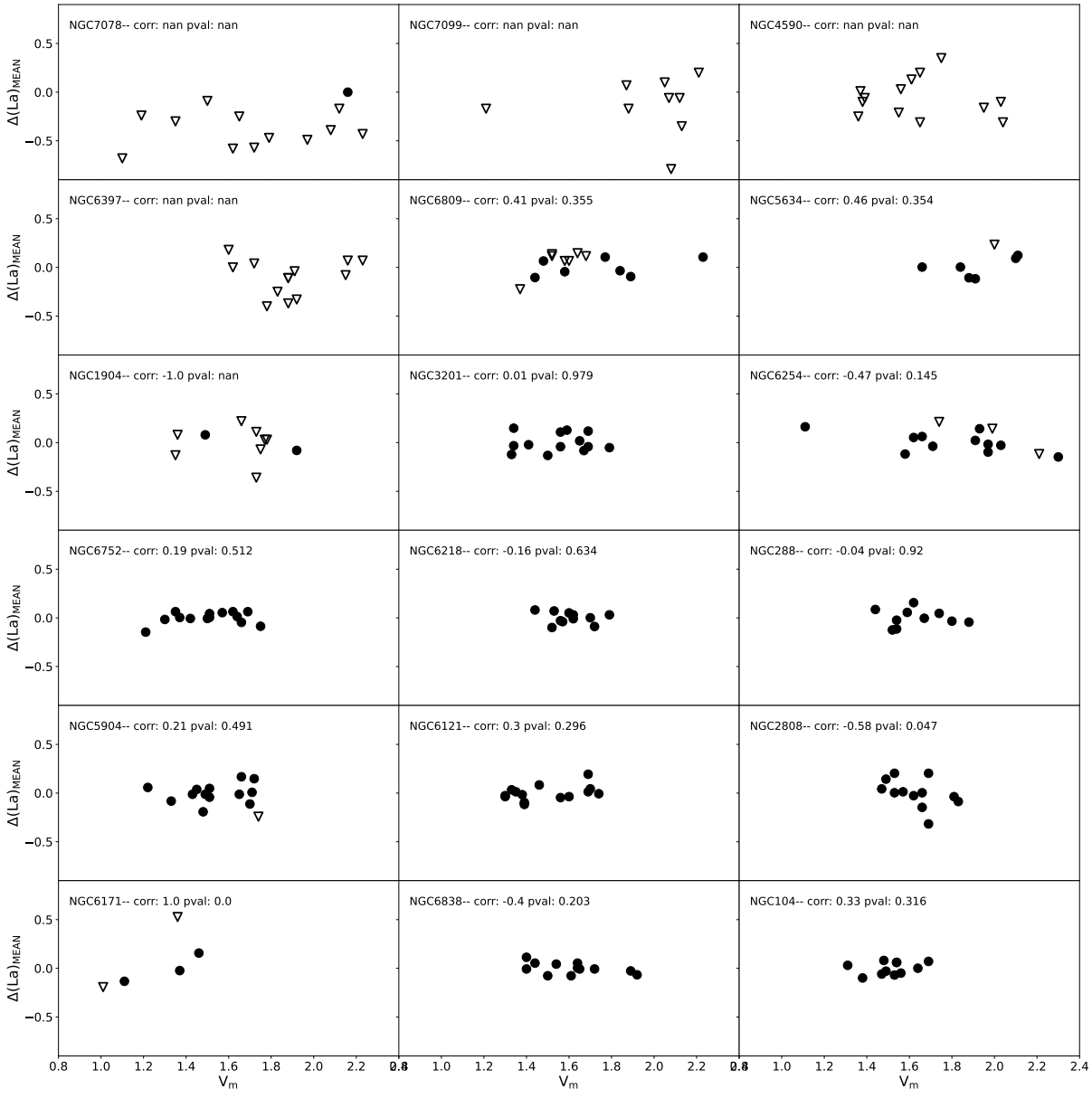

Figure 5.7 $\Delta(\mathrm{La})_{MEAN}$ along with V_m for each GCs of the sample. The respective Spearman coefficient and p-value are reported.

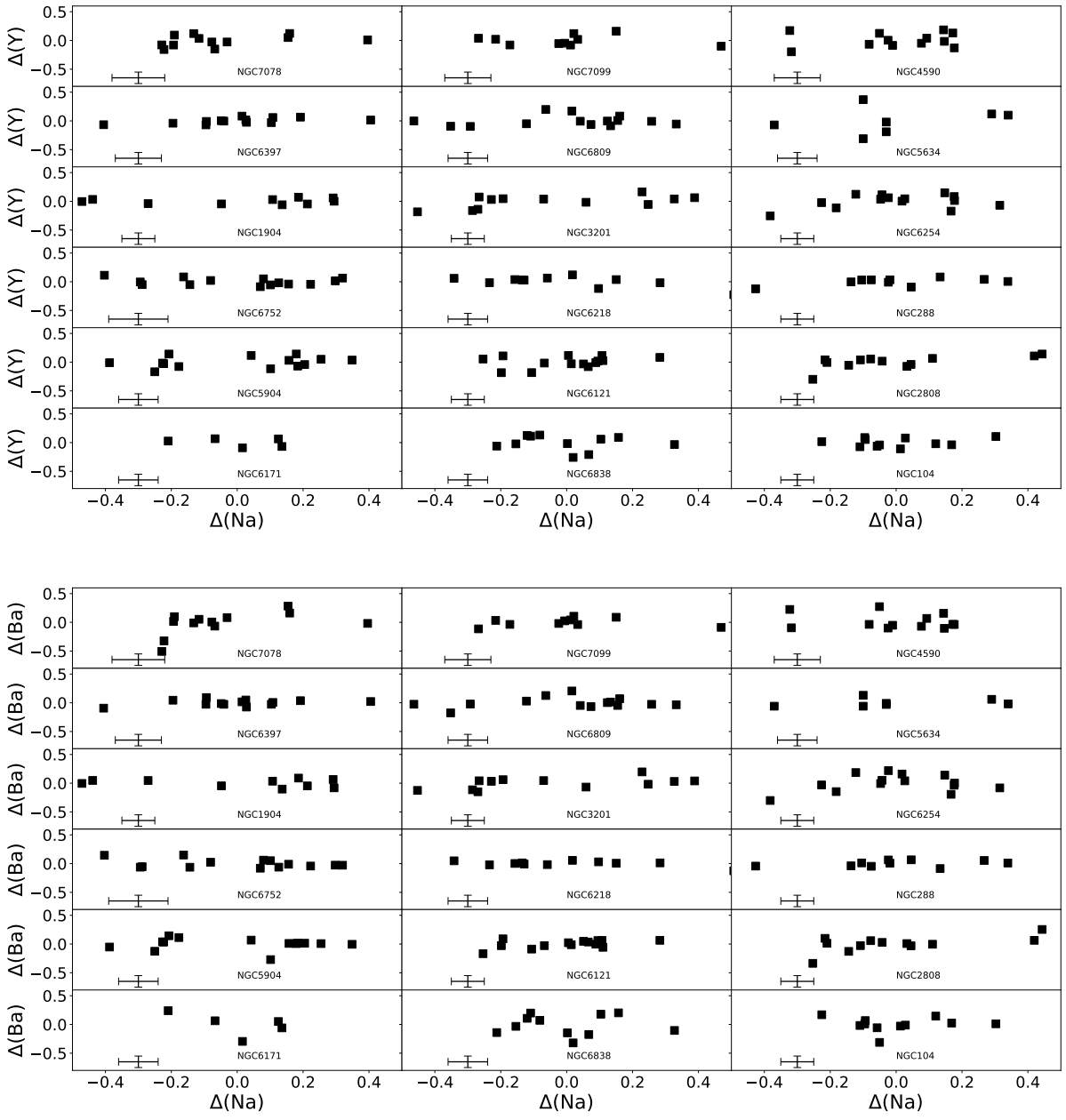

Figure 5.8 Δ (Y) (upper) and Δ (Ba) (lower) as a function of Δ (Na) for each cluster of the sample. Filled squares and empty triangles represent actual measurement and upper limits, respectively.

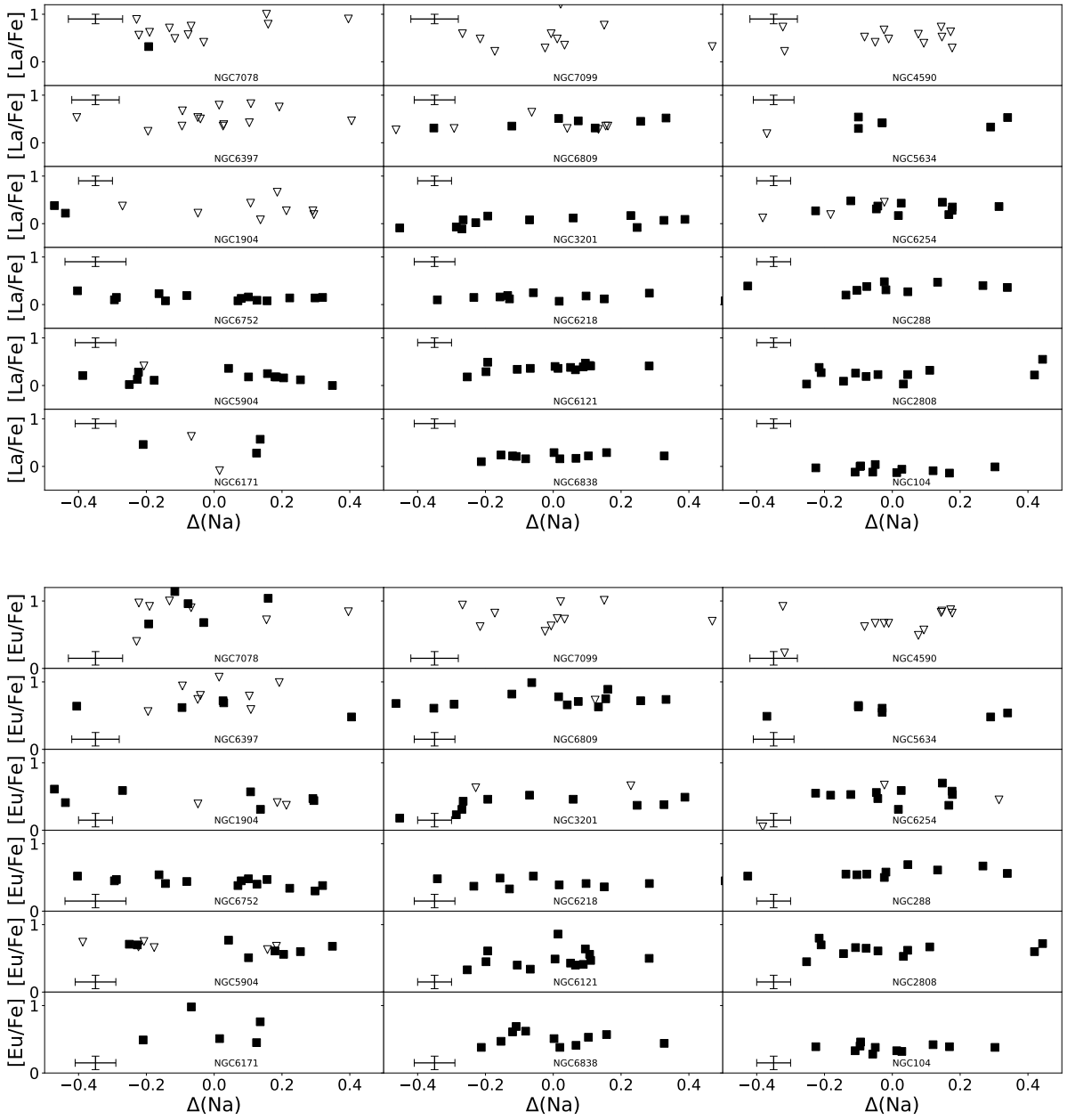

Figure 5.9 [La/Fe] (upper) and [Eu/Fe] (lower) as a function of Δ (Na) for each cluster of the sample. Filled squares and empty triangles represent actual measurement and upper limits, respectively.

Cluster	rms(Ba)$_{MEAN}$	σ(Ba)	rms(Y)$_{MEAN}$	σ(Y)	IQR$_{[Y/Fe]}$	IQR$_{[Ba/Fe]}$	IQR$_{[La/Fe]}$	IQR$_{[Eu/Fe]}$
NGC 7078	0.10	0.10	0.03	0.10	0.15	0.42	—	0.28
NGC 7099	0.06	0.10	0.03	0.10	0.11	0.12	—	—
NGC 4590	0.04	0.10	0.03	0.10	0.21	0.14	—	—
NGC 6397	0.03	0.10	0.01	0.10	0.03	0.15	—	0.07
NGC 6809	0.06	0.10	0.03	0.10	0.11	0.16	0.16	0.11
NGC 5634	0.06	0.10	0.09	0.10	0.20	0.20	0.15	0.10
NGC 1904	0.06	0.10	0.03	0.10	0.15	0.29	0.08	0.15
NGC 3201	0.05	0.10	0.04	0.10	0.25	0.32	0.16	0.14
NGC 6254	0.06	0.10	0.03	0.10	0.15	0.27	0.12	0.08
NGC 6752	0.05	0.10	0.03	0.10	0.10	0.23	0.06	0.08
NGC 6218	0.04	0.10	0.04	0.10	0.18	0.15	0.08	0.10
NGC 288	0.05	0.10	0.03	0.10	0.08	0.13	0.10	0.06
NGC 5904	0.05	0.10	0.03	0.10	0.15	0.23	0.09	0.11
NGC 6121	0.06	0.10	0.04	0.10	0.22	0.38	0.06	0.14
NGC 2808	0.04	0.11	0.03	0.12	0.10	0.11	0.12	0.08
NGC 6171	0.15	0.10	0.15	0.10	0.46	0.40	0.15	0.27
NGC 6838	0.07	0.10	0.04	0.10	0.19	0.34	0.08	0.18
NGC 104	0.06	0.10	0.03	0.10	0.10	0.18	0.12	0.06

Table 5.2 Observational and rms error (excluding the V_m contribution) for each cluster. In addition, the IQRs of [Y/Fe], [Ba/Fe], [La/Fe], and [Eu/Fe] for each cluster are reported considering the V_m effects. Upper limits were not considered for the IQRs computation.

However, it is worth noting that this weak correlation is significant for the mid-metallicity regime (mid-panels). In case of an actual correlation between those abundances, that metallicity regime should be the best one to spot it. In fact, the lines are strong enough to be scarcely affected by noise, but weak enough to have to be weakly affected by the V_m, so that a linear fit can appropriately address its contribution.

In particular, the present test shows that for the GCs with larger spreads NGC 6171 and NGC 7078 the Spearman coefficients between Δ(Y) and Δ(Na) are -0.30 (p-val=0.62) and 0.45 (p-val=0.12), respectively. Although they show a slight correlation, it is not significant. On the other hand, the same clusters have Spearman coefficients in between Δ(Ba) and Δ(Na) are -0.70 (p-val=0.19) and 0.57 (p-val=0.04). In both GCs, the correlations are higher with respect to the ones between Y and Na, but also they are more significant. While for NGC 7078 the idea of any relation between the production of Na and s-process elements is not statistically supported, the results suggest responsible for the Na enrichment in NGC 6171 produces the Ba spread.

The result is not conclusive, although it carries an intriguing suggestion which can be further analysed in a future study.

As mentioned in Chapter 1, the light element variation could be explained by the dilution of pristine material with the one produced in different polluters, however, the suggestion of a modest production of s-process elements could add another ingredient to disentangle the origin of the MSP in GCs. In this regard, the pure contribution of low-mass AGB stars to cluster pollution seems unlikely because the abundance of s-process elements detected in our results is quite minor. Similarly to our findings for NGC 6752 (Chapter 4) one possibility would be the presence of AGB stars with masses around 5-6$M_{\odot}$, which are able to reproduce the light element variation, but at the same time to produce a modest amount of s-process species. On the other hand, the contribution of massive interactive binaries to the s-process dispersion is discarded because they cannot explain the heavy s-process element enhancement Renzini et al. (2022). Another source of s-process elements is FRMS, however, according to models they would produce more efficiently the elements belonging to the first peak s-process species (Limongi and Chieffi, 2018), although their production depends strongly on the rotational velocities adopted by the models. Molero et al. (2023), considered 3 different rotational velocities (0, 150, and 300 km/s) and analysed the s-process production in those stars. According to their results, the Y production varies strongly in these 3 cases, however, the Ba production did not show considerable differences in the cases when rotation was included. Then, a contribution from FRMS with first-peak s-process elements should be considered. The last could be an explanation of the stronger trend in Δ(Y) and Δ(Na) than the one found in Δ(Ba) and Δ(Na).

5.2.3 Heavy elements distribution

Aiming to take a look at the overall content in n-capture elements, a comparison of the heavy elements analysed for the sample of GCs and the galactic field was performed. The Fig.5.11 shows, from the top to the bottom, the results obtained for [Y/Fe], [Ba/Fe], [La/Fe], and [Eu/Fe] along with the [Fe/H]. The latter results are summarised in Table5.1, which indicates the mean, spread, and the number of stars used to get the actual

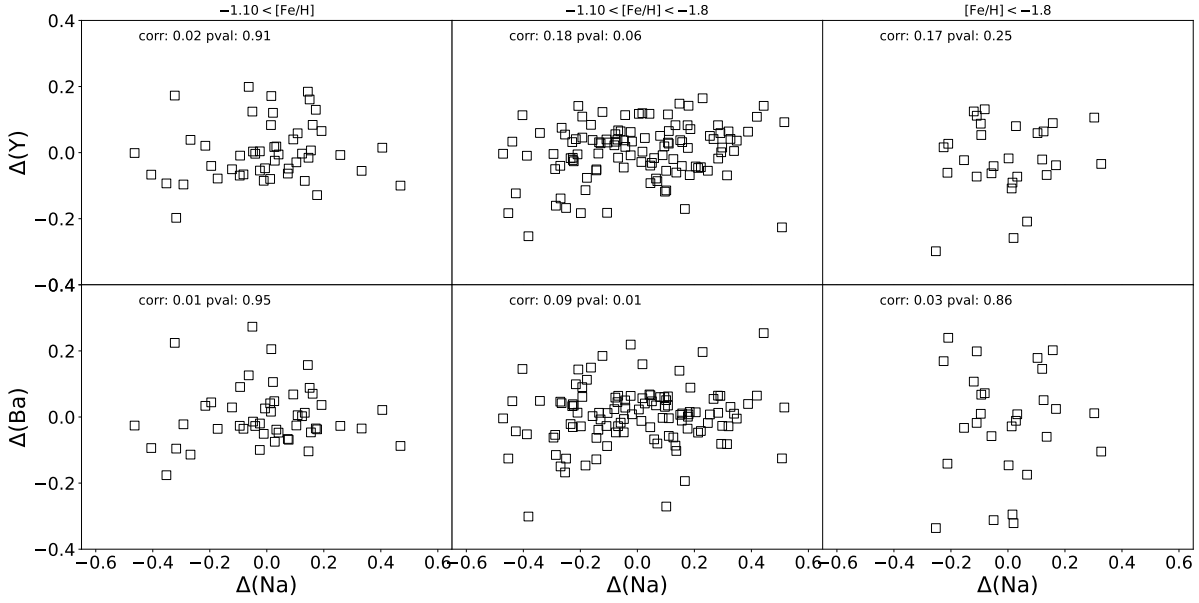

Figure 5.10 ΔY (upper panels) and ΔBa (lower panels) as a function of ΔNa for the whole survey sample. The sample was divided into three metallicity slots: [Fe/H]>-1.10 dex (metal-rich; left panels), -1.80 dex <[Fe/H]<-1.10 dex (metal-mid; green squares), and [Fe/H]<-1.80 dex (metal-poor; right panels). The respective Spearman coefficient and p-value are reported on each panel.

abundance for each element. The field star distribution (grey crosses) was taken from SAGA Database[1] Suda et al. (2008). Each GC is represented with a different colour. Squares and triangles are actual measurements and upper limits, respectively. Field stars show a Yttrium distribution slightly sub-solar abundance at low metallicities up to ∼-0.60 dex where Y increases constantly up to solar abundances. In the upper panel, most of the GCs analysed follow closely the trend displayed by field stars at the correspondent metallicity. NGC 6121 and NGC 6171 are the only exceptions showing larger Y abundances than the field star counterparts.

Barium, at solar metallicity, is mainly produced by s-process (85% Sneden et al., 2008). Ba shows similar behaviour to Y along with [Fe/H], however, the former displays slightly lower abundances than Y at [Fe/H]<-1.5 dex. In the second panel –similarly to the results for Y– the Ba abundance in almost all the GCs analysed follows the field stars

[1]Data compilation of Galactic abundances reported almost all the published article by 2019: **http://sagadatabase.jp/**

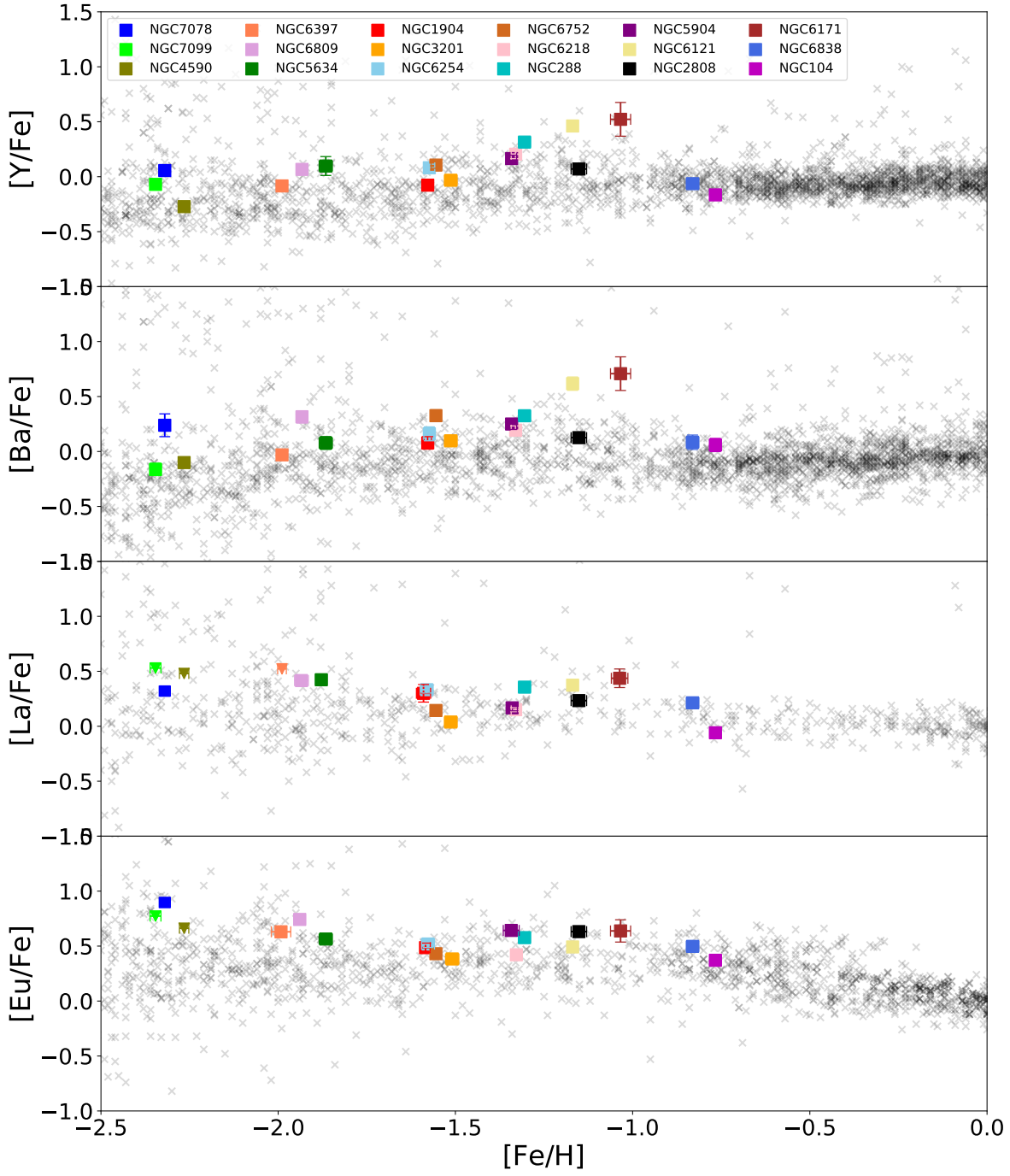

Figure 5.11 From the top to the bottom: [Y/Fe], [Ba/Fe], [La/Fe], and [Eu/Fe] as a function of the [Fe/H] for the whole sample. Coloured squares represent the GCs analysed in the present sample. Grey crosses show the field star abundances taken from SAGA Database (Suda et al., 2008).

trend. The GCs NGC 6121, NGC 6171, and NGC 7078 display higher abundance than expected for stars at that metallicity.

Field stars display a lanthanum distribution slightly super-solar at [Fe/H]<-1 dex, which becomes solar for richer metallicities. As shown in the third panel, the GCs surveyed fit the field stars trend. It is worth noticing, for the metal-poor GCs NGC 7099, NGC 4590, and NGC 6397 only the upper limit was set because the La lines became too weak. For NGC 7078 the La abundance was determined in only one star, then the result should be taken with caution.

Europium, at solar metallicity, is known to be a pure r-process element (97% Sneden et al., 2008). In the lowest panel, the Eu distribution in the field displays a quite constant over-abundant at [Fe/H]<-0.6 dex, which constantly decreases toward higher metallicities showing the iron production by SN Ia after 0.1-1 Gyr (Ballero et al., 2007). All the GCs analysed seem to follow closely the upper envelope of the distribution drawn by the field stars. We note that the GCs sample displays a lower spread in the n-capture elements with respect to the comparison literature sample, especially for what concerns Eu. There are several potential reasons. The abundances we report are the average over a number of stars, which leads to a more robust estimate, decreasing random errors. On the other hand the literature comparison dataset is a collection of abundances reported by a variety of sources, not homogenously analysed, and hence almost certainly affected by systematic offsets among different samples, leading to an increase of the scatter. Moreover, the literature sample is not limited to the Galactic halo, but includes also objects belonging to the Disk and dwarf galaxies. It is worth noticing, that for the GCs NGC 4590 and NGC 7099, the Eu detection was not possible. Moreover, the GC NGC 7078 display a slight Eu over-abundance with respect to the field stars at the same metallicity.

In general, most of the surveyed GCs follow closely the field distribution, meaning that they do not have a particular n-capture enrichment. On the other hand, off-the-trend GCs display (NGC 7078, NGC 6171, and NGC 6121) also a larger internal dispersion. Table 5.2 reports the IQRs of [Y/Fe], [Ba/Fe], [La/Fe], and [Eu/Fe]. Upper limits were not considered in the IQR computation for La and Eu. In this regard, NGC 7078 has been reported as GCs with the largest spread in both Ba and Eu. The present analysis reports

that the [Ba/Fe] abundance ranges from -0.24 dex to 1.04 dex. Previous studies have reported a difference of ∼0.55 dex (Sobeck et al., 2011) and ∼0.45 dex (Otsuki et al., 2006). The larger Ba spread found in the present analysis can be related to the larger V_m range compared to the cited articles. For comparison, when the Ba intrinsic spread (without considering the effect of V_m) is considered, it decreases to ∼0.80 dex.

Similarly, the [Eu/Fe] difference is at least 0.48 dex (upper limits could enlarge this difference). While Sobeck et al. (2011) found a difference of 0.57 dex in their sample of 3 RGB stars, Otsuki et al. (2006) reported a similar value (∼0.55 dex). The large dispersion reported in both Ba and Eu agrees with a peculiar r-process element enrichment. On the other hand, NGC 6171 display a large IQR in all the n-capture elements measured. O'Connell et al. (2011) analysed the La and Eu abundances in 13 stars of the cluster, which showed a good agreement with the present thesis (⟨[La/Fe]⟩=0.41±0.12 and ⟨[Eu/Fe]⟩=0.73±0.13). Moreover, they reported a large difference in the Eu (∼0.50) and La (∼0.40) content in their sample which agrees with the large IQR mentioned before arguing in favour of an early r-process enrichment. Finally, the GC NGC 6121 was found to show a Y bimodal distribution (Villanova and Geisler, 2011), which was later discarded by D'Orazi et al. (2013) and confirmed in the present analysis. The cluster was found to display an intrinsic high s-process enrichment due to a particular higher concentration of these species in the protocluster cloud (Yong et al., 2008), which agrees with the [Y/Fe]=0.44 dex and [Ba/Fe]=0.50 dex found by (D'Orazi et al., 2013) and (D'Orazi et al., 2010), respectively. Moreover, the La (0.48 dex) and Eu (0.40 dex) results from (Yong et al., 2008) are in good agreement with the ones presented here.

5.2.4 Clusters Comparison: Internal Spread

In order to assess whether the internal spread described above is real or due to observational effects, a comparison of a pair of spectra of stars with similar stellar parameters within a GC is shown in Fig. 5.12, for this purpose were selected the GCs with the largest IQR values for Ba and Y. The first row shows the spectra comparison of a couple of members of NGC 6171 (ID= c and d). The pair shows a similar abundance of Y and Eu, however, they vary in their heavy s-process elements. The second row shows

the comparison for the stars of NGC 7078 (ID= m and f). This couple also shares the same Na abundance. They show quite different Y and Ba abundances, showing that the difference is real and independent of the V_m. Unfortunately, the stars have a high temperature and low metallicity making it difficult to distinguish weak lines such as La and Eu.

In the case of the GC NGC 7078, this spread has been found previously in the literature and it was associated with enrichment in r-process species. On the other hand, the spread in s-process species found in NGC 6171 has not been reported before. In fact, O'Connell et al. (2011) claimed that there was not a considerable contribution of s-process to cluster pollution. The latter is probably due to larger errors that do not allow us to spot the spread found in the present thesis. However, as shown in the last figure, there is a clear variation in Y, Ba, and La abundance at constant Eu.

It is worth noticing that other clusters such as NGC 6121 and NGC 6838 have similar IQR in Ba. Unfortunately, these GCs do not have pair of stars to be compared, however, it is an intriguing suggestion that can be analysed further in the future.

5.2.5 [Ba/Eu] and [Ba/Y] ratios

Figure 5.13 the ratio between the Ba and Y (left panel) and Ba over Eu as a function of [Fe/H]. The ratio of these elements can provide means to disentangle the contribution of the r- and s-process to the heavy element content in the cluster. The symbols follow the same description as the previous figures.

As discussed before, the s-process is expected to be produced primarily in AGB stars (abundances varying depending on the stellar mass and metallicity). On the other hand, the r-process is thought to be synthesised in catastrophic events, such as core-collapse SNe and neutron star mergers.

The [Ba/Eu] distribution as a function of [Fe/H] reflects the process from which our Galaxy was enriched. The dotted horizontal lines at [Ba/Eu] -0.75 dex and 1 dex, reflect a pure enrichment coming from r-process and s-process species, respectively. The [Ba/Eu] pattern followed by the field stars goes from a pure r-process enrichment at

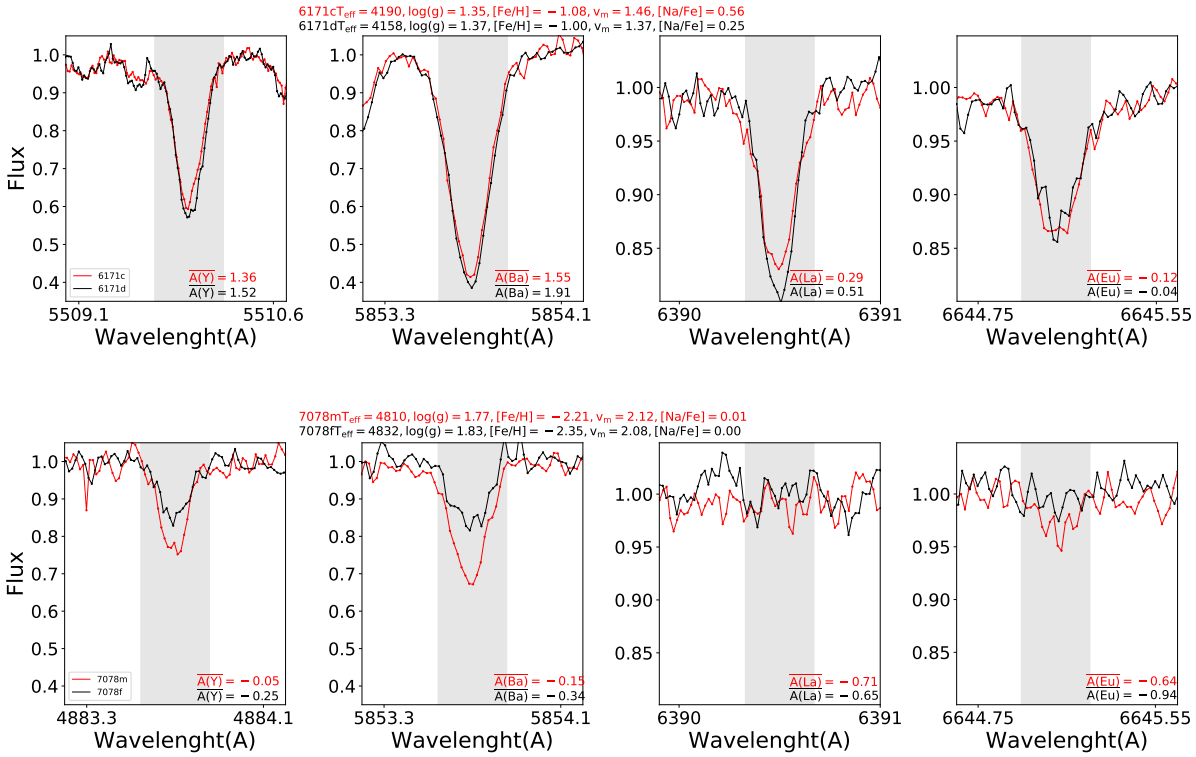

Figure 5.12 Pair of stars with similar stellar parameters as was reported by Carretta et al. (2009), but different n- capture abundances. From left to right: Y line at 4883Å, Ba line at 5853Å, La line at 6391Å, and Eu line at 6645Å.

low metallicities to a continuous contribution of s-process at solar metallicity. The results for the GCs display a similar behaviour as field stars. In addition, if [Fe/H] is considered as a proxy of time –being more metal-poor stars older than the ones with higher metallicity– it is possible to see the rise of the s-process element along the time. For the more metal-poor cluster, the results are compatible with higher r-process abundances meaning that their abundances are influenced by explosive events like SNe type II or merging neutron stars. As field stars, in GCs is clear the contribution of the s-process enrichment along with the time. It is worth noticing that for the GCs NGC 4590 and NGC 7099, We reported lower limits for the [Ba/Eu] ratios.

Generally speaking, Ba over Y ratio relates to second and first peak s-process elements, respectively. Thus it could be used to explore the produced by the heavy and light elements in AGB stars. However, it is important to consider that at low metallicities as

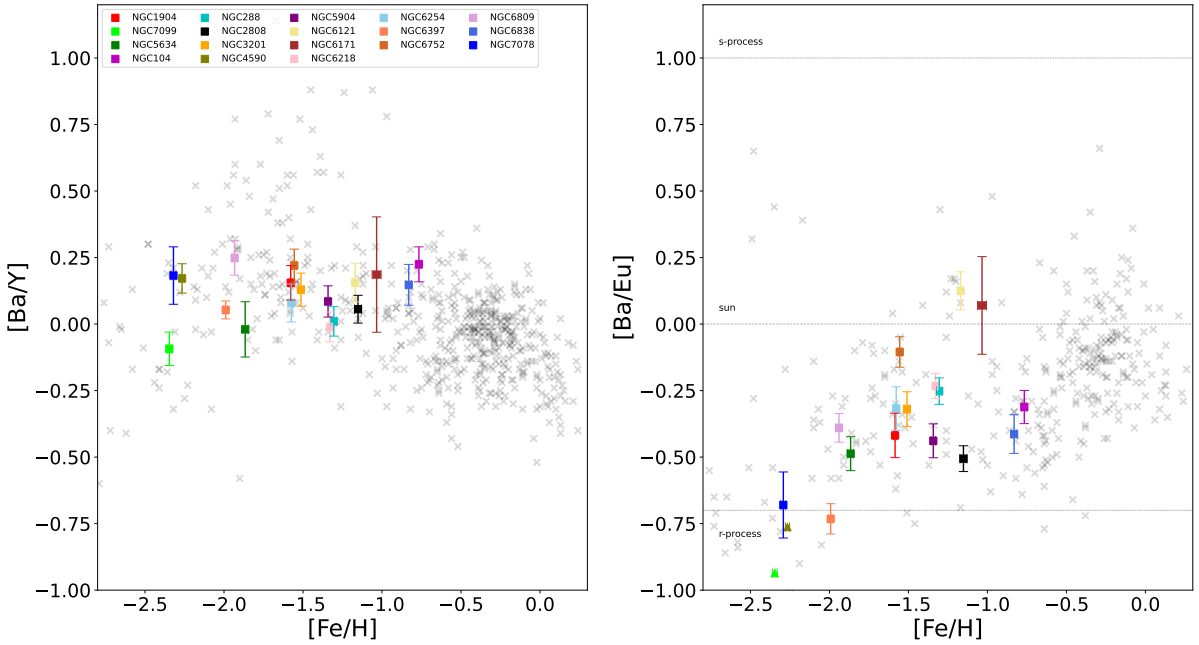

Figure 5.13 Left and right panels display the abundance ratios of Ba II over Y II and Ba II over Eu II as a function of [Fe/H], respectively. Dashed lines at [Ba/EU] 1.0 and -0.70 indicate the ratio for a full s-process and full r-process enrichment. The dashed line at [Ba/Eu] displays the solar ratio. Symbols and colours follow the description given in Fig. 5.11.

the ones found in metal-poor GCs, most of the heavy elements are the result of the r-process, as shown in Fig 5.13, hampering the possibility of using the Ba to Y ratio in this context. The results for the GC sample follow the pattern described by the field stars. Most of them display a clear overabundance of Ba over Y with the exception of the metal-poor GC NGC 7099.

5.2.6 Clusters Comparison: cluster-to-cluster difference

In order to assess the discrepant Ba/Y ratio recently reported, an analysis of the cluster-to-cluster difference is required to clarify if the overall is real. To do so, a pair of stars with similar stellar parameters in different clusters are selected. The comparison is shown in Fig. 5.14. The pairs also share similar Na abundance as reported by Carretta et al. (2009). In the first row of the figure, the comparison between the

stars of NGC 6121 (ID=d) and NGC 2808 (ID=a), two clusters with similar metallicities ([Fe/H]∼-1.2 dex), but quite different n-capture abundance. As the spectra comparison shows, there is higher abundance in their s-process element, however, this behaviour change for the r-process element. Because the stars have slightly different V_m, its effect cannot explain such a difference in the abundances. The latter suggests the large difference(∼0.6 dex) shown in Fig. 5.13 is real, meaning the NGC 6121 has a higher enrichment of s-process elements than NGC 2808 and the latter has a higher r-process enrichment.

The second row displays the comparison between a star pair, in GCs NGC 3201 (ID=b) and NGC 5904 (ID=e). The two stars with similar stellar parameters and Na abundance show a systematic overabundance in favour of the second one for all the elements analysed. The difference in Y, La, and Eu cannot be explained by the effect of V_m of the stars. The lower [Ba/Eu] ratio for NGC 5904 can be explained by its higher content of Eu.

5.2.7 Comparison with chemical evolution models

As mentioned in Chapter 1, the main nucleosynthetic sites for the s- and r-processes are mainly AGB stars – with some contribution of FRMS– and neutron star mergers and magneto-rotational driven (MRD) SNe, respectively. Cescutti and Chiappini (2014) proposed a model for the chemical enrichment of the halo considering different sources of heavy elements (for detail about the model, we refer the reader to the cited article). In particular, they tested the models with electron capture (EC) SNe or/and MRD SNe with/without an early enrichment of s-process elements from FRMS. According to Cescutti and Chiappini (2014), in order to better reproduce the observed n-capture element distribution in the Galactic halo, the model should take into account a mix of pollution coming from FRMS and MRD for the s- and r-process enrichment, respectively. Fig. 5.15 shows the comparison of our results (coloured symbols) and the predictions for Y, Ba, La, and Eu from the mentioned model (coloured by the number of stars in each bin). As shown in the present Figure, the model reproduces closely the observations with the exception of the [Ba/Fe] abundances in NGC 6121 and NGC 6171 which –as was

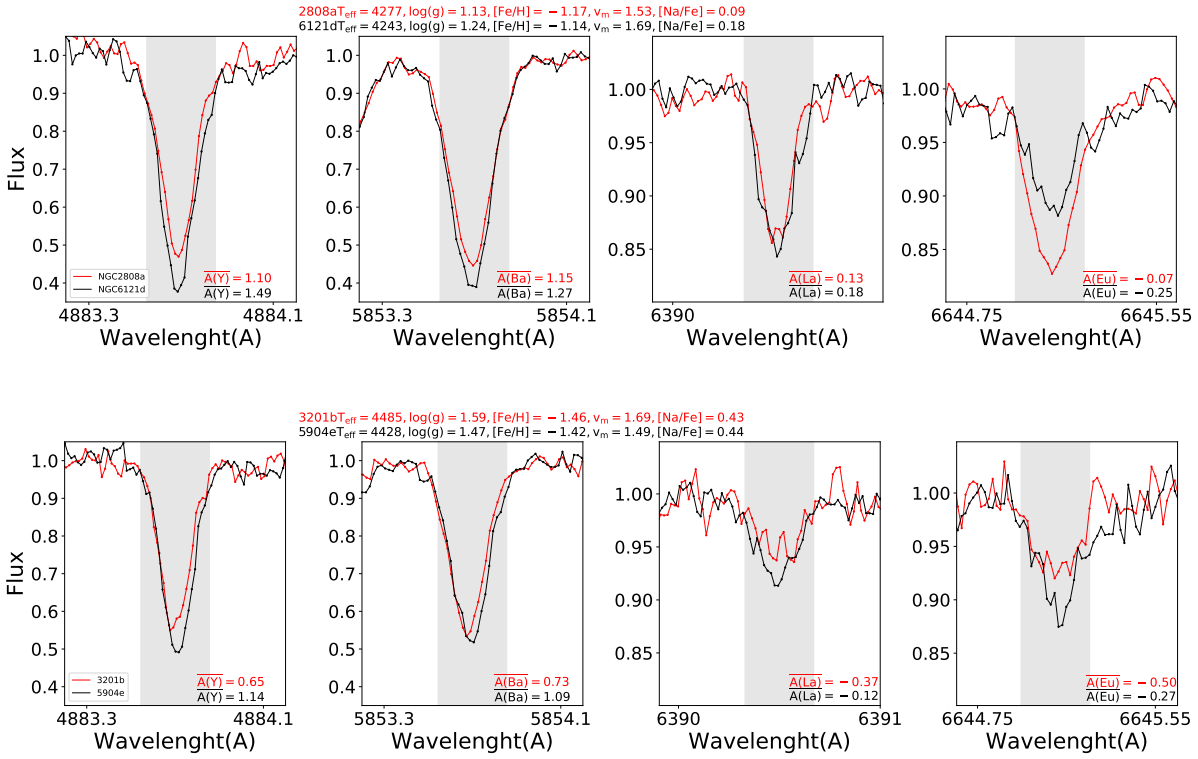

Figure 5.14 Pair of stars with similar stellar parameters and Na abundances as was reported by Carretta et al. (2009), but different n- capture abundances. From left to right: Y line at 4883Å, Ba line at 5853Å, La line at 6391Å, and Eu line at 6645Å.

discussed previously– show a particularly high Ba content. In addition, although those clusters show a La abundance in good agreement with the models, it is worth noticing that they are placed in the upper envelope of the model's distribution.

As commented by Cescutti and Chiappini (2014), both r-process sources analysed in their models (EC SNe and MRD) reproduced quite well the halo distribution of Eu, showing good agreement among these sources in the most metal-poor regime ([Fe/H]<-2 dex), however with some slight discrepancies at intermediate metallicities (-2 dex <[Fe/H]<-1 dex). The model used in the comparison with our results reflects good agreement with the metallicity of our sample being no discrepant with the MRD + FRMS scenario. We hope in the future with the present and other observational constraints, could shed light on the contributor sources of n-capture elements of the halo.

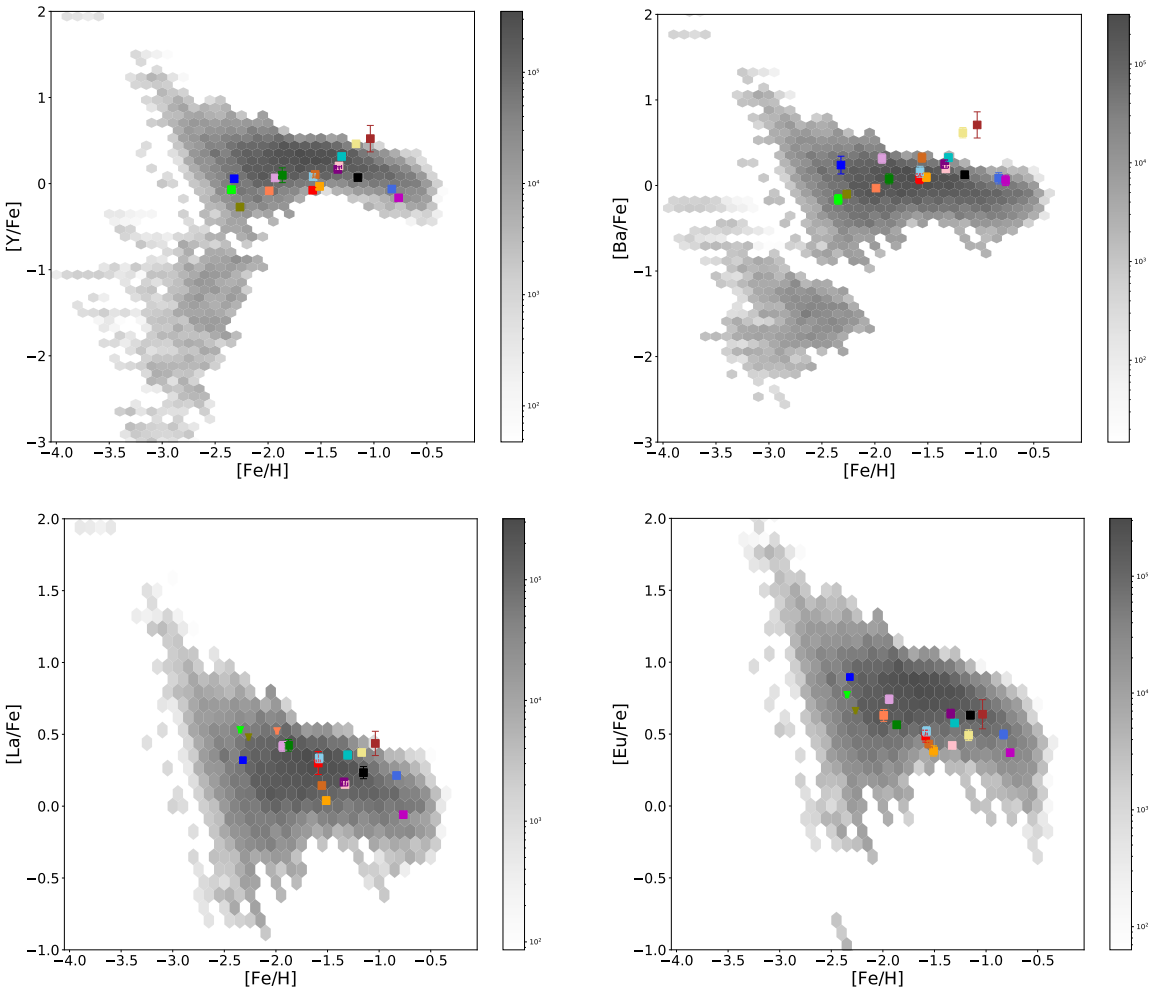

Figure 5.15 Comparison of our results with the chemical enrichment models of the Galactic halo from Cescutti and Chiappini (2014). In particular, we compared our results for [Y/Fe] (upper left panel), [Ba/Fe] (upper right panel), [La/Fe] (lower left panel), and [Eu/Fe] (lower right panel). The grey scale changes according to the number of stars in each bin, being darker for larger numbers. Coloured symbols follow the same description of Fig. 5.11.

5.3 Chemical abundance and cluster orbital energy

The birthplace of GCs leaves important information printed on GCs which is traceable through the analysis of both their chemical (Freeman and Bland-Hawthorn, 2002) and orbital properties (Horta et al., 2020). In the literature, both GCs born in-situ and accreted have been tried to be distinguished taking advantage of their different chemical signatures. For example, Fernández-Alvar et al. (2018) argues that the α-elements abundances are quite efficient in doing it. Similarly, Minelli et al. (2021) proposed iron-peak elements as a tracer of the origin of metal-rich stars.

In the present section, the abundance of n-capture elements is compared to the specific orbital energy (SOE) determined by Woody and Schlaufman (2021), who used the MW potential described by Bovy (2015) Woody and Schlaufman (2021) has 16 GCs in common with the present work. The Fig. 5.16 displays the abundances reported for Y, Ba, La, and Eu as a function of the SOE. In addition, the GCs are identified as in-situ (squares symbols) or ex-situ (circles symbols) according to the results given by Massari et al. (2019). It is worth noticing, that in the cited article, ex-situ GCs were associated with the Gaia-Enceladus stream. GCs with an uncertain origin and GCs with upper limits are represented with stars and empty symbols, respectively.

Interestingly, the results show that in-situ and ex-situ GCs behave in different fashions. According to the figure, in-situ GCs display a steeper negative correlation between the abundance of the different n-capture elements and their SOE compared to the flatter distribution found in the ex-situ ones. Although one could think that this trend is driven by NGC 6171 and its apparent overabundance in Y and Ba, the trend is also found in La and Eu –which are scarcely affected by uncertainties associated with V_m– in which the cluster behaves similarly to the other GCs.

To investigate this intriguing negative correlation and disentangle potential trends with stellar parameters, we can look at how the correlation behaves with respect to metallicity and V_m. Fig. 5.17 shows the same plot but colour-coded by the cluster metallicity. For Ba and Y there seems to be a trend with metallicity, as the most metal-rich ones have systematically higher abundances of these elements. As each of the clusters

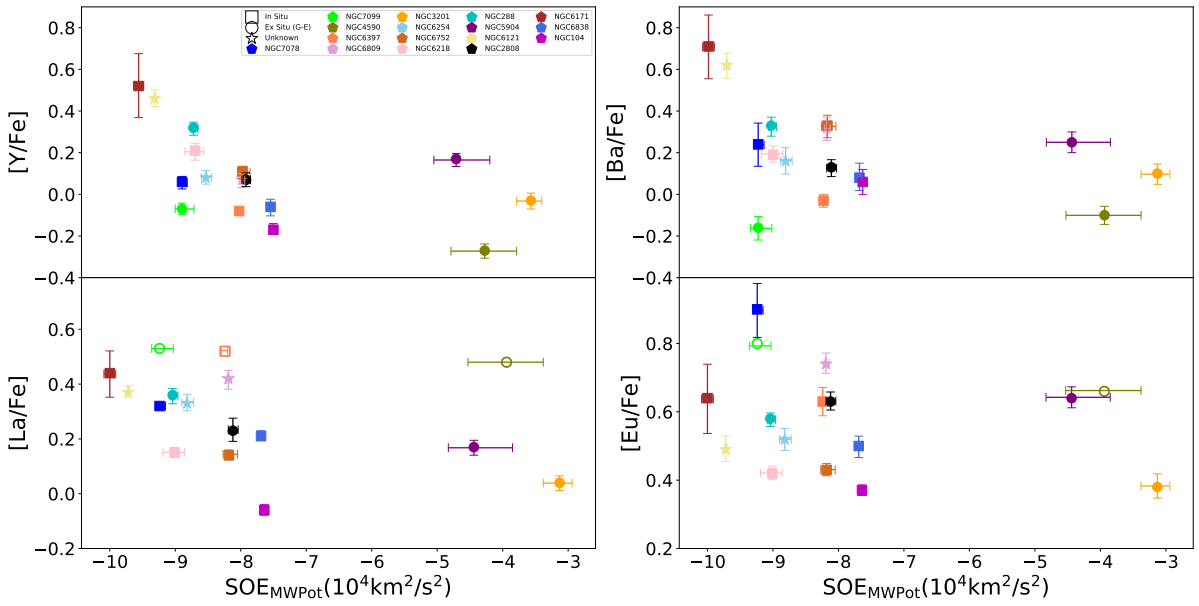

Figure 5.16 Y, Ba, La, and Eu abundances as a function of the specific orbital energy for every cluster in common with Woody and Schlaufman (2021). The potential used was the MW potential from Bovy (2015).

spans approximately the same evolutionary range, the Ba and Y transitions in metal-rich clusters are more likely to be saturated and measurements of abundances from them might potentially be affected by systematic errors. It is however worth noticing that this effect would not affect the observed trend with SOE and that in any case, the overall pattern as a function of metallicity is in good agreement with the field.

Fig. 5.18 shows the figure colour-coded by the maximum difference of V_m (ΔV_m) within each cluster. This difference seems to be quite homogeneous along the cluster with only two outliers. This suggests that the trend is not caused by different ranges in V_m. In fact, most of the GCs have a similar ΔV_m suggesting that V_m affect all these clusters similarly, then V_m is not the factor which drives the trend.

The potentially different chemical enrichment in n-capture elements between in-situ and accreted GCs will be further analysed in the future by comparing them with chemical evolution models.

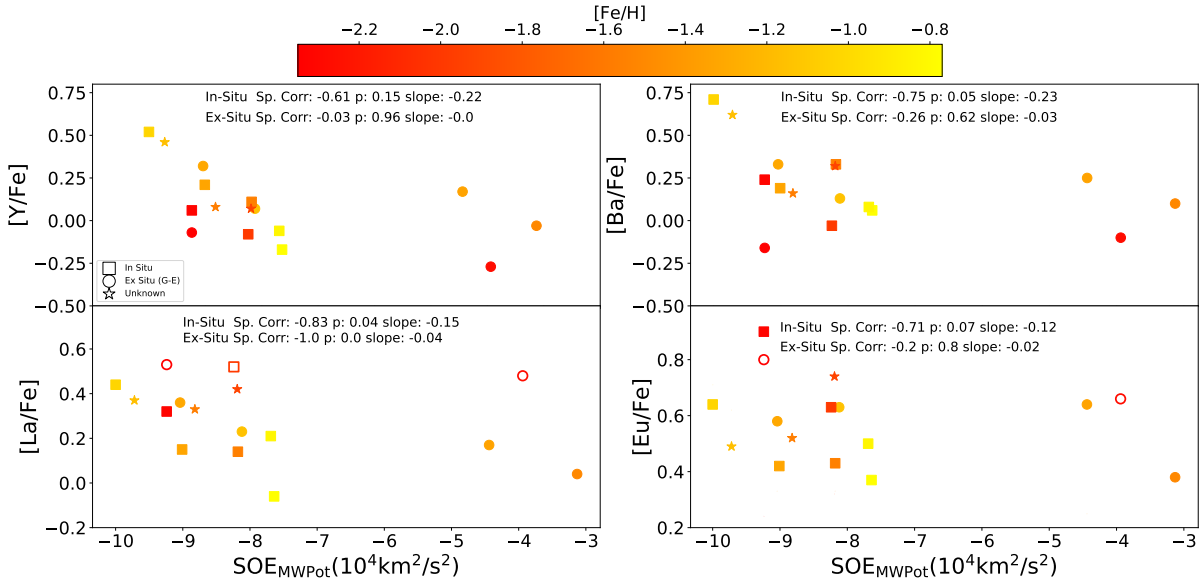

Figure 5.17 Y, Ba, La, and Eu abundances as a function of the specific orbital energy for every cluster in common with Woody and Schlaufman (2021). The potential used was the MW potential from Bovy (2015). Symbols follow the same description as Fig. 5.16. Error bars were not plotted for the clearness of the plot, but they follow the ones shown in Fig. 5.16.

5.4 Chemical abundances and cluster mass

Several studies have been done comparing the abundance patterns of GCs with global properties such as cluster mass. For example, Masseron et al. (2019) analysed a sample of 885 GC stars and they found evidence of a correlation of the Al spread present in GCs with the cluster mass. The latter suggested that the Mg-Al reaction decreases its importance in more massive GCs. It is interesting to perform a similar analysis using the n-capture element abundance. To do so, a comparison was performed against the absolute magnitude (MV_t), which is a proxy for the cluster mass. The MV_t were obtained from the Harris Catalog (Harris, 2010). The IQR for Y, Ba, La, and Eu can be seen in Fig. 5.19. All the mentioned IQRs display a quite flat distribution with a quite constant spread along the MV_t, meaning there is no evidence of any trends with cluster mass neither in s-process species nor Eu abundances. Hence, we find no evidence that cluster mass does play a role in retaining n-capture-enriched material.

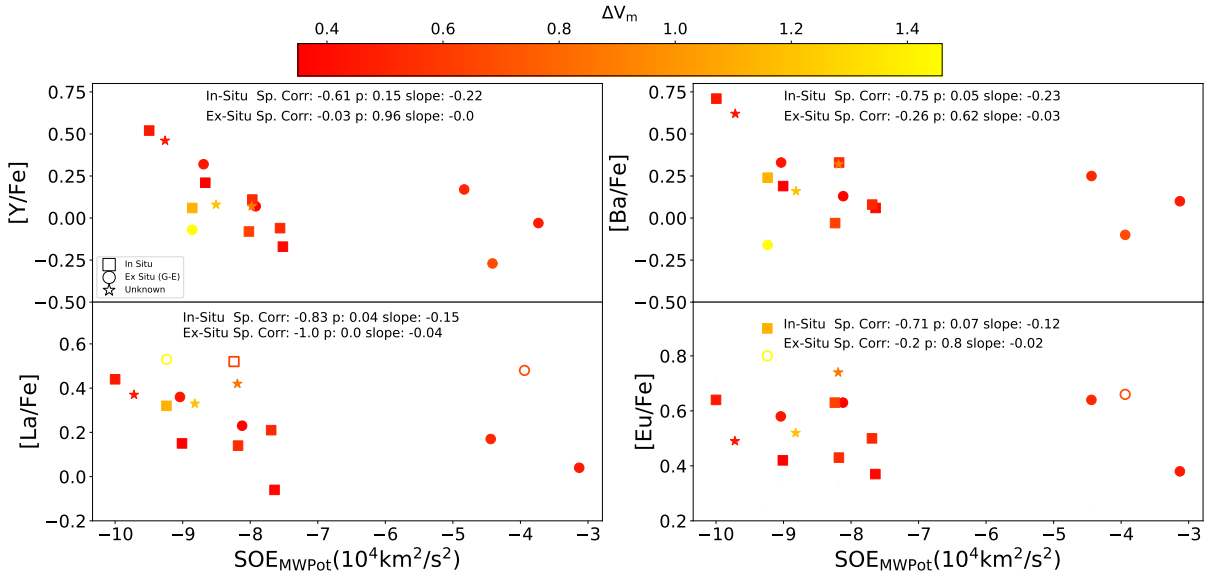

Figure 5.18 Y, Ba, La, and Eu abundances as a function of the specific orbital energy for every cluster in common with Woody and Schlaufman (2021). The potential used was the MW potential from Bovy (2015). Symbols follow the same description as Fig. 5.16. Error bars were not plotted for the clearness of the plot, but they follow the ones shown in Fig. 5.16.

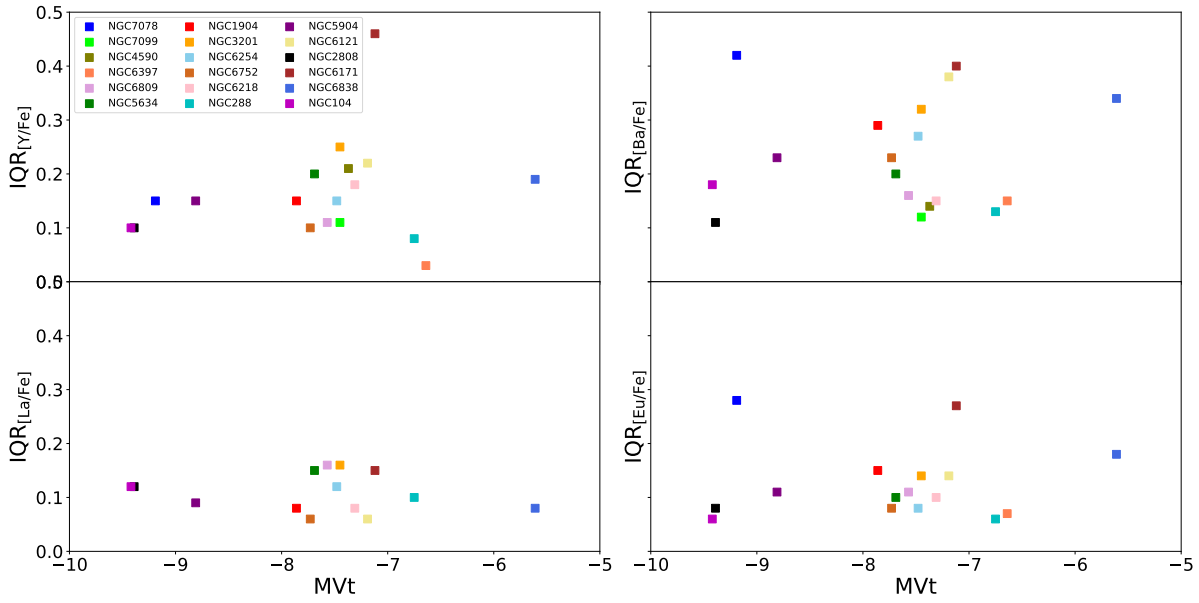

Figure 5.19 IQRs for Y, Ba, La, and Eu abundances as a function of the absolute visual magnitude for the whole sample. The MV_t were taken from the Harris Catalog (Harris, 2010).

Chapter 6

Summmary and Conclusions

The present thesis probes the phenomenon of multiple stellar populations in GCs looking at Li and n-capture elements. First, 217 dwarf and giant stars of the metal-poor GC NGC 6752 were analysed through spectrum synthesis to derive homogeneous abundances of Li, Na, Mg, Al, Ca, Sc, Cu, Y, and Ba plus upper limits for O and Eu. These species were studied to shed light on the polluter(s) responsible for the chemical patterns observed in SG stars in the cluster and, if possible, to study potential relations between hot H-burning and s-process elements. The latter can provide further constraints on the nature of the polluter(s) responsible for the chemical features found in SG stars in NGC 6752.

Because the sample covers both dwarves and giants, a uniform scale of stellar parameter determination was required. The sample shares 126 stars with G14, and we are in good agreement with their findings, with differences consistent with the slightly different temperature scale adopted.

The abundances of elements such as Mg, Ca, and Sc showed that the sample follows the expected field distribution at the metallicity of the cluster. Ca and Sc show no significant spread in the sample confirming previous results in the literature. As it is expected, Mg measurements display a larger spread, which anti-correlates with Na and Al results, which are in good agreement with the literature. This behaviour is a typical signature of the MSP phenomenon produced by polluters undergoing nucleosynthesis

typical of high temperatures of H-burning. Still, the temperature did not reach the point to involve heavier elements such as Ca or Sc. Unfortunately, because we could only set upper limits in O, we could not probe the well-studied Na-O anti-correlation.

Cu shows a quite constant abundance within the error and follows the field pattern at the same metallicity. Cu abundances do not display any correlation either with Na or Mg or with heavier elements.

We reported 153 Li measurements and 64 upper limits. Additionally, we reported 183 Al upper limits. The aluminium measurements were possible only in a small fraction of the sample (34 stars) where the Al line was strong enough to be detected. Although the sample is quite small, the Al distribution does not seem to be bi-modal, although, it cannot be discarded.

The Li abundances have an overall decrease from the TO to the RGB. The drop is expected because of stellar evolution. To disentangle the last effect from the MSP phenomenon in evolved stars, we defined Δ(Li). In this way, we could detect the presence of a Li-Al anti-correlation, which was also found in unevolved stars.

We explored the possible iron spread in the FG sample, as suggested by Legnardi et al. (2022). Although, we found a similar Fe spread among the FG stars of the sample. Differential analysis of four FG stars with similar stellar parameters ($\Delta T_{\rm eff}$=25 K) showed a Fe spread (Δ[Fe/H]=0.07 dex), which is within the associated errors. Interestingly, those stars showed a significant Li spread, which should have been present since the cluster's birth. Nevertheless, this hint should be taken with caution due to the small sample.

We detect Li-rich stars among both first- and second-generation stars, with generations defined on the bases of Na and Al as in (Carretta et al., 2009) and (Carretta et al., 2012), respectively.

The detection of Li-rich and Li-poor stars among SG (Al-rich) stars indicates the need for Li production, which is known to happen in AGB stars. Nevertheless, the latter result does not provide any insight into whether or not other sources of self-pollution (e.g., FRMS, supermassive stars, or massive binaries) were involved in the chemical evolution of the cluster. In addition, while Li content in SG stars implies that AGB

stars have contributed to the pollution of the SG stars in NGC 6752, it is not enough to constrain their nature.

As a representative of the first peak s-process element, [Y/Fe]II was analysed and we detected a strong correlation with the adopted V_m, which we minimised by using the mean weighted by their errors of all 3 Y II lines detectable in the spectra. We found a mildly significant [Y/Fe]II spread in the sample considering the associated errors. The analysis of Y II with Li, Na, Mg, and Al does not reveal any correlation, meaning that the results are not compatible with the considerable pollution of Y II in SG stars.

As a representative of the second peak s-process elements, we measured the Ba content in the sample, which shows a marginally significant spread in its distribution. The study of Ba together with Na, Mg, and Al does not show any difference between FG and SG stars, meaning that considerable Ba production in the polluters can be excluded. Additionally, we reported an FG star with particularly high Ba and Y abundances, likely a CH star.

According to models, intermediate-mass AGB stars are expected to have some production of s-process elements, which could be reflected in the spread that we found in these species. However, the comparison with the results reflects that the pollution of Y II and Ba II should be quite modest if any, and it could possibly be consistent with the predictions from the higher mass end available in the models considered (5-6 Msun). However, we cannot exclude the contribution of AGB stars of higher masses (up to $8\mathrm{M}_{\odot}$), due to the lack of models predicting the heavy element production in these stars. Furthermore, we did not find any relation in the Y II and Ba II content between the Li-rich SG and Li-poor SG stars suggesting that the Li necessary to reproduce the observed patterns is produced independently from Y and Ba.

We then analysed 210 UVES spectra of RGB stars belonging to 18 GCs with a large range of metallicities. The sample previously studied by Carretta et al. (2009) and Carretta et al. (2017), which were mainly focused on the determination of hot H-burning elements. For homogeneity, the present thesis used the same stellar parameters as in the mentioned articles to extend the analysis to Cu, Y, Ba, La, and Eu aiming to study the overall behaviour of n-capture elements in GCs. In addition to the latter, the thesis

aims to analyse the potential trend in the production of the enriched hot H-burning and s-process elements.

As was done for the NGC 6752, we developed an approach to account for the effect of V_m on the measured abundances. The abundances of Y, Ba, La, and Eu are generally quite constant in every GCs. The larger spread in Y and Ba for some clusters is attributed to the trends with V_m, which could not be completely removed.

The distribution of heavy elements (Y, Ba, La, and Eu) along with the metallicity was compared with field stars. Heavy elements in GCs display the same distribution as field stars, meaning that GCs have the same chemical enrichment and do not show considerable spread in the elements considered. A special case was found for NGC 7078 which displays the largest spread in heavy elements. The latter is in good agreement with the literature and it has been attributed to an initial spread in r-process enrichment.

The distribution with respect to the field, two GCs (NGC 6121 and NGC 6171) had a Y and Ba abundance over the field star patterns. A further examination revealed that the spread in their Y and Ba abundances is at least partially due to the V_m. However, a line-to-line comparison of stars with similar stellar parameters revealed a real spread in the abundances reported in both clusters.

In the same fashion as field stars, the [Ba/Eu] ratio in GCs shows a continuous s-process enrichment over time revealing that at the beginning (low metallicities) both field stars and GCs were mainly enriched by r-process sources, while at higher metallicities, the contribution of s-process sources (like AGB of different masses) becomes more important.

In addition, the present thesis analysed the Y and Ba abundances along with the Na abundances for the whole sample to study their overall behaviour in GCs. To do so, the sample was divided into three metallicity bins. In the mid-metallicity regime (-1.10 dex < [Fe/H] < -1.80 dex) there is a correlation in both Y and Ba with Na with a high significance. Although the trend is low, it could imply a modest production of these s-process elements with the same nucleosynthetic site where Na is produced. It is worth noticing that NGC 7078 was not considered due to its peculiar r-process enrichment.

We compared our results for Y, Ba, La, and Eu with the chemical enrichment models presented by Cescutti and Chiappini (2014). The model considered a chemical enrichment of the halo due to the contribution of MRD SNe and FRMS as the main contributors of the r- and s-process elements, respectively. The mentioned model reproduced closely the results obtained in this thesis.

The comparison between the n-capture abundances measured in the sample with the specific orbital energy shows that tighter-bound gravitational clusters display a slightly larger spread in s-process elements than the one shown for Eu. Secondly, according to the previous classification from Horta et al. (2020), GCs labelled as in-situ showed a larger correlation between the n-capture abundance and their SOE reported, meaning tighter bound GCs have higher n-capture element abundances than GCs labelled as accreted which show a flatter distribution.

Chapter 7

Future Perspectives

The work presented in this thesis sets the stage for some further investigations, that have been only briefly mentioned as they were beyond the original scope of the thesis. They are, however, of great interest in this context and are part of the plans for my future work.

7.1 Ba-rich stars

In the literature has been reported stars (e.g., D'Orazi et al., 2010) with particular abundances pattern of n-capture elements are not expected for low-mass single stars. The so-called Ba-stars, and their metal-poor counterparts CH-stars, are characterised by strong CH, and CN lines, but also enhanced s-process abundances. They are known to be part of binary systems, where the primary was a low-mass (1.5-4.0$M_{\odot}$) AGB star, which evolved long ago and is now a faint white dwarf. After its AGB phase, such a star transferred mass to the secondary –the star we are now observing (McClure, 1984)–, enriching the latter's atmosphere with shell nucleosynthesis products of low-mass AGB, notably C and s-process elements.

Ba- and CH-stars are the perfect objects to get insight into the nucleosynthesis of AGB stars themselves and even more so those in GCs. The CH, CN, and s-process element

features can give us important clues to constrain the nature of the former AGB star. For example, because the s-process nucleosynthesis depends on the neutron density of the star, being higher in intermediate-mass AGB stars, which leads to an overproduction of Rb with respect to Sr and Zr, then it can be an important mass indicator of the former star (Karakas et al., 2012).

Moreover, an important constraint can be set by analysing the ratios of first- and second-peak s-process elements, which provide additional indications of the former AGB star mass. This is possible as the ratios of s-process elements (as indexed among each other e.g. [Ba/Y] or [Pb/Ba] etc) in the atmosphere of the CH/Ba-star essentially reflect that in the AGB star, it received a mass transfer from (Cseh et al., 2022). The study of other chemical species, including C and N, on the other hand, requires assumptions on the initial (pre-mass transfer) composition of the observed star, generally assumed to match that of field stars, an approach that, however, hampers the reliability of the derived results.

There have been many studies of these stars, with the vast majority targeting field stars. A CH-star catalogue was published by Bartkevicius (1996), however, it contained just a handful of GCs. The list was enlarged (e.g., Cote et al., 1996, D'Orazi et al., 2010) arising the numbers to ∼20 stars in about 10 GCs. In particular, D'Orazi et al. (2010) reported four out of five Ba-rich stars to belong to the FG stars. Being part of binary systems supports the idea that the binary fraction is higher in FG than in SG stars (Lucatello et al., 2015) in GCs., which are formed in denser environments. No high-resolution, detailed chemical characterization exists for Ba/CH stars in GCs.

In this regard, GCs present a unique chance to study these objects in great detail not just because we can determine the stellar parameters with higher accuracy than most field stars, but also because the initial composition of the Ba star before the mass transfer is well known, as it shares it with all FG stars in the cluster. For those reasons, an extended and homogeneous analysis of these kinds of stars in GCs can provide a better understanding of the nucleosynthesis in low- and intermediate-mass AGB stars in population II. In this sense, the chemical characterisation can be directly compared –via differential analysis– with at least one template star which is a non-Ba-rich counterpart belonging to the FG, with the same stellar parameters. The advantage of this

analysis is the error minimisation, and the fact of using the result of Ba-normal FG stars as the pre-mass transfer composition of the Ba-stars will allow a more meaningful comparison with models (e.g., FRUITY Cristallo et al., 2011).

7.2 N-capture enrichment on different stellar populations

In the present thesis, we analysed for the first time in a homogeneous large sample of GCs with a large range of metallicities the abundances of different s-process and r-process elements along the Na content.

GCs such as NGC 7078, NGC 6171, and NGC 6121 have shown dispersion in n-capture elements which are not necessarily related to the MSP phenomenon, but to a particular r- or s-process enrichment.

As concluded from both the individual analysis of the GC NGC 6752 and the overall distribution of the 18 GCs analysed, there are no significant correlations between the Y and Ba content along the different populations. However, from the middle panel of Fig.5.10, there is an intriguing suggestion of a significant trend between the mentioned species. Although the correlation is weak, if there is at least modest production of Y and Ba in the polluter responsible for the Na enrichment in GCs. In the near future, we are going to look at the sample of 18 GCs, a pair of stars with similar stellar parameters and Na, but different n-capture content aiming to shed light on this suggestion. Some such pairs are already in the sample and they will be analysed through a differential analysis. The sample will be enlarged by requiring observing time for new couples.

Appendix A

Abundance Determination

TABLE A.1: Stellar parameters and their respective errors for the NGC 6752 sample. I adopted the [Fe/H] from C09.

Ids	$T_{\rm eff}$	σ	$\log g$	σ	[Fe/H]	σ	V_m	σ
3860	6040	69	3.9	0.06	-1.56	0.01	0.96	0.02
3849	6084	38	3.9	0	-1.56	0.01	0.96	0
3790	6057	38	3.9	0	-1.56	0.01	0.96	0
3778	6129	22	3.97	0	-1.56	0.01	0.94	0
3747	6168	68	3.97	0	-1.56	0.01	0.94	0
3726	6159	29	3.97	0	-1.56	0.01	0.94	0
3689	6162	119	3.97	0.06	-1.56	0.01	0.94	0.02
3624	6013	45	3.9	0.06	-1.56	0.01	0.96	0.02
3623	6211	114	4.03	0.06	-1.56	0.01	0.92	0.02
3611	6119	25	3.97	0	-1.56	0.01	0.94	0
3610	6100	37	3.97	0.06	-1.56	0.01	0.94	0.02
3609	6153	44	3.97	0	-1.56	0.01	0.94	0
3578	6036	73	3.9	0.06	-1.56	0.01	0.96	0.02
3577	6147	43	3.97	0	-1.56	0.01	0.94	0
3570	6179	24	4.03	0.06	-1.56	0.01	0.92	0.02
3561	5940	195	3.84	0.12	-1.56	0.01	0.98	0.04

Continued on next page

Table A.1 – continued from previous page

Ids	$T_{\rm eff}$	σ	$\log g$	σ	[Fe/H]	σ	V_m	σ
3547	6147	34	3.97	0	-1.56	0.01	0.94	0
3535	6095	132	3.97	0.12	-1.56	0.01	0.94	0.04
3526	6126	88	3.97	0.06	-1.56	0.01	0.94	0.02
3516	6070	24	3.9	0	-1.56	0.01	0.96	0
3504	6081	82	3.9	0	-1.56	0.01	0.96	0
3478	6096	42	3.97	0.06	-1.56	0.01	0.94	0.02
3468	6029	18	3.9	0	-1.56	0.01	0.96	0
3446	6065	36	3.9	0	-1.56	0.01	0.96	0
3428	6111	82	3.97	0.06	-1.56	0.01	0.94	0.02
3414	6121	24	3.97	0	-1.56	0.01	0.94	0
3401	6097	84	3.97	0.06	-1.56	0.01	0.94	0.02
3371	5928	21	3.84	0	-1.56	0.01	0.98	0
3326	6099	30	3.97	0.06	-1.56	0.01	0.94	0.02
3311	6027	64	3.9	0.06	-1.56	0.01	0.96	0.02
3302	5960	36	3.84	0	-1.56	0.01	0.98	0
3297	6051	49	3.9	0	-1.56	0.01	0.96	0
3295	6025	32	3.9	0	-1.56	0.01	0.96	0
3285	6002	20	3.9	0.06	-1.56	0.01	0.96	0.02
3279	6005	22	3.9	0.06	-1.56	0.01	0.96	0.02
3270	6050	26	3.9	0	-1.56	0.01	0.96	0
3265	6089	80	3.9	0	-1.56	0.01	0.96	0
3253	5993	60	3.84	0	-1.56	0.01	0.98	0
3232	6037	81	3.9	0.06	-1.56	0.01	0.96	0.02
3230	6022	72	3.9	0.06	-1.56	0.01	0.96	0.02
3228	5916	25	3.84	0	-1.56	0.01	0.98	0
3203	5886	36	3.79	0	-1.56	0.01	1	0
3190	5994	18	3.9	0.06	-1.56	0.01	0.96	0.02
3176	5927	92	3.84	0.06	-1.56	0.01	0.98	0.02
3174	5919	28	3.84	0	-1.56	0.01	0.98	0

Continued on next page

Table A.1 – continued from previous page

Ids	$T_{\rm eff}$	σ	$\log g$	σ	[Fe/H]	σ	V_m	σ
3171	6014	26	3.9	0.06	-1.56	0.01	0.96	0.02
3134	5985	46	3.84	0	-1.56	0.01	0.98	0
3131	5847	81	3.79	0.06	-1.56	0.01	1	0.02
3116	5810	20	3.79	0	-1.56	0.01	1	0
3111	5967	27	3.84	0	-1.56	0.01	0.98	0
3081	5954	16	3.84	0	-1.56	0.01	0.98	0
3061	5846	70	3.79	0	-1.56	0.01	1	0
3057	5928	53	3.84	0.06	-1.56	0.01	0.98	0.02
3031	6020	69	3.9	0.06	-1.56	0.01	0.96	0.02
3021	6004	38	3.9	0.06	-1.56	0.01	0.96	0.02
3002	5894	33	3.84	0.06	-1.56	0.01	0.98	0.02
2997	5897	71	3.84	0.06	-1.56	0.01	0.98	0.02
2996	5786	30	3.79	0.06	-1.56	0.01	1	0.02
2994	5932	99	3.84	0.06	-1.56	0.01	0.98	0.02
2984	5949	22	3.84	0	-1.56	0.01	0.98	0
2948	5871	20	3.79	0	-1.56	0.01	1	0
2921	5899	77	3.84	0.06	-1.56	0.01	0.98	0.02
2905	5926	41	3.84	0.06	-1.56	0.01	0.98	0.02
2897	5903	234	3.84	0.12	-1.56	0.01	0.98	0.04
2888	5929	58	3.84	0.06	-1.56	0.01	0.98	0.02
2877	5902	82	3.84	0.06	-1.56	0.01	0.98	0.02
2875	5735	35	3.72	0	-1.56	0.01	1.02	0
2872	5818	15	3.79	0	-1.56	0.01	1	0
2847	5784	19	3.79	0.06	-1.56	0.01	1	0.02
2794	5711	34	3.72	0	-1.56	0.01	1.02	0
2773	5808	57	3.79	0.06	-1.56	0.01	1	0.02
2759	5756	17	3.72	0	-1.56	0.01	1.02	0
2743	5715	33	3.72	0	-1.56	0.01	1.02	0
2742	5770	24	3.72	0	-1.56	0.01	1.02	0

Continued on next page

Table A.1 – continued from previous page

Ids	$T_{\rm eff}$	σ	$\log g$	σ	[Fe/H]	σ	V_m	σ
2646	5359	35	3.26	0.11	-1.56	0.01	1.17	0.04
2627	5653	35	3.66	0	-1.56	0.01	1.04	0
2616	5602	28	3.66	0.04	-1.56	0.01	1.04	0.01
2610	5627	80	3.66	0.05	-1.56	0.01	1.04	0.02
2601	5631	37	3.66	0	-1.56	0.01	1.04	0
2597	5641	21	3.66	0	-1.56	0.01	1.04	0
2575	5566	26	3.62	0.01	-1.56	0.01	1.05	0
2571	5472	22	3.54	0.06	-1.56	0.01	1.08	0.02
2569	5640	74	3.66	0.04	-1.56	0.01	1.04	0.01
2556	5623	27	3.66	0	-1.56	0.01	1.04	0
2546	5541	19	3.61	0.06	-1.56	0.01	1.06	0.02
2535	5613	12	3.66	0	-1.56	0.01	1.04	0
2517	5567	19	3.62	0.01	-1.56	0.01	1.05	0
2497	5544	21	3.61	0.06	-1.56	0.01	1.06	0.02
2479	5498	55	3.55	0.07	-1.56	0.01	1.08	0.02
2476	5586	14	3.62	0	-1.56	0.01	1.05	0
2472	5513	11	3.55	0	-1.56	0.01	1.08	0
2445	5594	40	3.66	0.05	-1.56	0.01	1.04	0.02
2414	5378	26	3.32	0.06	-1.56	0.01	1.15	0.02
2396	5332	35	3.2	0.1	-1.56	0.01	1.19	0.03
2391	5392	34	3.38	0.12	-1.56	0.01	1.13	0.04
2370	5387	34	3.32	0.06	-1.56	0.01	1.15	0.02
2337	5363	16	3.26	0.06	-1.56	0.01	1.17	0.02
2334	5387	41	3.32	0.12	-1.56	0.01	1.15	0.04
2280	5354	22	3.26	0.06	-1.56	0.01	1.17	0.02
2275	5334	63	3.2	0.21	-1.56	0.01	1.19	0.07
2246	5385	26	3.32	0.06	-1.56	0.01	1.15	0.02
2245	5387	18	3.32	0.06	-1.56	0.01	1.15	0.02
2224	5354	30	3.26	0.11	-1.56	0.01	1.17	0.04

Continued on next page

Table A.1 – continued from previous page

Ids	$T_{\rm eff}$	σ	$\log g$	σ	[Fe/H]	σ	V_m	σ
2211	5339	29	3.2	0.1	-1.56	0.01	1.19	0.03
2208	5289	12	3.04	0	-1.56	0.01	1.24	0
2176	5389	22	3.32	0.06	-1.56	0.01	1.15	0.02
2169	5317	13	3.14	0.05	-1.56	0.01	1.21	0.01
2151	5348	21	3.2	0.06	-1.56	0.01	1.19	0.02
2129	5374	23	3.32	0.06	-1.56	0.01	1.15	0.02
2117	5345	17	3.2	0.06	-1.56	0.01	1.19	0.02
2113	5376	35	3.32	0.12	-1.56	0.01	1.15	0.04
2110	5334	12	3.2	0.06	-1.56	0.01	1.19	0.02
2090	5339	15	3.2	0.06	-1.56	0.01	1.19	0.02
2089	5356	51	3.26	0.16	-1.56	0.01	1.17	0.05
2078	5372	57	3.32	0.18	-1.56	0.01	1.15	0.06
2027	5359	15	3.26	0.06	-1.56	0.01	1.17	0.02
2014	5345	12	3.2	0	-1.56	0.01	1.19	0
201217	5383	34	3.32	0.06	-1.56	0.01	1.15	0.02
201002	5523	36	3.55	0.01	-1.56	0.01	1.08	0
1983	5313	15	3.14	0.05	-1.56	0.01	1.21	0.01
1980	5311	56	3.1	0.17	-1.56	0.01	1.22	0.06
1976	5253	23	2.93	0.06	-1.56	0.01	1.28	0.02
1958	5350	24	3.26	0.11	-1.56	0.01	1.17	0.04
19113655-5959432	6116	71	3.97	0.06	-1.56	0.01	0.94	0.02
19113403-5957497	6100	57	3.97	0.06	-1.56	0.01	0.94	0.02
19113393-5958107	6224	70	4.03	0.06	-1.56	0.01	0.92	0.02
19113298-5958411	5113	16	2.59	0.05	-1.56	0.01	1.39	0.02
19113168-5957130	6147	67	3.97	0.06	-1.56	0.01	0.94	0.02
19113088-5957430	6194	72	4.03	0.06	-1.56	0.01	0.92	0.02
19113087-5958477	6108	53	3.97	0.06	-1.56	0.01	0.94	0.02
19113071-6003234	5196	35	2.81	0.11	-1.56	0.01	1.31	0.04
19112987-5956098	6266	67	4.07	0.04	-1.56	0.01	0.91	0.01

Continued on next page

Table A.1 – continued from previous page

Ids	$T_{\rm eff}$	σ	$\log g$	σ	[Fe/H]	σ	V_m	σ
19112818-6000436	6150	104	3.97	0.06	-1.56	0.01	0.94	0.02
19112749-5958445	6215	120	4.03	0.06	-1.56	0.01	0.92	0.02
19112720-5955225	5977	65	3.84	0	-1.56	0.01	0.98	0
19112587-5958553	6159	69	3.97	0.06	-1.56	0.01	0.94	0.02
19112451-6000104	6153	82	3.97	0.06	-1.56	0.01	0.94	0.02
19112339-6001385	6072	68	3.9	0	-1.56	0.01	0.96	0
19112258-6002380	6246	92	4.05	0.09	-1.56	0.01	0.91	0.03
19112132-5956542	6039	30	3.9	0	-1.56	0.01	0.96	0
19112091-6002411	6199	62	4.03	0.06	-1.56	0.01	0.92	0.02
19112071-5956287	6058	44	3.9	0	-1.56	0.01	0.96	0
19112070-6001057	6128	40	3.97	0.06	-1.56	0.01	0.94	0.02
19111828-6000139	5231	34	2.87	0.06	-1.56	0.01	1.3	0.02
19111644-6002253	6251	88	4.07	0.1	-1.56	0.01	0.91	0.03
19111612-5954443	6153	66	3.97	0.06	-1.56	0.01	0.94	0.02
19111338-6002243	6093	51	3.97	0.06	-1.56	0.01	0.94	0.02
19111078-5956406	5093	33	2.54	0.05	-1.56	0.01	1.4	0.02
19111018-5954267	5088	14	2.54	0.05	-1.56	0.01	1.4	0.02
19110907-5955546	5144	31	2.65	0.06	-1.56	0.01	1.37	0.02
19110863-5957569	5121	20	2.59	0.05	-1.56	0.01	1.39	0.02
19110798-6003588	6118	46	3.97	0.06	-1.56	0.01	0.94	0.02
19110785-5954515	6096	62	3.97	0.06	-1.56	0.01	0.94	0.02
19110616-6002522	6204	43	4.03	0.06	-1.56	0.01	0.92	0.02
19110598-5959013	5052	18	2.43	0	-1.56	0.01	1.44	0
19110533-5953490	6161	68	3.97	0	-1.56	0.01	0.94	0
19110501-5955274	5233	17	2.87	0	-1.56	0.01	1.3	0
19110429-6002404	6208	83	4.03	0.06	-1.56	0.01	0.92	0.02
19110207-5956317	6165	81	3.97	0.06	-1.56	0.01	0.94	0.02
19110152-6003444	6066	25	3.9	0	-1.56	0.01	0.96	0
19110151-6002511	6114	28	3.97	0.06	-1.56	0.01	0.94	0.02

Continued on next page

Table A.1 – continued from previous page

Ids	$T_{\rm eff}$	σ	$\log g$	σ	[Fe/H]	σ	V_m	σ
19110105-6004103	6087	27	3.9	0	-1.56	0.01	0.96	0
19110081-6005092	6319	102	4.2	0.17	-1.56	0.01	0.87	0.06
19110011-6006045	6083	83	3.9	0	-1.56	0.01	0.96	0
19105996-5959271	5129	19	2.65	0.06	-1.56	0.01	1.37	0.02
19105986-6002171	6094	23	3.97	0.06	-1.56	0.01	0.94	0.02
19105851-5955394	5210	59	2.81	0.11	-1.56	0.01	1.31	0.04
19105692-6000227	5093	14	2.54	0.05	-1.56	0.01	1.4	0.02
19105577-5957278	5225	21	2.87	0.06	-1.56	0.01	1.3	0.02
19105546-5953358	6191	70	4.03	0.06	-1.56	0.01	0.92	0.02
19105483-6003042	6093	29	3.97	0.06	-1.56	0.01	0.94	0.02
19105406-5958002	5202	8	2.81	0	-1.56	0.01	1.31	0
19105177-6000390	5105	13	2.59	0.05	-1.56	0.01	1.39	0.02
19105158-5954184	6228	69	4.05	0.09	-1.56	0.01	0.91	0.03
19105056-6006005	6165	45	3.97	0	-1.56	0.01	0.94	0
19104963-5953398	6283	82	4.12	0.1	-1.56	0.01	0.89	0.03
19104925-5954057	6281	78	4.12	0.1	-1.56	0.01	0.89	0.03
19104892-5958234	5125	17	2.59	0	-1.56	0.01	1.39	0
19104804-6002213	5191	13	2.76	0	-1.56	0.01	1.33	0
19104664-5954063	6018	59	3.9	0.06	-1.56	0.01	0.96	0.02
19104427-6004301	6129	22	3.97	0	-1.56	0.01	0.94	0
19104225-6004460	5099	11	2.54	0	-1.56	0.01	1.4	0
19103970-6001045	5101	9	2.54	0	-1.56	0.01	1.4	0
19103964-6003189	6211	59	4.03	0.06	-1.56	0.01	0.92	0.02
19103855-6003361	6162	22	3.97	0	-1.56	0.01	0.94	0
19103829-5955070	6283	89	4.12	0.1	-1.56	0.01	0.89	0.03
19103672-6002011	5308	50	3.1	0.11	-1.56	0.01	1.22	0.04
19103463-5956357	6123	35	3.97	0.06	-1.56	0.01	0.94	0.02
19102903-6002535	6176	38	3.97	0	-1.56	0.01	0.94	0
19102859-6003539	6120	53	3.97	0.06	-1.56	0.01	0.94	0.02

Continued on next page

Table A.1 – continued from previous page

Ids	$T_{\rm eff}$	σ	$\log g$	σ	[Fe/H]	σ	V_m	σ
19102726-5955194	6258	85	4.07	0.1	-1.56	0.01	0.91	0.03
19102685-5958251	5113	16	2.59	0.05	-1.56	0.01	1.39	0.02
19102677-6003089	6172	20	3.97	0	-1.56	0.01	0.94	0
19102675-5956553	6263	70	4.07	0.04	-1.56	0.01	0.91	0.01
19102577-6004439	5119	33	2.59	0.05	-1.56	0.01	1.39	0.02
19102525-5959409	5954	16	3.84	0	-1.56	0.01	0.98	0
19102415-6003445	5225	15	2.87	0.06	-1.56	0.01	1.3	0.02
19102395-5956202	6370	107	4.2	0.14	-1.56	0.01	0.87	0.04
19102370-6000209	5111	9	2.59	0.05	-1.56	0.01	1.39	0.02
19102328-6000498	6225	162	4.03	0.12	-1.56	0.01	0.92	0.04
19102293-6004232	6179	24	4.03	0.06	-1.56	0.01	0.92	0.02
19102223-5957192	6287	61	4.12	0.1	-1.56	0.01	0.89	0.03
19102204-5956597	6267	63	4.07	0.04	-1.56	0.01	0.91	0.01
19102158-5958179	6227	26	4.03	0	-1.56	0.01	0.92	0
19102135-6002166	6216	43	4.03	0.06	-1.56	0.01	0.92	0.02
19102025-5958306	5257	17	2.98	0.06	-1.56	0.01	1.26	0.02
19101923-5958596	6329	35	4.2	0.08	-1.56	0.01	0.87	0.02
19101748-6000324	6280	54	4.12	0.1	-1.56	0.01	0.89	0.03
19101652-6001094	6214	38	4.03	0.06	-1.56	0.01	0.92	0.02
19101610-6000035	6333	141	4.2	0.17	-1.56	0.01	0.87	0.06
19101589-6002252	6114	30	3.97	0.06	-1.56	0.01	0.94	0.02
19101000-5957525	6236	126	4.05	0.09	-1.56	0.01	0.91	0.03
19100961-5959534	6234	38	4.05	0.03	-1.56	0.01	0.91	0.01
19100576-6001009	6268	40	4.07	0.04	-1.56	0.01	0.91	0.01
1872	5276	15	3.04	0.06	-1.56	0.01	1.24	0.02
1846	5315	13	3.14	0.05	-1.56	0.01	1.21	0.01
1802	5383	44	3.32	0.12	-1.56	0.01	1.15	0.04

TABLE A.2: Abundances reported for the NGC 6752 sample.

Ids	f	Li	σ	f	[Al/Fe]	σ	f	[O/Fe]	f	[Na/Fe]	σ	f	[Mg/Fe]	σ	[Ca/Fe]	σ	[Sc/Fe]	σ	f	[Cu/Fe]	σ	f	[Y/Fe]	σ	f	[Ba/Fe]	σ	f	[Eu/Fe]
3860	<	1.79	0.08	<	0.89	0.1	<	–	<	0.02	0.11		0.06	0.27	–	–	–	–		–	0.1	<	-0.2	0.11	<	–	0.11	<	–
3849	<	1.48	0.06	<	0.79	0.1	<	–	<	0.25	0.11		0.31	0.11	–	–	–	–		–	0.1	<	0.3	0.11	<	–	0.11	<	-0.1
3790		2.21	0.06	<	-0.16	0.1	<	–	<	-0.42	0.11	<	0.35	0.11	–	–	–	–		–	0.1	<	–	0.11	<	–	0.11	<	0.1
3778		2.22	0.05	<	0.44	0.1	<	–	<	-0.19	0.11		0.2	0.11	–	–	–	–		–	0.1	<	0.1	0.11		0.25	0.12	<	–
3747		2.42	0.07	<	0.44	0.1	<	–	<	-0.09	0.11		0.17	0.11	–	–	–	–		–	0.1	<	0.48	0.11	<	–	0.11	<	–
3726		2.33	0.06	<	0.44	0.1	<	–	<	-0.5	0.11	<	0.65	0.11	–	–	–	–		–	0.1	<	–	0.11	<	–	0.11	<	–
3689		2.48	0.11	<	-0.26	0.1	<	–	<	–	0.11	<	–	0.11	–	–	–	–		–	0.1	<	–	0.11	<	–	0.11	<	1.1
3624		2.26	0.06	<	0.47	0.1	<	–		0.14	0.11		0.28	0.11	–	–	–	–		–	0.1	<	–	0.11	<	–	0.11	<	–
3623	<	2.43	0.1	<	1.12	0.1	<	–	<	0.23	0.11		0.25	0.11	–	–	–	–		–	0.1	<	0.18	0.11		0.2	0.12	<	–
3611		2.16	0.05	<	0.74	0.1	<	–	<	0.01	0.11	<	0.37	0.11	–	–	–	–		–	0.1	<	–	0.11	<	–	0.11	<	1.48
3610		2.16	0.06	<	0.24	0.1	<	–		0.2	0.02	<	0.35	0.11	–	–	–	–		–	0.1	<	0.4	0.11		0.21	0.12	<	0.2
3609	<	2.21	0.06	<	0.89	0.1	<	–		0.44	0.08		0.05	0.11	–	–	–	–		–	0.1	<	0.57	0.11		0.25	0.12	<	1.85
3578	<	1.95	0.08	<	0.34	0.1	<	–	<	–	0.11	<	–	0.11	–	–	–	–		–	0.1	<	–	0.11	<	–	0.11	<	–
3577		2.14	0.06	<	0.54	0.1	<	–		0.43	0.11	<	–	0.11	–	–	–	–		–	0.1	<	–	0.11	<	–	0.11	<	–
3570		2.3	0.05	<	-0.26	0.1	<	–	<	0.01	0.11		0.36	0.26	–	–	–	–		–	0.1	<	0.43	0.11	<	–	0.11	<	–
3561		2.13	0.16	<	0.21	0.11	<	–		0.53	0.18	<	–	0.11	–	–	–	–		–	0.1	<	–	0.11	<	–	0.11	<	–
3547		2.38	0.06	<	0.14	0.1	<	–		0.13	0.11		0.3	0.11	–	–	–	–		–	0.1	<	0.52	0.11	<	–	0.11	<	–
3535		2.37	0.12	<	0.89	0.1	<	–	<	–	0.11	<	–	0.11	–	–	–	–		–	0.1	<	–	0.11	<	–	0.11	<	–
3526		2.29	0.09	<	0.84	0.1	<	–		0.29	0.11	<	0.41	0.11	–	–	–	–		–	0.1	<	–	0.11	<	–	0.11	<	–
3516		2.25	0.05	<	-0.85	0.1	<	–	<	-0.04	0.11		0.45	0.11	–	–	–	–		–	0.1	<	0.08	0.11	<	–	0.11	<	0.00
3504		2.03	0.08	<	0.59	0.1	<	–	<	0.06	0.11		0.38	0.11	–	–	–	–		–	0.1	<	0.17	0.11	<	–	0.11	<	0.57
3478		2.37	0.06	<	0.34	0.1	<	–	<	-0.13	0.11		0.55	0.11	–	–	–	–		–	0.1	<	–	0.11	<	–	0.11	<	–
3468	<	2.09	0.05	<	-0.35	0.1	<	–	<	–	0.11	<	–	0.11	–	–	–	–		–	0.1	<	–	0.11	<	–	0.11	<	–
3446		2.28	0.06	<	0.6	0.1	<	–	<	-0.41	0.11		0.51	0.11	–	–	–	–		–	0.1	<	–	0.11	<	–	0.11	<	–
3428		2.21	0.08	<	-0.26	0.1	<	–		0.21	0.32		0.25	0.11	–	–	–	–		–	0.1		0.24	0.11		0.1	0.12	<	1.19
3414		2.34	0.05	<	0.34	0.1	<	–	<	-0.06	0.11	<	-0.2	0.11	–	–	–	–		–	0.1	<	–	0.11	<	–	0.11	<	0.1
3401		2.37	0.08	<	0.58	0.1	<	–		0.19	0.08		0.34	0.11	–	–	–	–		–	0.1	<	0.5	0.11		0.5	0.12	<	–
3371		2.19	0.05	<	0.01	0.1	<	–	<	-0.1	0.11		0.14	0.11	–	–	–	–		–	0.1	<	0.35	0.11	<	–	0.11	<	0.57
3326		2.29	0.06	<	0.6	0.1	<	–	<	-0.09	0.11		0.28	0.11	–	–	–	–		–	0.1	<	0.00	0.11	<	–	0.11	<	–
3311		2.43	0.07	<	-0.24	0.1	<	–	<	0.06	0.11		0.45	0.11	–	–	–	–		–	0.1	<	0.44	0.11		0.47	0.12	<	1.4
3302		2.31	0.06	<	0.59	0.1	<	–	<	-0.27	0.11	<	–	0.11	–	–	–	–		–	0.1	<	–	0.11	<	–	0.11	<	–
3297		2.06	0.06	<	-0.85	0.1	<	–	<	–	0.11	<	–	0.11	–	–	–	–		–	0.1	<	–	0.11	<	–	0.11	<	1.45

Continued on next page

Table A.2 – continued from previous page

Ids	f	Li	σ	f	[Al/Fe]	σ	f	[O/Fe]	f	[Na/Fe]	σ	f	[Mg/Fe]	σ	[Ca/Fe]	σ	[Sc/Fe]	σ	f	[Cu/Fe]	σ	f	[Y/Fe]	σ	f	[Ba/Fe]	σ	f	[Eu/Fe]
3295		2.23	0.06	<	-0.06	0.1	<	–	<	0.09	0.11		0.33	0.11	–	–	–	–		–	0.1	<	0.35	0.11		0.14	0.12	<	–
3285		2.29	0.05	<	-0.85	0.1	<	–		0.12	0.28		0.15	0.11	–	–	–	–		–	0.1	<	0.09	0.11		0.48	0.12	<	–
3279		2.24	0.05	<	0.64	0.1	<	–		0.38	0.11	<	–	0.11	–	–	–	–		–	0.1	<	0.15	0.11		0.49	0.12	<	–
3270		2.24	0.05	<	-0.85	0.1	<	–	<	-0.02	0.11	<	0.19	0.11	–	–	–	–		–	0.1	<	0.32	0.11	<	–	0.11	<	0.2
3265		2.33	0.08	<	0.49	0.1	<	–		0.26	0.24		0.38	0.11	–	–	–	–		–	0.1	<	0.54	0.11	<	–	0.11	<	-0.1
3253	<	2.31	0.07	<	0.54	0.1	<	–	<	–	0.11	<	–	0.11	–	–	–	–		–	0.1	<	0.27	0.11		0.4	0.12	<	-0.1
3232	<	2.12	0.08	<	0.08	0.1	<	–	<	–	0.11		0.42	0.11	–	–	–	–		–	0.1	<	0.16	0.11		0.4	0.12	<	1.28
3230	<	2.16	0.08	<	0.98	0.1	<	–	<	–	0.11	<	–	0.11	–	–	–	–		–	0.1	<	–	0.11	<	–	0.11	<	1.45
3228		2.19	0.05	<	-0.85	0.1	<	–	<	–	0.11	<	–	0.11	–	–	–	–		–	0.1	<	–	0.11	<	–	0.11	<	-0.1
3203		2.01	0.06	<	0.57	0.1	<	–		0.38	0.03		0.33	0.11	–	–	–	–		–	0.05	<	0.15	0.11	<	–	0.11	<	–
3190		2.08	0.05	<	0.14	0.1	<	–		0.07	0.11	<	–	0.11	–	–	–	–		–	0.1	<	–	0.11	<	–	0.11	<	–
3176		2.32	0.09	<	0.42	0.1	<	–	<	-0.12	0.11	<	0.51	0.11	–	–	–	–		–	0.1	<	0.1	0.11		0.5	0.12	<	–
3174		2.41	0.06	<	0.44	0.1	<	–	<	-0.39	0.11	<	–	0.11	–	–	–	–		–	0.1	<	0.19	0.11	<	–	0.11	<	–
3171		2.2	0.05	<	-0.14	0.1	<	–		0.15	0.11	<	–	0.11	–	–	–	–		–	0.1	<	0.34	0.11	<	–	0.11	<	0.35
3134		2.32	0.06	<	-0.45	0.1	<	–	<	-0.19	0.11		0.31	0.12	–	–	–	–		–	0.1	<	0.1	0.11	<	–	0.11	<	–
3131		2.22	0.08	<	-0.35	0.1	<	–		-0.04	0.11		0.43	0.11	–	–	–	–		–	0.05	<	-0.3	0.11	<	–	0.11	<	0.00
3116		2.25	0.05	<	-0.36	0.1	<	–	<	–	0.11	<	–	0.11	–	–	–	–		–	0.05	<	–	0.11	<	–	0.11	<	-0.1
3111		2.38	0.05	<	-0.37	0.1	<	–	<	-0.19	0.11		0.51	0.11	–	–	–	–		–	0.1	<	0.55	0.11		0.35	0.12	<	–
3081		2.19	0.05		0.57	0.1	<	–	<	-0.21	0.11	<	0.37	0.11	–	–	–	–		–	0.1	<	–	0.11	<	–	0.11	<	0.00
3061		2.09	0.08	<	0.14	0.1	<	–		0.26	0.11	<	–	0.11	–	–	–	–		–	0.05	<	–	0.11	<	–	0.11	<	0.85
3057	<	1.8	0.07	<	0.48	0.1	<	–		0.57	0.05		0.24	0.11	–	–	–	–		–	0.1	<	0.4	0.11		0.65	0.12	<	–
3031		2.27	0.07	<	0.38	0.1	<	–		0.23	0.11		0.37	0.02	–	–	–	–		–	0.1	<	0.18	0.11	<	–	0.11	<	–
3021		2.41	0.06	<	0.46	0.1	<	–	<	0.06	0.11	<	0.51	0.11	–	–	–	–		–	0.1	<	–	0.11	<	–	0.11	<	–
3002		2.18	0.06	<	0.04	0.1	<	–		0.1	0.15		0.27	0.11	–	–	–	–		–	0.1	<	0.00	0.11		0.59	0.12	<	0.45
2997		2.16	0.08	<	0.88	0.1	<	–		0.28	0.11	<	–	0.11	–	–	–	–		–	0.1	<	–	0.11	<	–	0.11	<	–
2996		1.92	0.06	<	-0.17	0.1	<	–		0.53	0.18	<	0.51	0.11	–	–	–	–		–	0.05	<	0.45	0.11		0.54	0.12	<	–
2994		2.31	0.09	<	-0.96	0.1	<	–	<	0.1	0.11		0.41	0.11	–	–	–	–		–	0.1	<	-0.06	0.11		0.6	0.12	<	0.00
2984		2.34	0.05	<	0.05	0.1	<	–	<	-0.27	0.11	<	0.65	0.11	–	–	–	–		–	0.1	<	–	0.11	<	–	0.11	<	–
2948	<	2.01	0.05	<	0.04	0.1	<	–		0.24	0.02	<	–	0.11	–	–	–	–		–	0.05	<	–	0.11	<	–	0.11	<	–
2921		2.35	0.08	<	-0.2	0.1	<	–	<	–	0.11	<	–	0.11	–	–	–	–		–	0.1	<	–	0.11	<	–	0.11	<	–
2905		2.28	0.06	<	0.76	0.1	<	–		0.19	0.11		0.41	0.08	–	–	–	–		–	0.1		0.00	0.11	<	–	0.11	<	–
2897		2.25	0.19	<	0.19	0.11	<	–		-0.06	0.11		0.56	0.02	–	–	–	–		–	0.1	<	0.65	0.11	<	–	0.11	<	–
2888		2.27	0.07	<	0.26	0.1	<	–	<	–	0.11	<	–	0.11	–	–	–	–		–	0.1	<	–	0.11	<	–	0.11	<	0.6

Continued on next page

Table A.2 – continued from previous page

Ids	f	Li	σ	f	[Al/Fe]	σ	f	[O/Fe]	f	[Na/Fe]	σ	f	[Mg/Fe]	σ	[Ca/Fe]	σ	[Sc/Fe]	σ	f	[Cu/Fe]	σ	f	[Y/Fe]	σ	f	[Ba/Fe]	σ	f	[Eu/Fe]
2877	<	1.82	0.08	<	0.34	0.1	<	–	<	–	0.11	<	–	0.11	–	–	–	–	–	0.1		0.00	0.11		0.64	0.12	<	0.00
2875		1.79	0.06	<	0.09	0.1	<	–		0.47	0.03		0.25	0.11	–	–	–	–	–	0.05	<	0.00	0.11		0.47	0.12	<	0.00
2872		1.99	0.05	<	0.1	0.1	<	–		0.12	0.02		0.22	0.06	–	–	–	–	–	0.05	<	-0.44	0.11	<	–	0.11	<	0.00
2847		2.01	0.05	<	0.09	0.1	<	–		0.25	0.11		0.15	0.11	–	–	–	–	–	0.05		0.32	0.11		0.26	0.12	<	1.32
2794		1.83	0.06		0.44	0.1	<	–		-0.05	0.11		0.37	0.02	–	–	–	–	–	0.05	<	0.3	0.11		0.57	0.12	<	0.00
2773		1.91	0.07	<	0.29	0.1	<	–	<	0.18	0.11		0.36	0.02	–	–	–	–	–	0.05	<	0.24	0.11	<	–	0.11	<	-0.1
2759		1.54	0.05	<	0.34	0.1	<	–		0.39	0.09		0.47	0.11	–	–	–	–	–	0.05		0.23	0.11		0.5	0.12	<	-0.1
2743		1.92	0.06	<	-0.16	0.1	<	–	<	-0.19	0.11		0.43	0.13	–	–	–	–	–	0.05	<	-0.5	0.11	<	–	0.11	<	0.5
2742		2.03	0.05	<	-0.4	0.1	<	–		-0.1	0.11		0.35	0.11	–	–	–	–	–	0.05	<	-0.2	0.11		0.4	0.12	<	0.6
2646		1.4	0.06	<	0.19	0.1	<	–		-0.2	0.11		0.37	0.02	–	–	–	–	–	0.05		0.01	0.11		0.13	0.12	<	0.6
2627		1.72	0.06	<	0.67	0.1	<	–	<	–	0.11	<	–	0.11	–	–	–	–	–	0.05	<	–	0.11	<	–	0.11	<	0.9
2616		1.82	0.05	<	-0.36	0.1	<	–		0.05	0.11		0.53	0.11	–	–	–	–	–	0.05	<	–	0.11	<	–	0.11	<	0.65
2610	<	1.38	0.08		0.54	0.1	<	–		0.33	0.01		0.15	0.11	–	–	–	–	–	0.05		0.43	0.11		0.47	0.12	<	-0.1
2601	<	1.4	0.06		0.64	0.1	<	–	<	–	0.11	<	–	0.11	–	–	–	–	–	0.05	<	–	0.11	<	–	0.11	<	0.3
2597	<	1	0.05	<	-0.16	0.1	<	–		0.47	0.07		0.25	0.18	–	–	–	–	–	0.05	<	0.09	0.11		0.09	0.12	<	-0.2
2575	<	1.51	0.05	<	0.68	0.1	<	–	<	–	0.11	<	–	0.11	–	–	–	–	–	0.05	<	–	0.11	<	–	0.11	<	-0.1
2571		1.52	0.05		0.46	0.1	<	–		0.22	0.02	<	0.4	0.11	–	–	–	–	–	0.05		0.12	0.11		0.05	0.12	<	-0.1
2569		1.65	0.08	<	-0.11	0.1	<	–		0.14	0.07		0.43	0.11	–	–	–	–	–	0.05	<	0.38	0.11	<	–	0.11	<	-0.1
2556		1.54	0.05	<	0.31	0.1	<	–		0.26	0.11		0.52	0.13	–	–	–	–	–	0.05	<	0.5	0.11	<	–	0.11	<	0.00
2546		1.51	0.05	<	0.38	0.1	<	–		0.32	0.04		0.35	0.14	–	–	–	–	–	0.05	<	0.4	0.11	<	–	0.11	<	0.1
2535		1.48	0.05		0.69	0.1	<	–	<	0.4	0.08		0.3	0.11	–	–	–	–	–	0.05	<	–	0.11	<	–	0.11	<	0.00
2517		1.65	0.05	<	-0.68	0.1	<	–	<	-0.49	0.11		0.5	0.11	–	–	–	–	–	0.05	<	–	0.11	<	–	0.11	<	-0.1
2497		1.78	0.05	<	-0.16	0.1	<	–	<	–	0.11	<	–	0.11	–	–	–	–	–	0.05	<	–	0.11	<	–	0.11	<	0.00
2479	<	1.09	0.07		0.72	0.1	<	–		0.28	0.17		0.2	0.08	–	–	–	–	–	0.05	<	-0.2	0.11		0.35	0.12	<	–
2476		1.42	0.05	<	0.54	0.1	<	–		0.47	0.02		0.4	0.11	–	–	–	–	–	0.05	<	–	0.11	<	–	0.11	<	1.03
2472		1.48	0.05	<	0.22	0.1	<	–		0.09	0.11		0.44	0.11	–	–	–	–	–	0.05	<	–	0.11	<	–	0.11	<	0.00
2445	<	1.2	0.06		0.58	0.1	<	–		0.72	0.09	<	0.47	0.11	–	–	–	–	–	0.05		0.15	0.11		0.49	0.12	<	0.1
2414		1.39	0.06	<	-0.21	0.1	<	–		-0.38	0.11		0.36	0.11	–	–	–	–	–	0.05	<	-0.4	0.11	<	–	0.11	<	0.5
2396		1.32	0.06	<	-0.46	0.1	<	–		-0.29	0.11		0.4	0.07	–	–	–	–	–	0.05	<	-0.04	0.11		0.1	0.12	<	–
2391		1.29	0.06	<	-0.06	0.1	<	–		0.13	0.13		0.21	0.11	–	–	–	–	–	0.05	<	–	0.11	<	–	0.11	<	-0.1
2370		1.49	0.06	<	-0.28	0.1	<	–	<	–	0.11	<	–	0.11	–	–	–	–	–	0.05	<	–	0.11	<	–	0.11	<	0.00
2337		1.39	0.05	<	-0.28	0.1	<	–		-0.24	0.11		0.41	0.08	–	–	–	–	–	0.05		0.03	0.11		0.09	0.12	<	0.5
2334		1.42	0.06	<	0.04	0.1	<	–		0.11	0.14		0.46	0.03	–	–	–	–	–	0.05		0.00	0.11		0.19	0.12	<	-0.1

Continued on next page

Table A.2 – continued from previous page

Ids	f	Li	σ	f	[Al/Fe]	σ	f	[O/Fe]	f	[Na/Fe]	σ	f	[Mg/Fe]	σ	[Ca/Fe]	σ	[Sc/Fe]	σ	f	[Cu/Fe]	σ	f	[Y/Fe]	σ	f	[Ba/Fe]	σ	f	[Eu/Fe]
2280		1.17	0.05	<	-0.27	0.1	<	–		-0.07	0.03		0.48	0.11	–	–	–	–		–	0.05	<	–	0.11	<	–	0.11	<	0.6
2275	<	1.27	0.08	<	0.62	0.11	<	–		-0.01	0.15		0.4	0.11	–	–	–	–		–	0.05	<	-0.6	0.11	<	–	0.11	<	-0.2
2246	<	0.29	0.06	<	0.54	0.1	<	–		0.43	0.11		0.34	0.12	–	–	–	–		–	0.05	<	0.16	0.11	<	–	0.11	<	–
2245		1.1	0.05		0.5	0.1	<	–		0.49	0.16		0.32	0.11	–	–	–	–		–	0.05		0.34	0.11		0.04	0.12	<	0.3
2224		1.35	0.06	<	0.25	0.1	<	–	<	–	0.11	<	–	0.11	–	–	–	–		–	0.05	<	–	0.11	<	–	0.11	<	0.3
2211	<	1.22	0.06	<	0.11	0.1	<	–		0.06	0.04		0.45	0.11	–	–	–	–		–	0.05	<	–	0.11	<	–	0.11	<	–
2208	<	1.37	0.05	<	0.34	0.1	<	–		-0.02	0.11	<	–	0.11	–	–	–	–		–	0.05	<	-0.6	0.11	<	–	0.11	<	-0.1
2176		1.1	0.05		0.37	0.1	<	–		0.19	0.16		0.31	0.04	–	–	–	–		–	0.05		0.32	0.11		0.2	0.12	<	-0.1
2169		1.17	0.05	<	-0.31	0.1	<	–		-0.22	0.35	<	–	0.11	–	–	–	–		–	0.05	<	0.1	0.11	<	–	0.11	<	0.49
2151		1.05	0.05		0.23	0.1	<	–		0.23	0.06		0.3	0.11	–	–	–	–		–	0.05	<	–	0.11	<	–	0.11	<	0.55
2129		1.36	0.06	<	0.34	0.1	<	–		0.16	0.21		0.35	0.02	–	–	–	–		–	0.05	<	0.14	0.11		0.31	0.12	<	0.00
2117		1.15	0.05	<	-0.06	0.1	<	–		-0.25	0.3		0.44	0.03	–	–	–	–		–	0.05	<	-0.6	0.11	<	–	0.11	<	0.12
2113	<	1.27	0.06	<	0.37	0.1	<	–		0.14	0.1		0.32	0.15	–	–	–	–		–	0.05		0.04	0.11		0.1	0.12	<	0.73
2110		1.27	0.05		0.52	0.1	<	–	<	–	0.11	<	–	0.11	–	–	–	–		–	0.05	<	–	0.11	<	–	0.11	<	0.00
2090		1.2	0.05	<	0.09	0.1	<	–		0.28	0.13		0.34	0.11	–	–	–	–		–	0.05	<	–	0.11	<	–	0.11	<	0.2
2089	<	1.1	0.07	<	0.64	0.1	<	–		-0.22	0.11		0.37	0.11	–	–	–	–		–	0.05		0.28	0.11		0.19	0.12	<	–
2078		1.29	0.08	<	0.27	0.1	<	–	<	-0.56	0.11	<	–	0.11	–	–	–	–		–	0.05	<	–	0.11	<	–	0.11	<	–
2027	<	0.49	0.05	<	0.22	0.1	<	–		0.33	0.11		0.21	0.15	–	–	–	–		–	0.05	<	–	0.11	<	–	0.11	<	0.24
2014	<	1.01	0.05	<	0.32	0.1	<	–	<	–	0.11	<	–	0.11	–	–	–	–		–	0.05		0.05	0.11		0.3	0.12	<	0.75
201217		1.03	0.06		0.55	0.1	<	–		0.34	0.11		0.37	0.1	–	–	–	–		–	0.05		0.27	0.11		0.22	0.12	<	0.00
201002		1.35	0.06		0.48	0.1	<	–	<	–	0.11		0.5	0.07	–	–	–	–		–	0.05	<	-0.2	0.11		0.21	0.12	<	0.1
1983	<	1.09	0.05		0.56	0.1	<	–		0.33	0.04		0.25	0.11	–	–	–	–		–	0.05	<	–	0.11	<	–	0.11	<	–
1980		1.18	0.08	<	0.04	0.1	<	–		-0.07	0.18		0.46	0.04	–	–	–	–		–	0.05		0.03	0.11		0.32	0.12	<	0.4
1976		1.23	0.06	<	-0.45	0.1	<	–		-0.23	0.11	<	–	0.11	–	–	–	–		–	0.05	<	0.23	0.11	<	–	0.11	<	0.1
1958	<	0.74	0.06		0.51	0.1	<	–		0.32	0.11		0.3	0.11	–	–	–	–		–	0.05	<	–	0.11	<	–	0.11	<	0.69
19113655-5959432		2.18	0.08	<	0.24	0.1	<	–	<	–	0.11	<	–	0.11	–	–	–	–		–	0.1	<	–	0.11		-0.25	0.12	<	–
19113403-5957497		2.12	0.07	<	0.41	0.1	<	–	<	–	0.11	<	–	0.11	–	–	–	–		–	0.1	<	–	0.11	<	–	0.11	<	–
19113393-5958107		2.06	0.08	<	0.82	0.1	<	–	<	–	0.11	<	–	0.11	–	–	–	–		–	0.1	<	–	0.11		-0.01	0.12	<	–
19113298-5958411	<	1.04	0.05		0.6	0.1	<	–	<	–	0.11	<	–	0.11	–	–	–	–		–	0.05	<	–	0.11		-0.1	0.12	<	–
19113168-5957130	<	1.59	0.07	<	-0.26	0.1	<	–	<	–	0.11	<	–	0.11	–	–	–	–		–	0.1	<	–	0.11		0.17	0.12	<	–
19113088-5957430	<	2.16	0.08	<	-0.26	0.1	<	–	<	–	0.11	<	–	0.11	–	–	–	–		–	0.1	<	–	0.11		-0.08	0.12	<	–
19113087-5958477	<	2.07	0.07	<	-0.35	0.1	<	–	<	–	0.11	<	–	0.11	–	–	–	–		–	0.1	<	–	0.11	<	–	0.11	<	–
19113071-6003234		1.12	0.06	<	0.27	0.1	<	-0.39		-0.04	0.03		0.3	0.11	0.03	0.06	-0.12	0.07		-0.59	0.05		-0.1	0.02		0.25	0.16	<	0.43

Continued on next page

Table A.2 – continued from previous page

Ids	f	Li	σ	f	[Al/Fe]	σ	f	[O/Fe]	f	[Na/Fe]	σ	f	[Mg/Fe]	σ	[Ca/Fe]	σ	[Sc/Fe]	σ	f	[Cu/Fe]	σ	f	[Y/Fe]	σ	f	[Ba/Fe]	σ	f	[Eu/Fe]
19112987-5956098		2.34	0.07	<	0.62	0.1	<	–	<	–	0.11	<	–	0.11	–	–	–	–		–	0.1	<	–	0.11		-0.07	0.12	<	–
19112818-6000436		2.28	0.1	<	0.63	0.1	<	–	<	–	0.11	<	–	0.11	–	–	–	–		–	0.1	<	–	0.11		0.00	0.12	<	–
19112749-5958445	<	2.03	0.11	<	0.91	0.1	<	–	<	–	0.11	<	–	0.11	–	–	–	–		–	0.1	<	–	0.11		0.2	0.12	<	–
19112720-5955225		2.05	0.07	<	0.54	0.1	<	–	<	–	0.11	<	–	0.11	–	–	–	–		–	0.1	<	–	0.11		-0.39	0.12	<	–
19112587-5958553		2.29	0.07	<	0.25	0.1	<	–	<	–	0.11	<	–	0.11	–	–	–	–		–	0.1	<	–	0.11		0.03	0.12	<	–
19112451-6000104		2.02	0.08	<	0.24	0.1	<	–	<	–	0.11	<	–	0.11	–	–	–	–		–	0.1	<	–	0.11		0.35	0.12	<	–
19112339-6001385		2.25	0.07		0.55	0.1	<	–	<	–	0.11	<	–	0.11	–	–	–	–		–	0.1	<	–	0.11		0.31	0.12	<	–
19112258-6002380	<	2.01	0.09	<	0.59	0.1	<	–	<	–	0.11	<	–	0.11	–	–	–	–		–	0.1	<	–	0.11		-0.03	0.12	<	–
19112132-5956542	<	1.99	0.06	<	0.8	0.1	<	–	<	–	0.11	<	–	0.11	–	–	–	–		–	0.1	<	–	0.11		0.18	0.12	<	–
19112091-6002411		2.34	0.07	<	0.52	0.1	<	–	<	–	0.11	<	–	0.11	–	–	–	–		–	0.1	<	–	0.11		0.33	0.12	<	–
19112071-5956287		2.09	0.06	<	0.1	0.1	<	–	<	–	0.11	<	–	0.11	–	–	–	–		–	0.1	<	–	0.11		0.55	0.12	<	–
19112070-6001057		2.07	0.06	<	0.04	0.1	<	–	<	–	0.11	<	–	0.11	–	–	–	–		–	0.1	<	–	0.11		0.14	0.12	<	–
19111828-6000139		1.2	0.06	<	0.1	0.1	<	0.44		-0.01	0.09		0.33	0.11	0.21	0.03	-0.14	0.05		-0.5	0.05		-0.11	0.06		0.19	0.18	<	0.70
19111644-6002253		2.12	0.09	<	-0.1	0.1	<	–	<	–	0.11	<	–	0.11	–	–	–	–		–	0.1	<	–	0.11		0.23	0.12	<	–
19111612-5954443		2.34	0.07	<	0.2	0.1	<	–	<	–	0.11	<	–	0.11	–	–	–	–		–	0.1	<	–	0.11		0.25	0.12	<	–
19111338-6002243		2.08	0.06	<	0.51	0.1	<	–	<	–	0.11	<	–	0.11	–	–	–	–		–	0.1	<	–	0.11		0.11	0.12	<	–
19111078-5956406		1.03	0.06	<	0.24	0.1	<	–	<	–	0.11	<	–	0.11	–	–	–	–		–	0.05	<	–	0.11		-0.3	0.12	<	–
19111018-5954267	<	0.98	0.05	<	0.02	0.1	<	–	<	–	0.11	<	–	0.11	–	–	–	–		–	0.05	<	–	0.11		0.04	0.12	<	–
19110907-5955546		0.99	0.06	<	0.05	0.1	<	–	<	–	0.11	<	–	0.11	–	–	–	–		–	0.05	<	–	0.11		-0.11	0.12	<	–
19110863-5957569	<	0.49	0.05		0.54	0.1	<	–	<	–	0.11	<	–	0.11	–	–	–	–		–	0.05	<	–	0.11		0.07	0.12	<	–
19110798-6003588	<	1.91	0.06	<	0.42	0.1	<	–	<	–	0.11	<	–	0.11	–	–	–	–		–	0.1	<	–	0.11		0.13	0.12	<	–
19110785-5954515		2.24	0.07	<	0.41	0.1	<	–	<	–	0.11	<	–	0.11	–	–	–	–		–	0.1	<	–	0.11	<	-0.11	0.12	<	–
19110616-6002522	<	2.19	0.06	<	0.61	0.1	<	–	<	–	0.11	<	–	0.11	–	–	–	–		–	0.1	<	–	0.11		0.54	0.12	<	–
19110598-5959013	<	0.8	0.05	<	-0.26	0.1	<	–	<	–	0.11	<	–	0.11	–	–	–	–		–	0.05	<	–	0.11		-0.11	0.12	<	–
19110533-5953490	<	2.14	0.07	<	0.49	0.1	<	–	<	–	0.11	<	–	0.11	–	–	–	–		–	0.1	<	–	0.11		0.06	0.12	<	–
19110501-5955274		1.03	0.05		0.37	0.1	<	0.59		0.11	0.07		0.46	0.11	0.15	0.07	-0.09	0.06		-0.48	0.05		-0.07	0.04		0.29	0.09	<	0.58
19110429-6002404		2.29	0.08	<	-0.35	0.1	<	–	<	–	0.11	<	–	0.11	–	–	–	–		–	0.1	<	–	0.11		0.23	0.12	<	–
19110207-5956317		2.03	0.08	<	0.53	0.1	<	–		0.37	0.24		0.28	0.11	0.18	0.06	–	–	<	-0.1	0.1	<	0.13	0.11		0.01	0.1	<	0.90
19110152-6003444	<	1.94	0.05		0.5	0.1	<	–	<	–	0.11	<	–	0.11	–	–	–	–		–	0.1	<	–	0.11		0.08	0.12	<	–
19110151-6002511		2.19	0.05	<	0.09	0.1	<	–	<	–	0.11	<	–	0.11	–	–	–	–		–	0.1	<	–	0.11		-0.11	0.12	<	–
19110105-6004103		2.2	0.05	<	0.01	0.1	<	–	<	–	0.11	<	–	0.11	–	–	–	–		–	0.1	<	–	0.11		-0.05	0.12	<	–
19110081-6005092	<	2.34	0.1	<	0.64	0.1	<	–	<	–	0.11	<	–	0.11	–	–	–	–		–	0.1	<	–	0.11	<	–	0.11	<	–
19110011-6006045		1.97	0.08	<	0.58	0.1	<	–	<	–	0.11	<	–	0.11	–	–	–	–		–	0.1	<	–	0.11		-0.11	0.12	<	–

Continued on next page

Table A.2 – continued from previous page

Ids	f	Li	σ	f	[Al/Fe]	σ	f	[O/Fe]	f	[Na/Fe]	σ	f	[Mg/Fe]	σ	[Ca/Fe]	σ	[Sc/Fe]	σ	f	[Cu/Fe]	σ	f	[Y/Fe]	σ	f	[Ba/Fe]	σ	f	[Eu/Fe]
19105996-5959271	<	0.6	0.05		0.44	0.1	<	–	<	–	0.11	<	–	0.11	–	–	–	–		–	0.05	<	–	0.11		0.05	0.12	<	–
19105986-6002171		2.34	0.05	<	0.86	0.1	<	1.24	<	-0.17	0.11		0.03	0.11	0.06	0.04	-0.24	0.04	<	0.03	0.1	<	-0.24	0.11		-0.01	0.28	<	1.00
19105851-5955394	<	1.09	0.08		0.78	0.1	<	–	<	–	0.11	<	–	0.11	–	–	–	–		–	0.05	<	–	0.11		0.1	0.12	<	–
19105692-6000227	<	0.92	0.05		0.34	0.1	<	–	<	–	0.11	<	–	0.11	–	–	–	–		–	0.05	<	–	0.11		-0.12	0.12	<	–
19105577-5957278		1.11	0.05	<	-0.06	0.1	<	–	<	–	0.11	<	–	0.11	–	–	–	–		–	0.05	<	–	0.11		-0.1	0.12	<	–
19105546-5953358		2.15	0.08	<	-0.16	0.1	<	–	<	–	0.11	<	–	0.11	–	–	–	–		–	0.1	<	–	0.11		0.02	0.12	<	–
19105483-6003042		2.23	0.06	<	0.7	0.1	<	–	<	–	0.11	<	–	0.11	–	–	–	–		–	0.1	<	–	0.11		-0.1	0.12	<	–
19105406-5958002	<	0.86	0.05		0.64	0.1	<	–	<	–	0.11	<	–	0.11	–	–	–	–		–	0.05	<	–	0.11		-0.01	0.12	<	–
19105177-6000390	<	0.64	0.05		0.66	0.1	<	–	<	–	0.11	<	–	0.11	–	–	–	–		–	0.05	<	–	0.11		-0.14	0.12	<	–
19105158-5954184		2.2	0.07	<	-0.2	0.1	<	–	<	–	0.11	<	–	0.11	–	–	–	–		–	0.1	<	–	0.11		0.17	0.12	<	–
19105056-6006005		2.13	0.06	<	0.39	0.1	<	–	<	–	0.11	<	–	0.11	–	–	–	–		–	0.1	<	–	0.11		0.19	0.12	<	–
19104963-5953398	<	1.94	0.08	<	0.39	0.1	<	–	<	–	0.11	<	–	0.11	–	–	–	–		–	0.1	<	–	0.11		0.05	0.12	<	–
19104925-5954057	<	2.09	0.08	<	0.44	0.1	<	–	<	–	0.11	<	–	0.11	–	–	–	–		–	0.1	<	–	0.11		0.16	0.12	<	–
19104892-5958234	<	1	0.05	<	0.26	0.1	<	–	<	–	0.11	<	–	0.11	–	–	–	–		–	0.05	<	–	0.11		-0.08	0.12	<	–
19104804-6002213		1.17	0.05	<	0.09	0.1	<	0.41		-0.28	0.02		0.31	0.11	0.13	0.05	-0.24	0.06		-0.73	0.05		-0.24	0.05		0.09	0.12	<	0.50
19104664-5954063		2.13	0.07	<	-0.06	0.1	<	–	<	–	0.11	<	–	0.11	–	–	–	–		–	0.1	<	–	0.11		-0.06	0.12	<	–
19104427-6004301		2.34	0.05	<	0.68	0.1	<	–	<	–	0.11	<	–	0.11	–	–	–	–		–	0.1	<	–	0.11		-0.1	0.12	<	–
19104225-6004460	<	0.99	0.05		0.66	0.1	<	–	<	–	0.11	<	–	0.11	–	–	–	–		–	0.05	<	–	0.11		-0.02	0.12	<	–
19103970-6001045	<	1.03	0.05		0.72	0.1	<	–	<	–	0.11	<	–	0.11	–	–	–	–		–	0.05	<	–	0.11		-0.06	0.12	<	–
19103964-6003189		2.26	0.07	<	0.04	0.1	<	–	<	–	0.11	<	–	0.11	–	–	–	–		–	0.1	<	–	0.11		-0.21	0.12	<	–
19103855-6003361	<	2.04	0.05	<	1.04	0.1	<	–	<	–	0.11	<	–	0.11	–	–	–	–		–	0.1	<	–	0.11	<	–	0.11	<	–
19103829-5955070		2.17	0.09	<	0.67	0.1	<	–	<	–	0.11	<	–	0.11	–	–	–	–		–	0.1	<	–	0.11		0.15	0.12	<	–
19103672-6002011	<	1.14	0.07		0.71	0.1	<	0.96		0.22	0.02		0.18	0.11	0.17	0.04	-0.16	0.07		-0.63	0.05		0.1	0.06		0.43	0.25	<	1.04
19103463-5956357	<	1.74	0.06	<	0.62	0.1	<	–	<	–	0.11	<	–	0.11	–	–	–	–		–	0.1	<	–	0.11		0.4	0.12	<	–
19102903-6002535		2.28	0.06	<	0.27	0.1	<	–	<	–	0.11	<	–	0.11	–	–	–	–		–	0.1	<	–	0.11		-0.09	0.12	<	–
19102859-6003539		2.26	0.07		0.49	0.1	<	–	<	–	0.11	<	–	0.11	–	–	–	–		–	0.1	<	–	0.11		0.2	0.12	<	–
19102726-5955194		2.36	0.08	<	-0.46	0.1	<	–	<	–	0.11	<	–	0.11	–	–	–	–		–	0.1	<	–	0.11		0.29	0.12	<	–
19102685-5958251	<	0.62	0.05	<	0.36	0.1	<	–	<	–	0.11	<	–	0.11	–	–	–	–		–	0.05	<	–	0.11		-0.29	0.12	<	–
19102677-6003089		2.49	0.05	<	0.27	0.1	<	0.99		0.01	0.2		0.21	0.11	0.13	0.06	-0.07	0.07	<	-0.34	0.1		0.23	0.11		0.69	0.13	<	0.83
19102675-5956553	<	2.05	0.08	<	0.52	0.1	<	–	<	–	0.11	<	–	0.11	–	–	–	–		–	0.1	<	–	0.11	<	–	0.11	<	–
19102577-6004439	<	0.54	0.06	<	0.29	0.1	<	–	<	–	0.11	<	–	0.11	–	–	–	–		–	0.05	<	–	0.11		-0.08	0.12	<	–
19102525-5959409		2.35	0.05	<	0.38	0.1	<	1.40		0.21	0.18		0.25	0.11	0.23	0.02	-0.04	0.03	<	-0.01	0.1		0.11	0.11		0.29	0.15	<	1.21
19102415-6003445		1.16	0.05	<	0.08	0.1	<	0.67		-0.13	0.11		0.42	0.11	0.24	0.05	-0.12	0.12		-0.6	0.05		-0.07	0.07		0.28	0.1	<	0.27

Continued on next page

Table A.2 – continued from previous page

Ids	f	Li	σ	f	[Al/Fe]	σ	f	[O/Fe]	f	[Na/Fe]	σ	f	[Mg/Fe]	σ	[Ca/Fe]	σ	[Sc/Fe]	σ	f	[Cu/Fe]	σ	f	[Y/Fe]	σ	f	[Ba/Fe]	σ	f	[Eu/Fe]
19102395-5956202	<	2.21	0.1	<	0.34	0.1	<	–	<	–	0.11	<	–	0.11	–	–	–	–		–	0.1	<	–	0.11		0.19	0.12	<	–
19102370-6000209		1.08	0.05	<	0.29	0.1	<	–	<	–	0.11	<	–	0.11	–	–	–	–		–	0.05	<	–	0.11		-0.09	0.12	<	–
19102328-6000498		2.35	0.14	<	0.14	0.11	<	–	<	–	0.11	<	–	0.11	–	–	–	–		–	0.1	<	–	0.11		-0.04	0.12	<	–
19102293-6004232		2.35	0.05	<	0.54	0.1	<	–	<	–	0.11	<	–	0.11	–	–	–	–		–	0.1	<	–	0.11		0.24	0.12	<	–
19102223-5957192		2.35	0.07	<	-0.45	0.1	<	–	<	–	0.11	<	–	0.11	–	–	–	–		–	0.1	<	–	0.11		0.00	0.12	<	–
19102204-5956597	<	1.79	0.07	<	0.52	0.1	<	–	<	–	0.11	<	–	0.11	–	–	–	–		–	0.1	<	–	0.11		0.08	0.12	<	–
19102158-5958179	<	1.99	0.05	<	-0.85	0.1	<	–	<	–	0.11	<	–	0.11	–	–	–	–		–	0.1	<	–	0.11		-0.7	0.12	<	–
19102135-6002166		2.27	0.06	<	-0.26	0.1	<	–	<	–	0.11	<	–	0.11	–	–	–	–		–	0.1	<	–	0.11		0.21	0.12	<	–
19102025-5958306		1.34	0.05	<	-0.35	0.1	<	0.72		-0.29	0.09		0.27	0.11	0.19	0.04	-0.07	0.11		-0.64	0.05		-0.02	0.04		0.39	0.18	<	0.58
19101923-5958596		2.42	0.06	<	0.05	0.1	<	–	<	–	0.11	<	–	0.11	–	–	–	–		–	0.1	<	–	0.11		0.33	0.12	<	–
19101748-6000324		1.97	0.07		0.8	0.1	<	–	<	–	0.11	<	–	0.11	–	–	–	–		–	0.1	<	–	0.11		0.2	0.12	<	–
19101652-6001094		2.06	0.06	<	0.29	0.1	<	–	<	–	0.11	<	–	0.11	–	–	–	–		–	0.1	<	–	0.11		-0.02	0.12	<	–
19101610-6000035		2.48	0.12	<	0.27	0.1	<	–	<	–	0.11	<	–	0.11	–	–	–	–		–	0.1	<	–	0.11		0.21	0.12	<	–
19101589-6002252		2.2	0.06		0.61	0.1	<	–	<	–	0.11	<	–	0.11	–	–	–	–		–	0.1	<	–	0.11		-0.2	0.12	<	–
19101000-5957525		2.24	0.11	<	0.63	0.1	<	–	<	–	0.11	<	–	0.11	–	–	–	–		–	0.1	<	–	0.11		0.09	0.12	<	–
19100961-5959534	<	1.92	0.06	<	0.73	0.1	<	–	<	–	0.11	<	–	0.11	–	–	–	–		–	0.1	<	–	0.11		0.26	0.12	<	–
19100576-6001009		2.32	0.06	<	0.56	0.1	<	–	<	–	0.11	<	–	0.11	–	–	–	–		–	0.1	<	–	0.11		0.3	0.12	<	–
1872		1.25	0.05	<	-0.06	0.1	<	–		-0.1	0.03		0.45	0.07	–	–	–	–		–	0.05		0.01	0.11		0.23	0.12	<	0.57
1846		1.22	0.05		0.24	0.1	<	–		0.01	0.21	<	–	0.11	–	–	–	–		–	0.05	<	0.25	0.11	<	–	0.11	<	0.2
1802	<	0.59	0.07		0.56	0.1	<	–	<	–	0.11	<	–	0.11	–	–	–	–		–	0.05	<	–	0.11	<	–	0.11	<	0.3

Appendix B

Comparison with G14

G14 reported (22) 99 measurements and (48) 25 upper limits for (Al) Li out of the 126 stars that spectra in the wavelength range covering Al and Li. Here we compare the measured Li and Al for these stars.

Figures B.1 and B.2 compare our measurements for Li and Al and the ones from G14 as a function of $T_{\rm eff}$. The best linear fit (red dashed line) is shown on the right panels with their respective correlation coefficient. In both cases, there is an indication of a trend. The difference between the Li measurements presented here and those in G14 are strongly correlated with the difference in $\rm T_{eff}$, as shown in the right panel of Fig B.1. It is noteworthy that the most discrepant points in this plot correspond to stars for which the spectra had poor SNR.

We note that, unlike Li, the trend in Al, in particular for unevolved stars, is based on very few stars. Then, it should be taken with great caution. Still, the measurements of Al abundances are similar in both studies. These comparisons indicate that the differences in Li and Al abundances between the present paper and G14 are consistent with the differences in adopted $T_{\rm eff}$.

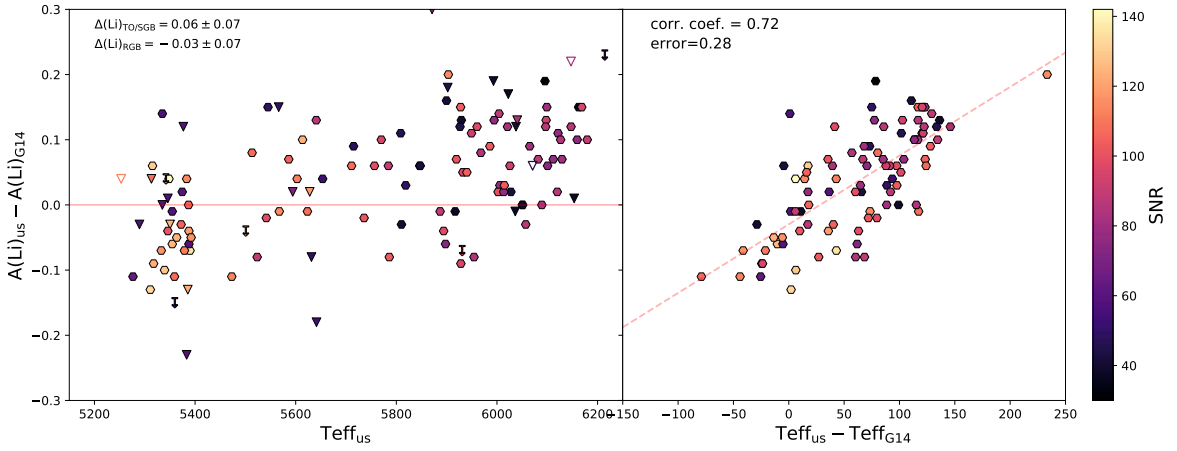

Figure B.1 Difference between our Li abundances and the ones reported by G14 as a function of T_{eff} (left), and as a function of the difference between our T_{eff} and the ones reported by G14 (right). Filled hexagons and down-pointing symbols represent measurements and upper limits, respectively. Empty triangles, filled triangles, and arrows show that we measured, and they did not; they and we reported upper limits, we report an upper limit, and they an actual measurement. Colours vary with the SNR.

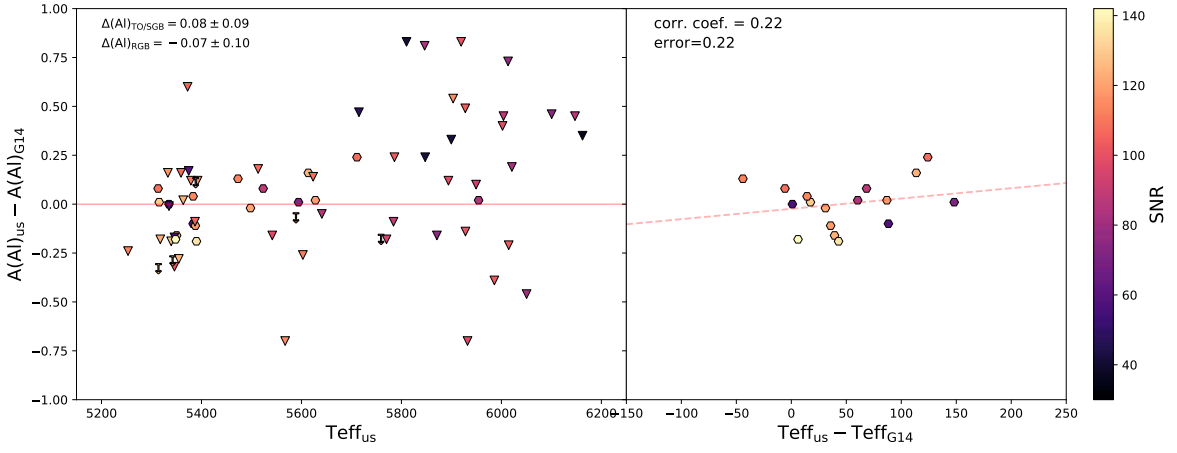

Figure B.2 Difference between our Al abundances and the ones reported by G14 as a function of T_{eff} (left), and as a function of the difference between our T_{eff} and the ones reported by G14 (right). Filled hexagons and down-pointing symbols represent measurements and upper limits, respectively. Empty triangles, filled triangles, and arrows show that we measured, and they did not; they and we reported upper limits, we report an upper limit, and they an actual measurement. Colours vary with the SNR.

Appendix C

Y and Ba trends along with Vm

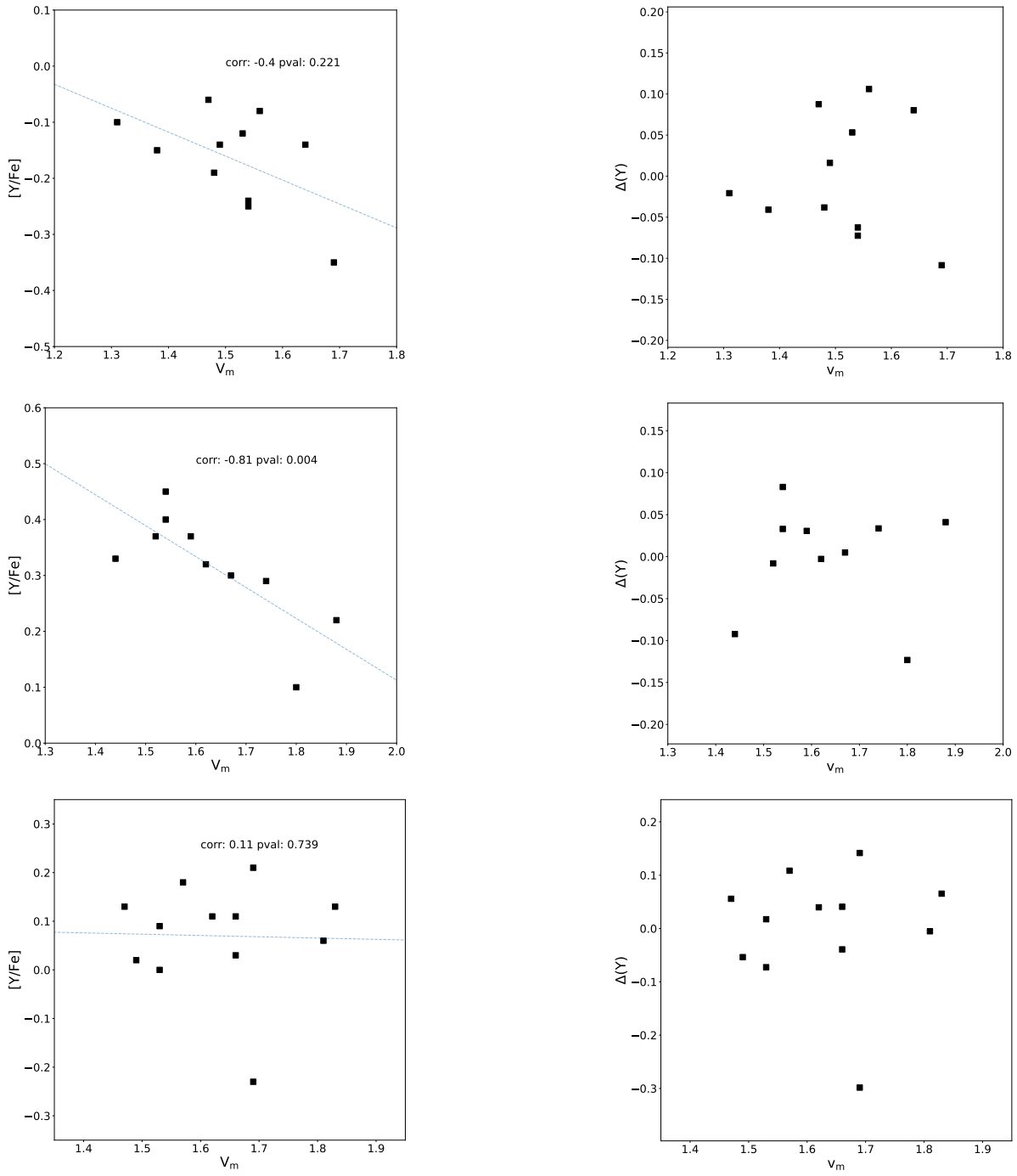

Figure C.1 ΔY GCs: NGC104, NGC288, NGC2808.

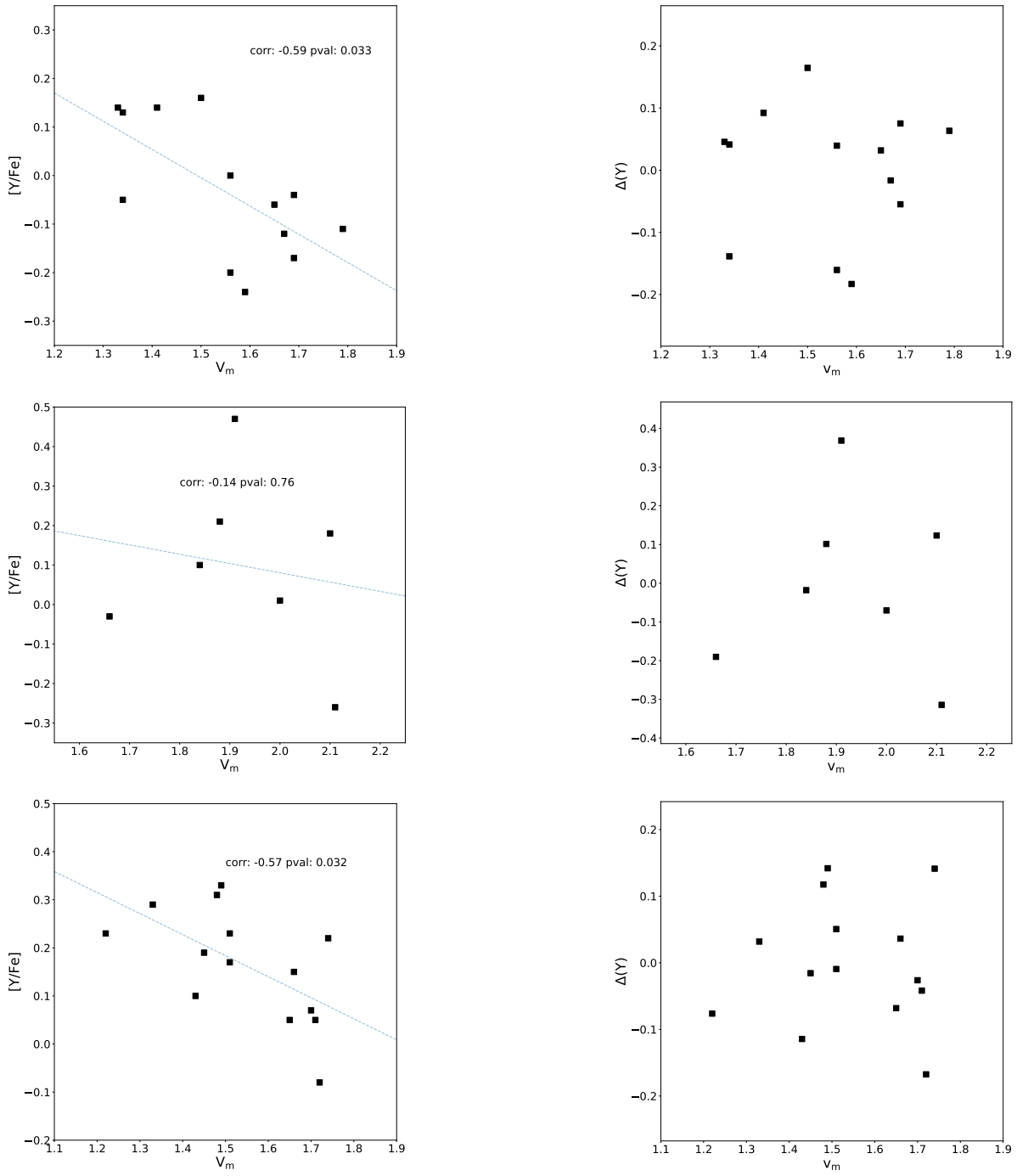

Figure C.2 ΔY GCs: NGC3201, NGC5634, and NGC5904

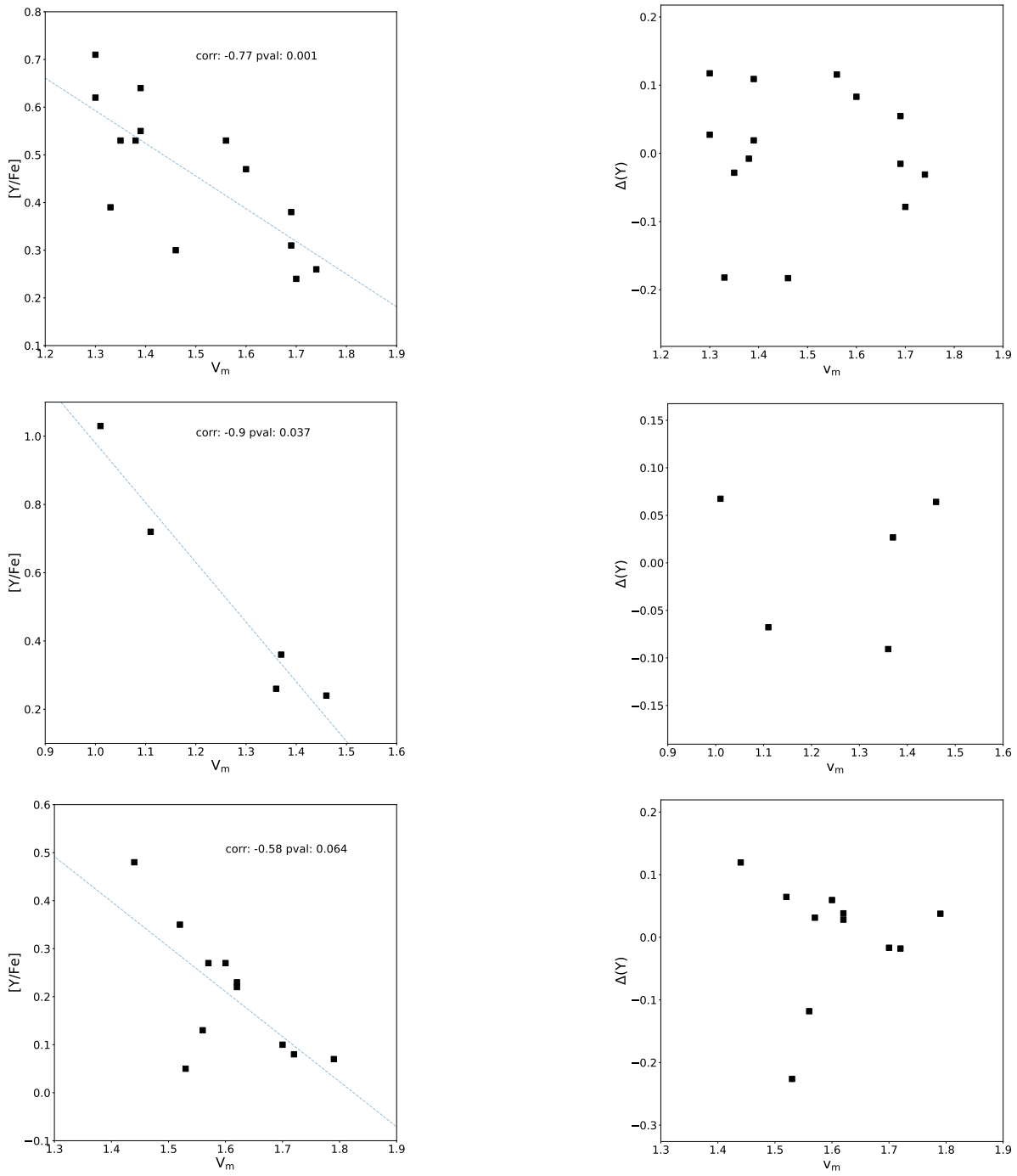

Figure C.3 ΔY GCs: NGC6121, NGC6171, and NGC6218.

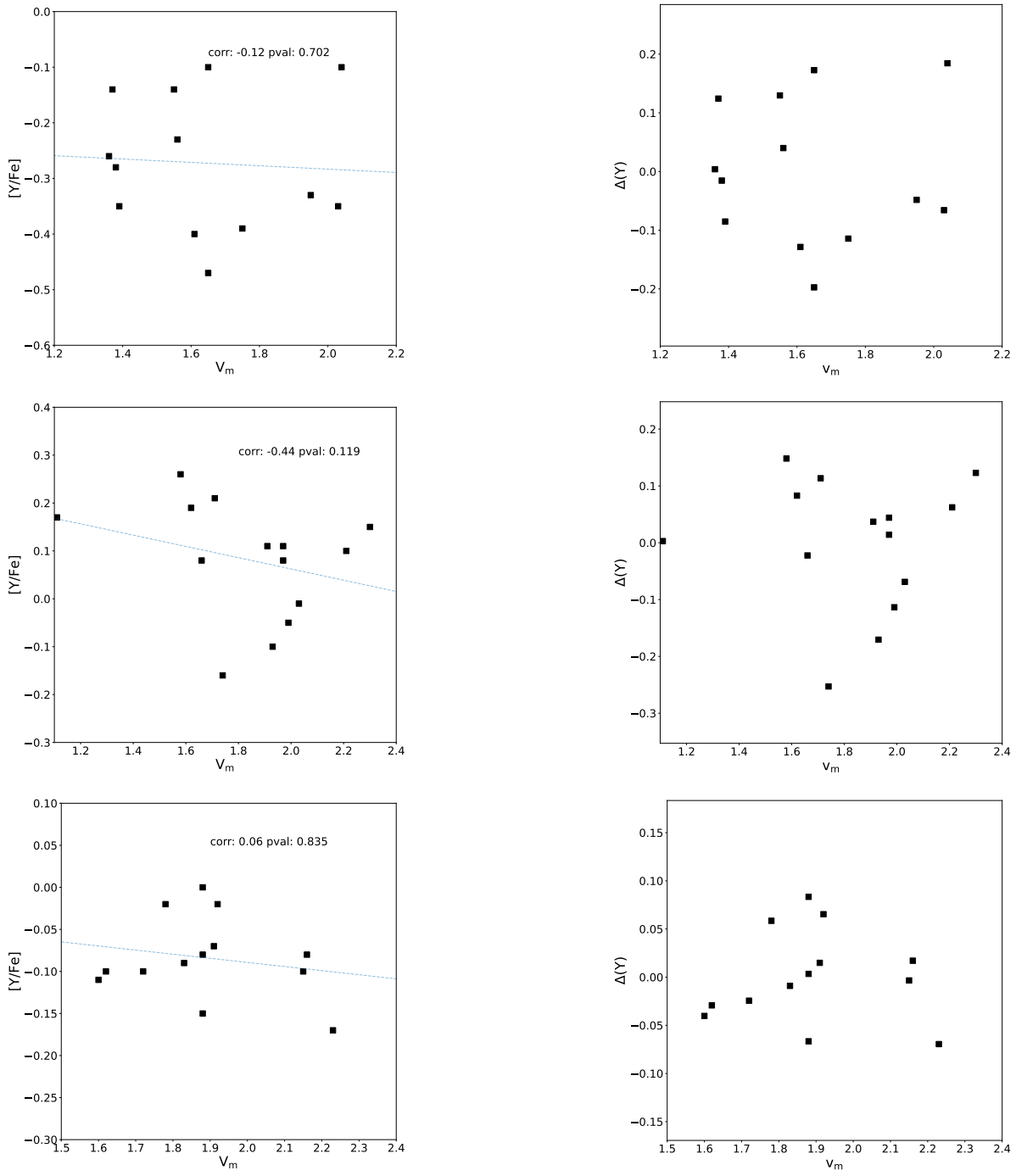

Figure C.4 ΔY GCs: NGC4590, NGC6254, and NGC6397.

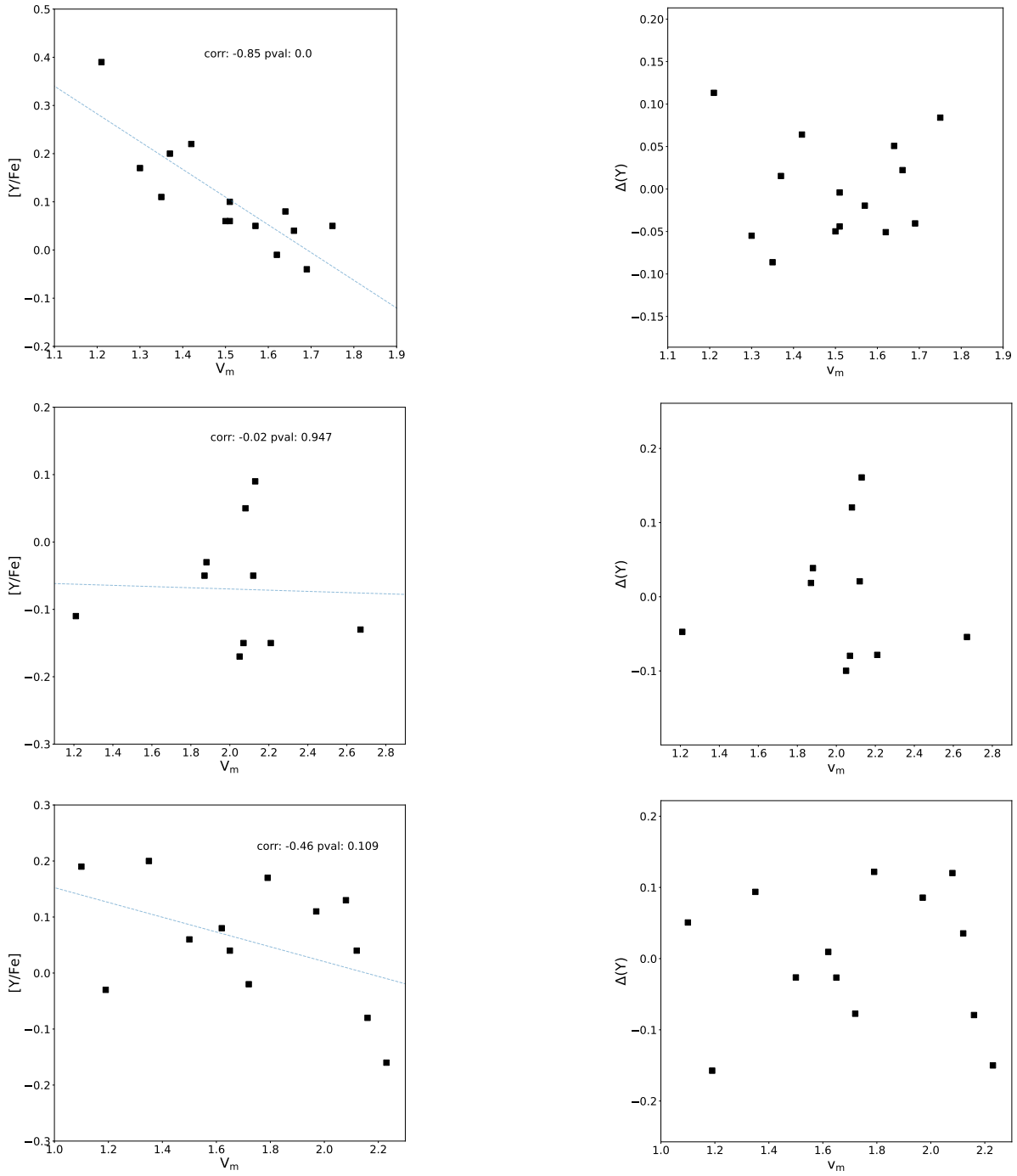

Figure C.5 ΔY GCs: NGC 6752, NGC 7099, and NGC 7078

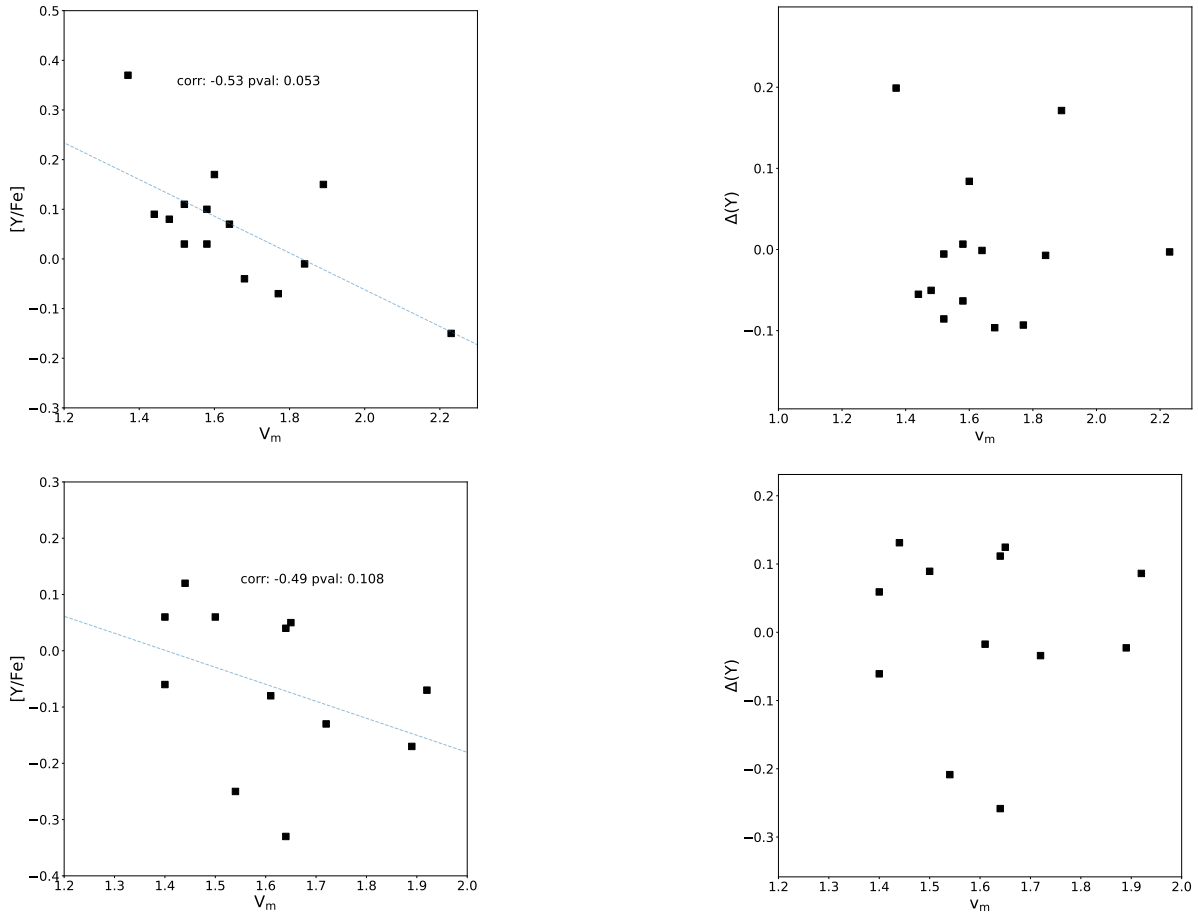

Figure C.6 ΔY GCs: NGC6809 and NGC 6838.

Appendix D

Line list

TABLE D.1: Line list used for the abundance determination.

Wavelength	Specie	EP's	$\log gf$
6707.899	3.0007	0.000	-0.804
6707.900	3.0007	0.000	-1.503
6707.918	3.0006	0.000	-0.730
6707.918	3.0006	0.000	-0.827
6707.923	3.0007	0.000	-0.804
6707.924	3.0006	0.000	-0.299
6707.924	3.0006	0.000	-0.827
6707.924	3.0006	0.000	-1.730
6707.925	3.0007	0.000	-0.804
5682.647	11.000	2.100	-0.670
5688.217	11.000	2.100	-0.370
5528.405	12.0	4.343	-0.62
5711.088	12.0	4.343	-1.83
6696.788	13.0	4.019	-2.72
5260.390	20.000	2.520	-1.720
5261.708	20.000	2.520	-0.580
5349.469	20.000	2.710	-0.310

Continued on next page

Table D.1 – continued from previous page

Wavelength	Specie	EP's	$\log gf$
5588.764	20.000	2.510	0.360
5590.126	20.000	2.510	-0.570
5594.471	20.000	2.510	0.100
5857.459	20.000	2.930	0.240
5867.572	20.000	2.930	-1.490
6161.295	20.000	2.520	-1.270
6163.754	20.000	2.520	-1.290
6166.440	20.000	2.520	-1.140
6169.044	20.000	2.520	-0.800
6169.564	20.000	2.520	-0.480
6439.083	20.000	2.520	0.390
6449.820	20.000	2.520	-0.500
6455.605	20.000	2.520	-1.290
6462.570	20.000	2.520	0.260
6471.668	20.000	2.520	-0.690
6493.788	20.000	2.520	-0.110
6499.654	20.000	2.520	-0.820
6572.795	20.000	0.000	-4.320
6717.687	20.000	2.710	-0.520
5318.361	21.100	1.360	-1.793
5526.821	21.100	1.770	0.134
5640.989	21.100	1.500	-1.353
5657.880	21.100	1.510	-0.603
5667.153	21.100	1.500	-1.309
5669.040	21.100	1.500	-1.120
5684.198	21.100	1.510	-0.852
6245.620	21.100	1.510	-0.980
6279.740	21.100	1.500	-1.210
6604.600	21.100	1.360	-1.309

Continued on next page

Table D.1 – continued from previous page

Wavelength	Specie	EP's	$\log gf$
5105.503	29.0065	1.388	-3.720
5105.505	29.0063	1.388	-3.720
5105.506	29.0065	1.388	-2.766
5105.509	29.0063	1.388	-2.766
5105.509	29.0065	1.388	-2.720
5105.510	29.0065	1.388	-3.896
5105.511	29.0063	1.388	-2.720
5105.512	29.0063	1.388	-3.896
5105.515	29.0065	1.388	-2.653
5105.517	29.0063	1.388	-2.653
5105.519	29.0065	1.388	-2.398
5105.520	29.0063	1.388	-2.398
5105.530	29.0065	1.388	-2.750
5105.531	29.0063	1.388	-2.750
5105.536	29.0063	1.388	-2.148
5105.536	29.0065	1.388	-2.148
5087.420	39.1	1.083	-0.17
5200.413	39.1	0.992	-0.57
5509.896	39.1	0.992	-1.01
5853.686	56.1137	0.604	-2.066
5853.687	56.1135	0.604	-2.066
5853.687	56.1137	0.604	-2.009
5853.688	56.1135	0.604	-2.009
5853.689	56.1135	0.604	-2.215
5853.689	56.1137	0.604	-2.215
5853.690	56.1134	0.604	-1.010
5853.690	56.1135	0.604	-1.466
5853.690	56.1135	0.604	-1.914
5853.690	56.1135	0.604	-2.620

Continued on next page

Table D.1 – continued from previous page

Wavelength	Specie	EP's	$\log gf$
5853.690	56.1136	0.604	-1.010
5853.690	56.1137	0.604	-1.466
5853.690	56.1137	0.604	-1.914
5853.690	56.1137	0.604	-2.620
5853.690	56.1138	0.604	-1.010
5853.691	56.1135	0.604	-2.215
5853.692	56.1137	0.604	-2.215
5853.693	56.1135	0.604	-2.009
5853.693	56.1137	0.604	-2.009
5853.694	56.1135	0.604	-2.066
5853.694	56.1137	0.604	-2.066
6141.725	56.1135	0.704	-2.456
6141.725	56.1137	0.704	-2.456
6141.727	56.1135	0.704	-1.311
6141.727	56.1137	0.704	-1.311
6141.728	56.1135	0.704	-2.284
6141.728	56.1137	0.704	-2.284
6141.729	56.1135	0.704	-0.503
6141.729	56.1135	0.704	-1.214
6141.729	56.1137	0.704	-0.503
6141.729	56.1137	0.704	-1.214
6141.730	56.1134	0.704	-0.077
6141.730	56.1136	0.704	-0.077
6141.730	56.1138	0.704	-0.077
6141.731	56.1135	0.704	-0.709
6141.731	56.1135	0.704	-1.327
6141.731	56.1137	0.704	-0.709
6141.731	56.1137	0.704	-1.327
6141.732	56.1135	0.704	-0.959

Continued on next page

Table D.1 – continued from previous page

Wavelength	Specie	EP's	$\log gf$
6141.732	56.1135	0.704	-1.281
6141.732	56.1137	0.704	-0.959
6141.733	56.1137	0.704	-1.281
6496.898	56.1137	0.604	-1.886
6496.899	56.1135	0.604	-1.886
6496.901	56.1137	0.604	-1.186
6496.902	56.1135	0.604	-1.186
6496.906	56.1135	0.604	-0.739
6496.906	56.1137	0.604	-0.739
6496.910	56.1134	0.604	-0.380
6496.910	56.1136	0.604	-0.380
6496.910	56.1138	0.604	-0.380
6496.916	56.1135	0.604	-1.583
6496.916	56.1137	0.604	-1.583
6496.917	56.1135	0.604	-1.186
6496.918	56.1137	0.604	-1.186
6496.920	56.1135	0.604	-1.186
6496.922	56.1137	0.604	-1.186

Appendix E

Sensitivity Matrix for Survey Sample

TABLE E.1: Element sensitivity to the stellar parameter variations (ΔT_{eff}=+50K, $\Delta \log g$=+0.2 dex, Δ[Fe/H]=+0.10, and ΔV_m=+0.10)

Cluster	Element	T_{eff}	$\log g$	[Fe/H]	V_m	star
NGC 104	A(Cu)	0.04	0.00	-0.04	-0.11	m
	A(Y)	-0.03	0.10	-0.05	-0.03	
	A(Ba)	0.02	0.07	0.00	-0.11	
	A(La)	0.08	0.16	0.10	0.07	
	A(Eu)	-0.03	0.07	0.03	0.00	
NGC 288	A(Cu)	0.08	0.02	-0.03	-0.05	e
	A(Y)	0.02	0.04	-0.04	-0.07	
	A(Ba)	0.05	0.09	0.01	-0.10	
	A(La)	0.05	0.10	0.05	0.02	
	A(Eu)	0.00	0.09	0.04	0.01	
NGC 1904	A(Cu)	0.09	0.00	0.01	0.01	e
	A(Y)	0.04	0.07	0.00	-0.02	
	A(Ba)	0.06	0.11	0.03	-0.06	
	A(La)	0.01	0.06	0.09	-0.01	
	A(Eu)	0.03	0.07	0.04	0.01	
NGC 2808	A(Cu)	0.04	0.03	-0.04	-0.06	m

Continued on next page

Table E.1 – continued from previous page

Cluster	Element	$T_{\rm eff}$	$\log g$	[Fe/H]	V_m	star
NGC 2808	A(Y)	0.03	0.06	-0.02	-0.05	m
	A(Ba)	0.01	0.06	0.01	-0.12	
	A(La)	0.02	0.09	0.03	0.00	
	A(Eu)	0.01	0.08	0.03	0.01	
NGC 3201	A(Cu)	0.04	0.01	-0.02	-0.02	a
	A(Y)	0.01	0.06	0.00	-0.06	
	A(Ba)	0.02	0.08	0.02	-0.08	
	A(La)	0.02	0.07	0.10	-0.01	
	A(Eu)	0.00	0.08	0.03	-0.02	
NGC 4590	A(Cu)	0.08	0.00	0.00	0.01	n
	A(Y)	0.04	0.07	0.01	-0.02	
	A(Ba)	0.03	0.07	0.00	-0.05	
	A(La)	0.06	0.09	0.02	0.03	
	A(Eu)	0.00	0.05	0.00	0.00	
NGC 5904	A(Cu)	0.07	0.03	0.00	-0.02	f
	A(Y)	0.01	0.07	0.01	-0.05	
	A(Ba)	0.02	0.10	0.03	-0.10	
	A(La)	0.03	0.10	0.04	0.01	
	A(Eu)	0.00	0.10	0.03	0.01	
NGC 6121	A(Cu)	0.01	0.01	-0.03	-0.10	b
	A(Y)	0.03	0.05	-0.02	-0.06	
	A(Ba)	0.03	0.09	0.04	-0.10	
	A(La)	0.02	0.09	0.04	0.02	
	A(Eu)	0.00	0.10	0.04	0.00	
NGC 6171	A(Cu)	0.10	0.08	0.02	-0.02	f
	A(Y)	0.03	0.06	-0.01	-0.05	
	A(Ba)	0.02	0.07	0.03	-0.09	
	A(La)	0.09	0.14	0.09	0.07	
	A(Eu)	0.00	0.05	0.01	-0.01	

Continued on next page

Table E.1 – continued from previous page

Cluster	Element	$T_{\rm eff}$	$\log g$	[Fe/H]	V_m	star
NGC 6218	A(Cu)	0.08	0.03	-0.02	-0.05	g
	A(Y)	0.04	0.07	-0.01	-0.05	
	A(Ba)	0.02	0.09	0.02	-0.09	
	A(La)	0.05	0.08	0.05	0.01	
	A(Eu)	0.00	0.1	0.03	0.01	
NGC 6254	A(Cu)	0.08	-0.02	-0.01	0.00	e
	A(Y)	0.03	0.07	0.01	-0.03	
	A(Ba)	0.03	0.08	0.02	-0.07	
	A(La)	0.02	0.08	0.10	0.00	
	A(Eu)	0.00	0.10	0.02	0.01	
NGC 6397	A(Cu)	0.07	-0.01	-0.02	0	b
	A(Y)	0.04	0.07	0.02	0.01	
	A(Ba)	0.04	0.06	0.01	-0.05	
	A(La)	0.03	0.08	0.04	0.02	
	A(Eu)	0.01	0.07	0.01	-0.01	
NGC 6752	A(Cu)	0.08	0.02	-0.02	-0.03	d
	A(Y)	0.02	0.05	-0.05	-0.05	
	A(Ba)	0.01	0.07	0.02	-0.12	
	A(La)	0.02	0.06	0.08	0.01	
	A(Eu)	0.11	0.13	0.09	0.07	
NGC 6809	A(Cu)	0.09	0.00	-0.02	0.01	h
	A(Y)	-0.01	0.04	0.00	-0.03	
	A(Ba)	0.02	0.07	0.02	-0.09	
	A(La)	0.03	0.07	0.03	0.01	
	A(Eu)	-0.01	0.09	0.03	0.01	
NGC 6838	A(Cu)	0.15	0.01	-0.01	-0.10	c
NGC 6838	A(Y)	0.01	0.12	-0.02	-0.06	c
	A(Ba)	-0.01	0.08	0.02	-0.19	
	A(La)	0.08	0.14	0.09	0.08	

Continued on next page

Table E.1 – continued from previous page

Cluster	Element	$T_{\rm eff}$	$\log g$	[Fe/H]	V_m	star
	A(Eu)	-0.02	0.09	0.02	-0.01	
NGC 7078	A(Cu)	0.09	-0.01	0.00	0.02	n
	A(Y)	0.03	0.05	0.01	0.00	
	A(Ba)	0.04	0.07	0.00	-0.06	
	A(La)	0.04	0.07	0.02	0.02	
	A(Eu)	0.00	0.03	0.01	-0.01	
NGC 7099	A(Cu)	0.08	-0.02	-0.01	0.00	e
	A(Y)	0.04	0.06	0.01	-0.01	
	A(Ba)	0.06	0.08	0.00	-0.04	
	A(La)	0.06	0.09	0.01	0.04	
	A(Eu)	0.04	0.08	0.03	0.04	

TABLE E.2: Stellar parameters from Carretta et al. (2009) of every star analysed. In addition, the abundances determined by the present thesis are displayed in the last columns.

Cluster	star	T_{eff}	$\log g$	[Fe/H]I	V_m	[Fe/H]II	fCu	[Cu/Fe]	[Y/Fe]	[Ba/Fe]	fLa	[La/Fe]	fEu	[Eu/Fe]
NGC104	a	3999	1.01	-0.77	1.48	-0.80		0.40	-0.19	0.13		-0.14		0.39
NGC104	b	4061	1.14	-0.75	1.64	-0.79		0.42	-0.14	-0.14		-0.06		0.32
NGC104	c	4183	1.30	-0.83	1.49	-0.84		0.68	-0.14	0.26		-0.03		0.39
NGC104	d	4231	1.47	-0.68	1.54	-0.67		0.61	-0.25	0.00		-0.12		0.33
NGC104	e	3992	0.99	-0.84	1.56	-0.82		0.51	-0.08	0.00		-0.01		0.38
NGC104	f	4202	1.42	-0.77	1.31	-0.75		0.90	-0.10	0.50		-0.09		0.42
NGC104	g	4142	1.30	-0.71	1.54	-0.72		0.27	-0.24	-0.04		-0.12		0.28
NGC104	h	4214	1.44	-0.78	1.38	-0.99		-0.05	-0.15	-0.06		0.04		0.38
NGC104	i	4072	1.16	-0.77	1.53	-0.90		0.40	-0.12	0.10		0.01		0.46
NGC104	l	4164	1.34	-0.83	1.47	-0.86		0.90	-0.06	0.13		0.00		0.40
NGC104	m	4119	1.25	-0.70	1.69	-0.66		0.40	-0.35	-0.23		-0.13		0.33
NGC1904	a	4603	1.67	-1.63	1.35	-1.58		-0.60	0.09	0.38	<	0.43		0.57
NGC1904	b	4378	1.23	-1.61	1.49	-1.58		-0.60	0.03	0.27		0.22		0.41
NGC1904	c	4560	1.60	-1.59	1.36	-1.53		-0.52	0.01	0.29	<	0.22	<	0.39
NGC1904	d	4544	1.55	-1.55	1.73	-1.51		-0.71	-0.11	-0.07	<	0.19		0.44
NGC1904	e	4512	1.51	-1.62	1.77	-1.64		-0.58	-0.07	0.04	<	0.27		0.47
NGC1904	f	4430	1.34	-1.54	1.66	-1.49		-0.70	-0.14	-0.03	<	0.08		0.31
NGC1904	g	4596	1.63	-1.55	1.73	-1.54		-0.61	-0.04	0.10	<	0.66	<	0.41
NGC1904	h	4583	1.61	-1.55	1.78	-1.52		-0.74	-0.18	-0.08	<	0.27	<	0.37
NGC1904	i	4612	1.70	-1.57	1.75	-1.54		-0.56	-0.16	0.04	<	0.37		0.59
NGC1904	l	4386	1.25	-1.57	1.92	-1.56		-0.70	-0.20	-0.16		0.38		0.61
NGC2808	a	4277	1.13	-1.17	1.53	-1.20		0.00	0.09	0.17		0.23		0.61
NGC2808	b	4322	1.22	-1.21	1.62	-1.24		0.08	0.11	0.10		0.26		0.66
NGC2808	c	4343	1.24	-1.18	1.66	-1.23		-0.07	0.11	0.22		0.38		0.80
NGC2808	d	4315	1.21	-1.21	1.66	-1.24		-0.02	0.03	0.09		0.23		0.62
NGC2808	e	4469	1.40	-1.19	1.57	-1.15		-0.09	0.18	0.20		0.22		0.60
NGC2808	f	4641	1.74	-1.13	1.83	-1.16		-0.27	0.13	0.09		0.32		0.67
NGC2808	g	4630	1.69	-1.17	1.69	-1.23		-0.06	0.21	0.37		0.55		0.72
NGC2808	h	4574	1.63	-1.12	1.81	-1.24		-0.12	0.06	0.11		0.27		0.70
NGC2808	i	4457	1.44	-1.27	1.47	-1.29		-0.10	0.13	0.21		0.19		0.65
NGC2808	l	4311	1.19	-0.98	1.69	-0.98		-0.29	-0.23	-0.22		0.03		0.45
NGC2808	m	4408	1.37	-1.13	1.49	-1.13		-0.13	0.02	0.02		0.09		0.57
NGC2808	n	4325	1.17	-1.06	1.53	-1.06		0.06	0.00	0.15		0.03		0.53
NGC288	a	4090	0.66	-1.35	1.74	-1.44		0.21	0.29	0.23		0.31		0.58
NGC288	b	4172	0.85	-1.33	1.88	-1.48		0.02	0.22	0.14		0.40		0.67
NGC288	c	4335	1.21	-1.37	1.67	-1.43		0.10	0.30	0.30		0.36		0.56
NGC288	d	4379	1.28	-1.34	1.59	-1.37		0.22	0.37	0.38		0.30		0.54
NGC288	e	4456	1.46	-1.30	1.62	-1.32		0.00	0.32	0.30		0.20		0.55
NGC288	f	4478	1.52	-1.30	1.44	-1.34		0.16	0.33	0.58		0.27		0.69
NGC288	g	4599	1.73	-1.21	1.80	-1.22		-0.17	0.10	0.12		0.39		0.52
NGC288	h	4694	1.92	-1.27	1.54	-1.32		0.12	0.40	0.37		0.38		0.55
NGC288	i	4711	1.97	-1.35	1.52	-1.34		0.30	0.37	0.50		0.48		0.50
NGC288	l	4738	2.09	-1.23	1.54	-1.24		-0.19	0.45	0.33		0.47		0.61
NGC3201	a	4442	1.47	-1.59	1.41	-1.55		-0.45	0.14	0.26		0.06	<	0.40
NGC3201	b	4485	1.59	-1.46	1.69	-1.39		-0.68	-0.17	-0.06		-0.08		0.37
NGC3201	c	4495	1.61	-1.50	1.59	-1.41		-0.77	-0.24	-0.07		-0.09		0.18
NGC3201	d	4311	1.16	-1.46	1.56	-1.53		-0.33	0.00	0.13		0.08		0.52
NGC3201	e	4496	1.61	-1.44	1.69	-1.38		-0.80	-0.04	0.00		0.08		0.43
NGC3201	f	4537	1.71	-1.46	1.67	-1.42		-0.63	-0.12	-0.09		0.12		0.46
NGC3201	g	4364	1.30	-1.48	1.79	-1.46		-0.45	-0.11	-0.10		0.09		0.49
NGC3201	h	4368	1.32	-1.60	1.34	-1.48		-0.50	-0.05	0.15		-0.11		0.31
NGC3201	i	4356	1.22	-1.59	1.56	-1.40		-0.70	-0.20	-0.03		-0.07		0.23
NGC3201	l	4437	1.47	-1.53	1.34	-1.48		-0.31	0.13	0.33		0.07		0.38
NGC3201	m	4410	1.40	-1.57	1.33	-1.54		-0.42	0.14	0.37		0.16		0.46
NGC3201	n	4496	1.61	-1.57	1.5	-1.59		-0.55	0.16	0.34		0.17	<	0.66
NGC3201	p	4530	1.70	-1.42	1.65	-1.42		-0.39	-0.06	0.03		0.02	<	0.63
NGC4590	a	4684	1.63	-2.27	1.95	-2.26	<	-1.25	-0.33	-0.26	<	0.58	<	0.49
NGC4590	b	4740	1.78	-2.26	1.38	-2.18	<	-0.85	-0.28	-0.13	<	0.52	<	0.85
NGC4590	c	4547	1.28	-2.19	1.75	-2.16		-0.65	-0.39	-0.33	<	0.07	<	0.40
NGC4590	e	4648	1.53	-2.20	2.03	-2.23	<	-0.82	-0.35	-0.25	<	0.52	<	0.62
NGC4590	f	4729	1.72	-2.25	1.39	-2.17	<	-0.80	-0.35	-0.08	<	0.48	<	0.67
NGC4590	g	4657	1.55	-2.31	2.04	-2.44	<	-0.52	-0.10	-0.06	<	0.73	<	0.83

Continued on next page

Table E.2 – continued from previous page

Cluster	star	T_{eff}	$\log g$	[Fe/H]I	V_m	[Fe/H]II	fCu	[Cu/Fe]	[Y/Fe]	[Ba/Fe]	fLa	[La/Fe]	fEu	[Eu/Fe]
NGC4590	h	4693	1.67	-2.24	1.61	-2.21	<	-0.82	-0.40	-0.13	<	0.29	<	0.82
NGC4590	i	4568	1.31	-2.23	1.65	-2.20	<	-0.80	-0.47	-0.20	<	0.22	<	0.23
NGC4590	l	4612	1.40	-2.28	1.56	-2.27		-0.70	-0.23	-0.01	<	0.39	<	0.57
NGC4590	m	4726	1.73	-2.29	1.55	-2.26	<	-0.67	-0.14	-0.11	<	0.63	<	0.87
NGC4590	n	4673	1.62	-2.25	1.65	-2.42	<	-0.71	-0.10	0.12	<	0.73	<	0.92
NGC4590	o	4710	1.71	-2.32	1.36	-2.29	<	-0.75	-0.26	-0.12	<	0.67	<	0.67
NGC4590	p	4700	1.67	-2.36	1.37	-2.37	<	-0.50	-0.14	0.25	<	0.41	<	0.67
NGC5634	a	4137	0.61	-1.91	2.11	-1.93		-0.61	-0.26	-0.14		0.30		0.63
NGC5634	b	4221	0.76	-1.86	2.10	-1.89		-0.35	0.18	-0.01		0.33		0.48
NGC5634	c	4376	1.06	-1.89	1.84	-1.92		-0.56	0.10	0.12		0.42		0.61
NGC5634	d	4376	1.04	-1.79	2.00	-1.88		-0.41	0.01	-0.05	<	0.19		0.49
NGC5634	e	4374	1.04	-1.82	1.88	-1.88		-0.42	0.21	0.10		0.53		0.54
NGC5634	f	4413	1.12	-1.93	1.66	-1.90		-0.50	-0.03	0.30		0.42		0.55
NGC5634	g	4415	1.11	-1.86	1.91	-1.93		-0.31	0.47	0.22		0.54		0.65
NGC5904	a	4289	1.21	-1.29	1.51	-1.29		-0.06	0.23	0.29		0.12		0.60
NGC5904	b	4312	1.26	-1.33	1.45	-1.38		-0.30	0.19	0.38		0.13		0.70
NGC5904	c	4370	1.37	-1.33	1.72	-1.32		-0.39	-0.08	-0.05		0.02		0.71
NGC5904	d	4413	1.44	-1.43	1.66	-1.42		-0.13	0.15	0.13		0.00		0.68
NGC5904	e	4428	1.47	-1.42	1.49	-1.40		-0.05	0.33	0.31		0.18		0.61
NGC5904	f	4437	1.50	-1.24	1.43	-1.19		-0.32	0.10	0.09		0.18		0.51
NGC5904	g	4463	1.55	-1.37	1.48	-1.34		-0.15	0.31	0.38		0.36		0.77
NGC5904	h	4495	1.60	-1.33	1.71	-1.29		-0.11	0.05	0.10		0.16		0.56
NGC5904	i	4549	1.70	-1.33	1.33	-1.31		-0.23	0.29	0.47		0.25	<	0.63
NGC5904	l	4568	1.72	-1.36	1.22	-1.37		-0.24	0.23	0.68		0.11	<	0.66
NGC5904	m	4578	1.74	-1.36	1.74	-1.42		-0.28	0.22	0.20	<	0.41	<	0.75
NGC5904	n	4585	1.76	-1.27	1.51	-1.28		-0.32	0.17	0.23		0.21	<	0.74
NGC5904	o	4294	1.23	-1.34	1.65	-1.38		-0.21	0.05	0.16		0.18	<	0.68
NGC5904	p	4355	1.34	-1.38	1.70	-1.41		-0.20	0.07	0.13		0.28	<	0.67
NGC6121	a	4284	1.35	-1.14	1.35	-1.12		0.62	0.53	0.79		0.36		0.86
NGC6121	b	4332	1.45	-1.15	1.60	-1.20		0.45	0.47	0.54		0.41		0.50
NGC6121	c	4408	1.67	-1.16	1.56	-1.19		0.12	0.53	0.59		0.42		0.56
NGC6121	d	4243	1.24	-1.14	1.69	-1.10		0.18	0.38	0.19		0.18		0.33
NGC6121	e	4448	1.72	-1.25	1.39	-1.25		0.37	0.55	0.81		0.47		0.64
NGC6121	f	4261	1.28	-1.28	1.70	-1.26		0.01	0.24	0.38		0.33		0.40
NGC6121	g	4279	1.39	-1.15	1.46	-1.11		0.31	0.30	0.63		0.29		0.45
NGC6121	h	4400	1.66	-1.13	1.38	-1.13		0.40	0.53	0.76		0.39		0.41
NGC6121	i	4380	1.58	-1.11	1.69	-1.10		0.09	0.31	0.33		0.36		0.34
NGC6121	l	4264	1.31	-1.15	1.74	-1.19		0.14	0.26	0.34		0.38		0.43
NGC6121	m	4420	1.70	-1.16	1.30	-1.15		0.45	0.62	0.81		0.41		0.47
NGC6121	n	4394	1.61	-1.18	1.39	-1.20		0.32	0.64	0.84		0.49		0.61
NGC6121	o	4380	1.58	-1.17	1.30	-1.17		0.50	0.71	0.89		0.40		0.49
NGC6121	p	4118	1.16	-1.2	1.33	-1.20		0.40	0.39	0.74		0.34		0.40
NGC6171	b	4604	2.25	-1.03	1.11	-1.03		0.40	0.72	0.87		0.57		0.76
NGC6171	c	4190	1.35	-1.08	1.46	-1.09		0.46	0.24	0.47		0.28		0.45
NGC6171	d	4158	1.37	-1.00	1.37	-1.05		0.80	0.36	0.79		0.46		0.49
NGC6171	e	4607	2.27	-1.11	1.01	-1.15		0.79	1.03	1.14	<	0.63		0.98
NGC6171	f	4574	2.18	-0.95	1.36	-1.02		1.25	0.26	0.27	<	-0.09		0.51
NGC6218	b	4223	1.06	-1.36	1.72	-1.42		0.07	0.08	0.07		0.24		0.41
NGC6218	c	4239	1.07	-1.31	1.79	-1.35		-0.05	0.07	-0.02		0.12		0.36
NGC6218	d	4235	1.08	-1.34	1.70	-1.37		0.14	0.10	0.06		0.15		0.37
NGC6218	e	4317	1.22	-1.33	1.62	-1.40		0.00	0.23	0.18		0.16		0.49
NGC6218	f	4357	1.34	-1.23	1.53	-1.25		-0.01	0.05	0.16		0.08		0.45
NGC6218	g	4383	1.39	-1.35	1.57	-1.38		0.15	0.27	0.25		0.19	<	—
NGC6218	h	4392	1.44	-1.34	1.62	-1.38		-0.04	0.22	0.17		0.12		0.33
NGC6218	l	4523	1.70	-1.38	1.44	-1.41		-0.05	0.48	0.45		0.07		0.39
NGC6218	m	4537	1.72	-1.29	1.56	-1.30		-0.22	0.13	0.28		0.18		0.41
NGC6218	n	4547	1.76	-1.33	1.52	-1.38		-0.15	0.35	0.28		0.25		0.52
NGC6218	p	4481	1.58	-1.37	1.60	-1.39		0.05	0.27	0.25		0.10		0.48
NGC6254	a	4381	1.29	-1.59	1.97	-1.66		-0.25	0.08	0.08		0.35		0.53
NGC6254	b	4425	1.36	-1.63	1.66	-1.61		-0.23	0.08	0.24		0.27		0.55
NGC6254	c	4591	1.63	-1.50	2.30	-1.59		-0.10	0.15	0.06		0.48		0.53
NGC6254	d	4511	1.51	-1.70	1.11	-1.61		-0.73	0.17	0.77		0.17		0.31
NGC6254	e	4535	1.55	-1.59	1.74	-1.46		-0.75	-0.16	-0.08	<	0.12	<	0.05
NGC6254	f	4512	1.50	-1.59	2.03	-1.62		-1.43	-0.01	-0.04		0.36	<	0.45
NGC6254	g	4540	1.55	-1.59	1.62	-1.61		-1.43	0.19	0.26		0.28		0.58

Continued on next page

Table E.2 – continued from previous page

Cluster	star	T_{eff}	$\log g$	[Fe/H]I	V_m	[Fe/H]II	fCu	[Cu/Fe]	[Y/Fe]	[Ba/Fe]	fLa	[La/Fe]	fEu	[Eu/Fe]
NGC6254	h	4495	1.46	-1.47	1.93	-1.43		-0.41	-0.1	-0.09		0.19		0.37
NGC6254	i	4503	1.47	-1.58	1.97	-1.67		-0.30	0.11	0.12		0.43		0.59
NGC6254	l	4482	1.43	-1.57	1.71	-1.64		-0.21	0.21	0.29		0.37		0.47
NGC6254	m	4570	1.59	-1.55	1.99	-1.57		-0.55	-0.05	-0.08	<	0.19		0.52
NGC6254	n	4565	1.58	-1.57	1.91	-1.61		-0.43	0.11	0.11		0.31		0.56
NGC6254	o	4584	1.62	-1.60	1.58	-1.65		-0.40	0.26	0.46		0.45		0.70
NGC6254	p	4737	1.94	-1.50	2.21	-1.60		-0.28	0.10	0.15	<	0.45	<	0.67
NGC6397	a	4863	1.87	-1.94	1.78	-1.99	<	-0.53	-0.02	0.03	<	0.82	<	0.59
NGC6397	b	4798	1.72	-1.97	1.88	-2.00	<	-0.35	-0.08	-0.04	<	0.53	<	0.74
NGC6397	c	4758	1.63	-2.03	1.60	-2.09	<	-0.86	-0.11	0.16	<	0.24	<	0.56
NGC6397	d	4760	1.65	-2.00	1.62	-2.04		-0.60	-0.10	0.08	<	0.42	<	0.79
NGC6397	e	4781	1.74	-2.04	1.72	-2.03		-0.45	-0.10	-0.02	<	0.38		0.69
NGC6397	f	4696	1.50	-1.92	2.23	-1.97		-0.54	-0.17	-0.23	<	0.35		0.62
NGC6397	g	4779	1.69	-1.93	1.88	-1.96		-0.85	-0.15	-0.12	<	0.53		0.64
NGC6397	h	4720	1.57	-2.04	2.16	-2.06		-0.61	-0.08	-0.12	<	0.35		0.72
NGC6397	i	4895	1.99	-1.98	1.88	-2.00	<	-0.65	0.00	-0.01	<	0.79	<	1.07
NGC6397	l	4953	2.11	-2.04	1.92	-2.09	<	-0.61	-0.02	-0.01	<	0.75	<	0.99
NGC6397	m	4856	1.87	-1.98	1.83	-2.02	<	-0.64	-0.09	0.09	<	0.67	<	0.94
NGC6397	n	4850	1.85	-1.96	2.15	-2.01	<	-0.60	-0.10	-0.19	<	0.50	<	0.80
NGC6397	o	4661	1.40	-2.03	1.91	-2.09		-0.56	-0.07	-0.02	<	0.46		0.48
NGC6752	a	4373	1.26	-1.53	1.42	-1.52		-0.42	0.22	0.40		0.15		0.38
NGC6752	b	4369	1.25	-1.59	1.51	-1.56		-0.45	0.10	0.26		0.10		0.45
NGC6752	c	4407	1.36	-1.60	1.62	-1.53		-0.50	-0.01	0.13		0.08		0.41
NGC6752	d	4366	1.24	-1.46	1.37	-1.44		-0.37	0.20	0.46		0.14		0.30
NGC6752	e	4286	1.05	-1.56	1.51	-1.52		-0.38	0.06	0.28		0.14		0.34
NGC6752	f	4310	1.11	-1.51	1.35	-1.47		-0.38	0.11	0.43		0.08		0.38
NGC6752	g	4400	1.34	-1.58	1.30	-1.51		-0.40	0.17	0.62		0.16		0.48
NGC6752	h	4532	1.63	-1.56	1.21	-1.53		-0.30	0.39	0.82		0.29		0.52
NGC6752	i	4325	1.16	-1.48	1.57	-1.45		-0.47	0.05	0.19		0.09		0.40
NGC6752	l	4312	1.10	-1.62	1.69	-1.61		-0.42	-0.04	0.10		0.08		0.47
NGC6752	m	4315	1.12	-1.61	1.50	-1.58		-0.47	0.06	0.28		0.15		0.47
NGC6752	n	4384	1.30	-1.61	1.75	-1.58		-0.41	0.05	0.19		0.23		0.54
NGC6752	o	4338	1.19	-1.55	1.66	-1.52		-0.43	0.04	0.17		0.19		0.44
NGC6752	p	4371	1.27	-1.51	1.64	-1.48		-0.43	0.08	0.23		0.13		0.45
NGC6809	a	4481	1.40	-1.86	1.52	-1.87		-0.70	0.03	0.44	<	0.28		0.63
NGC6809	b	4382	1.20	-1.93	1.58	-1.95		-0.54	0.10	0.33	<	0.35		0.75
NGC6809	c	4386	1.25	-2.07	1.64	-2.04		-0.73	0.07	0.30	<	0.27		0.68
NGC6809	d	4389	1.24	-1.96	1.84	-1.91		-0.58	-0.01	0.13		0.45		0.72
NGC6809	e	4398	1.24	-1.95	1.58	-1.91		-0.50	0.03	0.31		0.46		0.71
NGC6809	f	4412	1.28	-1.85	2.23	-1.81		-0.73	-0.15	-0.17		0.31	<	0.73
NGC6809	g	4433	1.32	-1.90	1.52	-1.89		-0.67	0.11	0.38	<	0.30		0.66
NGC6809	h	4444	1.33	-1.97	1.48	-1.97		-0.44	0.08	0.49		0.35		0.82
NGC6809	i	4458	1.38	-1.92	1.89	-1.96		-0.61	0.15	0.32		0.51		0.78
NGC6809	l	4470	1.41	-1.94	1.60	-1.96		-0.64	0.17	0.43	<	0.35		0.89
NGC6809	m	4474	1.40	-1.89	1.77	-1.83		-0.63	-0.07	0.04		0.31		0.61
NGC6809	n	4499	1.45	-1.85	1.68	-1.81		-0.77	-0.04	0.27	<	0.30		0.67
NGC6809	o	4499	1.43	-2.00	1.44	-2.00		-0.50	0.09	0.46		0.52		0.74
NGC6809	p	4522	1.52	-1.97	1.37	-2.03		-0.58	0.37	0.68	<	0.64		0.99
NGC6838	a	4024	1.23	-0.78	1.40	-0.78		0.37	-0.06	0.12		0.10		0.38
NGC6838	b	4196	1.39	-0.80	1.44	-0.84		0.80	0.12	0.30		0.16		0.62
NGC6838	c	4033	1.09	-0.84	1.40	-0.83		0.80	0.06	0.44		0.22		0.53
NGC6838	d	3968	0.91	-0.77	1.54	-0.73		0.13	-0.25	-0.03		0.17		0.41
NGC6838	e	3985	0.87	-0.83	1.72	-0.89		0.30	-0.13	-0.11		0.22		0.44
NGC6838	f	4235	1.47	-0.85	1.5	-0.91		0.70	0.06	0.38		0.29		0.57
NGC6838	g	4132	1.27	-0.85	1.64	-0.97		0.68	0.04	0.26		0.21		0.69
NGC6838	h	4164	1.30	-0.78	1.89	-0.84		0.14	-0.17	-0.18		0.24		0.47
NGC6838	l	4135	1.27	-0.95	1.65	-0.97		0.62	0.05	0.16		0.22		0.61
NGC6838	m	3985	0.90	-0.77	1.92	-0.76		0.27	-0.07	-0.01		0.28		0.36
NGC6838	n	3948	0.85	-0.81	1.64	-0.77		0.04	-0.33	-0.26		0.16		0.38
NGC6838	o	3967	0.85	-0.94	1.61	-0.96		0.20	-0.08	-0.06		0.29		0.51
NGC7078	a	4567	1.26	-2.31	1.50	-2.27	<	-0.74	0.06	0.51	<	0.41		0.68
NGC7078	b	4324	0.69	-2.23	2.16	-2.29		-0.57	-0.08	-0.10		0.32		0.66
NGC7078	d	4697	1.52	-2.34	2.23	-2.34	<	-0.30	-0.16	-0.24	<	0.75	<	0.90
NGC7078	e	4518	1.09	-2.30	1.97	-2.40		-0.68	0.11	0.26	<	0.81		0.90
NGC7078	f	4832	1.83	-2.35	2.08	-2.46	<	-0.29	0.13	-0.06	<	0.71	<	1.00

Continued on next page

Table E.2 – continued from previous page

Cluster	star	$T_{\mathbf{eff}}$	$\log g$	[Fe/H]I	V_m	[Fe/H]II	fCu	[Cu/Fe]	[Y/Fe]	[Ba/Fe]	fLa	[La/Fe]	fEu	[Eu/Fe]
NGC7078	g	4735	1.61	-2.41	1.72	-2.41	<	-0.40	-0.02	-0.26	<	0.89	<	0.40
NGC7078	h	4746	1.66	-2.35	1.19	-2.36	<	-0.40	-0.03	0.36	<	0.56	<	0.97
NGC7078	i	4623	1.34	-2.28	1.62	-2.28	<	-0.57	0.08	0.31	<	0.90	<	0.84
NGC7078	l	4754	1.64	-2.38	1.35	-2.40	<	-0.70	0.20	0.65	<	0.62	<	0.92
NGC7078	m	4810	1.77	-2.21	2.12	-2.30	<	-0.51	0.04	-0.03	<	0.49		1.14
NGC7078	n	4646	1.41	-2.34	1.79	-2.38	<	-0.38	0.17	0.35	<	0.79		1.04
NGC7078	o	4805	1.75	-2.30	1.10	-2.25	<	-0.60	0.19	1.04	<	1.00	<	0.72
NGC7078	l	4630	1.35	-2.36	1.65	-2.45	<	-0.69	0.04	0.31	<	0.57		0.96
NGC7099	a	4550	1.37	-2.36	2.21	-2.33		-0.58	-0.15	-0.28	<	0.22	<	0.82
NGC7099	b	4897	2.17	-2.31	2.08	-2.30	<	-0.60	0.05	-0.08	<	1.21	<	0.99
NGC7099	c	4539	1.35	-2.44	1.87	-2.37		-0.49	-0.05	-0.13	<	0.35	<	0.73
NGC7099	d	4497	1.26	-2.39	1.21	-2.31		-0.71	-0.11	0.23	<	0.59	<	0.63
NGC7099	e	4600	1.46	-2.31	2.07	-2.29		-0.50	-0.15	-0.14	<	0.48	<	0.74
NGC7099	f	4571	1.36	-2.30	2.05	-2.27		-0.71	-0.17	-0.26	<	0.32	<	0.70
NGC7099	g	4683	1.66	-2.30	1.88	-2.32	<	-0.61	-0.03	-0.21	<	0.59	<	0.94
NGC7099	h	4537	1.26	-2.35	2.12	-2.37		-0.54	-0.05	-0.17	<	0.48	<	0.62
NGC7099	i	4258	0.41	-2.31	2.67	-2.48		-0.62	-0.13	-0.47	<	0.29	<	0.55
NGC7099	l	4868	2.11	-2.39	2.13	-2.36	<	-0.30	0.09	-0.12	<	0.77	<	1.01

Bibliography

Alonso, A., S. Arribas, and C. Martinez-Roger (1996, September). The empirical scale of temperatures of the low main sequence (FOV-K5V). *A&A 313*, 873–890.

Alonso, A., S. Arribas, and C. Martínez-Roger (1999, December). The effective temperature scale of giant stars (F0-K5). II. Empirical calibration of T_{eff} versus colours and [Fe/H]. *A&AS 140*, 261–277.

Asplund, M., N. Grevesse, A. J. Sauval, and P. Scott (2009a, September). The Chemical Composition of the Sun. *ARA&A 47*(1), 481–522.

Asplund, M., N. Grevesse, A. J. Sauval, and P. Scott (2009b, September). The Chemical Composition of the Sun. *ARA&A 47*(1), 481–522.

Ballero, S. K., F. Matteucci, L. Origlia, and R. M. Rich (2007, May). Formation and evolution of the Galactic bulge: constraints from stellar abundances. *A&A 467*(1), 123–136.

Bartkevicius, A. (1996, January). A New Version of the Catalog of CH and Related Stars (CH95 Catalog). *Baltic Astronomy 5*, 217–229.

Bastian, N., I. Cabrera-Ziri, and M. Salaris (2015, May). A general abundance problem for all self-enrichment scenarios for the origin of multiple populations in globular clusters. *MNRAS 449*(3), 3333–3346.

Bastian, N. and C. Lardo (2018, September). . *ARA&A 56*, 83–136.

Battistini, C. and T. Bensby (2015, May). The origin and evolution of the odd-Z iron-peak elements Sc, V, Mn, and Co in the Milky Way stellar disk. *A&A 577*, A9.

Bekki, K., S. W. Campbell, J. C. Lattanzio, and J. E. Norris (2007, May). Origin of abundance inhomogeneity in globular clusters. *MNRAS 377*(1), 335–351.

Bovy, J. (2015, February). galpy: A python Library for Galactic Dynamics. *ApJS 216*(2), 29.

Bragaglia, A., E. Carretta, R. G. Gratton, M. Tosi, G. Bonanno, P. Bruno, A. Calì, R. Claudi, R. Cosentino, S. Desidera, G. Farisato, M. Rebeschini, and S. Scuderi (2001, January). Metal Abundances of Red Clump Stars in Open Clusters. I. NGC 6819. *AJ 121*(1), 327–336.

Bressan, A., P. Marigo, L. Girardi, B. Salasnich, C. Dal Cero, S. Rubele, and A. Nanni (2012, November). PARSEC: stellar tracks and isochrones with the PAdova and TRieste Stellar Evolution Code. *MNRAS 427*(1), 127–145.

Busso, M. M., K.-L. Kratz, S. Palmerini, W. Akram, and V. Antonuccio-Delogu (2022, October). Production of solar abundances for nuclei beyond Sr: The s- and r-process perspectives. *Frontiers in Astronomy and Space Sciences 9*, 956633.

Cameron, A. G. W. and W. A. Fowler (1971, February). Lithium and the s-PROCESS in Red-Giant Stars. *ApJ 164*, 111.

Carretta, E. and A. Bragaglia (2021, February). Excess of Ca (and Sc) produced in globular cluster multiple populations: a first census in 77 Galactic globular clusters. *A&A 646*, A9.

Carretta, E., A. Bragaglia, R. Gratton, V. D'Orazi, and S. Lucatello (2009, December). Intrinsic iron spread and a new metallicity scale for globular clusters. *A&A 508*(2), 695–706.

Carretta, E., A. Bragaglia, R. Gratton, and S. Lucatello (2009, October). Na-O anticorrelation and HB. VIII. Proton-capture elements and metallicities in 17 globular clusters from UVES spectra. *A&A 505*(1), 139–155.

Carretta, E., A. Bragaglia, R. G. Gratton, S. Lucatello, G. Catanzaro, F. Leone, M. Bellazzini, R. Claudi, V. D'Orazi, Y. Momany, S. Ortolani, E. Pancino, G. Piotto, A. Recio-Blanco, and E. Sabbi (2009, October). Na-O anticorrelation and HB. VII. The chemical composition of first and second-generation stars in 15 globular clusters from GIRAFFE spectra. *A&A 505*(1), 117–138.

Carretta, E., A. Bragaglia, R. G. Gratton, S. Lucatello, and V. D'Orazi (2012, May). Chemical Tagging of Three Distinct Populations of Red Giants in the Globular Cluster NGC 6752. *ApJL 750*(1), L14.

Carretta, E., A. Bragaglia, R. G. Gratton, S. Lucatello, and Y. Momany (2007, March). Na-O anticorrelation and horizontal branches. II. The Na-O anticorrelation in the globular cluster NGC 6752. *A&A 464*(3), 927–937.

Carretta, E., A. Bragaglia, R. G. Gratton, A. Recio-Blanco, S. Lucatello, V. D'Orazi, and S. Cassisi (2010, June). Properties of stellar generations in globular clusters and relations with global parameters. *A&A 516*, A55.

Carretta, E., A. Bragaglia, S. Lucatello, V. D'Orazi, R. G. Gratton, P. Donati, A. Sollima, and C. Sneden (2017, April). Chemical characterisation of the globular cluster NGC 5634 associated to the Sagittarius dwarf spheroidal galaxy. *A&A 600*, A118.

Carretta, E., A. Bragaglia, S. Lucatello, R. G. Gratton, V. D'Orazi, and A. Sollima (2018, July). Aluminium abundances in five discrete stellar populations of the globular cluster NGC 2808. *A&A 615*, A17.

Carretta, E., R. G. Gratton, A. Bragaglia, V. D'Orazi, and S. Lucatello (2013, February). An aluminium tool for multiple stellar generations in the globular clusters 47 Tucanae and M 4. *A&A 550*, A34.

Cayrel, R. (1988, January). The impact of very high S/N spectroscopy on stellar physics: proceedings of the 132nd Symposium of the International Astronomical Union held in Paris, France, June 29-July 3, 1987. In *The Impact of Very High S/N Spectroscopy on Stellar Physics*, Volume 132.

Cescutti, G. and C. Chiappini (2014, May). Explaining the Ba, Y, Sr, and Eu abundance scatter in metal-poor halo stars: constraints to the r-process. *A&A 565*, A51.

Cohen, J. G. (1999, May). The Spectra of Main-Sequence Stars in Galactic Globular Clusters. II. CH and CN Bands in M71. *AJ 117*(5), 2434–2439.

Cohen, J. G. (2011, October). No Heavy-element Dispersion in the Globular Cluster M92. *ApJL 740*(2), L38.

Cohen, J. G. and E. N. Kirby (2012, November). The Bizarre Chemical Inventory of NGC 2419, An Extreme Outer Halo Globular Cluster. *ApJ 760*(1), 86.

Cote, P., M. Zoccali, F. D. A. Hartwick, and J. B. Oke (1996, December). Carbon Stars in Globular Clusters. In *American Astronomical Society Meeting Abstracts*, Volume 189 of *American Astronomical Society Meeting Abstracts*, pp. 64.01.

Cottrell, P. L. and G. S. Da Costa (1981, April). Correlated cyanogen and sodium anomalies in the globular clusters 47 TUC and NGC 6752. *ApJL 245*, L79–L82.

Cowan, J. J. and F.-K. Thielemann (2004). R-process nucleosynthesis in supernovae. *Physics Today 57*(10), 47–53.

Cowan, J. J., F.-K. Thielemann, and J. W. Truran (1991). The r-process and nucleochronology. *Physics Reports 208*(4), 267–394.

Crawford, D. L. (1975, August). Four-colour and Hbeta photometry of O-type stars. *PASP 87*, 481–494.

Cristallo, S., L. Piersanti, O. Straniero, R. Gallino, I. Domínguez, C. Abia, G. Di Rico, M. Quintini, and S. Bisterzo (2011, December). Evolution, Nucleosynthesis, and Yields of Low-mass Asymptotic Giant Branch Stars at Different Metallicities. II. The FRUITY Database. *ApJS 197*(2), 17.

Cristallo, S., O. Straniero, L. Piersanti, and D. Gobrecht (2015, August). Evolution, Nucleosynthesis, and Yields of AGB Stars at Different Metallicities. III. Intermediate-mass Models, Revised Low-mass Models, and the ph-FRUITY Interface. *ApJS 219*(2), 40.

Cseh, B., B. Világos, M. P. Roriz, C. B. Pereira, V. D'Orazi, A. I. Karakas, B. Soós, N. A. Drake, S. Junqueira, and M. Lugaro (2022, April). Barium stars as tracers of s-process nucleosynthesis in AGB stars. I. 28 stars with independently derived AGB mass. *A&A 660*, A128.

Cunha, K., V. V. Smith, N. B. Suntzeff, J. E. Norris, G. S. Da Costa, and B. Plez (2002, July). The Evolution of Copper in the Globular Cluster ω Centauri. *AJ 124*(1), 379–388.

D'Antona, F., P. Ventura, A. Fabiola Marino, A. P. Milone, M. Tailo, M. Di Criscienzo, and E. Vesperini (2019a, January). The Lithium Test for Multiple Populations in Globular Clusters: Lithium in NGC 2808. *ApJL 871*(1), L19.

D'Antona, F., P. Ventura, A. Fabiola Marino, A. P. Milone, M. Tailo, M. Di Criscienzo, and E. Vesperini (2019b, January). The Lithium Test for Multiple Populations in Globular Clusters: Lithium in NGC 2808. *ApJL 871*(1), L19.

de Mink, S. E., O. R. Pols, N. Langer, and R. G. Izzard (2009, November). Massive binaries as the source of abundance anomalies in globular clusters. *A&A 507*(1), L1–L4.

Decressin, T., C. Charbonnel, and G. Meynet (2007, December). Origin of the abundance patterns in Galactic globular clusters: constraints on dynamical and chemical properties of globular clusters. *A&A 475*(3), 859–873.

Decressin, T., G. Meynet, C. Charbonnel, N. Prantzos, and S. Ekström (2007, March). Fast rotating massive stars and the origin of the abundance patterns in galactic globular clusters. *A&A 464*(3), 1029–1044.

Denissenkov, P. A. and F. D. A. Hartwick (2014, January). Supermassive stars as a source of abundance anomalies of proton-capture elements in globular clusters. *MNRAS 437*(1), L21–L25.

D'Ercole, A., F. D'Antona, and E. Vesperini (2011, August). Formation of multiple populations in globular clusters: constraints on the dilution by pristine gas. *MNRAS 415*(2), 1304–1309.

D'Ercole, A., F. D'Antona, and E. Vesperini (2016, October). Accretion of pristine gas and dilution during the formation of multiple-population globular clusters. *MNRAS 461*(4), 4088–4098.

Doherty, C. L., P. Gil-Pons, H. H. B. Lau, J. C. Lattanzio, L. Siess, and S. W. Campbell (2014, June). Super and massive AGB stars - III. Nucleosynthesis in metal-poor and very metal-poor stars - Z = 0.001 and 0.0001. *MNRAS 441*(1), 582–598.

D'Orazi, V., G. C. Angelou, R. G. Gratton, J. C. Lattanzio, A. Bragaglia, E. Carretta, S. Lucatello, and Y. Momany (2014, August). Lithium Abundances in Globular Cluster Giants: NGC 6218 (M12) and NGC 5904 (M5). *ApJ 791*(1), 39.

D'Orazi, V., S. W. Campbell, M. Lugaro, J. C. Lattanzio, M. Pignatari, and E. Carretta (2013, July). On the internal pollution mechanisms in the globular cluster NGC 6121 (M4): heavy-element abundances and AGB models. *MNRAS 433*(1), 366–381.

D'Orazi, V., R. Gratton, S. Lucatello, E. Carretta, A. Bragaglia, and A. F. Marino (2010, August). Ba Stars and Other Binaries in First and Second Generation Stars in Globular Clusters. *ApJL 719*(2), L213–L217.

D'Orazi, V., R. G. Gratton, G. C. Angelou, A. Bragaglia, E. Carretta, J. C. Lattanzio, S. Lucatello, Y. Momany, and A. Sollima (2015, March). On the Serendipitous Discovery of a Li-rich Giant in the Globular Cluster NGC 362. *ApJL 801*(2), L32.

D'Orazi, V., R. G. Gratton, G. C. Angelou, A. Bragaglia, E. Carretta, J. C. Lattanzio, S. Lucatello, Y. Momany, A. Sollima, and G. Beccari (2015, June). Lithium abundances in globular cluster giants: NGC 1904, NGC 2808, and NGC 362. *MNRAS 449*(4), 4038–4047.

D'Orazi, V. and A. F. Marino (2010, June). Lithium Abundances in Red Giants of M4: Evidence for Asymptotic Giant Branch Star Pollution in Globular Clusters? *ApJL 716*(2), L166–L169.

Drake, J. J., V. V. Smith, and N. B. Suntzeff (1992, August). Sodium, Aluminum, and Oxygen Abundance Variations in Giants in the Globular Cluster M4. *ApJL 395*, L95.

Dufton, P. L., R. S. I. Ryans, S. Simón-Díaz, C. Trundle, and D. J. Lennon (2006, May). B-type supergiants in the Small Magellanic Cloud: rotational velocities and implications for evolutionary models. *A&A 451*(2), 603–611.

Ernandes, H., B. Barbuy, A. C. S. Friaça, V. Hill, M. Zoccali, D. Minniti, A. Renzini, and S. Ortolani (2020, August). Cobalt and copper abundances in 56 Galactic bulge red giants. *A&A 640*, A89.

Fernández-Alvar, E., L. Carigi, W. J. Schuster, C. R. Hayes, N. Ávila-Vergara, S. R. Majewski, C. Allende Prieto, T. C. Beers, S. F. Sánchez, O. Zamora, D. A. García-Hernández, B. Tang, J. G. Fernández-Trincado, P. Tissera, D. Geisler, and S. Villanova (2018, January). Disentangling the Galactic Halo with APOGEE. II. Chemical and Star Formation Histories for the Two Distinct Populations. *ApJ 852*(1), 50.

Fernández-Trincado, J. G., T. C. Beers, B. Barbuy, D. Minniti, C. Chiappini, E. R. Garro, B. Tang, A. Alves-Brito, S. Villanova, D. Geisler, R. R. Lane, and D. G. Diaz (2022, July). Galactic ArchaeoLogIcaL ExcavatiOns (GALILEO). I. An updated census of APOGEE N-rich giants across the Milky Way. *A&A 663*, A126.

Freeman, K. and J. Bland-Hawthorn (2002, January). The New Galaxy: Signatures of Its Formation. *ARA&A 40*, 487–537.

Fu, X., A. Bressan, P. Molaro, and P. Marigo (2015, September). Lithium evolution in metal-poor stars: from pre-main sequence to the Spite plateau. *MNRAS 452*(3), 3256–3265.

Gaia Collaboration, A. G. A. Brown, A. Vallenari, T. Prusti, J. H. J. de Bruijne, C. Babusiaux, M. Biermann, O. L. Creevey, D. W. Evans, L. Eyer, A. Hutton, F. Jansen, C. Jordi, S. A. Klioner, U. Lammers, L. Lindegren, X. Luri, F. Mignard, C. Panem, D. Pourbaix, S. Randich, P. Sartoretti, C. Soubiran, N. A. Walton, F. Arenou, C. A. L. Bailer-Jones, U. Bastian, M. Cropper, R. Drimmel, D. Katz, M. G. Lattanzi, F. van Leeuwen, J. Bakker, C. Cacciari, J. Castañeda, F. De Angeli, C. Ducourant, C. Fabricius, M. Fouesneau, Y. Frémat, R. Guerra, A. Guerrier, J. Guiraud, A. Jean-Antoine Piccolo, E. Masana, R. Messineo, N. Mowlavi, C. Nicolas, K. Nienartowicz, F. Pailler, P. Panuzzo, F. Riclet, W. Roux, G. M. Seabroke, R. Sordo, P. Tanga, F. Thévenin, G. Gracia-Abril, J. Portell, D. Teyssier, M. Altmann, R. Andrae, I. Bellas-Velidis, K. Benson, J. Berthier, R. Blomme, E. Brugaletta, P. W. Burgess, G. Busso, B. Carry, A. Cellino, N. Cheek, G. Clementini, Y. Damerdji, M. Davidson, L. Delchambre, A. Dell'Oro, J. Fernández-Hernández, L. Galluccio, P. García-Lario, M. Garcia-Reinaldos, J. González-Núñez, E. Gosset, R. Haigron, J. L. Halbwachs, N. C. Hambly, D. L. Harrison, D. Hatzidimitriou, U. Heiter, J. Hernández, D. Hestroffer, S. T. Hodgkin, B. Holl, K. Janßen, G. Jevardat de Fombelle, S. Jordan, A. Krone-Martins, A. C. Lanzafame, W. Löffler, A. Lorca, M. Manteiga, O. Marchal, P. M. Marrese, A. Moitinho, A. Mora, K. Muinonen, P. Osborne, E. Pancino, T. Pauwels, J. M. Petit, A. Recio-Blanco, P. J. Richards, M. Riello, L. Rimoldini, A. C. Robin, T. Roegiers, J. Rybizki, L. M. Sarro, C. Siopis, M. Smith, A. Sozzetti, A. Ulla, E. Utrilla, M. van Leeuwen, W. van Reeven, U. Abbas, A. Abreu Aramburu, S. Accart, C. Aerts, J. J. Aguado, M. Ajaj, G. Altavilla, M. A. Álvarez, J. Álvarez Cid-Fuentes, J. Alves, R. I. Anderson, E. Anglada Varela, T. Antoja, M. Audard,

D. Baines, S. G. Baker, L. Balaguer-Núñez, E. Balbinot, Z. Balog, C. Barache, D. Barbato, M. Barros, M. A. Barstow, S. Bartolomé, J. L. Bassilana, N. Bauchet, A. Baudesson-Stella, U. Becciani, M. Bellazzini, M. Bernet, S. Bertone, L. Bianchi, S. Blanco-Cuaresma, T. Boch, A. Bombrun, D. Bossini, S. Bouquillon, A. Bragaglia, L. Bramante, E. Breedt, A. Bressan, N. Brouillet, B. Bucciarelli, A. Burlacu, D. Busonero, A. G. Butkevich, R. Buzzi, E. Caffau, R. Cancelliere, H. Cánovas, T. Cantat-Gaudin, R. Carballo, T. Carlucci, M. I. Carnerero, J. M. Carrasco, L. Casamiquela, M. Castellani, A. Castro-Ginard, P. Castro Sampol, L. Chaoul, P. Charlot, L. Chemin, A. Chiavassa, M. R. L. Cioni, G. Comoretto, W. J. Cooper, T. Cornez, S. Cowell, F. Crifo, M. Crosta, C. Crowley, C. Dafonte, A. Dapergolas, M. David, P. David, P. de Laverny, F. De Luise, R. De March, J. De Ridder, R. de Souza, P. de Teodoro, A. de Torres, E. F. del Peloso, E. del Pozo, M. Delbo, A. Delgado, H. E. Delgado, J. B. Delisle, P. Di Matteo, S. Diakite, C. Diener, E. Distefano, C. Dolding, D. Eappachen, B. Edvardsson, H. Enke, P. Esquej, C. Fabre, M. Fabrizio, S. Faigler, G. Fedorets, P. Fernique, A. Fienga, F. Figueras, C. Fouron, F. Fragkoudi, E. Fraile, F. Franke, M. Gai, D. Garabato, A. Garcia-Gutierrez, M. García-Torres, A. Garofalo, P. Gavras, E. Gerlach, R. Geyer, P. Giacobbe, G. Gilmore, S. Girona, G. Giuffrida, R. Gomel, A. Gomez, I. Gonzalez-Santamaria, J. J. González-Vidal, M. Granvik, R. Gutiérrez-Sánchez, L. P. Guy, M. Hauser, M. Haywood, A. Helmi, S. L. Hidalgo, T. Hilger, N. Hładczuk, D. Hobbs, G. Holland, H. E. Huckle, G. Jasniewicz, P. G. Jonker, J. Juaristi Campillo, F. Julbe, L. Karbevska, P. Kervella, S. Khanna, A. Kochoska, M. Kontizas, G. Kordopatis, A. J. Korn, Z. Kostrzewa-Rutkowska, K. Kruszyńska, S. Lambert, A. F. Lanza, Y. Lasne, J. F. Le Campion, Y. Le Fustec, Y. Lebreton, T. Lebzelter, S. Leccia, N. Leclerc, I. Lecoeur-Taibi, S. Liao, E. Licata, E. P. Lindstrøm, T. A. Lister, E. Livanou, A. Lobel, P. Madrero Pardo, S. Managau, R. G. Mann, J. M. Marchant, M. Marconi, M. M. S. Marcos Santos, S. Marinoni, F. Marocco, D. J. Marshall, L. Martin Polo, J. M. Martín-Fleitas, A. Masip, D. Massari, A. Mastrobuono-Battisti, T. Mazeh, P. J. McMillan, S. Messina, D. Michalik, N. R. Millar, A. Mints, D. Molina, R. Molinaro, L. Molnár, P. Montegriffo, R. Mor, R. Morbidelli, T. Morel, D. Morris, A. F. Mulone, D. Munoz, T. Muraveva, C. P. Murphy, I. Musella, L. Noval, C. Ordénovic, G. Orrù, J. Osinde, C. Pagani, I. Pagano, L. Palaversa, P. A. Palicio, A. Panahi, M. Pawlak, X. Peñalosa Esteller, A. Penttilä, A. M. Piersimoni, F. X. Pineau, E. Plachy, G. Plum, E. Poggio, E. Poretti, E. Poujoulet, A. Prša, L. Pulone, E. Racero, S. Ragaini, M. Rainer, C. M. Raiteri, N. Rambaux, P. Ramos, M. Ramos-Lerate, P. Re Fiorentin, S. Regibo, C. Reylé, V. Ripepi, A. Riva,

G. Rixon, N. Robichon, C. Robin, M. Roelens, L. Rohrbasser, M. Romero-Gómez, N. Rowell, F. Royer, K. A. Rybicki, G. Sadowski, A. Sagristà Sellés, J. Sahlmann, J. Salgado, E. Salguero, N. Samaras, V. Sanchez Gimenez, N. Sanna, R. Santoveña, M. Sarasso, M. Schultheis, E. Sciacca, M. Segol, J. C. Segovia, D. Ségransan, D. Semeux, S. Shahaf, H. I. Siddiqui, A. Siebert, L. Siltala, E. Slezak, R. L. Smart, E. Solano, F. Solitro, D. Souami, J. Souchay, A. Spagna, F. Spoto, I. A. Steele, H. Steidelmüller, C. A. Stephenson, M. Süveges, L. Szabados, E. Szegedi-Elek, F. Taris, G. Tauran, M. B. Taylor, R. Teixeira, W. Thuillot, N. Tonello, F. Torra, J. Torra, C. Turon, N. Unger, M. Vaillant, E. van Dillen, O. Vanel, A. Vecchiato, Y. Viala, D. Vicente, S. Voutsinas, M. Weiler, T. Wevers, Ł. Wyrzykowski, A. Yoldas, P. Yvard, H. Zhao, J. Zorec, S. Zucker, C. Zurbach, and T. Zwitter (2021, May). Gaia Early Data Release 3. Summary of the contents and survey properties. *A&A 649*, A1.

Gallagher, A. (1967, May). Oscillator Strengths of Ca II, Sr II, and Ba II. *Physical Review 157*(1), 24–30.

Gieles, M., C. Charbonnel, M. G. H. Krause, V. Hénault-Brunet, O. Agertz, H. J. G. L. M. Lamers, N. Bastian, A. Gualandris, A. Zocchi, and J. A. Petts (2018, August). Concurrent formation of supermassive stars and globular clusters: implications for early self-enrichment. *MNRAS 478*(2), 2461–2479.

Gratton, R., A. Bragaglia, E. Carretta, V. D'Orazi, S. Lucatello, and A. Sollima (2019, November). What is a globular cluster? An observational perspective. *A&ARv 27*(1), 8.

Gratton, R., C. Sneden, and E. Carretta (2004, September). Abundance Variations Within Globular Clusters. *ARA&A 42*(1), 385–440.

Gratton, R. G., P. Bonifacio, A. Bragaglia, E. Carretta, V. Castellani, M. Centurion, A. Chieffi, R. Claudi, G. Clementini, F. D'Antona, S. Desidera, P. François, F. Grundahl, S. Lucatello, P. Molaro, L. Pasquini, C. Sneden, F. Spite, and O. Straniero (2001, April). The O-Na and Mg-Al anticorrelations in turn-off and early subgiants in globular clusters. *A&A 369*, 87–98.

Gratton, R. G. and E. Carretta (2010, October). Diluting the material forming the second generation stars in globular clusters: the contribution by unevolved stars. *A&A 521*, A54.

Gratton, R. G., E. Carretta, and A. Bragaglia (2012, February). Multiple populations in globular clusters. Lessons learned from the Milky Way globular clusters. *A&ARv 20*, 50.

Gratton, R. G., E. Carretta, S. Desidera, S. Lucatello, P. Mazzei, and M. Barbieri (2003, July). Abundances for metal-poor stars with accurate parallaxes. II. alpha -elements in the halo. *A&A 406*, 131–140.

Gratton, R. G., E. Carretta, K. Eriksson, and B. Gustafsson (1999, October). Abundances of light elements in metal-poor stars. II. Non-LTE abundance corrections. *A&A 350*, 955–969.

Gratton, R. G., C. Sneden, E. Carretta, and A. Bragaglia (2000, February). Mixing along the red giant branch in metal-poor field stars. *A&A 354*, 169–187.

Grillmair, C. J. and O. Dionatos (2006, May). Detection of a 63° Cold Stellar Stream in the Sloan Digital Sky Survey. *ApJL 643*(1), L17–L20.

Grundahl, F., M. Catelan, W. B. Landsman, P. B. Stetson, and M. I. Andersen (1999, October). Hot Horizontal-Branch Stars: The Ubiquitous Nature of the "Jump" in Strömgren u, Low Gravities, and the Role of Radiative Levitation of Metals. *ApJ 524*(1), 242–261.

Gruyters, P., A. J. Korn, O. Richard, F. Grundahl, R. Collet, L. I. Mashonkina, Y. Osorio, and P. S. Barklem (2013, July). Atomic diffusion and mixing in old stars. IV. Weak abundance trends in the globular cluster NGC 6752. *A&A 555*, A31.

Gruyters, P., T. Nordlander, and A. J. Korn (2014, July). Atomic diffusion and mixing in old stars. V. A deeper look into the globular cluster NGC 6752. *A&A 567*, A72.

Harris, W. E. (1996, October). A Catalog of Parameters for Globular Clusters in the Milky Way. *AJ 112*, 1487.

Harris, W. E. (2010, December). A New Catalog of Globular Clusters in the Milky Way. *arXiv e-prints*, arXiv:1012.3224.

Horta, D., R. P. Schiavon, J. T. Mackereth, T. C. Beers, J. G. Fernández-Trincado, P. M. Frinchaboy, D. A. García-Hernández, D. Geisler, S. Hasselquist, H. Jönsson, R. R. Lane, S. R.

Majewski, S. Mészáros, C. M. Bidin, D. M. Nataf, A. Roman-Lopes, C. Nitschelm, J. Vargas-González, and G. Zasowski (2020, April). The chemical compositions of accreted and in situ galactic globular clusters according to SDSS/APOGEE. *MNRAS 493*(3), 3363–3378.

Ishigaki, M. N., W. Aoki, and M. Chiba (2013, July). Chemical Abundances of the Milky Way Thick Disk and Stellar Halo. II. Sodium, Iron-peak, and Neutron-capture Elements. *ApJ 771*(1), 67.

Karakas, A. I. (2010, January). Nucleosynthesis of Low and Intermediate-mass Stars. In *Principles and Perspectives in Cosmochemistry*, Volume 16 of *Astrophysics and Space Science Proceedings*, pp. 107.

Karakas, A. I. (2011, September). Current Status of Stellar Evolutionary Models for AGB Stars. In F. Kerschbaum, T. Lebzelter, and R. F. Wing (Eds.), *Why Galaxies Care about AGB Stars II: Shining Examples and Common Inhabitants*, Volume 445 of *Astronomical Society of the Pacific Conference Series*, pp. 3.

Karakas, A. I., D. A. García-Hernández, and M. Lugaro (2012, May). Heavy Element Nucleosynthesis in the Brightest Galactic Asymptotic Giant Branch Stars. *ApJ 751*(1), 8.

Karakas, A. I. and J. C. Lattanzio (2014, July). The Dawes Review 2: Nucleosynthesis and Stellar Yields of Low- and Intermediate-Mass Single Stars. *PASA 31*, e030.

Karakas, A. I., M. Lugaro, M. Carlos, B. Cseh, D. Kamath, and D. A. García-Hernández (2018, June). Heavy-element yields and abundances of asymptotic giant branch models with a Small Magellanic Cloud metallicity. *MNRAS 477*(1), 421–437.

Kasen, D., B. Metzger, J. Barnes, E. Quataert, and E. Ramirez-Ruiz (2017, November). Origin of the heavy elements in binary neutron-star mergers from a gravitational-wave event. *Nature 551*(7678), 80–84.

Kirby, E. N., G. Duggan, E. Ramirez-Ruiz, and P. Macias (2020, March). The Stars in M15 Were Born with the r-process. *ApJL 891*(1), L13.

Kobayashi, C., A. I. Karakas, and M. Lugaro (2020, September). The Origin of Elements from Carbon to Uranium. *ApJ 900*(2), 179.

Kobayashi, C., T. Tsujimoto, K. Nomoto, I. Hachisu, and M. Kato (1998, August). Low-Metallicity Inhibition of Type IA Supernovae and Galactic and Cosmic Chemical Evolution. *ApJL 503*(2), L155–L159.

Koch, A., E. K. Grebel, and S. L. Martell (2019, May). Purveyors of fine halos: Re-assessing globular cluster contributions to the Milky Way halo buildup with SDSS-IV. *A&A 625*, A75.

Korn, A. J., F. Grundahl, O. Richard, L. Mashonkina, P. S. Barklem, R. Collet, B. Gustafsson, and N. Piskunov (2007, December). Atomic Diffusion and Mixing in Old Stars. I. Very Large Telescope FLAMES-UVES Observations of Stars in NGC 6397. *ApJ 671*(1), 402–419.

Kroupa, P., M. G. Petr, and M. J. McCaughrean (1999, December). Binary stars in young clusters: models versus observations of the Trapezium Cluster. 4(7), 495–519.

Kurucz, R. (1993, January). ATLAS9 Stellar Atmosphere Programs and 2 km/s grid. *ATLAS9 Stellar Atmosphere Programs and 2 km/s grid. Kurucz CD-ROM No. 13. Cambridge 13*.

Kurucz, R. L. (1992, January). Model Atmospheres for Population Synthesis. In B. Barbuy and A. Renzini (Eds.), *The Stellar Populations of Galaxies*, Volume 149 of *International Astronomical Union / Union Astronomique Internationale*, pp. 225.

Kurucz, R. L. and B. Bell (1995). *Atomic line list*. Cambridge: SAO.

Lada, C. J. and E. A. Lada (2003, January). Embedded Clusters in Molecular Clouds. *ARA&A 41*, 57–115.

Langer, G. E. (1985, May). Bimodal cyanogen distributions in moderately metal-poor globular clusters. II. Evidence for "mixing" and "saturation". *PASP 97*, 382–392.

Lattanzio, J. C., L. Siess, R. P. Church, G. Angelou, R. J. Stancliffe, C. L. Doherty, T. Stephen, and S. W. Campbell (2015, January). On the numerical treatment and dependence of thermohaline mixing in red giants. *MNRAS 446*(3), 2673–2688.

Lawler, J. E., M. E. Wickliffe, E. A. den Hartog, and C. Sneden (2001, December). Improved Laboratory Transition Parameters forEu II and Application to the Solar Europium Elemental and Isotopic Composition. *ApJ 563*(2), 1075–1088.

Lee, J.-W. (2015, July). Multiple Stellar Populations of Globular Clusters from Homogeneous Ca by Photometry. I. M22 (NGC 6656). *ApJS 219*(1), 7.

Lee, Y.-W., J. J. Kim, C. I. Johnson, C. Chung, S. Jang, D. Lim, and Y. Kang (2019, jun). The globular cluster origin of the milky way outer bulge: Evidence from sodium bimodality. *The Astrophysical Journal Letters 878*(1), L2.

Legnardi, M. V., A. P. Milone, L. Armillotta, A. F. Marino, G. Cordoni, A. Renzini, E. Vesperini, F. D'Antona, M. McKenzie, D. Yong, E. Dondoglio, E. P. Lagioia, M. Carlos, M. Tailo, S. Jang, and A. Mohandasan (2022, June). Constraining the original composition of the gas forming first-generation stars in globular clusters. *MNRAS 513*(1), 735–751.

Limongi, M. and A. Chieffi (2018, July). Presupernova Evolution and Explosive Nucleosynthesis of Rotating Massive Stars in the Metallicity Range -3 $\leq$ [Fe/H] $\leq$ 0. *ApJS 237*(1), 13.

Lind, K., M. Asplund, and P. S. Barklem (2009, August). Departures from LTE for neutral Li in late-type stars. *A&A 503*(2), 541–544.

Lind, K., M. Asplund, P. S. Barklem, and A. K. Belyaev (2011, April). Non-LTE calculations for neutral Na in late-type stars using improved atomic data. *A&A 528*, A103.

Lucatello, S., A. Sollima, R. Gratton, E. Vesperini, V. D'Orazi, E. Carretta, and A. Bragaglia (2015, December). The incidence of binaries in globular cluster stellar populations. *A&A 584*, A52.

Lugaro, M., A. I. Karakas, and S. Bisterzo (2008, January). Models and observations of the s process in AGB stars. In *Nuclei in the Cosmos (NIC X)*, pp. E34.

Magrini, L., R. Smiljanic, E. Franciosini, L. Pasquini, S. Randich, G. Casali, C. Viscasillas Vázquez, A. Bragaglia, L. Spina, K. Biazzo, G. Tautvaišienė, T. Masseron, M. Van der Swaelmen, E. Pancino, F. Jiménez-Esteban, G. Guiglion, S. Martell, T. Bensby, V. D'Orazi, M. Baratella, A. Korn, P. Jofre, G. Gilmore, C. Worley, A. Hourihane, A. Gonneau, G. G. Sacco, and L. Morbidelli (2021, November). Gaia-ESO survey: Lithium abundances in open cluster Red Clump stars. *A&A 655*, A23.

Marino, A. F., A. P. Milone, G. Piotto, S. Villanova, L. R. Bedin, A. Bellini, and A. Renzini (2009, October). A double stellar generation in the globular cluster NGC 6656 (M 22). Two stellar groups with different iron and s-process element abundances. *A&A 505*(3), 1099–1113.

Marino, A. F., A. P. Milone, A. Renzini, F. D'Antona, J. Anderson, L. R. Bedin, A. Bellini, G. Cordoni, E. P. Lagioia, G. Piotto, and M. Tailo (2019, August). The Hubble Space Telescope UV Legacy Survey of Galactic Globular Clusters - XIX. A chemical tagging of the multiple stellar populations over the chromosome maps. *MNRAS 487*(3), 3815–3844.

Marino, A. F., C. Sneden, R. P. Kraft, G. Wallerstein, J. E. Norris, G. Da Costa, A. P. Milone, I. I. Ivans, G. Gonzalez, J. P. Fulbright, M. Hilker, G. Piotto, M. Zoccali, and P. B. Stetson (2011, August). The two metallicity groups of the globular cluster M 22: a chemical perspective. *A&A 532*, A8.

Marks, M., P. Kroupa, J. Dabringhausen, and M. S. Pawlowski (2012, May). Evidence for top-heavy stellar initial mass functions with increasing density and decreasing metallicity. *MNRAS 422*(3), 2246–2254.

Martell, S. L., J. P. Smolinski, T. C. Beers, and E. K. Grebel (2011, October). Building the Galactic halo from globular clusters: evidence from chemically unusual red giants. *A&A 534*, A136.

Martins, F., W. Chantereau, and C. Charbonnel (2021, June). Maximum helium content of multiple populations in the globular cluster NGC 6752. *A&A 650*, A162.

Massari, D., H. H. Koppelman, and A. Helmi (2019, October). Origin of the system of globular clusters in the Milky Way. *A&A 630*, L4.

Masseron, T., D. A. García-Hernández, S. Mészáros, O. Zamora, F. Dell'Agli, C. Allende Prieto, B. Edvardsson, M. Shetrone, B. Plez, J. G. Fernández-Trincado, K. Cunha, H. Jönsson, D. Geisler, T. C. Beers, and R. E. Cohen (2019, February). Homogeneous analysis of globular clusters from the APOGEE survey with the BACCHUS code. I. The northern clusters. *A&A 622*, A191.

Matteucci, F., M. Molero, D. S. Aguado, and D. Romano (2021, July). The evolution of Lithium: implications of a universal Spite plateau. *MNRAS 505*(1), 200–206.

McClure, R. D. (1984, feb). The barium stars. *Publications of the Astronomical Society of the Pacific 96*(576), 117.

Mészáros, S., T. Masseron, D. A. García-Hernández, C. Allende Prieto, T. C. Beers, D. Bizyaev, D. Chojnowski, R. E. Cohen, K. Cunha, F. Dell'Agli, G. Ebelke, J. G. Fernández-Trincado, P. Frinchaboy, D. Geisler, S. Hasselquist, F. Hearty, J. Holtzman, J. Johnson, R. R. Lane, I. Lacerna, P. Longa-Peña, S. R. Majewski, S. L. Martell, D. Minniti, D. Nataf, D. L. Nidever, K. Pan, R. P. Schiavon, M. Shetrone, V. V. Smith, J. S. Sobeck, G. S. Stringfellow, L. Szigeti, B. Tang, J. C. Wilson, and O. Zamora (2020, February). Homogeneous analysis of globular clusters from the APOGEE survey with the BACCHUS code - II. The Southern clusters and overview. *MNRAS 492*(2), 1641–1670.

Meynet, G., S. Ekström, and A. Maeder (2006, February). The early star generations: the dominant effect of rotation on the CNO yields. *A&A 447*(2), 623–639.

Milone, A. P., A. F. Marino, F. D'Antona, L. R. Bedin, G. Piotto, H. Jerjen, J. Anderson, A. Dotter, M. di Criscienzo, and E. P. Lagioia (2017, March). Multiple stellar populations in Magellanic Cloud clusters - V. The split main sequence of the young cluster NGC 1866. *MNRAS 465*(4), 4363–4374.

Milone, A. P., G. Piotto, I. R. King, L. R. Bedin, J. Anderson, A. F. Marino, Y. Momany, L. Malavolta, and S. Villanova (2010, February). Multiple Stellar Populations in the Galactic Globular Cluster NGC 6752. *ApJ 709*(2), 1183–1194.

Milone, A. P., G. Piotto, A. Renzini, A. F. Marino, L. R. Bedin, E. Vesperini, F. D'Antona, D. Nardiello, J. Anderson, I. R. King, D. Yong, A. Bellini, A. Aparicio, B. Barbuy, T. M. Brown, S. Cassisi, S. Ortolani, M. Salaris, A. Sarajedini, and R. P. van der Marel (2017, January). The Hubble Space Telescope UV Legacy Survey of Galactic globular clusters - IX. The Atlas of multiple stellar populations. *MNRAS 464*(3), 3636–3656.

Minelli, A., A. Mucciarelli, D. Massari, M. Bellazzini, D. Romano, and F. R. Ferraro (2021, September). A New Set of Chisels for Galactic Archeology: Sc, V, and Zn as Taggers of Accreted Globular Clusters. *ApJL 918*(2), L32.

Molero, M., L. Magrini, F. Matteucci, D. Romano, M. Palla, G. Cescutti, C. Viscasillas Vázquez, and E. Spitoni (2023, April). Origin of neutron capture elements with the Gaia-ESO survey: the evolution of s- and r-process elements across the Milky Way. *arXiv e-prints*, arXiv:2304.06452.

Mori, K., M. Kusakabe, A. B. Balantekin, T. Kajino, and M. A. Famiano (2021, May). Enhancement of lithium in red clump stars by the additional energy loss induced by new physics. *MNRAS 503*(2), 2746–2753.

Mucciarelli, A. (2011, April). Microturbulent velocity from stellar spectra: a comparison between different approaches. *A&A 528*, A44.

Mucciarelli, A. and P. Bonifacio (2020, August). Facing problems in the determination of stellar temperatures and gravities: Galactic globular clusters. *A&A 640*, A87.

Mucciarelli, A., L. Monaco, P. Bonifacio, M. Salaris, I. Saviane, B. Lanzoni, Y. Momany, and G. Lo Curto (2021, August). Curiouser and curiouser: the peculiar chemical composition of the Li- and Na-rich star in ω Centauri. *A&A 652*, A139.

Mucciarelli, A., M. Salaris, and P. Bonifacio (2012, January). Giants reveal what dwarfs conceal: Li abundance in lower red giant branch stars as diagnostic of the primordial Li. *MNRAS 419*(3), 2195–2205.

Mucciarelli, A., M. Salaris, P. Bonifacio, L. Monaco, and S. Villanova (2014, October). The cosmological lithium problem outside the Galaxy: the Sagittarius globular cluster M54. *MNRAS 444*(2), 1812–1820.

Mucciarelli, A., M. Salaris, L. Lovisi, F. R. Ferraro, B. Lanzoni, S. Lucatello, and R. G. Gratton (2011, March). Lithium abundance in the globular cluster M4: from the turn-off to the red giant branch bump. *MNRAS 412*(1), 81–94.

Nordlander, T. and K. Lind (2017, November). Non-LTE aluminium abundances in late-type stars. *A&A 607*, A75.

Norris, J., P. L. Cottrell, K. C. Freeman, and G. S. Da Costa (1981, February). The abundance spread in the giants of NGC 6752. *ApJ 244*, 205–220.

O'Connell, J. E., C. I. Johnson, C. A. Pilachowski, and G. Burks (2011, October). Chemical Abundances of Red Giant Stars in the Globular Cluster M107 (NGC 6171). *PASP 123*(908), 1139.

Odenkirchen, M., E. K. Grebel, W. Dehnen, H.-W. Rix, B. Yanny, H. J. Newberg, C. M. Rockosi, D. Martínez-Delgado, J. Brinkmann, and J. R. Pier (2003, November). The Extended Tails of Palomar 5: A 10° Arc of Globular Cluster Tidal Debris. *AJ 126*(5), 2385–2407.

Osborn, W. (1971, December). Two new CN-strong globular cluster stars. *The Observatory 91*, 223–224.

Otsuki, K., S. Honda, W. Aoki, T. Kajino, and G. J. Mathews (2006, April). Neutron-Capture Elements in the Metal-poor Globular Cluster M15. *ApJL 641*(2), L117–L120.

Peterson, R. C. (1980, May). Evidence from sodium-abundance variations among red giants of M 13 for inhomogeneities in the protocluster gas. *ApJL 237*, L87–L91.

Pietrinferni, A., S. Hidalgo, S. Cassisi, M. Salaris, A. Savino, A. Mucciarelli, K. Verma, V. Silva Aguirre, A. Aparicio, and J. W. Ferguson (2021, February). Updated BaSTI Stellar Evolution Models and Isochrones. II. α-enhanced Calculations. *ApJ 908*(1), 102.

Piotto, G., L. R. Bedin, J. Anderson, I. R. King, S. Cassisi, A. P. Milone, S. Villanova, A. Pietrinferni, and A. Renzini (2007, May). A Triple Main Sequence in the Globular Cluster NGC 2808. *ApJL 661*(1), L53–L56.

Placco, V. M., C. Sneden, I. U. Roederer, J. E. Lawler, E. A. Den Hartog, N. Hejazi, Z. Maas, and P. Bernath (2021, April). Linemake: An Atomic and Molecular Line List Generator. *Research Notes of the American Astronomical Society 5*(4), 92.

Popper, D. M. (1947, January). Spectral Types of Stars in the Globular Clusters Messier 3 and Messier 13. *ApJ 105*, 204.

Rain, M. J., S. Villanova, C. Munõz, and C. Valenzuela-Calderon (2019, February). Chemical evolution of the metal-poor globular cluster NGC 6809. *MNRAS 483*(2), 1674–1685.

Raiteri, C. M., R. Gallino, and M. Busso (1992, March). S-Processing in Massive Stars as a Function of Metallicity and Interpretation of Observational Trends. *ApJ 387*, 263.

Renzini, A. (2008, November). Origin of multiple stellar populations in globular clusters and their helium enrichment. *MNRAS 391*(1), 354–362.

Renzini, A., F. D'Antona, S. Cassisi, I. R. King, A. P. Milone, P. Ventura, J. Anderson, L. R. Bedin, A. Bellini, T. M. Brown, G. Piotto, R. P. van der Marel, B. Barbuy, E. Dalessandro, S. Hidalgo, A. F. Marino, S. Ortolani, M. Salaris, and A. Sarajedini (2015, December). The Hubble Space Telescope UV Legacy Survey of Galactic Globular Clusters - V. Constraints on formation scenarios. *MNRAS 454*(4), 4197–4207.

Renzini, A., A. F. Marino, and A. P. Milone (2022, June). The formation of globular clusters as a case of overcooling. *MNRAS 513*(2), 2111–2117.

Romano, D. and F. Matteucci (2007, June). Contrasting copper evolution in ω Centauri and the Milky Way. *MNRAS 378*(1), L59–L63.

Sanna, N., E. Franciosini, E. Pancino, A. Mucciarelli, M. Tsantaki, C. Charbonnel, R. Smiljanic, X. Fu, A. Bragaglia, N. Lagarde, G. Tautvaišiene, L. Magrini, S. Randich, T. Bensby, A. J. Korn, A. Bayo, M. Bergemann, G. Carraro, and L. Morbidelli (2020, July). The Gaia-ESO Survey: an extremely Li-rich giant in globular cluster NGC 1261. *A&A 639*, L2.

Schaller, G., D. Schaerer, G. Meynet, and A. Maeder (1992, December). New Grids of Stellar Models from 0.8-SOLAR-MASS to 120-SOLAR-MASSES at Z=0.020 and Z=0.001. *A&AS 96*, 269.

Shen, Z. X., P. Bonifacio, L. Pasquini, and S. Zaggia (2010, December). Li - O anti-correlation in NGC 6752: evidence for Li-enriched polluting gas. *A&A 524*, L2.

Shingles, L. J., A. I. Karakas, R. Hirschi, C. K. Fishlock, D. Yong, G. S. Da Costa, and A. F. Marino (2014, November). The s-Process Enrichment of the Globular Clusters M4 and M22. *ApJ 795*(1), 34.

Simmerer, J., C. Sneden, I. I. Ivans, R. P. Kraft, M. D. Shetrone, and V. V. Smith (2003, April). A Comparison of Copper Abundances in Globular Cluster and Halo Field Giant Stars. *AJ 125*(4), 2018–2028.

Skrutskie, M. F., R. M. Cutri, R. Stiening, M. D. Weinberg, S. Schneider, J. M. Carpenter, C. Beichman, R. Capps, T. Chester, J. Elias, J. Huchra, J. Liebert, C. Lonsdale, D. G. Monet,

S. Price, P. Seitzer, T. Jarrett, J. D. Kirkpatrick, J. E. Gizis, E. Howard, T. Evans, J. Fowler, L. Fullmer, R. Hurt, R. Light, E. L. Kopan, K. A. Marsh, H. L. McCallon, R. Tam, S. Van Dyk, and S. Wheelock (2006, February). The Two Micron All Sky Survey (2MASS). *AJ 131*(2), 1163–1183.

Smith, G. H. and J. Norris (1982, March). The cyanogen distributions in NGC 3201, M 55, and M 71. *ApJ 254*, 149–161.

Smith, G. H. and G. D. Wirth (1991, November). The Behavior of Magnesium and Sodium Lines Among Giants Within Bimodal-CN Globular Clusters. *PASP 103*, 1158.

Sneden, C. (1973, September). The nitrogen abundance of the very metal-poor star HD 122563. *ApJ 184*, 839.

Sneden, C., J. J. Cowan, and R. Gallino (2008, September). Neutron-capture elements in the early galaxy. *ARA&A 46*, 241–288.

Sneden, C., R. P. Kraft, C. F. Prosser, and G. E. Langer (1991, December). Oxygen Abundance in Halo Giants. I. Giants in the Very Metal-poor Globular Clusters M92 and M15 and the Metal-Poor Halo Field. *AJ 102*, 2001.

Sneden, C., R. P. Kraft, C. F. Prosser, and G. E. Langer (1992, December). Oxygen Abundances in Halo Giants. III. Giants in the Mildly Metal-Poor Globular Cluster M5. *AJ 104*, 2121.

Sobeck, J. S., R. P. Kraft, C. Sneden, G. W. Preston, J. J. Cowan, G. H. Smith, I. B. Thompson, S. A. Shectman, and G. S. Burley (2011, June). The Abundances of Neutron-capture Species in the Very Metal-poor Globular Cluster M15: A Uniform Analysis of Red Giant Branch and Red Horizontal Branch Stars. *AJ 141*(6), 175.

Sousa, S. G., N. C. Santos, G. Israelian, M. Mayor, and M. J. P. F. G. Monteiro (2007, July). A new code for automatic determination of equivalent widths: Automatic Routine for line Equivalent widths in stellar Spectra (ARES). *A&A 469*(2), 783–791.

Spite, M., F. Spite, E. Caffau, P. Bonifacio, and P. François (2022, November). Detailed analysis of a sample of field metal-poor N-rich dwarfs. *A&A 667*, A139.

Straniero, O., S. Cristallo, and L. Piersanti (2014, April). Heavy Elements in Globular Clusters: The Role of Asymptotic Giant Branch Stars. *ApJ 785*(1), 77.

Suda, T., Y. Katsuta, S. Yamada, T. Suwa, C. Ishizuka, Y. Komiya, K. Sorai, M. Aikawa, and M. Y. Fujimoto (2008, October). Stellar Abundances for the Galactic Archeology (SAGA) Database — Compilation of the Characteristics of Known Extremely Metal-Poor Stars. *PASJ 60*, 1159.

Vanbeveren, D., N. Mennekens, and J. P. De Greve (2012, July). The effect of intermediate-mass close binaries on the chemical evolution of globular clusters. *A&A 543*, A4.

VandenBerg, D. A., K. Brogaard, R. Leaman, and L. Casagrande (2013, October). The Ages of 55 Globular Clusters as Determined Using an Improved VÂB_TO Method along with Color-Magnitude Diagram Constraints, and Their Implications for Broader Issues. *ApJ 775*(2), 134.

Venn, K. A., M. Irwin, M. D. Shetrone, C. A. Tout, V. Hill, and E. Tolstoy (2004, September). Stellar Chemical Signatures and Hierarchical Galaxy Formation. *AJ 128*(3), 1177–1195.

Ventura, P. and F. D'Antona (2008, April). Self-enrichment by asymptotic giant branch stars in globular clusters: comparison between intermediate and high metallicities. *MNRAS 385*(4), 2034–2040.

Ventura, P. and F. D'Antona (2009, June). Massive AGB models of low metallicity: the implications for the self-enrichment scenario in metal-poor globular clusters. *A&A 499*(3), 835–846.

Ventura, P., F. D'Antona, M. Di Criscienzo, R. Carini, A. D'Ercole, and E. vesperini (2012, December). Super-AGB-AGB Evolution and the Chemical Inventory in NGC 2419. *ApJL 761*(2), L30.

Ventura, P., F. D'Antona, I. Mazzitelli, and R. Gratton (2001, March). Predictions for Self-Pollution in Globular Cluster Stars. *ApJL 550*(1), L65–L69.

Ventura, P., M. di Criscienzo, R. Schneider, R. Carini, R. Valiante, F. D'Antona, S. Gallerani, R. Maiolino, and A. Tornambé (2012, August). Dust formation around AGB and SAGB stars: a trend with metallicity? *MNRAS 424*(3), 2345–2357.

Villanova, S. and D. Geisler (2011, November). Bimodality of light and s-elements in M4 (NGC 6121). A hint for the massive main-sequence star pollution scenario. *A&A 535*, A31.

Wang, E. X., T. Nordlander, M. Asplund, A. M. Amarsi, K. Lind, and Y. Zhou (2021, January). 3D NLTE spectral line formation of lithium in late-type stars. *MNRAS 500*(2), 2159–2176.

Wehrhahn, A. (2021, March). PySME - Spectroscopy Made Easier. In *The 20.5th Cambridge Workshop on Cool Stars, Stellar Systems, and the Sun (CS20.5)*, Cambridge Workshop on Cool Stars, Stellar Systems, and the Sun, pp. 1.

Woody, T. and K. C. Schlaufman (2021, August). The Age-Metallicity-Specific Orbital Energy Relation for the Milky Way's Globular Cluster System Confirms the Importance of Accretion for Its Formation. *AJ 162*(2), 42.

Woosley, S. E. and T. A. Weaver (1995, November). The Evolution and Explosion of Massive Stars. II. Explosive Hydrodynamics and Nucleosynthesis. *ApJS 101*, 181.

Worley, C. C., V. Hill, J. Sobeck, and E. Carretta (2013, May). Ba and Eu abundances in M 15 giant stars. *A&A 553*, A47.

Yong, D., F. Grundahl, P. E. Nissen, H. R. Jensen, and D. L. Lambert (2005, August). Abundances in giant stars of the globular cluster NGC 6752. *A&A 438*(3), 875–888.

Yong, D., A. I. Karakas, D. L. Lambert, A. Chieffi, and M. Limongi (2008, December). Heavy Element Abundances in Giant Stars of the Globular Clusters M4 and M5. *ApJ 689*(2), 1031–1043.

Yong, D., I. U. Roederer, F. Grundahl, G. S. Da Costa, A. I. Karakas, J. E. Norris, W. Aoki, C. K. Fishlock, A. F. Marino, A. P. Milone, and L. J. Shingles (2014, July). Iron and neutron-capture element abundance variations in the globular cluster M2 (NGC 7089)*. *MNRAS 441*(4), 3396–3416.

Zhang, J., J.-R. Shi, H.-L. Yan, Y. Li, Q. Gao, C.-Q. Li, X. Zhang, S. Liu, S. Bi, G. Zhao, and Y. Li (2021, September). Lithium Evolution of Giant Stars Observed by LAMOST and Kepler. *ApJL 919*(1), L3.